

Joseph, Ijuptil Kwajighu (2025) *Mathematical modelling of active fluids in a channel*. PhD thesis

https://theses.gla.ac.uk/85589/

Copyright and moral rights for this work are retained by the author

A copy can be downloaded for personal non-commercial research or study, without prior permission or charge

This work cannot be reproduced or quoted extensively from without first obtaining permission from the author

The content must not be changed in any way or sold commercially in any format or medium without the formal permission of the author

When referring to this work, full bibliographic details including the author, title, awarding institution and date of the thesis must be given

Enlighten: Theses
https://theses.gla.ac.uk/
research-enlighten@glasgow.ac.uk

Mathematical Modelling of Active Fluids in a Channel

Ijuptil Kwajighu Joseph

Submitted in fulfilment of the requirements for the Degree of Doctor of Philosophy

School of Mathematics and Statistics

College of Science and Engineering

University of Glasgow



Abstract

Active fluids, such as active nematics, consist of self-driven units that convert energy into directed motion. Examples include suspensions of cytoskeletal filaments, motor proteins, bacteria, schools of fish, cellular layers, and cell tissues. This thesis presents a theoretical and computational study of active nematics using an adapted Ericksen-Leslie dynamical theory, with a focus on understanding how activity, external fields, and geometry influence flow and director patterns in confined systems. In one dimension, we investigate the effects of an orienting field on extensile and contractile nematics under planar and homeotropic anchoring. Extensile systems with planar anchoring exhibit minimal director distortion, whereas contractile systems display significant distortion when the orienting field exceeds a threshold from the initial homeotropic alignment. A kickback effect is observed in contractile nematics, which diminishes in extensile systems as activity increases. Nonlinear analyses reveal uniform, symmetric, and antisymmetric states, with activity enhancing flow and inducing bistability in contractile systems. In two-dimensional channels, we analyse the influence of activity and non-constant boundary conditions. Under inlet/outlet normal flow conditions, low activities produce localised flows, while higher activities generate spatial fluctuations in contractile systems. Extensile nematics at high activity exhibit transitions from unidirectional to bidirectional flow. For inlet/outlet periodic conditions, the system behaviour is similar to that under normal flow conditions. Variation in the splay-to-bend elastic constant ratio leads to transitions from positive to negative flux, demonstrating that active stresses can dominate elastic forces and produce unidirectional flow with positive flux for extensile systems. We also explore time-dependent boundary conditions as a conceptual demonstration of object sensing, showing that the speed of anchoring transitions affects flow patterns: slower transitions delay system activation, while faster transitions reduce bidirectional flows. These results indicate that small local disturbances can produce large-scale flows. In a biological context, such as wound healing, the tissue edge acts as a dynamic boundary where cells actively migrate and reorganise. Our findings on time-dependent boundary anchoring and activity-driven flows suggest that localised changes at wound margins can trigger large-scale tissue flows, mimicking the collective migration observed during wound closure. Overall, this work provides a theoretical framework for understanding how activity and confinement can be harnessed in systems that respond sensitively to local perturbations, highlighting potential applications for active-nematic-based sensing.

Contents

Α	bstra	ct			:
D	Dedication xive Acknowledgements xvi Declaration xvi				
\mathbf{A}_{0}					
D					
\mathbf{A}	bbre	viation	ıs		xviii
1	Intr	oduct	ion: Pass	sive and Active Liquid Crystals	1
	1.1	Histor	ical backg	ground of liquid crystals	. 5
		1.1.1	Synthesi	is of liquid crystals and their phase formation	. 5
		1.1.2	Mathem	atical foundations of liquid crystals	. 8
		1.1.3	Classific	ation of liquid crystals	. 9
			1.1.3.1	Nematic liquid crystals	. 10
			1.1.3.2	Smectic liquid crystals	. 11
			1.1.3.3	Cholesteric liquid crystals	. 12
	1.2	Active	e fluids .		. 12
		1.2.1	Classific	ations of active fluids	. 13
			1.2.1.1	Classification based on damping	. 14
			1.2.1.2	Classification based on symmetry	. 15
		1.2.2	Low Rey	ynolds number flow of active fluids	. 15

		1.2.3	Hydrodynamic instabilities in active fluids	20
	1.3	Active	e nematics	22
		1.3.1	Hydrodynamics of active nematics	23
		1.3.2	Kickback and backflow mechanisms	30
		1.3.3	Fréedericksz transition	31
			1.3.3.1 D- and S-modes in active hydrodynamic instabilities .	32
	1.4	Active	e nematics in confinement	35
	1.5	Exper	imental observations of active fluids	38
	1.6	Sensor	rs and sensing devices	40
		1.6.1	ERF sensors	40
		1.6.2	MRF Sensors	42
		1.6.3	Liquid crystal biosensors	43
		1.6.4	Toward active nematic-based sensors	44
2	The	eoretic	al Frameworks for Passive and Active Nematic Liquid Crys-	
2	The tals		al Frameworks for Passive and Active Nematic Liquid Crys-	46
2				
2	tals	Introd	uction	46
2	tals	Introd Frank	luction	46
2	tals 2.1 2.2	Introd Frank Electr	luction	46 46 47
2	tals 2.1 2.2 2.3	Introd Frank Electr	luction	46 46 47 57
2	tals 2.1 2.2 2.3	Introd Frank Electr Ericks	duction	46 46 47 57 59
2	tals 2.1 2.2 2.3	Introd Frank Electr Ericks 2.4.1	luction	46 46 47 57 59
2	tals 2.1 2.2 2.3	Introd Frank Electr Ericks 2.4.1 2.4.2	duction	46 46 47 57 59 59
2	tals 2.1 2.2 2.3	Introd Frank Electr Ericks 2.4.1 2.4.2 2.4.3	duction	466 477 577 599 656
2	tals 2.1 2.2 2.3	Introd Frank Electr Ericks 2.4.1 2.4.2 2.4.3 2.4.4	duction	466 477 577 599 656 666 677
2	tals 2.1 2.2 2.3	Introd Frank: Electr Ericks 2.4.1 2.4.2 2.4.3 2.4.4 2.4.5	duction	466 477 577 599 656 666 677 688
2	tals 2.1 2.2 2.3 2.4	Introd Frank Electr Ericks 2.4.1 2.4.2 2.4.3 2.4.4 2.4.5	duction	46 46 47 57 59 65 66 67 68

3	Епе	ects or	Activity on Kickback/Backhow in a One-dimensional Ge	; -
	ome	m etry		76
	3.1	Introd	uction	76
	3.2	Model	formulation	78
	3.3	Linear	analysis for activity-driven channel flow	81
		3.3.1	Linearising about planar alignment in the absence of an orienting	
			field	82
			3.3.1.1 Characteristic length and time scales	83
			3.3.1.2 Solution of the linearised system	85
		3.3.2	Linearising about planar alignment in the presence of an orienting	
			field	92
		3.3.3	Linearsing about homeotropic alignment in the absence of an ori-	
			enting field	97
	3.4	Nonlin	near analysis under planar alignment subject to an orienting field	103
		3.4.1	Finite difference approximation for Ericksen-Leslie equations	104
		3.4.2	Characterisation of the solution profiles	111
			3.4.2.1 Summary of transitions in the director distortion solution	s117
		3.4.3	Prediction of critical activity, ξ_{c2}	128
	3.5	Nonlin	near analysis of activity in a hybrid aligned nematic Channel	132
		3.5.1	Mathematical model	133
		3.5.2	Solution regimes for contractile and extensile active nematics	134
	3.6	Conclu	usions	136
		3.6.1	Linear analysis	136
		3.6.2	Nonlinear analysis	137
1	۸ ـ ـ ـ ـ ـ ـ ـ ـ ـ ـ ـ ـ ـ ـ ـ ـ ـ ـ ـ	:: <u>4</u>	and Competiis Effects in a True Dimensional Model in	_
4		v	and Geometric Effects in a Two-Dimensional Model in	
		nnel	restion.	139
	4.1		formulation	139
	4.2	IMOUN	formulation	140

	4.2.1	Governi	ng equations	141
	4.2.2	Boundar	ry conditions	146
4.3	Numer	rical calcu	alations I: normal flow conditions	148
	4.3.1	Effects o	of varying channel width	149
	4.3.2	Effects of	of varying activity strength and HAN region width for	
		contract	ile nematics	153
		4.3.2.1	Solution profiles for a fixed HAN region width and vary-	
			ing activity strengths	153
		4.3.2.2	Flux measurement for varying activity strength and HAN	
			region width	154
		4.3.2.3	Oscillatory flow for a fixed HAN region width	156
		4.3.2.4	Oscillatory flow measure for varying activity and HAN	
			region width	160
	4.3.3	Effects of	of varying activity strength and HAN region width for	
		extensile	e nematics	161
		4.3.3.1	Solution profiles for a fixed HAN region width and vary-	
			ing activity strength	161
		4.3.3.2	Flow measure for varying activity and fixed HAN region	
			width	163
		4.3.3.3	Flow profiles for varying activity and HAN region width	165
	4.3.4	Numeric	eal calculations II: periodic conditions	168
		4.3.4.1	Investigation of flow profiles for contractile nematics .	168
		4.3.4.2	Investigation of flow profiles for extensile nematics	170
	4.3.5	Effect of	f the elastic constant ratio on director orientation and	
		flow velo	ocity	173
		4.3.5.1	Flux measurement for varying splay/bend scaling ratio	179
		4.3.5.2	Tracking circulation relative to the splay/bend scaling	
			ratio	179
	4.3.6	Conclusi	ion	184

			4.3.6.1	Normal flow boundary conditions	184
			4.3.6.2	Periodic boundary conditions	185
5	Two	o-Dime	ensional '	Transient Flow during HAN State Formation	187
	5.1	Introd	uction		187
	5.2	Model	formulat	ion	188
		5.2.1	Transien	t flow for contractile active nematics	190
		5.2.2	Quantifi	cation of travelling waves	195
	5.3	Transi	ent flow f	or extensile active nematics	199
	5.4	Conclu	usions		201
6	Sun	nmary	and Fut	ure Work	205
	6.1	Summ	ary		205
	6.2	Future	e work		208
		6.2.1	Extension	ons to other active matter systems	208
		6.2.2	Higher-d	limensional and complex geometries	209
		6.2.3	Geometr	ric and activity-driven effects	209
		6.2.4	Transien	at dynamics and switch-on/off states	210
		6.2.5	Critical	assumptions and limitations	210
\mathbf{A}	ppen	dices			212
	A	Deriva	ation of the	ne 2D versions of the elastic free energy and dissipation	
		function	on		212
	В	Splay/	bend scal	ling ratio and their corresponding splay and bend elastic	
		consta	nts .		217

List of Tables

1.1	Table of parameter values	18
1.2	Reynolds numbers for 1D and 2D flows for weak and high activity cases.	19
6	Table of splay/bend scaling ratio, κ and their corresponding splay and	
	bend elastic constants	217

List of Figures

1.1	Sketches of traditional liquid crystal phases: nematic, smectic and cholesteric	e. 10
1.2	Schematic depicting an idealised nematic liquid crystal	11
1.3	A sketch showing some examples of active fluids	13
1.4	Schematic showing bacteria align into a nematic phase	23
1.5	Schematics of active particles: (a) polar particle, (b) apolar particle, and	
	(c) self-propelling particles	23
1.6	Snapshots of the director field (labeled A-D) where the colour represents	
	the scalar order parameter. Additionally, the vorticity field is displayed	
	with arrows indicating the velocity, and the $\pm 1/2$ and $\pm 1/2$ topological	
	defects are represented by red and blue colours, respectively. [105]	29
1.7	Geometry of the classical Fréedericksz transition, where θ is the director	
	angle, n makes with x -axis	32
1.8	Time evolution of director angle in a contractile active nematic	34
1.9	Sketches of the equilibrium director configurations	35
1.10	Plot showing the flow profiles for various activity parameter values	37
2.1	Graphical representations of the distortions of splay, twist, and bend and	
	their associated elastic constants, K_1 , K_2 and K_3	50
2.2	Schematic sketches of the local flow induced by the active systems	69
2.3	Geometry of the force dipole	70

3.1	Active nematic in a channel between two solid plates at $z = 0$ and $z = d$	
	with flow parallel to the x -direction	80
3.2	Plot of the function $r(q)$ as a function of q for $\xi = [-0.15, 0, 0.06]$ Pa.	
	The blue and black markers indicate the values of q_1 corresponding to	
	$\xi=-0.15$ Pa and $\xi=0.06$ Pa, respectively	88
3.3	Plot of the director angle perturbation as a function of t at $z=d/2$	91
3.4	The director angle perturbation $\hat{\theta}$ and flow velocity \hat{v} as a function of t	
	for various values of activity and orienting field	97
3.5	The director angle perturbation $\hat{\theta}$ and flow velocity perturbation \hat{v} as a	
	function of z for various time, respectively	99
3.6	Plot of the director angle perturbation as a function of time $t.$	100
3.7	The director angle perturbation $\hat{\theta}$ and the flow velocity perturbation \hat{v}	
	in the absence of a field for various time t	101
3.8	Director angle and flow velocity plots for an orienting field for $\varrho=0$ Pa.	113
3.9	Director angle and flow velocity plots for an orienting field for $\varrho=0.5.$	113
3.10	Director angle and flow velocity plots for an orienting field for $\varrho=1.5.$	114
3.11	Director angle and flow velocity plots for an orienting field for $\varrho=2.$.	115
3.12	Director angle and flow velocity plots for an orienting field for $\varrho=2.5.$	116
3.13	Sketch of the director angle at the middle, quarter and third quarter of	
	the channel for $\varrho = 0$, with $\xi_{c1} = \xi_c - 0.13$ Pa	118
3.14	Sketch of the director angle at the middle, quarter and third quarter of	
	the channel for $\varrho=0.5.$	119
3.15	Sketch of the director angle at the middle, quarter, and third quarter of	
	the channel for $\varrho=1,$ with $\xi_{c1}=-0.138$ Pa and $\xi_{c2}=-0.003$ Pa	120
3.16	Sketch of the director angle at the middle, quarter, and third quarter of	
	the channel for $\varrho = 1.025$, with $\xi_{c1} = -0.138$ Pa and $\xi_{c2} = 0.006$ Pa	121

3.17	Sketch of the director angle at the middle, quarter, and third quarter	
	of the channel for $\varrho=1.5$, with $\xi_{c1}=-0.138$ Pa and $\xi_{c2}=0.31$ Pa.	
	The vertical dashed line separates the two types of director profiles, dis-	
	tinguishing those that tend to align near $\pi/2$ rad from those that align	
	below it	122
3.18	Sketch of the director angle at the middle, quarter, and third quarter of	
	the channel, for $\varrho=2.0.$	123
3.19	Sketch of the director angle at the middle, quarter, and third quarter of	
	the channel, for $\varrho=2.5.$	124
3.20	The boundaries between the various late-time solutions in (ϱ, ξ) param-	
	eter space	127
3.21	Contour plot of total active dissipation, D_a against the orienting field	
	and activity	129
3.22	Contour plot of total nematic elastic energy, ω_d against the orienting field	
	and activity	130
3.23	Comparison of analytical and numerical solutions for the transition from	
	an undistorted to a distorted state. The red and green lines represent	
	the analytical solution, while the solid blue line denotes the numerical	
	solution	132
3.24	Active nematic in a channel between two solid plates at $z=0$ and	
	z=d/2 with flow parallel to the x-direction	133
3.25	Sketch of the director angle at the middle of the channel for $-2 \le \xi \le 2$	
	Pa	135
4.1	Active nematic sandwiched between two solid plates at $z=-d/2$ and	
	z = d/2	141
4.2	A schematic showing the division of the channel into planar left, HAN,	
	planar right and transition regions	150
4.3	Plot of the director angle for various region widths	151

4.4	Plot of the director angle for various activity parameter values	199
4.5	Plot of $\int u_L dz$ against activity and HAN region width, $l.$	156
4.6	The director angle as a function along the centreline $z=0.$	157
4.7	Plot of spatial frequency (Hz) against the mode magnitude for $\xi = -100$	
	Pa	158
4.8	Sketches showing oscillations for planar left and planar right regions	
	spanning (ξ, l)	162
4.9	Plot of the director angle in region (x, z) for various and fixed channel	
	widths	163
4.10	Plot of $\int u_L dz$ and $\int u_L dz$	164
4.11	Plot showing the different solutions states as ξ and l vary	167
4.12	Plot of the mode magnitude versus the spatial frequency	169
4.13	Plot of the frequency of oscillations for planar left and right regions as	
	functions ξ and l	171
4.14	Plot of velocity at the inlet/outlet for fixed l and varying ξ	172
4.15	Plot of the velocity in the region spanned by x and z	172
4.16	Plot showing the different solutions states as ξ and l vary	173
4.17	Plot illustrating the variation of splay and bend elastic constants with	
	respect to the scaling ratio	176
4.18	Schematic showing the director distortion from homeotropic to planar	
	anchoring as κ increases	177
4.19	Plot of director angle in the centre of the channel as function of κ for	
	various activity parameter values	178
4.20	Plot of the flux on the left boundary as a function of κ	179
4.21	Plot of the velocity in the $x-$ direction for various splay/bend ratios	181
4.22	Plot of the velocity in the $x-$ direction for various splay/bend ratios	182
4.23	Plot of the velocity in the x -direction in the region spanned by (x, z)	
	for $\kappa = 1.35 \ \kappa = 1.55$, $\kappa = 2.00 \ \text{and} \ \kappa = 4.80$	183

5.1	The velocity field for $\xi = -0.1$ Pa and (a) $t = 0$, (b) $t = 0.52$, (c) $t = 1.1$	
	and (d) $t = 1.5$ seconds	192
5.2	The velocity field for $\xi = -100$ Pa and (a) $t = 0$, (b) $t = 0.52$, (c) $t = 0.6$,	
	(d) $t = 1.1$ and (e) $t = 1.5$ seconds	193
5.3	Plot of the mode magnitude against the temporal frequency of the di-	
	rector angle in the center of the channel	194
5.4	Plot of spatial frequency for the left planar region	196
5.5	Plot of spatial frequency in the HAN region	197
5.6	Plot of the director angle along $z=0$, for x and $t>0$, $\xi=-100$ Pa and	
	$S_{rf} = 15$	199
5.7	Plot of transition times from BB to UU in ξ - S_{rf} parameter space	201
5.8	Transition times from BB to UU in \mathcal{E} - S_{rf} space	202

Dedication

This thesis is dedicated to my beloved mother, Victoria Joseph, and to the memory of my late father, Joseph Papka Kwajighu.

Acknowledgements

I express my deepest gratitude to God Almighty for His love, mercy, and grace throughout my academic journey, especially during my PhD programme. I am profoundly indebted to my esteemed supervisors, Professor Nigel J. Mottram, Dr. Katarzyna N. Kowal, Dr. Joseph R. Cousins and Dr. Alexander Houston. Their dedication to my academic growth has been a constant encouragement and inspiration. I sincerely thank the College of Science and Engineering, University of Glasgow, for funding my PhD. Without their support, I would not have reached this significant milestone. My profound gratitude goes to my mother, whose love, care, and support have been my strength and motivation. Dad, I wish you were here to witness this achievement. To my loving wife, Bar. Gloria Verensarenso Ijuptil, I owe a special thanks for her endless support, encouragement, and understanding throughout this journey. My son, David Ijakirayu, you arrived at just the right time - your birth has been a blessing and a source of courage for me. I am also deeply grateful to my indefatigable uncle, Professor Lucas W. Lumbi, for his invaluable advice, encouragement, and support. Your mentorship has been a guiding light throughout my academic journey. I acknowledge the prayers and character formation of my sisters, Hanatu, Catherine, Magdalene, Kwata, Ijapari, Athariju, Godiya, and Theresa, whose encouragement has been a constant source of strength. Special appreciation goes to Rev. Fr. Justine John Dyikuk, my spiritual mentor and friend, whose wise counsel and prayers have sustained me. To the family of Dr. Wandiahyel Gaiuson Yaduma, I extend my heartfelt thanks for their unwavering support. Finally, I extend my appreciation to Mr Ayodeji Osatuyi, Mr Sunday

Lucas, and the family of Mr Reuben Soja, along with all my relatives, non-relatives, and friends who have shown me love and support throughout my pursuit of a Doctor of Philosophy Degree in Applied Mathematics. I also appreciate my friends, Sunday Burbur, Obadiah Gabriel, Obed Emmanuel, Ijabla Pius Papaka, and Adam Raymond, for their continued support and encouragement. Finally, I extend my gratitude to all who have shown me love and support throughout my pursuit of a Doctor of Philosophy Degree in Applied Mathematics.

Declaration

With the exception of Chapters 1 and 2, which contain introductory material, all work in this thesis was carried out by the author, unless otherwise explicitly stated.

Abbreviations

LC	Liquid crystal
LCD	Liquid Crystal Displays
HAN	Hybrid-aligned nematics
UU	Unidirectional—Unidirectional flow
UB	Unidirectional–Bidirectional flow
BU	Bidirectional—Unidirectional flow
BB	Bidirectional–Bidirectional flow
SPP	Self-Propelled Particles
LCD	Liquid Crystal Display
MBBA	$N\hbox{-}(4\hbox{-}Methoxy benzylidene)\hbox{-} 4\hbox{-}butylaniline$

Chapter 1

Introduction: Passive and Active

Liquid Crystals

Active fluids are systems composed of self-driven units that consume and convert energy into directed motion [42, 45, 76, 187, 236]. Typical examples of active fluids include a suspension of cytoskeletal filaments [126] and motor protein [78, 188, 211], as well as cellular layers and cell tissues [44,255]. In this thesis, we focus on active nematics, which are a type of active fluid characterised by nematic symmetry, which may arise from the elongated shape of the self-driven units similar to the rod-like molecules in nematic liquid crystals or an abstract orientational symmetry exhibited by the constituents [40,211].

The behaviour and flow patterns of active fluids, particularly active nematics, have been a growing area of interest in the active matter physics community. Recently, research has also focused on their practical applications, such as microfluidic pumps [230], biomedical applications related to tumour dynamics [44], the spread of bacterial biofilms [144, 251], embedding responsive control systems within biomimetic materials [80] and the growth of bacterial biofilms [79], further expanding the scope of the field.

Studies have shown that active fluids exhibit spontaneous flows and vortices [147,197], along with backflow resulting from internal activity in active nematics [60, 183]. Var-

ious flow patterns, ranging from steady flow to turbulent flow, have been observed in a confined infinitely long channel [41, 197], depending on the activity strength or channel width and the study of confined active nematics has potential applications in morphogenesis, biofilm formation, and wound healing/closure [6,69,144].

Controlling the behaviour of active fluids is crucial to their potential applications in microfluidic devices and energy harvesting [211], yet achieving effective control has proven to be challenging. One well-established method for attaining this control is by confinement [43,77,248], and a promising application of active nematics in a confinement is in the design of sensors, since small changes in alignment or external forces can lead to significant effects, such as flow, in the active system. However, the effect of applied orienting fields, such as electric and magnetic fields, on the behaviour of these systems, as well as the influence of local disturbances on flow, remains an open question.

To address these gaps, we develop a theoretical and computational study of active nematics using a modified form of the Ericksen-Leslie equations. Our work aims to deepen the understanding of active nematics, which will provide insights into potential future devices such as sensors and understanding of biological processes such as biofilm formations and morphogenesis.

A key finding of our study is that local disturbances drive global flow in active nematic systems. This is demonstrated in the two-dimensional models, where localised disturbances at the center of a channel induce global flow. Similarly, in the 1D model, a high orienting field causes a significant director orientation. This behaviour is important for sensing applications, as small alignment changes can lead to large-scale flow and director distortion.

The thesis is organised as follows. In the remainder of Chapter 1, we begin by reviewing the historical background of liquid crystals, including their synthesis, phase formation, and mathematical foundations. Particular attention is given to the classical classification of liquid crystals into nematic, smectic, and cholesteric phases, with emphasis on nematic liquid crystals. This emphasis is motivated by our adoption of

the Ericksen-Leslie framework for modelling active nematics, as well as the capacity of nematic liquid crystals to align and flow under external fields [202], in addition to their wide range of technological applications [23, 82, 145, 146, 239]. We then provide an overview of active fluids, their classifications based on damping and symmetry, and their behaviour in low-Reynolds-number regimes. This naturally leads to a discussion of hydrodynamic instabilities in active fluids. We subsequently focus on active nematics as a class of wet active systems, presenting their hydrodynamic theory and governing equations, including active length and time scales. Special attention is given to kickback and backflow mechanisms, as well as the Fréedericksz transition and the associated Dand S-mode instabilities. The chapter concludes with a review of active nematics under confinement, which is directly relevant to the present study, followed by an overview of experimental observations of active fluids. Finally, we highlight applications in sensing technologies, including electrorheological and magnetorheological sensors, liquid crystal biosensors, and efforts toward the development of active nematic-based sensing devices. In Chapter 2, we review the mathematical theories centered around the Ericksen-Leslie framework, including the formulation of Frank-Oseen elastic energy and the Ericksen-Leslie dynamic theory of nematic liquid crystals, which forms the underlying theory of our study. This formulation is based on the conservation laws of mass, linear momentum, and angular momentum. Recognising the importance of activity in these systems, we also derive the activity term, which introduces an extra stress term into the original Ericksen-Leslie equations for passive nematics. We conclude the chapter by discussing anchoring conditions, focusing on planar, homeotropic anchoring and the hybrid aligned (HAN) nematic cell, as well as the no-slip and no-penetration flow boundary conditions, which will be used in Chapters 3, 4, and 5.

Chapters 1 and 2 present a comprehensive literature review that establishes the foundational context for this research, highlighting key theories, methodologies, and previous findings relevant to the study, while the remaining chapters focus on our original contributions. To achieve the first objective of this research: examining the effect of the orienting field on the behaviour of active nematics, Chapter 3 presents a linear analysis

using planar and homeotropic alignments, as well as a nonlinear analysis, both under the influence of an orienting field. We begin by linearising the governing equations around a uniform director to understand early-time dynamics, followed by solving the nonlinear analysis for longer times using a numerical approximation. We characterise the solution based on activity strength and orienting field. Since mixed boundary conditions will later be used, we conclude Chapter 3 by investigating the system in a simple hybrid-aligned nematic (HAN) cell without an orienting field.

Chapter 4 presents a two-dimensional model of active nematics in a channel, considering the effects of activity strength and channel width. To achieve the second objective of this research: investigating the system using planar and homeotropic alignments, we first examine the system under inlet/outlet normal flow conditions, which mimics a single disturbance in anchoring, and characterises the solution by varying the activity strength while fixing the channel width. We then investigate the system by varying both activity and channel width. Next, we consider the system under periodic conditions, inlet/outlet flow, which mimics a periodic disturbance in anchorings, where we also examine the effect of the elastic constant ratio on director orientation and flow.

Chapter 5 focuses on the two-dimensional transient dynamics of HAN state formation, which aligns with our third objective: understanding the transient dynamics of HAN state formation. While Chapters 3 and 4 applied static boundary conditions on the top solid wall, Chapter 5 introduces dynamic boundary conditions, enabling control of the top boundary and allowing the system to switch from planar to homeotropic alignment.

Chapter 6 provides a summary of each chapter and offers suggestions for further work, including the consideration of the three-dimensional form of this model and conducting experimental validation for sensor design.

1.1 Historical background of liquid crystals

In this section, we provide an overview of the historical background of liquid crystals and their traditional classifications, which include nematic, smectic, and cholesteric phases. While we discuss these three phases, our primary focus for the rest of the thesis will be on nematic liquid crystals, the most relevant phase for active fluids.

Understanding the origins of liquid crystal helps us appreciate how this state of matter was discovered and how its study evolved to become essential in both physics and biology. Instead of a simple chronology of names and dates, this history reveals key conceptual advances and how early research laid the ground for modern studies of active nematics.

We divide the historical background into two aspects: the chemistry of liquid crystals, focusing on their synthesis, and the mathematical foundation, beginning with the Frank-Oseen elastic energy and ending with Ericksen-Leslie theory. These theories form the mathematical basis of this thesis and will be discussed in detail in Chapter 2.

1.1.1 Synthesis of liquid crystals and their phase formation

Liquid crystals (LCs) are materials that possess intermediate phases of matter between a crystalline solid and an isotropic liquid [25,35]. These intermediate phases are referred to as mesomorphic phases. This means that LCs exhibit fluidity like that of viscous fluids, which allows their molecules to flow or rearrange. At the same time, they retain certain properties of solid crystals, such as specific optical behaviours [202]. LCs are also anisotropic, meaning their physical properties vary depending on orientation [166,202]. Some notable properties of liquid crystals include electric anisotropy [8, 29], magnetic anisotropy [180], anisotropic elasticity, and anisotropic viscosity [166].

The early history begins with Virchow in 1854 [233], who observed an unusual liquid state formed by dissolving myelin in water. Myelin–a fatty substance found in nerve cells, which exhibits intermediate phase properties between solid and liquid. This phase

of matter displayed double refraction (birefringence), a phenomenon where light splits into two rays with different velocities, indicating an anisotropic internal structure. In 1857, Mettenheimer [132] further studied this optical behaviour and documented the unique properties of myelin suspensions under polarised light.

The birefringence of myelin was one of the first experimental pieces of evidence that certain fluids can have directional order. These early studies linked biology with the physics of soft matter, suggesting that the anisotropic phases were not just found as curiosities but could also be observed in living tissues.

Following this, in 1861, Valentin [228] extended these observations by investigating plant and animal tissues under polarised light microscopy, revealing that such lyotropic liquid crystal phases (formed by dissolving amphiphilic molecules in solvents like water) may have been observed before the known thermotropic phases (formed by temperature changes). This highlights the biological relevance of liquid crystals and foreshadows the role of anisotropic ordering in cellular and tissue structures.

The formal discovery of liquid crystals is credited to Friedrich in 1888 [180], who studied cholesterol derivatives and observed two distinct melting points: a cloudy intermediate phase followed by a clear liquid phase. This "mesophase" showed both fluidity and crystalline optical properties, which led Lehmann to describe these materials as "flowing crystals" in 1889 [112]. These discoveries established liquid crystals as a new phase of matter, distinct from solids and isotropic liquids.

In 1911, Manguin studied the optical properties of liquid crystals. He aligned a liquid crystal by rubbing glass with paper and observed that light polarisation followed the nematic director [131]. Hence, the idea that liquid crystals can influence light was established. By 1922 [56], Friedel introduced the foundational concept of "orientational order" and classified liquid crystals into nematic, smectic, and cholesteric phases. This classification describes how molecules organise in different patterns and how defects and external fields affect their behaviour, which remains central to understanding liquid crystals and active nematics today.

The ability to control molecular orientation in liquid crystals using external fields, such as magnetic or electric fields [25, 35, 55, 89, 104, 254], has been a major focus since the early 20th century, exemplified by the Fréedericksz transition observed in 1933 [54], where an applied field reorients the average orientation of LC molecules, above a threshold strength. Such control mechanisms are crucial in applications ranging from displays to modern research on active nematics.

More recently, Guillamat et al. [71] demonstrated how magnetic fields can control active nematic turbulence, using a mixture of biologically relevant microtubule gels coupled to passive thermotropic liquid crystals. The study shows that a magnetic field can indirectly transform the chaotic "active turbulence" (a chaotic, self-sustained flow regime observed in active nematic systems at high activity, characterised by the spontaneous creation, motion, and annihilation of topological defects and vortices on mesoscopic scales) of an active nematic into ordered laminar flows by coupling it to a passive thermotropic liquid crystal: 4'-Octyl-4-biphenylcarbonitrile (8CB) that responds to magnetic alignment. When the 8CB is cooled into its smectic-A phase under a uniform magnetic field, its layered "bookshelf" structure orients perpendicular to the field, creating an anisotropic interfacial resistance that channels active flows into straight, antiparallel lanes. This alignment is reversible and reconfigurable, which, when heated above the smectic-A transition, restores turbulence, while rotating the magnetic field rotates the layers. This represents a direct link from liquid crystal to the current interest in active nematics, which are non-equilibrium systems driven by internal energy consumption. Extending this concept to sensing, an object placed above the active nematic layer could locally perturb the surface anchoring, for example, through an electrostatic effect, applied force, or torque, which would reorient the director locally. In an active nematic, this small local perturbation can then be amplified by activity-driven flows to produce a global, detectable response, effectively translating a microscopic stimulus into a macroscopic signal.

In our study, we will consider the effect of an external field, such as a magnetic field,

on the behaviour of the active nematics.

Beyond these historical accounts, there are many other significant developments in the chemical aspects of liquid crystals. For a more comprehensive review of these histories, refer to [20, 95, 166]. In the next section, we will shift our focus to the historical background of the mathematical theories that have shaped our understanding of liquid crystals, which lay a foundation for their theoretical modelling and applications.

1.1.2 Mathematical foundations of liquid crystals

The mathematical understanding of liquid crystals has evolved through key theoretical breakthroughs, which together provide the foundation for modelling their complex behaviours. This section outlines the major developments relevant to nematic liquid crystals and active nematics, which emphasise the physical insights each theory contributed.

The notion of orientational order introduced by Friedel in the early 20th century inspired the first mathematical description of nematic liquid crystals by Oseen in 1929 [148]. He formulated how anisotropic molecules tend to align along a common direction, called the director, capturing the essential ordered structure of nematics. Building on this, in 1933, Fréedericksz and Zolina [55], experimentally discovered the "Fréedericksz transition", a fundamental phenomenon where applying an external electric or magnetic field above a threshold causes the liquid crystal molecules to reorient. This demonstrated how external fields can dynamically control molecular alignment, which is crucial to both applications like Liquid Crystal Displays (LCDs) and current active nematic research. Around the same time, Zöcher [260], further explored magnetic field effects, which deepens the understanding of how fields influence liquid crystal properties.

While early theories treated nematics as continuous media, a molecular-level explanation was needed to connect microscopic interactions with macroscopic behaviour. In 1959, Maier and Saupe [124] proposed a molecular theory describing how correlations and flexibility between rod-like molecules determine the nematic order parameter,

quantifying the degree of alignment. Their theory also explained the first-order phase transition from isotropic (disordered) to nematic (ordered) phases, clarifying the molecular origins of liquid crystal behaviour.

A crucial advance came in the 1960s with the development of continuum hydrodynamic theories to describe how nematic liquid crystals flow and deform under stress. Ericksen, in 1962 [47], introduced a hydrostatic theory that accounted for elastic deformations and orientational order. Building on this, Leslie, [113], formulated a dynamical theory incorporating viscous and elastic effects, resulting in the well-known Ericksen–Leslie theory. This framework successfully couples flow and director dynamics, enabling accurate predictions of nematic behaviours under various conditions, and is foundational to many applications and further research.

Active nematics differ from traditional liquid crystals because their constituent particles consume energy to generate internal stresses and flows, driving the system out of equilibrium [45, 176, 212, 236]. In this thesis, we adopt an active nematic extension of the Ericksen–Leslie theory, where an additional stress term captures these active contributions. This extension allows us to model spontaneous flows, instabilities, and complex dynamics observed in biological and synthetic active nematic systems.

Building on this foundational work, we will explore the effect of external fields, particularly magnetic fields, on the behaviour of active nematics. This includes understanding how such fields interact with the internal dynamics of active nematics. Chapter 3 will present a detailed discussion of these effects and their implications.

1.1.3 Classification of liquid crystals

Liquid crystals exhibit several distinct phases characterised by varying degrees of molecular order. While this thesis focuses primarily on the nematic phase due to its fundamental role in modelling active nematics, as well as its remarkable ability to undergo alignment and flow behaviours [202] under external fields, as well as their applications in force sensors [85], pressure sensors [155], light sensors [82, 239], chemical sensors

sors [23, 145, 146] and emerging potential application in designing sensors. However, a brief overview of other traditional phases, such as smectic and cholesteric, is provided for context and completeness. However, smectic and cholesteric phases are not directly involved in the models or analyses presented in this thesis.

Liquid crystals are classified using either their molecular structure or their phase structure. The molecular structure is the geometrical representation of liquid crystals in terms of the constituent mesogenic molecules. The mesogenic molecules can include disk-shaped, lath-shaped, and rod-shaped molecules. The most common form of liquid crystal is derived from rod-shaped molecules, which are termed calamitic from the Greek word "calamos", which means "rod". Liquid crystal phases can also be classified by their dependence on the temperature and concentration in the solvent [20,25]. The phase structure is then characterised by the conformation and intermolecular interaction of the molecules, and the arrangements of these include the nematic, smectic and cholesteric phases as shown in Figure 1.1.

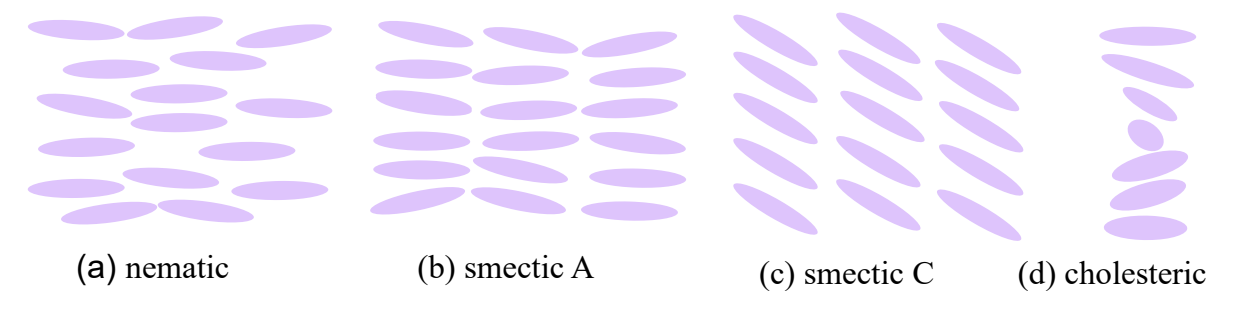


Figure 1.1: Sketches of liquid crystal phases, where the blue ellipsoids represent molecules.

1.1.3.1 Nematic liquid crystals

The nematic phase has long-range orientational order but no positional order [57,67,96]. In the nematic phase, the long axes of the constituent molecules tend to align parallel to a preferred direction, often called the anisotropic axis. In modelling nematic liquid crystals, a unit vector **n**, called the director, is used to describe the average direction of the long molecular axes of all molecules in the liquid crystal. While maintaining this alignment on average, the molecules can still translate freely [202]. Although

individual nematogen molecules can be polar, with a permanent dipole moment, the nematic phase as a whole is apolar. This is because the molecules tend to align along a common axis but with no preferred head or tail direction, resulting in a head-to-tail symmetry. Consequently, the macroscopic order is invariant under inversion of the director (that is, $\mathbf{n} \to \mathbf{n}$), so the nematic phase lacks large-scale polarity [202]. Because the relevant molecular axis is rotationally symmetric, the only distinguished direction in the nematic phase is this anisotropic axis defined by \mathbf{n} . Hence, the nematic phase is uniaxial. The stability of this phase and electro-optic anisotropy make it very useful in LCDs [149, 179].

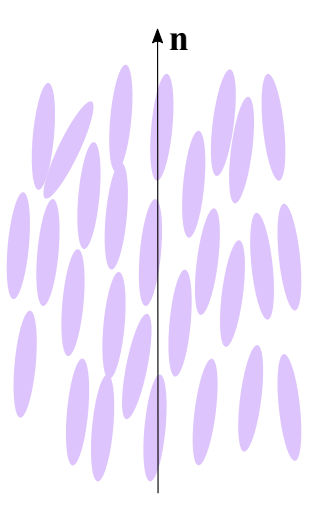


Figure 1.2: Schematic depicting an idealised nematic liquid crystal, where molecules align with the director **n**, demonstrating orientational order [141].

1.1.3.2 Smectic liquid crystals

Unlike nematics, the smectic phase has both long-range orientational order and a one-dimensional positional order [25,150]. Smectics are usually found at a lower temperature than nematic liquid crystals. There are many subclassifications of smectic liquid crystals, but the most important are smectic A and C [8]. The smectic A phase consists of classical rod-shaped molecules that align along the layer normal, whereas the smectic C phase features a tilted molecular arrangement [25,35].

1.1.3.3 Cholesteric liquid crystals

Cholesteric liquid crystals, also called "chiral nematics", involve a nematic alignment of molecules, which varies throughout the medium. They differ from the nematic phase in that the director varies in direction throughout the medium in a regular way [7]. The structure of the cholesteric liquid crystals defines a distance (called the pitch of the cholesteric) measured along an axis over which the director rotates [7, 30, 38]. It is the molecular chirality that induces an azimuthal twist from one layer to the next, producing this spiral twist of the molecules along an axis.

Having introduced the concept of classical liquid crystals and their discovery, from a chemical aspect to developing mathematical theories, we now shift our focus to active fluids. The remainder of this chapter will cover active fluids, beginning with a general overview before and concluding with active nematics, which is our primary area of interest.

1.2 Active fluids

This section covers active fluids and their classification based on symmetry properties and damping mechanism, distinguishing between "wet" and "dry" active systems. Before the classification, we will briefly introduce the concept of active fluids and their hydrodynamic properties. In this thesis, we specifically focus on wet active systems, with particular emphasis on active nematic liquid crystals.

Active fluids are composed of self-driven elongated units and exhibit collective behaviour due to the interplay between activity and liquid crystalline order, making an interesting study of nonequilibrium dynamics [61, 126, 243, 252, 257]. These self-driven units consume and convert energy into directed motion. Some examples of active fluids include schools of fish [52], flocks of birds [191], bacteria [157], motor proteins and insects or animals [76] as shown in Figure 1.3. Another class of active fluids is active gels, which include cytoskeletal networks [76, 173]. Active fluids possess physical properties

such as the appearance of defect structures, hydrodynamic instabilities, and unusual viscoelastic properties [22, 120, 217].

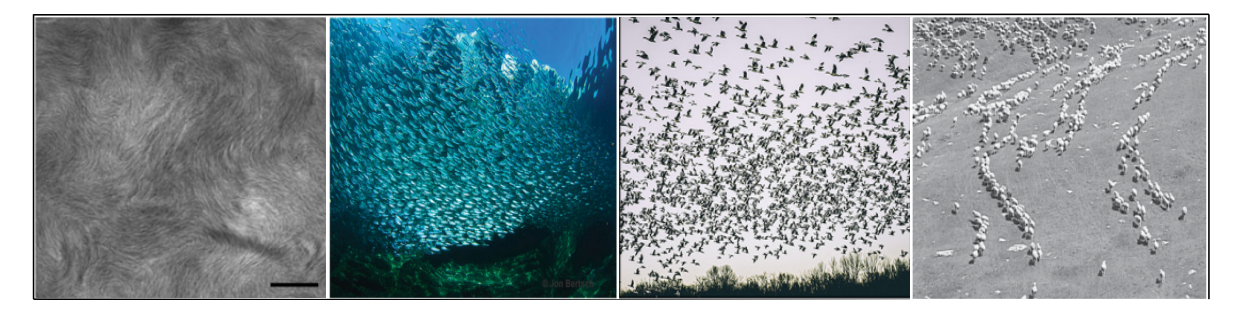


Figure 1.3: A sketch showing some examples of active fluids: From the left to the right, we have bacteria [157], a school of fish [52], a flock of birds [191], and a group of sheep [66].

Our next focus is the classification of active fluids to provide a background for understanding their behaviour, properties, and interactions, which are essential for modelling these systems.

1.2.1 Classifications of active fluids

Active fluids can be classified based on damping mechanisms and symmetry properties [126]. This section provides a review of these different classifications of active fluids. However, our primary focus in this thesis is on the dynamics of active nematic liquid crystals, which are classified based on symmetry and fall under the category of "wet" active systems. These systems exhibit hydrodynamic interactions, distinguishing them from "dry" active systems where frictional damping dominates over viscous dissipation [126].

In our study, we specifically consider both contractile and extensile active nematics. Contractile systems are characterised by internal stresses that pull the surrounding fluid inward along their symmetry axis, leading to flow patterns distinct from those of extensile systems, which push fluid outward along their symmetry axis [45]. Understanding their behaviours is essential for characterising their flow regimes and emergent properties, as well as exploring potential applications, such as the design of sensors.

1.2.1.1 Classification based on damping

Active fluids move within a medium that facilitates interactions with the substrate or induces frictional damping [126, 198, 213].

Active particles suspended in a viscous fluid with viscosity η and subject to frictional drag γ can generally be described as a fluid/particle system that either conserve momentum or that do not, depending on physical factors such as particle density and the relevant length scales [126]. When the fluid acts simply as an inert background providing frictional resistance, the ensemble of active particles transferring momentum to the fluid can be modelled with overdamped dynamics that ignore particle momentum conservation [209]. Such systems are referred to as "dry." In this system, it is always assumed that momentum is damped by friction with the substrate. In other words, the viscous dissipation in the dry active system is dominated by friction. The conserved quantity is the number of particles, which is characterised by the density number, and the associated hydrodynamic field is the local density of active units [126]. Examples of such systems include flocks or herds of animals, birds [66, 191], schools of fish [52], vibrated granular particles on a plate [213, 220], and the collective motion of self-propelled hard rods [9]. On the other hand, if hydrodynamic interactions mediated by the solvent play a significant role, the fluid's dynamics must be explicitly included, resulting in a coupled description of both the active particles and the fluid, where total momentum is conserved [135]. These are known as "wet" systems. Examples include unicellular organisms such as bacteria [10], algae [126] and also cytoskeleton biopolymers and suspensions [40]. It is important to note that labelling a system as wet or dry pertains to the modelling approach and the scale of observation, rather than an intrinsic property of the system itself. Generally, hydrodynamic effects can be neglected only at length scales larger than $\sqrt{\eta/\gamma}$ [126]. In wet active systems, the long-range hydrodynamic interactions between self-propelled particles play a crucial role in the dynamics [135, 209].

1.2.1.2 Classification based on symmetry

Active fluids can also be classified based on their symmetry. The first symmetry classification consists of polarity, where self-propelled units can interact to affect polar order. In polar systems, the units align head-to-head and tail-to-tail, examples include schools of fish and flocks of flying birds or self-propelled rods [164, 232, 253]. Apolar systems also exists, examples of which include fibroblasts [189] and melanocytes [69], which can form an apolar nematic liquid crystal at high cell densities [69], which exhibit interactions that align particles in opposite directions on the same axis regardless of their polarity [188]. Beyond polar and apolar systems, active fluids can also be described by scalar and hexatic order parameters. Scalar active fluids lack orientational order, and their behaviour is governed primarily by variations in density or concentration [216]. Hexatic active fluids exhibit sixfold orientational symmetry, with units arranging locally in hexagonal patterns without long-range positional order, as seen in certain bacterial colonies or colloidal monolayers [103].

In the next section, we will explore the active fluids in the low Reynolds number regime.

This review provides a foundation for modelling active systems in which viscous forces
dominate over inertial effects.

1.2.2 Low Reynolds number flow of active fluids

Even though our primary focus is on the collective behaviour of active nematics, it is useful to briefly discuss individual microswimmers in low Reynolds number regimes, as they illustrate the fundamental mechanisms of self-propelled motion in highly viscous, inertia-negligible environments. Reynolds number is defined as the ratio of inertial to viscous forces. Specifically, studying microswimmers helps understand how propulsion arises purely from active stresses, how hydrodynamic interactions affect trajectories, and how collective patterns emerge from individual motions. In this thesis, we neglect the inertia term because the Reynolds number is small. To provide a foundation for this approach, we first review microswimmers and then follow with continuum models

of microswimmers.

Microswimmers such as bacteria exhibit motility by self-propelling in fluids using flagella or cilia arranged in various geometric patterns [111,161]. Their shapes, behaviours, and ability to rotate about their swimming direction [13] can all be used in mathematical models to describe their motion.

Several mathematical models have been developed to describe their behaviours, beginning with Taylor's model in 1951 [208], which examined how a self-propelled organism moves in a highly viscous medium. Although originally formulated for a single swimmer, this model illustrates how individual propulsion generates flow fields, a concept that underlies the active stresses driving collective motion in active nematics. Building on this, Lighthill [118] introduced the concept of a spherical deformable body that swims by performing small oscillations of its surface, demonstrating how individual surface motions generate local flows even in the absence of inertia. Blake [16] extended this idea through the spherical envelope model, which approximates the dense cilia of a microorganism as a continuous waving envelope, allowing calculation of propulsion velocities and efficiency, while accounting for collective ciliary motion. These models provide a foundational framework for understanding how individual self-propelled units generate flow and hydrodynamic interactions, which are central to emergent patterns in active matter. Building on this, Pedley and Kessler [161] explored the swimming behaviour of microorganisms such as Chlamydomonas and Bacillus, focusing on their responses to external stimuli like chemical gradients (chemotaxis), shear (rheotaxis), and magnetic fields (magnetotaxis). These studies also contributed to the understanding of bioconvection, where the collective movement of microorganisms generates fluid flow patterns [98,160], providing further context for the emergence of collective dynamics in active nematics.

At low Reynolds numbers, viscosity dominates fluid dynamics, as emphasised by Purcell [174], who formulated the "Scallop Theorem," demonstrating that reciprocal motion alone cannot generate net propulsion in this regime. He simplified the Navier-Stokes

equation to the Stokes equation, where inertia is negligible, highlighting the distinct mechanics governing microswimmers compared to macroscopic organisms. Further studies, such as mesoscale hydrodynamic simulations of *E. coli*, have revealed that propulsion mechanisms rely on coordinated flagellar and cell body rotation [84]. Additionally, Huber *et al.* [86] showed that hydrodynamic interactions significantly affect their swimming efficiency and trajectories.

The mathematical theories underlying the study of active fluids can be viewed at different length scales. This includes macro, micro, and molecular scales depending on the Reynolds number. The corresponding Reynolds numbers, might for, instance be 10^4 for macroscopic turbulent flows, 10^2 for certain mesoscopic systems, and 10^{-2} or smaller for microscale active suspensions [11]. In this Thesis, our focus is on the hydrodynamic theories governing microscale active fluids, which typically operate in the low-Reynolds-number regime where viscous forces dominate over inertia.

The Reynolds number in a typical fluid is defined as

$$Re = \frac{\rho UL}{\eta},\tag{1.1}$$

which quantifies the ratio of inertial to viscous forces, where ρ is the fluid density, U a characteristic velocity, L a characteristic length scale, and η the fluid viscosity.

In this thesis, we assume $Re \ll 1$, so that fluid inertia can be neglected. Since the flow velocity is induced by activity, we define the velocity scale as $U = |\xi| d/\eta_3$, where $|\xi|$ is the magnitude of the activity, d is the characteristic length scale, and η_3 is the fluid viscosity. This velocity scale will be explained and justified later in Section 3.3.1.1 (see equation (3.27)), where the characteristic active length and time scales are derived from the linearised hydrodynamic equations.

Substituting this into the definition of Re gives

$$Re = \frac{\rho|\xi|d^2}{\eta_3^2} \ll 1. \tag{1.2}$$

Specifically, we use the physical parameters of the nematic LC N-(4-Methoxybenzylidene) -4-butylaniline (MBBA) at 25°C throughout this thesis, as outlined in Table 1.1. MBBA is chosen because its material parameters are well-characterised and widely reported, making it a convenient reference for setting physical scales. We emphasise, however, that MBBA has no explicit relation to active nematics, which may exhibit a broad range of properties. The parameter values marked by ** are the varying parameters.

Quantity	Description	MBBA 25°C		
Elastic constant (N)				
K_1	Splay elastic constant	6×10^{-12}		
K_2	Twist elastic constant	3.8×10^{-12}		
K_3	Bend elastic constant	7.5×10^{-12}		
Viscosity (Pa s)				
α_1	Leslie viscosity	-0.0181		
α_2	Leslie viscosity	-0.1104		
α_3	Leslie viscosity	-0.001104		
$lpha_4$	Leslie viscosity	0.0826		
$lpha_5$	Leslie viscosity	0.0779		
$lpha_6$	Leslie viscosity	-0.0336		
η_1	Miesowicz viscosity	0.0240		
η_2	Miesowicz viscosity	0.1361		
η_3	Miesowicz viscosity	0.0413		
$\gamma_1 = \alpha_3 - \alpha_2$	Rotational viscosity	0.1093		
$\gamma_2 = \alpha_3 + \alpha_2$	Torsion viscosity	-0.1121		
Leslie angle (rad)				
$\overline{ heta_L}$	Leslie angle	0.099		
χ_a (dimensionless)	Magnetic anisotropy	1.219×10^{-6}		
$\rho ({\rm Kg/m^3})$	Density	1088		
Activity strength (Pa)				
ξ	1D	[-2, 2]		
	2D	[-100, 150]		
Geometry (μm)				
\overline{d}	channel height (1D)	200		
d	channel height (2D)	2		
w	channel width (2D)	20**		
l	HAN region length	[w/1000, w/3]		
Applied field (A m ⁻¹)				
Н	Orienting field	$[0,5]^{**}$		
H_c	Critical field strength	$(\pi/d)(\sqrt{K_1/\chi_a})$		
-				

Table 1.1: Table of parameter values

The Reynolds numbers corresponding to the range of activity values considered in this

study, $\xi = \pm 0.0001, \pm 0.3$, and ± 150 , are summarised Table 1.2. These values confirm

Dimension	Characteristic length d (μ m)	Activity ξ (Pa)	Reynolds number (Re)
1D	200	0.001	2.5515×10^{-5}
1D	200	0.3	7.6544×10^{-3}
1D	200	2	5.1029×10^{-2}
2D	2	0.001	2.5515×10^{-9}
2D	2	100	2.5515×10^{-4}
2D	2	150	3.8272×10^{-4}

Table 1.2: Reynolds numbers for 1D and 2D flows for weak and high activity cases.

that both 1D and 2D flows are in the low-Reynolds-number regime, justifying the neglect of inertia in our simulations.

The choice of different activity values for 1D and 2D systems arises from both scaling considerations and practical motivations. In the 1D channel geometry ($d = 200\mu m$), relatively small activity values ($\xi = 0.0001-2$ Pa) are sufficient to generate measurable hydrodynamic effects because the larger characteristic length amplifies the impact of active stresses. By contrast, in the 2D case ($d = 2\mu m$), the smaller system size necessitates higher activity parameters (up to $\xi = 150$ Pa) to produce comparable flow instabilities. Moreover, exploring strong activity in 2D is motivated by potential applications in the design of microscale sensors, where enhanced active stresses could be exploited to improve sensitivity and response.

The choice of a 2 µm channel height in the present study is primarily motivated by potential applications in sensor design, rather than experimental convenience. While experimentally filling channels of this dimension is challenging, and typical confinements in active nematic systems are larger (5–50 µm for microtubule–kinesin networks and 1–10 µm for bacterial suspensions) [40,188,242], a 2 µm channel provides a highly confined geometry that is relevant for integrating active nematics into micro- and nano-fluidic devices. At this height, microtubules (diameter 25 nm) would form only about 80 layers across the channel, which is sufficient to capture collective dynamics while maintaining a quasi-two-dimensional flow regime. Therefore, despite being smaller than typical experimental channels, this choice allows exploration of active nematic behaviour under

conditions directly relevant to sensing applications.

Having established this background by reviewing studies on active fluids, we now focus on hydrodynamic instabilities in these systems.

1.2.3 Hydrodynamic instabilities in active fluids

This section reviews various instabilities in active fluids, with a primary focus on active nematics. To provide context, we first examine the broader literature on active fluids, highlighting the types of flow, instabilities, and hydrodynamic interactions in these systems. Specifically, Section 1.5 covers active nematics and their hydrodynamic interactions.

Hydrodynamic theory-based studies on active matter have been ongoing, covering both microscopic and macroscopic modelling [91, 107, 126]. One approach to developing a hydrodynamic theory for these systems is to start with a microscopic model and apply statistical physics tools to coarse-grain it, deriving the long-wavelength and long-time-scale equations [108, 120]. For example, large density fluctuations due to the continuous energy input at the microscopic scale [136, 176] have been observed in active systems.

Theoretical and computational studies, supported by simulations and experiments, have predicted or observed spontaneous flow in active fluids [65,127,236]. These systems may exhibit steady flows [61] with instabilities that disrupt nematic order, often triggering motion [214, 219, 236]. A study of active systems such as active nematics shows that the interaction between non-uniform nematic order, activity, and flow leads to spatially modulated relaxation oscillations [62,63]. In our study, we will later demonstrate that active nematics exhibit oscillatory flow in contractile active systems. Other studies have observed turbulence in active systems even at a low Reynolds number [212,214]. In all these studies, the stress term, dependent on the nematic tensor, and the order parameter are important activity parameters [178].

Hydrodynamic instabilities in active fluids occur due to their intrinsic non-equilibrium

nature [46,126,175,185,237]. Unlike passive liquid crystals, where instabilities typically arise from external perturbations or thermal fluctuations [83], active fluids experience internally generated stresses that can lead to spontaneous flow patterns [44,236] and symmetry breaking [37,218]. These instabilities are crucial for understanding the self-organisation observed in active matters, including bacteria suspensions, self-propelled rods and active gels.

For instance, linear stability analysis of collective hydrodynamics behaviour of selfpropelled hard rods reveals that fluctuations in the isotropic state are stable for low density but unstable for high density [9]. Similarly, a study of the hydrodynamics of bacterial suspensions using statistical mechanics indicates that the homogeneous isotropic suspension of contractile systems becomes unstable at concentrations above the critical concentration and is stable at concentrations below the critical concentration [10]. In these contractile systems, the homogeneous ordered state is destabilised by the growth of the splay configuration, while growth of a bend configuration destabilises the homogeneous ordered state in extensile systems [1]. In further investigations of the viscoelastic properties of active filament solutions under different phases (isotropic, polarised, and nematic), a molecular model suggests that the system is disturbed from its equilibrium state by external energy sources, such as shear stress, and internal sources (like motor activity) [121]. A study of active gels indicates that the interaction between the elasticity of semiflexible filaments and the mechanical properties of the system results in the contractile behaviour of the active gels [122]. In many such systems, these instabilities can be controlled by confining the system or applying an external shear [49, 128, 140].

The analysis of hydrodynamic instabilities in active fluids demonstrates how continuous energy input at the microscale generates spontaneous flows and complex spatiotemporal patterns. In low-Reynolds-number regimes, as encountered in microswimmer systems, viscous forces dominate over inertia, leading to creeping flows where activity-induced stresses drive the dynamics. This highlights the importance of self-driven activity and

anisotropic interactions in shaping the collective behaviour of active fluids. Active nematics extend these concepts by considering elongated, rod-like particles whose alignment and activity produce characteristic defect structures, spontaneous flows, and rich nonequilibrium phenomena, making them an ideal system to study the interplay of activity, symmetry, and hydrodynamic instabilities.

1.3 Active nematics

As previously mentioned, active nematics are a class of active fluids that operate out of equilibrium, driven by the continuous energy consumption of their constituent particles [215]. This intrinsic energy dissipation leads to instabilities and topological defects in the system, making them fascinating subjects of study [40, 182, 214, 236]. Although lyotropic active nematics are composed of suspensions of elongated particles rather than molecular liquid crystals, their orientational order and defect dynamics can be described using the continuum theory of thermotropic nematics. This is because the coarse-grained alignment and elastic stresses in both systems are governed by similar symmetry principles and free-energy considerations, which allows the well-established hydrodynamic equations of thermotropic nematics to be applied to lyotropic active systems.

Figure 1.4 is a sketch that shows bacteria aligning in a nematic phase, where **n** represents the self-driven units aligned along a local axis. We use the hydrodynamic theory of thermotropic nematic liquid crystals to study the collective behaviour of active nematic liquid crystals [64, 69, 106, 107].

In terms of phase formation, active fluids can exhibit either nematic apolar or polar ordering [64,126]. Active polar fluids consist of head-tail structures, forming polar or ferromagnetic orders, as illustrated in Figure 1.5(a) [126,135]. These systems may also form apolar states, where the particles align in either direction along the same axis of mean orientation, exhibiting global symmetry of $\mathbf{n} \to -\mathbf{n}$ (Figure 1.5(b)). The steric interactions between particles often dominate, leading to nematic phase formation [1].



Figure 1.4: Schematic showing bacteria align into a nematic phase.

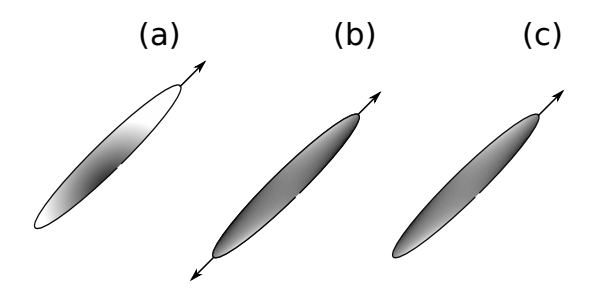


Figure 1.5: Schematics of active particles: (a) polar particle, (b) apolar particle, and (c) self-propelling particles.

1.3.1 Hydrodynamics of active nematics

In active nematics, the key idea is that the constituent particles, such as elongated biological filaments or synthetic rods, consume energy to generate motion. Unlike passive systems, where disturbances typically decay over time due to viscosity and friction, active nematics can increase disturbances because of the continuous input of energy at the microscopic level. Imagine a uniform alignment of rod-like particles (the nematic director field). If there is a small bend or splay in this alignment, the active stresses generated by the particles push or pull the fluid around them, which will either enhance or suppress the distortion. These flows, driven by active stresses, couple with the orientation of the nematic field. If this coupling is strong enough, the feedback loop leads to a hydrodynamic instability: the nematic order breaks into chaotic, swirling patterns known as active turbulence [2, 10, 126].

Continuum theory of active nematics, building on the system's symmetries, extends the

theory of liquid crystals, particularly the hydrodynamic theory of thermotropic nematic liquid crystals by incorporating activity term in the stress tensor [107, 211, 221]. This theory can be applied to systems operating over extended periods and on length scales that are significantly larger than the size of active particles [227].

Many recent studies [2,9,15,87,123] have explored the phase transitions and collective behaviour of active nematics. For example, in 2D systems, activity can drive transitions from homogeneous states to chaotic ones, with the formation of vortices and spontaneous flow [64,176,256]. In one-dimensional geometry, active systems exhibit inherent hydrodynamic instabilities under planar anchoring [215,243,252]. These hydrodynamic instabilities in active nematics can also be suppressed by shear near walls [215], and interactions between director orientation and flow can lead to sustained steady spontaneous flow [126]. These hydrodynamic instabilities can also drive the emergence of topological defects [105].

One of the foundational models of polar active matter, which later inspired the development of theories for active nematics, can be traced back to the Vicsek model in 1995 [232], which reveals that self-propelled agents interacting via simple alignment rules and subjected to noise undergo a genuine phase transition from disordered to ordered motion. This demonstrated that long-range order and collective dynamics can emerge in dry active matter systems. Despite its success in capturing essential features of collective motion, the Vicsek model has several notable limitations. First, it assumes particles move on a fixed substrate and neglects fluid interactions or hydrodynamics. Second, the model lacks steric or volume exclusion effects; the particles are treated as point-like and can freely overlap, thereby ignoring physical constraints and interactions. Moreover, the alignment rule is overly simplistic, relying only on local averaging and not accounting for more realistic mechanisms such as delayed responses or torque-driven reorientation. Another limitation is the assumption of constant particle speed, even in conditions where crowding or interactions would realistically alter velocity. Furthermore, due to its stochastic and discrete nature, the model is analytically intractable,

meaning that most of the understanding relies heavily on numerical simulations rather than exact theory.

Later in 1998, Toner and Tu developed a theory of flocking [220], to describe a collective motion in systems of self-propelled particles (SPPs) that break rotational symmetry and exhibit macroscopic order. This theory provided the theoretical justification for the observations in the Vicsek model and generalised its results beyond the computational setting. They write down the most general continuum equations of motion for a long-wavelength description of the flock, which is consistent with symmetries and conservation laws, including a continuity equation for density, a Navier-Stokes-like equation for the velocity with nonlinear convective terms, active stresses, and noise.

The Toner–Tu theory thus elevated the Vicsek model from a simulation-based description of polar active matter to a continuum hydrodynamic framework for flocking. It predicted groundbreaking features such as long-range order in two dimensions, giant number fluctuations, and propagating density modes. However, since both the Vicsek and Toner–Tu models describe polar systems, where particles possess a head–tail asymmetry, they cannot capture the full richness of active nematics, which exhibit apolar symmetry. Moreover, their simplifying assumptions, such as motion over a solid substrate with friction (which damps momentum) and the neglect of hydrodynamic interactions, mean they cannot describe phenomena that require later developments, such as the Simha–Ramaswamy or active gel theories.

While the Simha–Ramaswamy theory describes hydrodynamic instabilities in active nematic systems, it was primarily a linearised treatment, which focuses only on the onset of instabilities without exploring the nonlinear steady states that can emerge, such as active turbulence. Additionally, the theory assumed a fixed concentration or small fluctuations around a homogeneous density, limiting its applicability to systems where density inhomogeneities or motility-induced phase separation play a crucial role. It also did not account for viscoelastic effects, complex rheological responses, or cytoskeletal mechanics, which are central to biologically active matter such as actomyosin gels or

the cell cortex. Later in 2003, Ramaswamy et al. [176] constructed the more general universal equations of motion, valid for all systems of dry active nematogenic particles.

However, this theory is only applicable to dry active systems and cannot be applied to wet active systems. Additionally, the theory is limited by its linear approximation, neglect of fluid flow, viscoelasticity, defect dynamics, strong density fluctuations, boundary effects, and simplified noise assumptions.

Beyond these theories, Kruse et al. [106] developed a generalised hydrodynamic theory for active viscoelastic gels composed of polar filaments, motivated by the cytoskeleton dynamics in living cells. The theory describes how continuous chemical energy consumption drives these gels out of equilibrium, which produces flows and stresses not possible in passive materials. The cytoskeletal network is modelled as a polar viscoelastic gel with macroscopic polarity described by a polarisation field. The constitutive hydrodynamic equations were derived, combining the flow velocity field and the polarisation dynamics, including active terms proportional to the ATP chemical potential difference driving the system. The model generalises liquid crystal hydrodynamics by incorporating active stresses generated by molecular motors and polymerisation processes.

Analyses of the governing equations reveal distinct patterns of filament orientation, such as asters (radial), vortices (circular), and rotating spirals, and demonstrate that when active stress exceeds a critical threshold, these defects spontaneously begin to rotate.

The limitation of this theory is that it assumes small activity near equilibrium, simplified geometry, uniform ATP concentration, and neglects complex motor dynamics, boundary effects, chirality and fluctuations. However, a hydrodynamic theory for multicomponent active polar gels was developed to capture possible chiral symmetry of the filaments [90], and later describe the physics of active gels [173].

We now shift from continuum-level ideas to mesoscopic models because continuum

theories, which capture large-scale behaviours, often miss crucial particle-level details such as defect core structure, steric interactions, and noise. However, microscopic theories, though more detailed, can be computationally intensive and may lack the ability to generalise emergent collective behaviour. This makes mesoscopic models a practical middle ground that incorporates nematic alignment, active stresses, and defect dynamics.

A study of the collective motion of self-propelled particles with noisy local interactions provided a microscopic foundation for the study of active systems [15]. Bertin, et al. [14], derived a mesoscopic theory of active nematics, starting with a simple Vicsekstyle model for active nematics, using a combination of kinetic theory and Itô calculus approaches (a framework in stochastic calculus used to handle integration and differentiation when randomness is involved). Other mesoscopic and kinetic theories include a nonlinear field theory for aligning self-propelled rods [165], which bridges microscopic Vicsek-type models to mesoscopic equations using a Boltzmann-Ginzburg-Landau expansion; kinetic theory using the Smoluchowski equation for hard rods with nematic alignment, which leads to continuum equations for density and order parameter fields [9]; theories of binary fluid mixtures, which extend the Doi-Onsager kinetic theory for passive liquid crystals to include activity, enabling the mesoscopic description of defect dynamics, flows, and spontaneous ordering [24]; a nonlinear model of active suspensions, which uses the Smoluchowski equation to describe distribution functions of swimmers, incorporating alignment, hydrodynamic interactions, and noise to derive continuum descriptions [186]; and the dynamics of active Brownian particles using Fokker-Planck equations, which lead to mesoscopic phase-field models for motilityinduced phase separation (MIPS) [246]. Mesoscopic theories often simplify microscopic details and fluctuations, sometimes missing complex hydrodynamic effects and exact defect behaviour.

We conclude the sections on microscopic and mesoscopic theories of active systems by summarising the governing equations for active nematics, including the dry and wet active systems.

Active nematic theories, whether wet or dry, are constructed based on fundamental conservation laws. These include conservation of mass, linear momentum, angular momentum, and particle number. The dynamics of the nematic is described by an order parameter whose evolution depends on the interplay of elastic stresses, active stresses, and viscous dissipation. As earlier mentioned, in wet active nematics, momentum is conserved and hydrodynamic interactions play a key role, while in dry active nematics, substrate friction dominates and momentum is effectively dissipated. Activity enters the theory as an additional stress or flux term that drives spontaneous flows and defect formation. For a detailed formulation of the governing equations, see [39,196,240].

These governing equations have been solved by the hybrid lattice Boltzmann method by Wang and Zhang [240]. The results suggest unsteady director dynamics in a 2D study of self-assembled active nematics below threshold activity. This behaviour of the system is invariant with the interplay between active stress and driven flow. The study also suggests that the system exhibits discontinuity for activity values above the threshold activity, leading to a complex periodic spatiotemporal director pattern.

Simulations have also been used to bridge the gap between microscopic and mesoscopic theories. For example, Duclos *et al.* [44], investigates the emergence of spontaneous shear flows in confined cellular nematics, using experiments, theory, and simulations to understand how activity and confinement lead to self-organised flow patterns. Kozhukhov and Shendruk [105] introduce an algorithm for simulating active nematics using multi-particle collision dynamics.

The accompanying figures (A-D) provide visual representations of the local director field, with the colour denoting the scalar order parameter, while additional figures (i-iv) illustrate vorticity, with arrows depicting velocity. At an initial time step (0), the director remains undistorted, accompanied by a uniform flow field, as depicted in Figures 1.6 (A) and 1.6(i) respectively. Subsequently, at time step 110, the system displays bend instabilities characterised by high-bend kink boundaries with a net force

density parallel to the bend (refer to Figures 1.6 (B) and 1.6(ii)). Progressing to time step 160, a pair of $\pm 1/2$ topological defects emerge, distinguished by the red and blue colours (see Figures 1.6 (C) and 1.6(iii)). Finally, at time step 245, the system evolves into active turbulence, as illustrated in Figures 1.6 (D) and 1.6(iv).

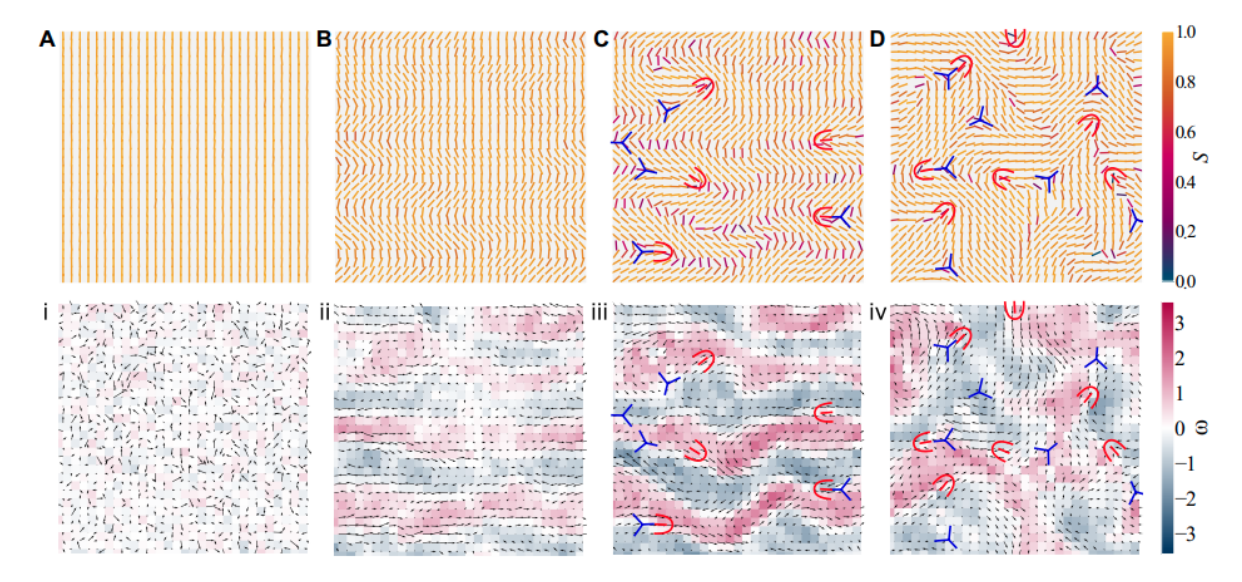


Figure 1.6: Snapshots of the director field (labeled A-D) where the colour represents the scalar order parameter. Additionally, the vorticity field is displayed with arrows indicating the velocity, and the +1/2 and -1/2 topological defects are represented by red and blue colours, respectively. [105].

Other simulations include simulations of microswimmer-driven dynamics in active nematics Mondal et al. [137]. Giomi [59] performed numerical simulations of active nematics in a two-dimensional channel. These studies showed that activity drives spontaneous flows and the creation and annihilation of topological defects. Stronger activity leads to finer spatial structures and faster defect dynamics. The simulations revealed that turbulence emerges when the characteristic defect spacing is intermediate between the defect core size and the system size. As activity increases, the number of defects grows until reaching a saturation point. These results highlight how the interplay between activity, elasticity, and viscous dissipation controls the patterns and dynamics in active nematic systems [59,81].

In the next section, we introduce the concepts of kickback and backflow mechanisms, starting with kickback in passive liquid crystals and concluding with backflow in active nematics. One objective of this study is to investigate the effect of activity on kickback and the interplay between activity and the orienting field.

1.3.2 Kickback and backflow mechanisms

Kickback is an effect observed in nematic liquid crystals in which the director orientation, instead of relaxing monotonically after the removal of an external orienting field (electric or magnetic), initially increases in magnitude beyond its equilibrium orientation. This leads to a temporary overshoot and a slower eventual relaxation to the final state [68]. This occurs due to the response delay in the flow field created by backflow [223], which acts after the external forcing is removed. Essentially, the director tries to return to equilibrium, but the backflow–driven flow pushes the director away from equilibrium, resulting in a kickback mechanism.

Beyond fundamental studies, backflow dynamics have been found to influence several physical processes, including defect core advection [17, 222, 225], as well as the alteration and anisotropic aggregation of colloidal particles [168, 169]. Additionally, Kos and Ravnik [259] demonstrated that backflow can generate microflows under the influence of external fields.

While these effects are well understood in passive nematics, their role in active nematics, where internal activity drives continuous energy injection, remains an open question. Unlike passive systems, backflow in active nematics arises not only from external fields but also from intrinsic active stresses that generate spontaneous flow and director distortions [60, 183, 259]. In particular, when an orienting field is present in the limit of zero activity, the system behaves like a classical "Fréedericksz transition", where the director realigns with the field. However, as activity increases, it perturbs this transition, modifying the interplay between backflow and field-induced alignment.

In summary, backflow in Ericksen–Leslie theory arises from the coupling terms in the stress tensor, particularly the Leslie viscous stress, where the reorientation of the director feeds back into the flow field. This effect is crucial for capturing phenomena such as director relaxation, defect dynamics, and spontaneous flow, and plays a more prominent role in active nematic systems.

Understanding the effect of activity on kickback and the interplay between the orienting field and the backflow mechanism is crucial to advancing theoretical models of active nematics. Chapter 3 aims to explore the influence of activity on kickback-driven dynamics and the hydrodynamic interactions of external fields and activity.

We now discuss the "classical Fréedericksz transition" in the next section.

1.3.3 Fréedericksz transition

Fréedericksz transition is a fundamental phenomenon in the physics of liquid crystals that describes how the orientation of liquid crystal molecules changes in response to an external field, such as an electric or magnetic field [54, 202]. In the undistorted state, the molecules are uniformly aligned due to surface anchoring at the boundaries, which enforces a stable configuration. When an external field (magnetic or electric field) is applied perpendicular to this alignment, it exerts a torque on the anisotropic molecules, trying to reorient them along the field direction. However, the surface anchoring resists this change, and the orientation remains undistorted until the field strength exceeds a critical threshold, also known as the *Fréedericksz threshold*. At this threshold, the torque from the external field becomes strong enough to overcome the anchoring, making the uniform state unstable. This makes the liquid crystal molecules reorient to form a new configuration that minimises the combined elastic and field energies. This transition leads to deformations (such as splay, bend, or twist) of the director, depending on the geometry and the nature of the applied field.

For example, consider a sample of liquid crystal sandwiched between two parallel plates, a distance d apart, of splay geometry (a situation where the director, \mathbf{n} , is strongly anchored parallel to the plates) as shown in Figure 1.7. In this setup, it can be shown that the Fréedericksz threshold is $H_c = (\pi/d)\sqrt{K_1/\chi_a}$, where χ_a is the anisotropy of the magnetic susceptibility, and K_1 is the splay elastic constant. Assuming $\chi_a > 0$, which

indicates that the director tends to align with the magnetic field. For $H < H_c$, the sample of liquid crystal parallel to the plates remains undistorted (see Figure 1.7(a)), but as H increases via the Fréedericksz threshold H_c , a Fréedericksz transition occurs when $H > H_c$, the director reorients in response to the effect of the magnetic field \mathbf{H} (see Figure 1.7(b)).

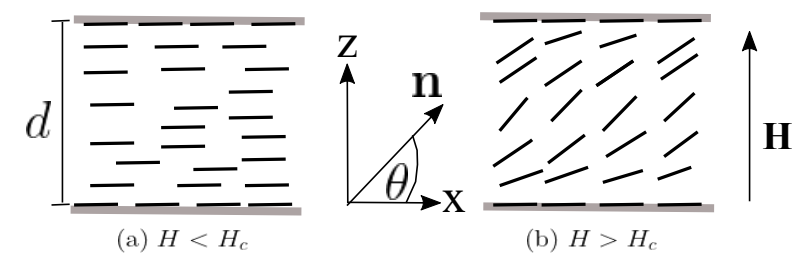


Figure 1.7: Geometry of the classical Fréedericksz transition, where θ is the director, \mathbf{n} makes with x-axis. Note that the magnetic field \mathbf{H} is initially perpendicular to the director \mathbf{n} . (a) The original state of the liquid crystal sample, where $H < H_c$, shows no reorientation. (b) When $H > H_c$, the applied magnetic field induces a reorientation of the director toward alignment with \mathbf{H} .

In active nematics, recent experimental work by Alam *et al.* [3], demonstrates how active nematic droplets in 3D undergo Fréedericksz transition. The study shows that increasing droplet size beyond a critical diameter triggers a shift from a quiescent to a spontaneously flowing state. The critical threshold depends on activity, elasticity, and geometry, while energy consumption remains constant, which confirms the inactivity phase as a stable nonequilibrium state.

In the next Section, we discuss active instabilities, which will be essential in Chapter 3 for analysing homeotropic and planar alignments.

1.3.3.1 D- and S-modes in active hydrodynamic instabilities

We review here the spontaneous flow transition observed in active nematics, reminiscent of the classical Fréedericksz transition in passive liquid crystals but driven by activity rather than external fields. Building on the analysis presented in Walton's thesis, we review the reorientation dynamics of active nematic liquid crystals under external fields, with particular focus on how activity modifies the accessible director configurations [238].

Activity destabilises the uniform director state, leading to two distinct eigenmodes: the symmetric (S-mode) and the degenerate (D-mode) [172], also referred to as Mode I and Mode II [238]. The S-mode corresponds to the director tilting away from the vertical with an "S-shaped" profile across the cell thickness: at one boundary, the tilt is in one direction, while at the opposite boundary it reverses. This mode breaks inplane rotational symmetry by selecting a preferred axis (e.g. the x-axis) and generates shear flow along it. The D-mode also involves titling of the director but produces a "D-shaped" director profile with maximum distortion at mid-cell and vanishing tilt at the boundaries.

Figure 1.8 illustrates how strong external orienting fields drive the reorientation dynamics of contractile active nematics, comparing symmetric and anti-symmetric director responses. In both cases, the director aligns with the applied field during switch-on and relaxes back after switch-off, with no evidence of kickback at the chosen moderate activity strength [238].

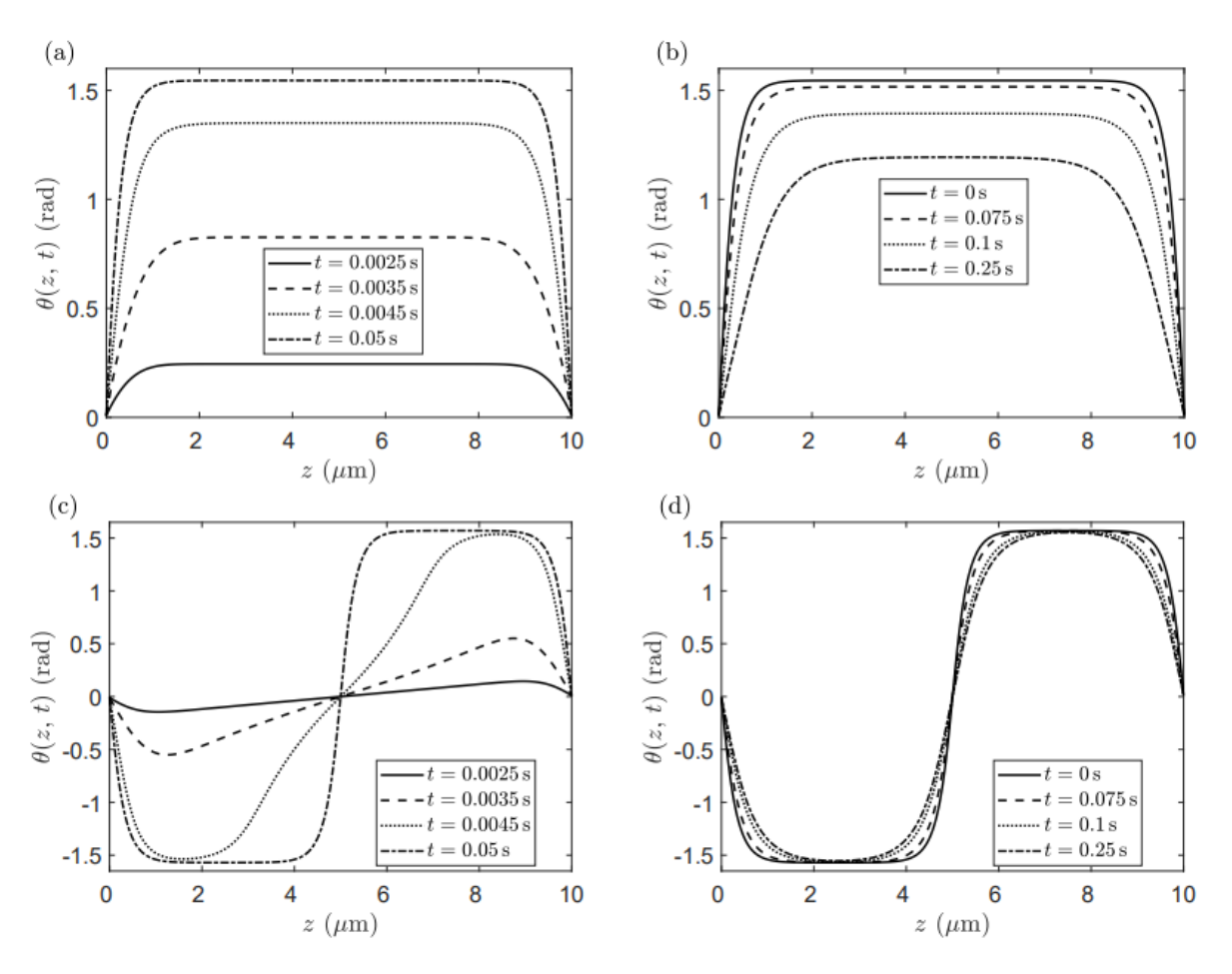


Figure 1.8: Time evolution of the director angle $\theta(z,t)$ for a contractile active nematic with activity $\xi = 50\,\mathrm{Pa}$ during switch-on and switch-off of a strong external orienting field. Panels (a) and (b) show the symmetric mode: (a) rapid alignment of the director in the bulk during switch-on, reaching $\theta \approx \pi/2$, and (b) relaxation to the symmetric equilibrium configuration after field removal, with no kickback. Panels (c) and (d) show the anti-symmetric mode (Mode II): (c) director aligns with the field across the channel during switch-on, and (d) relaxation after field removal, where the anti-symmetric structure is transiently maintained due to system symmetry, remaining largely unchanged over long times with no kickback [238].

In the classical Fréedericksz transition, a uniform director becomes unstable when an external electric or magnetic field exceeds a critical threshold, the field torque overcoming the elastic restoring torque. By contrast, the spontaneous flow transition in active nematics is internally driven: instability occurs once active stresses exceed a threshold set by the balance of elasticity and viscous dissipation.

Other studies also investigated in- vs out-of-plane instabilities in active films, which conceptually maps to S/D-modes [199]. Other instabilities include wrinkling instability

in bulk 3D active nematics [203], where the director field spontaneously buckles.

In Chapter 3 of the thesis, we will investigate the combined effect of internal active stresses and external fields on active nematics. This aims to develop a comprehensive understanding of how these competing influences govern director orientation, flow instabilities, and pattern formation. This combined effect promises to bridge classical liquid crystal theory with emerging phenomena in active soft matter.

1.4 Active nematics in confinement

Since our study concerns active nematics in a channel, this section will review the existing literature on active nematics in confined geometries, ranging from circular confinement to periodic boundary conditions.

Since our study involves the HAN geometry, which includes both planar and homeotropic alignments, it is worth mentioning that HAN anchoring occurs when the director is parallel to one wall and perpendicular to the other. The planar alignment and the HAN geometry setups are given in Figures 1.9(a) and 1.9(b), respectively.

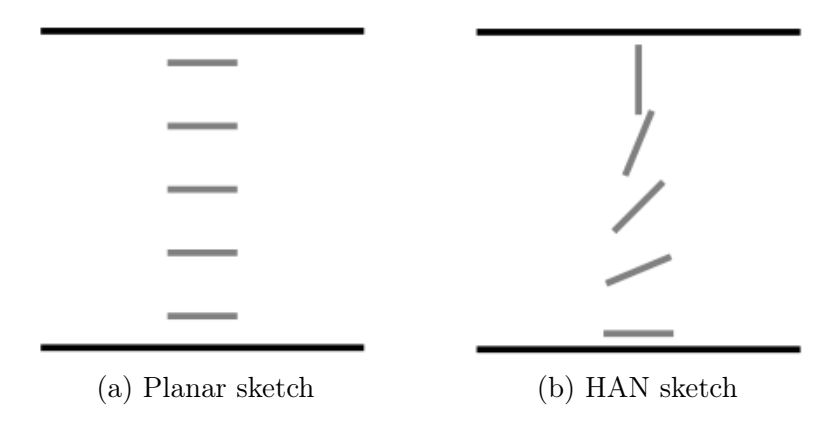


Figure 1.9: Sketches of the equilibrium director configurations in the limit of no flow for the planar and HAN anchoring.

In circular confinement, active nematics exhibit periodic, steady, or vortical flow depending on their hydrodynamic interactions, surface interactions, or spatial forces between particles [42, 245]. In confined nematic liquid crystals, the input energy of the active stresses can be dissipated by friction on the substrate and viscous flows [135]. Ac-

tive nematics confined to a quasi-one-dimensional geometry in hybrid alignment show different velocity profiles compared to homogeneous alignment [184]. Boundary layers in confined active nematics in an annular-shaped channel are also a factor in active turbulence, characterised by topological defects [77].

Flow patterns of active nematics confined in a channel with periodic boundary conditions are summarised in Figure 1.10 [41, 197]. The flow ranges from no flow to active turbulence flow depending on the channel height or activity strength, which allows flows to wrap around and mimic an effectively unbounded system while maintaining computational feasibility. Doostmohammadi et al. [41] and Shendruk et al. [197] demonstrated that confinement, boundary conditions, and activity strength critically shape these turbulent flows, with defects exhibiting coordinated patterns ("dancing disclinations") under narrow channel confinement. A similar study of active nematics confined in a two-dimensional channel with planar anchoring [187] demonstrated that the system exhibits a rich variety of flow behaviours depending on the activity strength. At low activity, the nematic aligns along the channel, producing unidirectional laminar flow with minimal defect formation. As the activity increases, the system transitions to more complex flow regimes, including bidirectional flow and vortex-like structures, eventually culminating in fully developed active turbulence characterised by the spontaneous creation, motion, and annihilation of topological defects. Their results highlight how confinement and boundary conditions interact with activity to shape the spatiotemporal dynamics of active nematics, providing insight into both the fundamental physics of active fluids and potential applications where controlled flow patterns are desirable. A recent study by Chimming et al. [190] show that spatially patterned activity in 2D active nematics can drive transitions from chaotic active turbulence to ordered vortex states. If active nematics are going to be used for technological applications, such as sensors, controlling their behaviour is of immense importance. As mentioned earlier, one way to control the behaviour of active nematics is via confinement.

While studies such as [42,187,245] focused on extensile active systems in a channel using

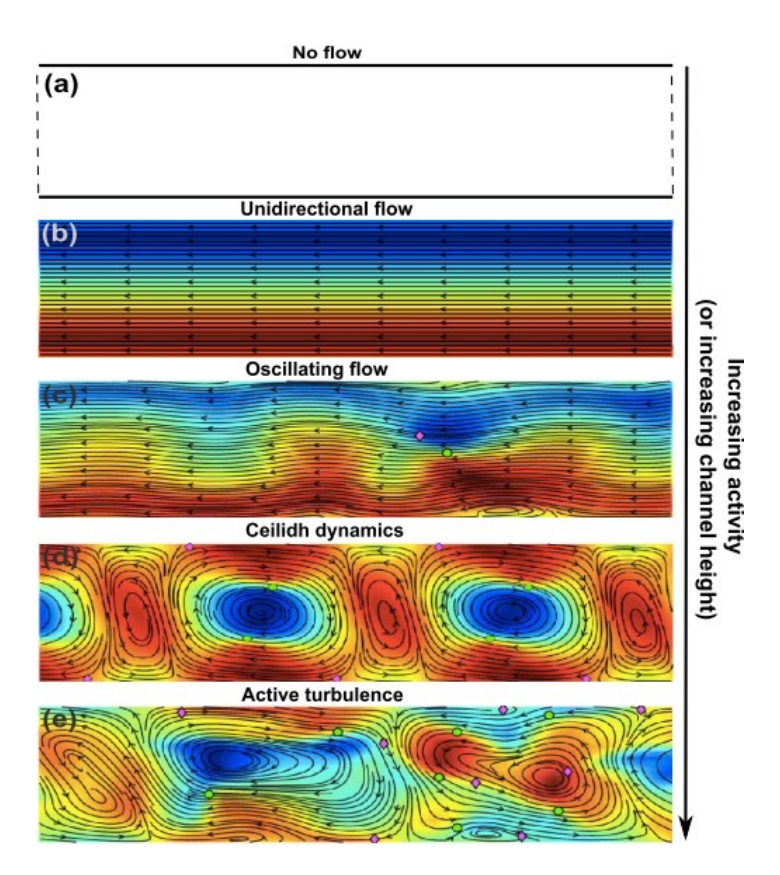


Figure 1.10: Plot showing the flow profiles for various activity parameter values. Black lines (streamlines), black arrows (direction of the flow), colourmap (vorticity field), circles (green), and diamonds (magenta) mark +1/2 and -1/2 topological defects, respectively [41].

planar anchoring, our study focuses on both extensile and contractile active nematics in a channel using a combination of planar and homeotropic anchoring. Building on these studies, we have developed one-dimensional and two-dimensional hydrodynamic models to explore the behaviour of active nematics subjected to orienting fields. As previously mentioned, the one-dimensional model covered in Chapter 3, incorporating infinite planar anchoring, demonstrates that the application of an orienting field reduces the kickback effect in extensile nematics but sustains the kickback in contractile nematics. Additionally, the nonlinear aspects of the model reveal different solution states, such as uniform, symmetric, and antisymmetric states.

In the two-dimensional model (covered in Chapters 4 and 5), we combine planar and hybrid anchoring. In contractile systems, the flow patterns include non-flow, circulatory, and oscillatory states, while in extensile systems, we observe unidirectional and bidirectional flows, as well as combinations of unidirectional and bidirectional flow in extensile systems has not been observed in previous studies. Additionally, the transient dynamics of active nematics using the periodic boundaries show how the hybrid state evolves and how bidirectional transitions to unidirectional flow occur.

1.5 Experimental observations of active fluids

So far, we have reviewed the theoretical studies of active matters in a confined and unconfined geometry. The experimental study of active matter has been developing for many years. Research increasingly shows a correlation between computational and experimental active matter. Wioland et al. [244] experimentally and computationally studied the collective motion of bacteria under channel confinement using a thin periodic racetrack and periodic boundary conditions, respectively. Experimentally, the suspension of the dense bacteria into a thin periodic racetrack suggests stable circulation. Computationally, the net flow and correlation profile as a function of the channel width suggests fluid flows generated by the bacteria. The hydrodynamics interactions

and the confinement lead to microscopic flow circulation. The study also suggests that strong confinement stabilises the turbulence collection motion of the bacteria streamline.

The effects of boundary layers on confined active nematics have been studied experimentally by placing a mixture of a few kinesin/tubulin active microliters in a custom-made open pool covered with silicon oil [77]. The results show active turbulence away from the walls with $\pm 1/2$ topological defects formed due to the boundary layers. It also suggests that bulk active flow can be controlled by direct intervention of the active boundary layer via indentations that are smaller than the length of the active nematics.

Other experimental work [42] suggests that active turbulence can be suppressed giving rise to steady or periodic flow. In circular confinement, the active matter exhibits either periodic, steady, or vortical flow depending on the hydrodynamics interactions of the active matters, surface interactions, or spatial inter–particle forces [42, 245]. Doostmohammadi et al. [39] experimentally studied the microtubule-motor systems by placing the active layer in contact with a smectic A liquid crystal, giving rise to different flow patterns accompanied by $\pm 1/2$ topological defects. Varghese et al., also experimentally demonstrated that confinement can control bend instability [229] in active nematics.

Other studies, such as [72, 73], have also demonstrated the controllability of active nematics by changing the properties of the viscous fluid lying next to the active layer. A recent study by Repula et al. [181] demonstrates the dual role of light as both an energy source and a control signal for active nematics composed of filamentous, phototactic cyanobacteria—organisms capable of transforming light into energy and motion. The study employed patterned illumination to locally activate the motility of these cells, which facilitated their self-assembly into organised nematic states. The intensity of the light influenced both the speed of this ordering process and the degree of alignment achieved among the cells.

Since our goal is to explore active nematics for potential applications in sensor design,

the next section reviews the existing literature on sensors and sensing devices based on smart materials with tunable rheological properties, including electrorheological fluids, magnetorheological materials, and liquid crystal-based sensors.

1.6 Sensors and sensing devices

The use of active fluids in sensor design presents a promising direction due to their unique ability to translate small local changes, such as the alignment of self-driven units, into long-range effects in flow and orientation. This sensitivity to local perturbations makes active fluids attractive candidates for developing highly responsive sensing systems. Motivated by this potential, it is essential to review existing sensors and sensing devices based on smart materials with tunable rheological properties, such as electrorheological fluids (ERFs) and magnetorheological materials (MRMs). These materials exhibit controllable stiffness and damping under external stimuli, electric fields for ERFs and magnetic fields for MRMs, and have already found use in diverse applications requiring dynamic response and precision [151]. By examining current sensor technologies based on ERFs and MRMs, we aim to identify principles and strategies that could inform the development of next-generation sensors, including those leveraging the emergent properties of active fluids. We also review liquid crystal biosensors to ensure a comprehensive understanding of smart materials that respond to environmental changes through alterations in molecular alignment and optical properties.

1.6.1 ERF sensors

An electrorheological fluid is a suspension made up of fine dielectric particles dispersed in a viscous carrier oil. As a result, it demonstrates rapidly varying rheological properties when an electric field is applied. In other words, its stiffness and damping characteristics depend on the strength of the applied electric field [151].

Studies on ERFs have explored methods to enhance their field-dependent properties by utilising various particles, carrier fluids, and additives, such as liquid crystals and carbon nanotubes. Other studies have also focused on their dynamic behaviour, rheological models, and flow modes [19,110,119,241]. Due to their quick response and controllable viscosity, ERFs have been applied in shock absorbers, vibration control, medical devices, brakes, clutches, and energy systems [34,201,250].

Kim et al. [99] developed a wave transmission sensor by incorporating an ERF into aluminium sandwich structures, using a small piezoelectric patch as both the transmitter and receiver. Their findings showed that the magnitude and frequency of the transmitted signals, as well as the device's sensitivity, could be determined in either the time or frequency domain. In another work, a bidirectional clutch incorporating a spherical ERF joint was developed, where torque is measured as a function of the applied electric field intensity [75]. Zhang et al. [258] designed a sensor combining an ERF actuator and a conducting polymer sensor, capable of accurately measuring displacements up to 20 Hz. At higher frequencies, the conducting polymer sensor's performance declined. This system shows potential for applications like ERF microvalves and precision microchip control. A sensing mechanism using a strain gauge and an ERF-filled viscous brake was developed to measure pressing force based on motor speed and applied voltage. The goal was to create a device to exert a constant pressing force that maintains a constant pressing force, enabling optimal control of braking force in various brake and clutch systems [200].

A novel type of ERF has been developed using a nano-silica grafting method to overcome the limitations of traditional ERFs, which typically use carbonyl iron particles. These particles have high electrical conductivity, which can restrict the fluid's field-responsive rheological behaviour [158]. Another limitation of ERF-based sensors lies in their operational constraints. While they are capable of detecting high-frequency signals in dynamic settings and offer high sensitivity in tactile sensing applications, they are typically suited only for low-force measurements and require high voltage input to function effectively. In contrast, MRF-based sensors, though slightly limited in signal sampling frequency compared to ERF sensors, offer broader applicability and avoid the

high-voltage requirement [151].

1.6.2 MRF Sensors

Magnetorheological fluids exhibit field-dependent rheological characteristics, such as yield stress, which are significantly higher and more stable than those of ERFs, owing to their responsiveness to magnetic fields rather than high voltages. As a result, MRFs have a broader range of applications in actuators and sensors compared to ERFs [151].

The use of MRFs for in vitro cancer therapy by blocking blood flow to tumours using magnetic fields [51]. In another study, a black—box model was developed to identify magnetorheological damper behaviour using self-sensing capabilities. The resulting model functions as a virtual sensor for measuring damping force in vibration control systems with MR dampers [224]. Kaluvan et al. [93] introduced a novel method to measure the dynamic response of MRF under squeeze mode. This method enabled the measurement of field—dependent dynamic forces and vibration amplitude reductions across various actuation angles. Other innovative tactile and sensing devices using MRFs have been developed for biomedical and automotive applications. These include tactile sensors mimicking human organ viscoelasticity for robotic surgery [101,152–154], advanced vehicle suspension systems with sensor-integrated MR dampers [163], and a magnetic-field-sensitive displacement sensor based on soft MRF films [116]. These studies demonstrate the ability of MRF-based systems to replicate dynamic biological motions, control repulsive forces, and improve system responsiveness through magnetic field manipulation.

Recent advances in magnetorheological elastomer and magnetorheological fluid technologies have enabled the development of various sensor and feedback systems. MREs, composed of magnetizable particles like Cabonyl Iron Particles, are responsive to magnetic fields and suitable for applications such as pressure and force sensors [94, 117].

ERF-based sensors face specific limitations, such as the requirement for high voltage input and suitability only for low-force measurements. Similarly, MRF-based sensors

are constrained by lower sampling frequencies and slower response times. These challenges in ERF and MRF technologies have led researchers to explore alternative smart materials such as liquid crystals, which offer unique advantages for biosensing applications. Liquid crystal biosensors respond to molecular interactions through changes in optical properties, enabling label-free, highly sensitive detection, particularly valuable in biomedical and biochemical systems.

1.6.3 Liquid crystal biosensors

The optical properties of LC, such as birefringence [92,149], as well as high sensitivity of the molecules to external stimuli, such as electromagnetic fields [129,210], surface effects [21, 206], optics [231], temperature [205], and chemical analytes [12] have made LCs useful for sensing applications [171]. Their ability to amplify and transmit molecular-scale changes to macroscopic signals underpins LC-based biosensing strategies [143,247], particularly in detecting biological interactions through changes in molecular orientation and birefringence [48,142]. Surface—induced orientation changes can be amplified over distances up to 100 μ m, which enables label-free detection [249]. These principles have supported the development of advanced LC-based optoelectronic biosensors [58,159]. LC optical anisotropy and fluidic nature make them ideal for optofluidic systems, which combine optics and microfluidics for biomedical sensing [32,195]. Such systems integrate sample handling, detection, and data transfer in a single platform, enhancing sensitivity and efficiency.

Based on their sensing interfaces, LC biosensors are generally categorised into three types: LC-solid interface [204], LC-aqueous interface [27], and LC-droplet interface [27]. Each configuration offers distinct advantages for biomolecule detection. The LC-solids interface is straightforward in design and allows for the creation of array structures. The LC-aqueous interface provides direct contact with biological samples, enhancing mobility and accessibility for biotargets. Sensitivity can be further increased by integrating LC droplets with laser spectroscopy techniques. Additionally, microflu-

idic technology can be employed to fabricate LC biosensors with varied geometries, reducing manual errors, enabling precise determination of sensing parameters, and improving overall sensitivity [239].

1.6.4 Toward active nematic-based sensors

The use of active fluids in sensor design represents an exciting frontier due to their intrinsic ability to amplify local disturbances, such as changes in surface alignment, into long-range orientational and flow effects. This responsiveness positions active fluids as promising candidates for next-generation sensing technologies. Existing studies on smart materials, including ERFs, MRFs, and LCs, provide foundational principles and technological benchmarks, yet they also reveal certain limitations which active nematics may overcome. RF and MRF offer field-controllable mechanical properties, such as stiffness and damping. However, these systems are inherently limited to responding to applied external fields and typically require active electronics and feedback loops to detect mechanical perturbations. Their spatial resolution and sensitivity are often constrained to the localised region of stimulus application, and the signal propagation is not inherently built into the material's dynamics. LC-based biosensors, particularly those using nematic and cholester phases, utilise their optical anisotropy and sensitivity to surface alignment changes to detect biological and chemical analytes [12,32]. Such sensors work by translating surface anchoring alterations, caused by molecular interactions or physical forces, into detectable optical signals through birefringence changes. While these systems enable label-free detection and work well in optofluidic platforms, the effects remain spatially confined. That is, surface-induced distortions typically affect only the liquid crystal orientation within a narrow region, which limits their effectiveness for detecting small, localised stimuli unless they occur directly within the optical path. This is where active nematic liquid crystals might be useful.

Our proposed sensor system exploits the intrinsic activity of the material to convert a local anchoring change, caused by the presence of a small object at the upper boundary

of the LC layer, into a global response throughout the entire domain. In passive systems, such a perturbation would be localised, which makes it difficult to detect. But in active nematics, this same perturbation induces flow that reorients the director configuration far beyond the source of disturbance. This allows for the indirect detection of the object through the observation of long-range distortions in the director or flow patterns, even when the object itself is invisible or microscale. The mechanism is analogous to throwing a small pebble into a calm lake: although the pebble is tiny, its impact creates ripples that spread widely across the water's surface. Similarly, the active nematic medium propagates director disturbances initiated at the anchoring surface, turning localised anchoring changes into large-scale, observable effects.

In Chapter 4 of this thesis, we will develop a two-dimensional model incorporating a combination of anchoring conditions. This setup allows changes in the top surface anchoring, which we imagine to have been caused by an object that we wish to detect, to induce flow, which in turn can influence the liquid crystal director far from the region of disturbance.

In the next chapter, we will focus on the mathematical framework, including the formulation of the Frank-Oseen elastic energy and the Ericksen-Leslie dynamic theory of nematic liquid crystals, as they form the underlying theory of our study. We will then summarise the Ericksen-Leslie theory for active nematics, which serves as the main theory behind the governing equations we will investigate, and conclude with a discussion of the anchoring and boundary conditions relevant to this research.

Chapter 2

Theoretical Frameworks for Passive and Active Nematic Liquid Crystals

2.1 Introduction

In this chapter, we explore the mathematical theories of nematic liquid crystals. We focus on the Ericksen-Leslie theory for both passive and active nematic liquid crystals. We begin by introducing the Frank-Oseen static elastic energy, detailing the contributions from splay, twist, and bend configurations in Section 2.2. Section 2.3 covers electric and magnetic fields, as our study involves the contribution of an external field. Section 2.4 reviews the dynamic Ericksen-Leslie theory of nematic liquid crystals. In Section 2.4.1, we formulate Ericksen-Leslie's theory for active nematics and discuss energy dissipation in Section 2.4.2. We outline the Ericksen-Leslie equations for active nematics in Section 2.5, and discuss activity strength and derive the active stress tensor in Sections 2.5.1 and 2.5.1.1, respectively. Section 2.6 addresses the boundary conditions for the director and velocity, including infinite planar and homeotropic anchorings and a hybrid aligned nematic (HAN) state for the director, as well as the no-slip and no-penetration conditions for velocity. Finally, in Section 2.7, we summarise the parameter values we use in this thesis.

2.2 Frank-Oseen elastic energy

Oseen's 1933 paper "The Theory of Liquid Crystals" [148] was one of the first attempts to build a mathematical framework for describing liquid crystals. He represented molecules as rigid bodies with symmetry axes, described by unit vectors (e.g., \mathbf{L}_1 and \mathbf{L}_2 , where \mathbf{L}_i denotes the unit vector along the symmetry axis of the i^{th} molecule), and initially characterised their relative configuration using the intermolecular separation vector \mathbf{r}_{12} (defined as the vector pointing from the centre of molecule 1 to that of molecule 2), together with angular relationships between their axes. However, these four quantities were insufficient to fully specify the configuration because they could not distinguish between mirror-image (left- and right-handed) arrangements, known as "chirality." To resolve this, Oseen introduced a fifth scalar quantity, $(\mathbf{L}_1 \times \mathbf{L}_2) \cdot \mathbf{r}_{12}$, which explicitly accounts for chirality by changing sign under inversion. His analysis further suggested that the molecular interactions giving rise to cholesteric ordering cannot be explained solely by simple electrostatic considerations but must also involve orientationdependent forces that favour a particular handedness. This work provided the basis for the Oseen-Frank elastic theory, in which macroscopic distortions such as splay, twist, and bend are described in terms of underlying molecular interactions. This theory is limited in that the equilibrium configurations do not account for the dynamic behaviour of the liquid crystal. It also lacks hydrodynamic coupling, which means the interactions between molecular orientation and fluid flow are ignored. Moreover, singularities in the director field, such as defects, lead to predictions of infinite energy, which is physically unrealistic. The model assumes constant density and rigid molecules, which neglects both density variations and thermal or molecular fluctuations.

In an attempt to study the curvature properties of liquid crystals, F.C. Frank in 1958 extended Oseen's work, which paved the way for the exact experimental determination of the elastic constants [53]. In general, Frank-Oseen elastic theory explains how the director field can be distorted away from a uniform state [53, 148, 193]. The free energy

density is the result of the possible changes in the orientation of the director **n**, which result in six components of the curvature called *curvature strains* [202]. Here, we will summarise the Frank-Oseen static elastic theory, which will serve as a foundation for the subsequent chapters.

We consider a unit vector field \mathbf{n} called the *director*, which describes the mean molecular alignment at a point \mathbf{x} in a given volume S so that $\mathbf{n} = \mathbf{n}(\mathbf{x})$, and $\mathbf{n} \cdot \mathbf{n} = 1$.

It is assumed that the system is isothermal and in the nematic phase, so that distortions in the orientation of the anisotropic axis (represented by the director field \mathbf{n}) incur an energy cost. This energy cost is captured by the elastic component of the Helmholtz free energy, referred to here as the elastic free energy density. The term total Helmholtz elastic free energy refers to the internal energy stored in the distortion of the director when temperature is held constant. This assumption of constant temperature is important because it means the model does not account for temperature changes or phase transitions. In line with [202], we assume that the free energy density w depends on both the local orientation \mathbf{n} and its spatial gradient $\nabla \mathbf{n}$

$$w = w\left(\mathbf{n}, \nabla \mathbf{n}\right),\tag{2.1}$$

where ∇ denotes the spatial gradient operator. The total elastic free energy W over the domain V is then given by

$$W = \int_{V} w(\mathbf{n}, \nabla \mathbf{n}) \ dV. \tag{2.2}$$

By focusing solely on the elastic energy from director distortions, the model excludes bulk free energy terms that represent the thermotropic effect. Such bulk terms appear in more general theories (like Landau–de Gennes bulk free energy terms), where temperature influences the material's order and phase behaviour [35,36]. In other words, since temperature effects are not included here, the free energy only captures how the spatial variation costs energy of the director, not how temperature changes the degree

of order of the liquid crystal.

The liquid crystal sample associated with this energy (2.2) is assumed to be incompressible [202]. Since the nematic liquid crystals are apolar, the director \mathbf{n} has the same physical meaning as $-\mathbf{n}$.

It is also assumed that the energy density remains unchanged under rigid body rotations. This means that if the entire liquid crystal configuration is rotated, the energy should remain the same. Mathematically, this requires that the function w, which defines the energy density, must be *invariant* under rotations.

In practical terms, if both the director \mathbf{n} and its spatial gradient $\nabla \mathbf{n}$ are transformed by a proper orthogonal linear map $Q: \mathbb{R}^3 \to \mathbb{R}^3$, with $\det(Q) = 1$, then the value of wshould not change. That is,

$$w\left(\mathbf{n}, \nabla \mathbf{n}\right) = w\left(Q\mathbf{n}, Q\nabla \mathbf{n}Q^{T}\right),\tag{2.3}$$

where Q is a linear map that preserves lengths and angles, and its matrix representation in an orthonormal basis belongs to the special orthogonal group. This invariance reflects the physical principle that the internal energy of the system depends only on the relative distortions of the director field, not on its absolute orientation in space.

To derive the elastic free energy density for nematic liquid crystals, we begin by considering a local Cartesian coordinate system x, y, z, with the undistorted director aligned along the z-axis:

$$\mathbf{n}_0 = (0, 0, 1). \tag{2.4}$$

In this reference configuration, distortions in the director field are characterised by six independent components of curvature strain, corresponding to the classical deformation modes: splay, twist, and bend. These are defined as follows:

Splay:
$$s_1 = \frac{\partial n_x}{\partial x}$$
, $s_2 = \frac{\partial n_y}{\partial y}$,
Twist: $t_1 = -\frac{\partial n_y}{\partial x}$, $t_2 = \frac{\partial n_x}{\partial y}$,
Bend: $b_1 = \frac{\partial n_x}{\partial z}$, $b_2 = \frac{\partial n_y}{\partial z}$, (2.5)

where (n_x, n_y, n_z) are the components of the director field \mathbf{n} [53,202]. These quantities represent local changes in the orientation of the director field due to spatial gradients. Splay terms correspond to divergence-like distortions (expansion or compression along the director), twist terms represent rotational distortions of the director axis, and bend terms capture curvature of the director away from its initial orientation. Together, they form the foundation of the Frank-Oseen theory of elastic distortions in nematic liquid crystals.

The graphical representations of the distortions of splay, twist, and bend and their associated elastic constants, K_1 , K_2 and K_3 , are given in Figure (2.1) [226].

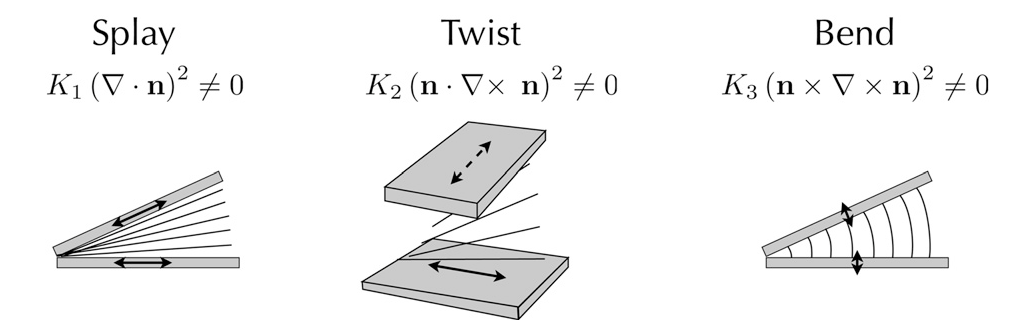


Figure 2.1: Graphical representations of the distortions of splay, twist, and bend and their associated elastic constants, K_1 , K_2 and K_3 [192].

The director field $\mathbf{n}(\mathbf{x})$ is defined as a unit vector at every point \mathbf{x} in the 3D domain $\Omega \subset \mathbb{R}^3$ occupied by the liquid crystal, so that $\mathbf{n} \cdot \mathbf{n} = 1$ everywhere in Ω . Taking the gradient of this identity yields $\nabla(\mathbf{n} \cdot \mathbf{n}) = 0$, which can be expanded as $0 = \nabla(n_i n_i) = 2 \mathbf{e}_j n_i n_{i,j}$, where n_i are the components of \mathbf{n} , $n_{i,j} = \partial n_i / \partial x_j$, and \mathbf{e}_j are the basis

vectors in \mathbb{R}^3 for j=1,2,3. This implies

$$n_i n_{i,j} = 0, \quad j = 1, 2, 3,$$
 (2.6)

meaning that the directional derivative of \mathbf{n} along itself vanishes; any spatial variation of the director lies in the plane orthogonal to \mathbf{n} .

Using the reference (undistorted) configuration from equation (2.4), where $\mathbf{n}_0 = (0, 0, 1)$, the only nonzero component is $n_z = 1$. In this uniform state, the derivative of the z-component with respect to any spatial coordinate vanishes. The notation

$$n_{z,j}(0) = 0, \quad j = 1, 2, 3,$$
 (2.7)

refers to evaluation at the "reference director" \mathbf{n}_0 , not at the spatial origin (x, y, z) = (0, 0, 0). This clarification ensures that in the undistorted state, all spatial derivatives of n_z vanish.

To analyse the local structure of the director field, we perform a Taylor expansion of its components about the origin. Using the undistorted reference state defined in equation (2.4), and applying the orthogonality condition from equation (2.6), the director field \mathbf{n} near the origin can be written as

$$n_{x} = a_{1}x + a_{2}y + a_{3}z + \mathcal{O}(|x|^{2}),$$

$$n_{y} = a_{4}x + a_{5}y + a_{6}z + \mathcal{O}(|x|^{2}),$$

$$n_{z} = 1 + \mathcal{O}(|x|^{2}),$$
(2.8)

where the a_i are constants determined by the first derivatives of the director field components, and higher-order terms in the expansion are denoted by $\mathcal{O}(|x|^2)$.

These linear terms can be re-expressed using partial derivatives of the director field

components as follows

$$n_{x} = x \frac{\partial n_{x}}{\partial x} + y \frac{\partial n_{x}}{\partial y} + z \frac{\partial n_{x}}{\partial z} + \mathcal{O}(|x|^{2}),$$

$$n_{y} = x \frac{\partial n_{y}}{\partial x} + y \frac{\partial n_{y}}{\partial y} + z \frac{\partial n_{y}}{\partial z} + \mathcal{O}(|x|^{2}),$$

$$n_{z} = 1 + \mathcal{O}(|x|^{2}).$$
(2.9)

Relating these terms to the curvature strain components (splay, twist, and bend) defined earlier in equation (2.5), we obtain the identifications

$$a_1 = s_1, \quad a_2 = t_2, \quad a_3 = b_1, \quad a_4 = -t_1, \quad a_5 = s_2, \quad a_6 = b_2.$$
 (2.10)

Using this expansion, the elastic free energy density can now be approximated as a quadratic function of the six independent curvature strain components. This yields the general form

$$w = K_i a_i + \frac{1}{2} K_{ij} a_i a_j, \quad i, j = 1, 2, \dots, 6,$$
 (2.11)

where K_i and K_{ij} are material-dependent curvature constants that account for the elastic response of the nematic liquid crystal to different types of distortions [53, 202].

However, since physical properties must remain invariant under rigid body rotations, we can equivalently describe the system in a rotated coordinate frame (x', y', z'). This invariance implies that the energy density has the same functional form in the rotated frame

$$w = K_i a_i' + \frac{1}{2} K_{ij} a_i' a_j', \quad i, j = 1, 2, \dots, 6.$$
(2.12)

The requirement of rotational invariance plays a crucial role in constraining the form of the elastic free energy. Specifically, the functional form of the energy density must remain invariant under coordinate rotations, as the physical properties of the liquid crystal are unchanged by such transformations. This symmetry requirement significantly reduces the number of allowable terms in the energy expression. A comprehensive discussion of how these arguments lead to the general structure of the elastic energy can be found in Stewart [202, p. 19].

By enforcing the requirement of rotational invariance, specifically under a rotation of $\pi/2$ about the z-axis, and applying symmetry arguments along with the transformation properties of the strain tensor $A' = QAQ^T$, we obtain the constraint

$$a_1(k_1 - k_5) + a_2(k_2 + k_4) + a_3(k_3 + k_6)$$

+ $a_4(k_2 + k_4) + a_5(k_5 - k_1) + a_6(k_6 - k_3) = 0.$ (2.13)

Next, noting that the quadratic terms in the free energy must also be rotationally invariant, and using the fact that $k_{ij}a_ia_j/2 = k_{ij}a_i'a_j'/2$, and further impose rotational symmetry under another $\pi/2$ rotation and derive the transformation of the curvature strain components

$$(a_i') = \left(\frac{1}{2}(a_1 + a_2 + a_4 + a_5), \quad \frac{1}{2}(a_2 + a_5 - a_1 - a_4), \right.$$

$$\frac{1}{\sqrt{2}}(a_6 + a_3), \quad \frac{1}{2}(a_4 + a_5 - a_1 - a_2),$$

$$\frac{1}{2}(a_1 + a_5 + a_2 - a_4), \quad \frac{1}{\sqrt{2}}(a_6 - a_3)\right).$$

$$(2.14)$$

Substituting these transformed variables into the energy density and requiring invariance under such rotations, we arrive at a specific symmetric form for the coefficient matrix $[k_{ij}]$. The resulting matrix, consistent with the Oseen-Frank elastic theory and

Stewart's derivation [202, p. 19], is

$$[k_{ij}] = \begin{pmatrix} k_{11} & k_{12} & 0 & -k_{12} & k_{11} - k_{22} - k_{24} & 0 \\ k_{12} & k_{22} & 0 & k_{24} & k_{12} & 0 \\ 0 & 0 & k_{3} & 0 & 0 & 0 \\ -k_{12} & k_{24} & 0 & k_{22} & -k_{12} & 0 \\ k_{11} - k_{22} - k_{24} & k_{12} & 0 & -k_{12} & k_{11} & 0 \\ 0 & 0 & 0 & 0 & 0 & k_{33} \end{pmatrix}.$$
 (2.15)

This matrix structure reflects the physical constraints imposed by rotational symmetry and simplifies the elastic energy density to a form with fewer independent elastic constants. The entries capture interactions between the curvature modes (splay, twist, and bend) and account for possible couplings such as k_{12} and k_{24} .

The elastic energy density for a nematic liquid crystal in terms of the curvature strain components can now be written as

$$w = k_1(s_1 + s_2) + k_2(t_1 + t_2) + \frac{1}{2}k_{11}(s_1 + s_2)^2 + \frac{1}{2}k_{22}(t_1 + t_2)^2 + \frac{1}{2}k_{33}(b_1 + b_2)^2 + k_{12}(s_1 + s_2)(t_1 + t_2) - (k_{22} + k_{24})(s_1s_2 + t_1t_2),$$
(2.16)

where s_1, s_2 denote splay components, t_1, t_2 correspond to twist, and b_1, b_2 to bend, as defined in equation (2.5). The constants $k_1, k_2, k_{11}, k_{22}, k_{33}, k_{12}$, and k_{24} are material-dependent elastic coefficients.

To simplify the energy density further and incorporate intrinsic curvature terms, we define new constants $s_0 = -k_1/k_{11}$, $t_0 = -k_2/k_{22}$. Using these, we can rewrite the energy density in a shifted quadratic form by introducing a new free energy term

$$w_F = w + \frac{1}{2}k_{11}s_0^2 + \frac{1}{2}k_{22}t_0^2, (2.17)$$

which leads to a more compact and physically meaningful expression

$$w_F = \frac{1}{2}k_{11}(s_1 + s_2 - s_0)^2 + \frac{1}{2}k_{22}(t_1 + t_2 - t_0)^2 + \frac{1}{2}k_{33}(b_1 + b_2)^2 + k_{12}(t_1 + t_2)(s_1 + s_2) - (k_{22} + k_{24})(s_1s_2 + t_1t_2).$$
(2.18)

This formulation is often advantageous in applications, as it centers the energy about a preferred (nonzero) curvature, which reflects the spontaneous distortions that may be present in the material.

To connect the curvature strain terms with standard vector calculus operations, we recall the following identities

$$(s_{1} + s_{2}) = \frac{\partial n_{x}}{\partial x} + \frac{\partial n_{y}}{\partial y} = \nabla \cdot \mathbf{n},$$

$$-(t_{1} + t_{2}) = \frac{\partial n_{y}}{\partial x} - \frac{\partial n_{x}}{\partial y} = \mathbf{n} \cdot (\nabla \times \mathbf{n}),$$

$$(b_{1}^{2} + b_{2}^{2}) = \left(\frac{\partial n_{x}}{\partial z}\right)^{2} + \left(\frac{\partial n_{y}}{\partial z}\right)^{2} = |\mathbf{n} \times (\nabla \times \mathbf{n})|^{2},$$

$$-(s_{1}s_{2} + t_{1}t_{2}) = \frac{\partial n_{y}}{\partial x} \frac{\partial n_{x}}{\partial y} - \frac{\partial n_{x}}{\partial x} \frac{\partial n_{y}}{\partial y} = \frac{1}{2} \nabla \cdot \left[(\mathbf{n} \cdot \nabla)\mathbf{n} - (\nabla \cdot \mathbf{n})\mathbf{n}\right].$$

$$(2.19)$$

These vector identities allow for the elastic free energy density to be expressed more compactly. The expressions for splay, twist, and bend given in equation (2.19) represent intrinsic geometric distortions of the liquid crystal director field that do not depend on the choice of coordinate system. These quantities are formulated using vector calculus operators, which describe how the director field can deform in space.

Thus, the coordinate-independent splay, twist, and bend can be represented by simple combinations of the linearised derivatives of the director components. This justifies expressing the elastic free energy density in terms of these linearised curvature strains, to ensure consistency between the fundamental geometric definitions of distortion and their approximations used in practical calculations near a uniform director configuration.

Using equation (2.19), equation (2.18) can be rewritten in vector form as

$$w_{F} = \frac{1}{2}k_{11}\left(\nabla \cdot \mathbf{n} - s_{0}\right)^{2} + \frac{1}{2}k_{22}\left(\mathbf{n} \cdot \nabla \times \mathbf{n} - t_{0}\right)^{2} + \frac{1}{2}k_{33}\left|\mathbf{n} \times \nabla \times \mathbf{n}\right|^{2} - k_{12}\left(\nabla \cdot \mathbf{n}\right)\left(\mathbf{n} \cdot \nabla \times \mathbf{n}\right) + \frac{1}{2}\left(k_{22} + k_{24}\right)\left[\left(\mathbf{n} \cdot \nabla\right)\mathbf{n} - \left(\nabla \cdot \mathbf{n}\right)\mathbf{n}\right]^{2}.$$
(2.20)

For nematic liquid crystals, the spontaneous splay and twist parameters vanish, i.e., $s_0 = t_0 = 0$. When s_0 and t_0 are nonzero, they describe chiral or polar nematic phases, or systems exhibiting intrinsic distortions due to molecular asymmetry or external fields. The parameter k_{12} , when nonzero, introduces anisotropic coupling between splay and twist deformations, modifying the balance of elastic distortions, which potentially affects phase transition thresholds.

We now redefine the Frank elastic constants as $K_1 = k_{11}$, $K_2 = k_{22}$, $K_3 = k_{33}$, and $K_4 = k_{24}$, the free energy density simplifies to

$$w_F = \frac{1}{2}K_1 (\nabla \cdot \mathbf{n})^2 + \frac{1}{2}K_2 (\mathbf{n} \cdot \nabla \times \mathbf{n})^2 + \frac{1}{2}K_3 |\mathbf{n} \times \nabla \times \mathbf{n}|^2 + \frac{1}{2}(K_2 + K_4) \left[\operatorname{tr} \left((\nabla \mathbf{n})^2 \right) - (\nabla \cdot \mathbf{n})^2 \right],$$
(2.21)

where the constants K_1 , K_2 , and K_3 correspond to the *splay*, *twist*, and *bend* elastic moduli, respectively. The term $K_2 + K_4$ is known as the *saddle-splay* constant. The saddle-splay term is often omitted in practical problems with strong boundary anchoring because it can be expressed as the divergence of a vector field and therefore does not affect the bulk equilibrium equations [235]. While it can influence surface phenomena, its contribution to bulk energy minimisation is typically small.

The Oseen–Frank free energy functional is phenomenological, motivated by experimental observations and symmetry considerations rather than derived from molecular theory. Additional terms, such as the saddle-splay term or couplings to external fields, are sometimes included to capture more complex effects. Their inclusion is guided by invariance principles or experimental data, and must be critically assessed to ensure they are physically justified.

In this Thesis, we neglect the saddle-splay contribution because it is very small compared with the bulk elastic terms. Using the values of K_1 and K_2 in Table 1.1 and estimating $K_4 = (K_1 - K_2)/2$ [234], we find that the saddle-splay term is non-zero but negligible. Experimental studies [5,102,134] indicate that K_4 is difficult to measure accurately and subject to large uncertainties. As noted by Selinger [194], the saddle-splay term K_{24} should not automatically be treated as a surface term, particularly in systems with defects or internal surfaces, where it can contribute to the bulk elastic free energy.

It is common practice to align LC samples using external fields, such as magnetic or electric fields, which cause nematics to align parallel or perpendicular to the field [202, 235]. The following section will introduce the concepts of electric and magnetic fields, as this study considers active nematics subject to an orienting field.

2.3 Electric and magnetic fields

Since this work incorporates the contribution of external fields, such as electric and magnetic fields, it is essential to discuss the concepts of these fields and their associated energies in the context of liquid crystals.

The general form of electric displacement is given by [202]

$$\mathbf{D} = \epsilon_0 \epsilon_\perp \mathbf{E} + \epsilon_0 \epsilon_a (\mathbf{n} \cdot \mathbf{E}) \mathbf{n}, \tag{2.22}$$

where **E** is the applied electric field to a sample of nematic, ϵ_0 is the permittivity of the free space, $\epsilon_a = \epsilon_{\parallel} | -\epsilon_{\perp}$ is the dielectric anisotropy of the nematic, ϵ_{\perp} is the dielectric constant when the field and director are perpendicular and ϵ_{\parallel} is the dielectric constant when the field and director are parallel, where these last three constants are dimensionless, all of which are dimensionless since they are measured relative to the ϵ_0 . The dielectric anisotropy is $\epsilon_a > 0$ when the energetic preference is for the director to align parallel to the field and $\epsilon_a < 0$ when the preference is for the director to be perpendicular to the field [25, 35].

The commonly used electric energy density in modelling nematics is then given by [35,70]

$$w_{elec} = -\frac{1}{2}\epsilon_0 \epsilon_a (\mathbf{n} \cdot \mathbf{E})^2. \tag{2.23}$$

For a magnetic field, **H**, the equivalent of the electric displacement is the magnetisation, **M**, which is due to the weak magnetic dipole moments imposed on the molecular alignments by the magnetic field. The magnetisation and magnetic energy, expressed in Gaussian units, are given in the following forms, respectively

$$\mathbf{M} = \chi_{m_{\perp}} \mathbf{H} + \chi_{a} (\mathbf{n} \cdot \mathbf{H}) \mathbf{n}, \tag{2.24}$$

$$w_{mag} = -\frac{1}{2}\mathbf{M} \cdot \mathbf{H}, \tag{2.25}$$

Equation (2.24) represents the magnetisation \mathbf{M} as a sum of the contributions from $\chi_{m_{\perp}}$ and χ_a , where $\chi_{m_{\perp}}$ denotes the diamagnetic susceptibility when the field and director are perpendicular to each other and χ_a is the magnetic anisotropy. It should be noted that the effects of gravity are neglected in this thesis. For details, refer to [202].

In the next section, we will explore the Ericksen–Leslie dynamic theory of nematic liquid crystals, which serves as the fundamental framework for this study. This theory is formulated based on the principles of conservation laws, including the conservation of mass, linear momentum, and angular momentum, as detailed in Stewart [202]. By incorporating these fundamental physical laws, the Ericksen-Leslie theory provides a comprehensive description of the hydrodynamics of nematic liquid crystals, capturing both their viscous and elastic properties. This theory will be essential for our analysis and will be used to develop the mathematical models presented in Chapters 3, 4 and 5.

2.4 Ericksen-Leslie dynamic theory of nematic liquid crystals

This section introduces the Ericksen–Leslie dynamic theory of nematic liquid crystals, which has been widely successful in providing a mathematical framework for describing the behaviour of liquid crystals [47]. This theory describes the coupling between the velocity field and the orientational dynamics of the liquid crystal molecules [113,162]. By establishing this framework, we can extend our discussion to active nematics. Active nematics theory builds upon the Ericksen–Leslie formulation by incorporating additional stresses arising from activity, leading to hydrodynamic instabilities [45, 236].

Building on the theories of Oseen and Frank, mentioned above, Ericksen [47] developed a more general theory of liquid crystals. Later, Leslie [113] extended Ericksen's work to derive the governing equations for the hydrodynamic theory of nematics, now known as the Ericksen–Leslie theory.

We now focus on the formulation of the Ericksen-Leslie dynamic theory in the section, and subsequently summarise the active nematics theory.

2.4.1 Ericksen-Leslie dynamic theory

Ericksen–Leslie theory was formulated using the conservation laws of mass, linear momentum and angular momentum, and the point-wise equations for mass, linear momentum, and angular momentum are given [202] by

$$\frac{\partial v_i}{\partial x_i} = 0, (2.26)$$

$$\rho \frac{Dv_i}{Dt} - \rho F_i - \frac{\partial t_{ij}}{\partial x_j} = 0, \qquad (2.27)$$

$$\rho K_i + \epsilon_{ijk} t_{kj} + \frac{\partial l_{ij}}{\partial x_i} = 0, \qquad (2.28)$$

where ρ denotes fluid density, F_i are the components of the external body force per

unit mass, K_i are the components of the external moments per unit area, t_{ij} are the components of the stress tensor, l_{ij} are the components of the couple stress tensor, and ϵ_{ijk} is the Levi-Civita symbol (also known as the alternator), with indices i, j, k = 1, 2, 3. For a detailed derivation, refer to Stewart [202]. We apply the summation convention here and throughout this work. The Ericksen-Leslie equations can be viewed as the Navier-Stokes equations supplemented by an additional equation accounting for the balance of angular momentum, often referred to as the director equation.

The incompressibility condition $\partial v_i/\partial x_i = 0$ (equation (2.26)) assumes that the fluid density is constant. This is a common assumption for liquid crystals under standard conditions, but may not hold if density variations or compressibility effects are significant, such as in flows under extreme pressure or temperature gradients. Equation (2.27) generalises the Navier–Stokes momentum equation by incorporating anisotropic stress components t_{ij} , which depend on both velocity gradients and director distortions. It captures the coupling between fluid flow and the director orientation. However, the precise constitutive form of t_{ij} is phenomenological and requires experimentally determined material parameters (Leslie viscosities), which can vary widely between different liquid crystal materials and phases. Equation (2.28) introduces the balance of torques acting on the director field via the couple stress tensor l_{ij} and the antisymmetric parts of the stress tensor, which is captured via the Levi-Civita symbol ϵ_{ijk} . This additional balance is critical for describing director reorientation dynamics.

While the Ericksen–Leslie theory is powerful for modelling nematic liquid crystals, it has several limitations. Firstly, the theory relies on several experimentally determined material parameters, such as the Leslie viscosities and elastic constants, which can vary significantly between different materials and phases, making parameter identification challenging and limiting predictive accuracy for new systems. The assumption of incompressibility, reflected in the mass conservation equation, restricts the model to flows with constant density, which may not be valid in scenarios involving high-speed flows or significant thermal gradients where compressibility effects become important. Addition-

ally, the continuum approximation inherent in these equations neglects molecular-level fluctuations, discrete defects, and nanoscale effects, which can be crucial near phase transitions or in confined geometries. Furthermore, thermal fluctuations and stochastic noise are also ignored, despite their importance in defect nucleation and dynamics in some contexts. In particular, the theory cannot capture topological defects in the director field, such as disclinations, which play a central role in the dynamics of nematic materials. Furthermore, thermal fluctuations and stochastic noise are also ignored, despite their importance in defect nucleation and dynamics in some contexts.

Following the work of Leslie [113], the energy gain or loss is accounted for through viscous dissipation, \mathcal{D} [202], given as

$$\left(t_{ij} + \frac{\partial w_F}{\partial n_{p,j}} n_{p,i}\right) v_{i,j} + \left(t_{ij} - \epsilon_{iqp} n_q \frac{\partial w_F}{\partial n_{p,j}} w_{p,i}\right) w_{i,j} + w_i \epsilon_{iqp} \left(t_{pq} - \frac{\partial w_F}{\partial n_{k,p}} n_{k,q}\right) = \mathcal{D},$$
(2.29)

where $n_{p,i} = \partial_i n_p$ denotes the spatial gradient of the director components, ϵ_{iqp} is the Levi-Civita symbol. Equation (2.29) quantifies the rate at which mechanical energy is irreversibly lost due to viscous processes in a nematic liquid crystal. This formulation arises from the rate of work postulate and represents the residual energy after accounting for changes in free energy w_F associated with distortions in the director field \mathbf{n} . It is assumed that all kinetic energy input from body and surface forces is either stored elastically or dissipated. The first term in the left-hand side of equation (2.29) measures the viscous contribution to the rate of work due to strain rate $v_{i,j}$, corrected for contributions from director field gradients, second term accounts for dissipation due to gradients in the angular velocity of the director field and a torque contribution, respectively. The third term vanishes when the stress tensor is symmetric or when director dynamics are decoupled from antisymmetric stress parts.

This framework assumes passive dissipation, implying that the dissipation function \mathcal{D} is always non-negative. However, in active nematic systems where energy is continu-

ously injected at the microscale, and extending this analysis to active systems demands caution and potential modifications to the dissipation framework. In the latter part of this Chapter, we will derive the active stress and dissipation separately from their viscous (passive) counterparts.

Since the rate of viscous dissipation is always positive for passive liquid crystals. We therefore consider equation (2.29) as only having passive components, and since the sign of w_i , $w_{i,j}$ and $v_{i,j}$ can be chosen arbitrarily, any terms linear in these quantities must vanish. As a result, the stress tensor t_{ij} and the couple stress tensor l_{ij} appearing in equations (2.27), (2.28) and (2.29) are given by

$$t_{ij} = -p\delta_{ij} - \frac{\partial w_F}{\partial n_{p,j}} n_{p,i} + \tilde{t}_{ij}, \qquad (2.30)$$

$$l_{ij} = \epsilon_{ipq} n_p \frac{\partial w_F}{\partial n_{q,j}} + \tilde{l}_{ij}, \qquad (2.31)$$

where p is the isotropic pressure and δ_{ij} is the Kronecker delta. The terms \tilde{t}_{ij} and \tilde{l}_{ij} correspond to dynamic dissipative contributions to the stress and couple stress tensors, respectively.

Physically, the stress tensor t_{ij} describes the internal forces per unit area within the nematic liquid crystal, which combines the isotropic fluid pressure, elastic distortions related to director gradients through the free energy derivative term, and viscous stresses arising from flow. The couple stress tensor l_{ij} arises due to the microstructure of the liquid crystal, accounting for internal moments transmitted across surfaces, which do not appear in classical fluids. The inclusion of l_{ij} reflects the anisotropic and orientational degrees of freedom unique to nematic phases, capturing the effects of director rotations and elastic torques.

The dependency on the spatial gradients of the director field through $\partial \dot{w}_F/\partial n_{p,j}$ links these stresses directly to the elastic free energy, thus coupling mechanical deformations with orientational order. This coupling is essential to model phenomena such as defect dynamics, director reorientation under flow, and the response to external fields.

However, there are important limitations and considerations in these formulations. The separation into an elastic free energy contribution and a viscous dissipative part assumes a clear distinction between reversible and irreversible processes, which may not always hold, especially in active or out-of-equilibrium systems. The Ericksen-Leslie framework, from which these expressions derive, presumes a continuum approximation valid at scales large compared to molecular dimensions, neglecting microscopic fluctuations and stochastic effects that can dominate near defects or phase transitions. Moreover, the treatment assumes smooth director fields and well-defined gradients, which can break down in the presence of singularities or topological defects.

Finally, while the couple stress l_{ij} introduces additional complexity compared to isotropic fluids, it is often neglected or simplified in some models for computational tractability, especially when the focus is on macroscopic flow behaviour rather than detailed microstructural dynamics. However, omitting l_{ij} may overlook important torque balance effects critical for accurately capturing nematic rheology and stability.

To complete the discussion of the Ericksen–Leslie dynamic equations for nematic liquid crystals, we write the dynamic viscous stress \tilde{t}_{ij} is given via the constitutive equations as follows

$$\tilde{t}_{ij} = \alpha_1 n_k A_{kp} n_p n_i n_j + \alpha_2 N_i n_j + \alpha_3 n_i N_j + \alpha_4 A_{ij} + \alpha_5 n_j A_{ik} n_k + \alpha_6 n_i A_{jk} n_k, \quad (2.32)$$

$$A_{ij} = \frac{1}{2} (v_{i,j} + v_{j,i}), \qquad (2.33)$$

$$N_i = \dot{n}_i - W_{ij} n_j, \quad W_{ij} = \frac{1}{2} (v_{i,j} - v_{j,i}),$$
 (2.34)

where A_{ij} and W_{ij} are the rate of strain tensor and vorticity tensor, respectively, $\alpha_1, \alpha_2, \ldots, \alpha_6$ are the Leslie viscosities, and N_i is the co-rotational time flux of the director \mathbf{n} [202]. \mathbf{N} is the co-rotational derivative of the director, \dot{n}_i is the material derivative of n_i , defined as $\dot{n}_i = Dn_i/Dt = \partial n_i/\partial t + v_j(\partial n_i/\partial x_j)$. Physically, \mathbf{N} captures how the director evolves in time relative to the local rotation of the fluid. It represents the intrinsic rotation of the director field due to molecular reorientation, ex-

cluding contributions from the rigid body rotation of the surrounding fluid. Therefore, while \mathbf{n} describes molecular orientation, \mathbf{N} describes its rate of change in a deforming and rotating flow, which makes it essential for describing viscous dissipation and director dynamics in the Leslie-Ericksen theory.

The elastic energy, w_F for nematics given by equation (2.21),can be written in a Cartesian component form as

$$w_F = \frac{1}{2} (K_1 - K_2 - K_4) (n_{i,i})^2 + \frac{1}{2} K_2 n_{i,j} n_{i,j} + \frac{1}{2} K_4 n_{j,i} n_{j,i}$$

$$+ \frac{1}{2} (K_3 - K_2) n_j n_{i,j} n_k n_{i,k}.$$
(2.35)

The viscous dissipation inequality, following from equation (2.29) together with restriction by the Parodi relation, $\gamma_2 = \alpha_6 - \alpha_5 = \alpha_2 + \alpha_3$ [156], is given by

$$\mathcal{D} = \frac{1}{2} \left[\alpha_1 (n_i A_{ij} n_j)^2 + (\alpha_2 + \alpha_3 + \gamma_2) N_i A_{ij} n_j + \alpha_4 A_{ij} A_{ij} + (\alpha_5 + \alpha_6) n_i A_{ij} A_{jk} n_k + \gamma_1 N_i N_i \right] \ge 0.$$
(2.36)

The requirement for the viscous dissipation function, \mathcal{D} , to be semi-positive definite results in a set of inequalities that nematic viscosities must satisfy. These inequalities derived by Leslie in [113] are given explicitly by

$$\gamma_1 = \alpha_3 - \alpha_2 \ge 0, \tag{2.37}$$

$$\alpha_4 \ge 0, \tag{2.38}$$

$$\alpha_4 + \frac{1}{2}(\alpha_5 + \alpha_5) \ge 0,$$
 (2.39)

$$2\alpha_1 + 3\alpha_4 + 2\alpha_5 + 2\alpha_2 \ge 0, (2.40)$$

$$\gamma_1(2\alpha_4 + \alpha_5 + \alpha_6) \ge \frac{1}{4}(\gamma_1 + \alpha_2 + \alpha_3)^2.$$
(2.41)

The viscosities α_i can be challenging to describe physically but can be determined through experimental measurements, as presented by [133]. The measured viscosities,

known as Miesowicz viscosities, can then be expressed in terms of Leslie viscous coefficients as

$$\eta_1 = (\alpha_3 + \alpha_4 + \alpha_6)/2,$$
(2.42)

$$\eta_2 = (\alpha_4 + \alpha_5 - \alpha_2)/2, \tag{2.43}$$

$$\eta_3 = \alpha_4/4,\tag{2.44}$$

$$\gamma_1 = \alpha_3 - \alpha_2, \tag{2.45}$$

$$\gamma_2 = \alpha_6 - \alpha_5 = \alpha_3 + \alpha_2, \tag{2.46}$$

$$\gamma_{12} = \alpha_1, \tag{2.47}$$

where γ_1 is the rotational viscosity, which determines the relaxation of the director via rotation, γ_2 is the torsion viscosity and satisfies the Parodi relation $\gamma_2 = \eta_1 - \eta_2$ [156]. The remaining viscosities η_1 , η_2 , η_3 [133, 202] and γ_{12} [139], can be measured experimentally by analysing the orientation of the director \mathbf{n} with respect to the velocity \mathbf{v} and the velocity gradient. For details on these measurements, refer to [133,202]. The combination of viscosities α_2 and α_3 is crucial in determining the flow alignment of the director in nematic liquid crystals. When both $\alpha_2\alpha_3 > 0$ and $\alpha_2 < \alpha_3 < 0$, the nematic liquid crystal is referred to as "flow-aligning." Conversely, when $\alpha_2\alpha_3 < 0$, the liquid crystal is considered "non-flow aligning [202]."

We now discuss the Leslie viscosities α_2 and α_3 in relation to the director angle and the shear flow.

2.4.2 Leslie angle

The Leslie angle, also known as flow aligning angle, often denoted θ_L is the steady-state angle between the director and the flow direction in a simple shear flow. In nematic liquid crystals, when a shear is applied between two plates moving in opposite directions, the director tends to align at a fixed angle rather than perfectly along or perpendicular to the flow. This angle results from the balance between viscous torques, which arise

from the fluid motion, and elastic restoring torques due to the molecular alignment.

In the Leslie-Ericksen theory [167, 202], the Leslie angle, defined as

$$\theta_L = \tan^{-1}\left(\sqrt{\alpha_3/\alpha_2}\right). \tag{2.48}$$

Using the values of α_2 and α_3 from Table 1.1 and equation (2.48), the predicted Leslie angle is $\theta_L \approx 0.099$ rad. This helps in understanding how the liquid crystal director responds even in the presence of an external field and boundary effects.

2.4.3 Reformulation of Ericksen-Leslie dynamic theory

We now rewrite the Ericksen–Leslie dynamic equations, to ensure that the unit-length constraint of the director \mathbf{n} is naturally enforced, by parameterising the director in terms of angular variables.

The Ericksen–Leslie dynamic equations for nematic liquid crystals at constant temperature, under the assumption of negligible director inertia, are given as

$$v_{i,i} = 0, (2.49)$$

$$\rho F_i - (p + w_F)_{,i} + \tilde{g}_j n_{j,i} + G_{j,i} + \tilde{t}_{ij,j} = \rho \dot{v}_i, \tag{2.50}$$

$$\left(\frac{\partial w_F}{\partial n_{i,j}}\right)_{,j} - \frac{\partial w_F}{\partial n_i} + \tilde{g}_i + G_i = \lambda n_i,$$
(2.51)

where F_i are the components of the external body force per unit mass, t_{ij} are the components of the dynamic viscous stress tensor, the vector \tilde{g}_i , defined as $\tilde{g}_i = -\gamma_1 N_i - \gamma_2 A_{ip} n_p$ are the components of the vector expressed in terms of the viscosities γ_1 and γ_2 , w_F is the elastic energy density for nematic liquid crystals. The generalized body force is denoted by G_i , and is defined as $G_i = \chi_a n_k H_k H_i$, where \mathbf{H} is the magnetic field and χ_a is the magnetic anisotropy. The scalar function λ denotes the Lagrange multiplier associated with the condition that \mathbf{n} is a unit vector, and p is the pressure.

To describe explicitly the dynamics of the nematic liquid crystal orientation, we rewrite

the balance of angular and linear momentum in terms of the director angles. The director is defined as

$$\mathbf{n} = (\cos \theta_1 \cos \theta_2, \cos \theta_1 \sin \theta_2, \sin \theta_1), \tag{2.52}$$

where $\theta_1 = \theta_1(\mathbf{x}, t)$ is the polar (tilt) angle measuring the out-of-plane inclination of the director, and $\theta_2 = \theta_2(\mathbf{x}, t)$ is the azimuthal (twist) angle describing the inplane rotation about the vertical axis. These angular variables provide a compact representation of the three-dimensional director field \mathbf{n} . This formulation naturally incorporates the orientational degrees of freedom, simplifies the handling of constraints such as fixed director length without explicitly introducing Lagrange multipliers, and facilitates coupling between the director dynamics and the flow field.

Following the derivation in [113,202], the angular momentum balance can be expressed as

$$\frac{\partial}{\partial x_i} \left(\frac{\partial w_F}{\partial (\partial_i \theta_\alpha)} \right) - \frac{\partial w_F}{\partial \theta_\alpha} - \frac{\partial \mathcal{D}}{\partial \dot{\theta}_\alpha} + \frac{\partial \Psi_m}{\partial \theta_\alpha} = 0, \quad \alpha = 1, 2, \tag{2.53}$$

while the linear momentum equation can be reformulated as

$$\rho \dot{v}_i = \left(\frac{\partial \mathcal{D}}{\partial v_{i,j}}\right)_{,j} - \frac{\partial \mathcal{D}}{\partial \dot{\theta}_{\alpha}} \theta_{\alpha,i} - \tilde{p}_{,i}, \quad \alpha = 1, 2.$$
 (2.54)

These equations enable the dynamic behaviour of the nematic system to be described more succinctly and efficiently, without the explicit need for the Lagrange multiplier λ used to enforce director length constraints in other formulations.

2.4.4 Energy dissipation

As mentioned previously, active nematics rely on the continuous production of energy by the individual self-driven units. The emergence of dynamic structures in active systems is heavily influenced by the role of nonequilibrium forces, and understanding these effects the system are crucial. In active systems, the stress and dissipation functions can be thought of as consisting of active and viscous parts [4].

The concept of active dissipative can be confusing, as it does not exactly fall under the category of "energy dissipation" since it is not positive definite. However, it can be considered as the "rate of energy input," as mentioned in a study by Tang et al. [207]. Paarth et al. [74] also consider this approach and suggest that viscous dissipation plays a role in balancing the active dissipation and stabilising the uniform state in the bulk of the system.

The rate of dissipation using Ericksen-Leslie's theory of nematics [4,202] is often given by the sum of the classical viscous dissipation and a single term denoting the active dissipation,

$$\mathcal{D}_{a} = \frac{1}{2} \left[\alpha_{1} (n_{i} A_{ij} n_{j})^{2} + (\alpha_{2} + \alpha_{3} + \gamma_{2}) N_{i} A_{ij} n_{j} + \alpha_{4} A_{ij} A_{ij} + (\alpha_{5} + \alpha_{6}) n_{i} A_{ij} A_{jk} n_{k} + \gamma_{1} N_{i} N_{i} \right] + \xi n_{i} A_{ij} n_{j},$$
(2.55)

where ξ is the activity strength coefficient. The last term in equation (2.55) is then the active dissipation (derived from the active forces exerted by collections of active systems), while the first term is the usual viscous dissipation, given by equation (2.36). In the next section, we will derived the active stress in equation (2.55).

2.4.5 Activity strength

The magnitude and sign of the activity coefficient ξ depends on the influence of the active fluid on the surrounding flow [187]. In an active system, flows can be induced depending on the activity strength [45,187], and spontaneous symmetry breaking can occur as the activity increases, and flow is induced. Increasing the activity can lead to oscillatory flow, and at higher activity, the so-called ceilidh dancing flow [65,187,197] is observed.

A collection of active living organisms are characterised by the activity coefficient ξ and

the sign of ξ has a significant physical meaning: $\xi > 0$ is associated with extensile agents (pushers) and $\xi < 0$ is associated with contractile agents (pullers), which describe the dipolar flow field (see Figure 2.2) [1].

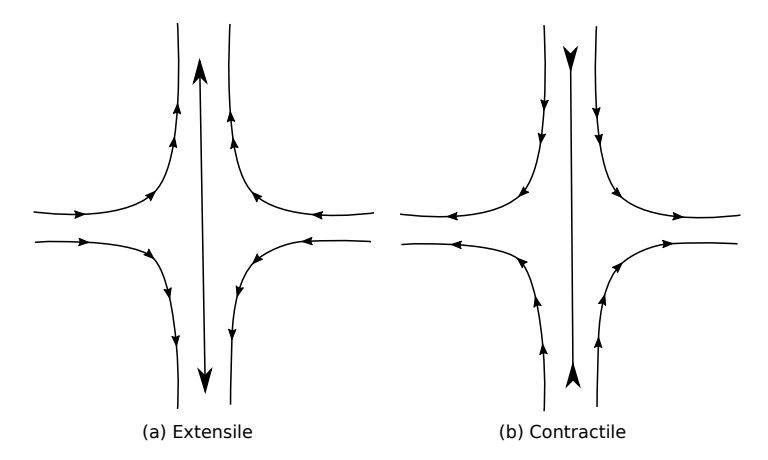


Figure 2.2: Schematic sketches of the local flow induced by the active systems, (a) extensile $(\xi > 0)$ and (b) contractile $(\xi < 0)$ flow, where straight vertical arrows represent the director field.

Next, we will discuss the activity strength, ξ , in equation (2.55), and derive the active stress.

2.4.5.1 Derivation of the active stress tensor

The concept of "active stress" in living things was first mentioned in the work by Finlayson and Scriven in 1969 [50]. They suggested that active stress is responsible for convective instabilities in living things. Traditionally, active stress can arise from either bulk, interfacial or slip surfaces, which depend on strain or rate of strain.

In this section, we will summarise the derivation of the active stress $\sigma^a = \xi(\mathbf{n} \otimes \mathbf{n})$ mentioned above. We derive the active stress based on Newton's third law of motion, which states that the force exerted by the self-propelled particle (SPP) on the fluid is equal and opposite to the force exerted by the fluid on the SPP.

We follow the work of [1,10], where the i^{th} SPP is considered to have an axis $\mathbf{n}_i(t)$ at a time, t, and opposite point forces of equal magnitude, F, at each end of the SPP, which is centered at \mathbf{R}_i (see Figure 2.3). We assume that the shape of the SPP is symmetric

around the midpoint between the two forces, which ensures that the stress distribution is evenly balanced around the midpoint. This means that the center of mass \mathbf{R}_i is equidistant from the point forces.

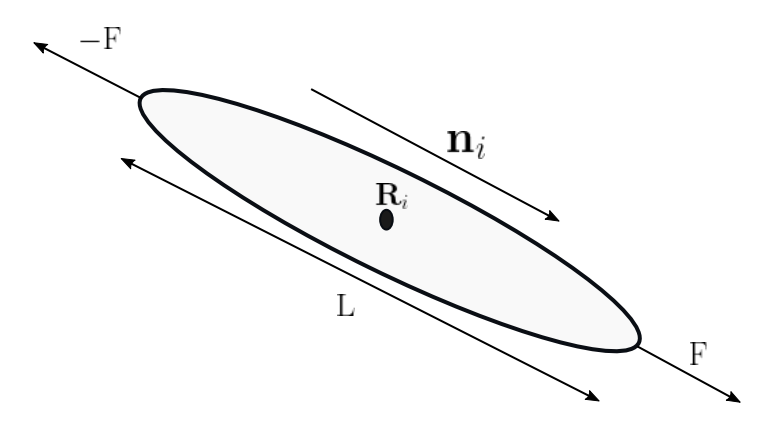


Figure 2.3: Geometry of the force dipole, where \mathbf{n}_i is the SPP orientation and L is the length of the SPP.

We model a single force dipole of magnitude F, oriented along the director \mathbf{n}_i , centered at position \mathbf{R}_i , and displaced by $\pm L/2$ along \mathbf{n}_i . Instead of using a Dirac delta, we use a smooth, symmetric approximation $\delta_{\epsilon}(\mathbf{r})$, such as a normalised Gaussian kernel

$$\delta_{\epsilon}(\mathbf{r}) = \frac{1}{(2\pi\epsilon^2)^{3/2}} \exp\left(-\frac{|\mathbf{r}|^2}{2\epsilon^2}\right), \tag{2.56}$$

which satisfies $\lim_{\epsilon \to 0} \delta_{\epsilon}(\mathbf{r}) = \delta(\mathbf{r})$ in the distributional sense.

The force density, $f(\mathbf{r})$, acting in the fluid solvent due to a single dipole magnitude F is [1,10].

$$\mathbf{f}(\mathbf{r}) = F\mathbf{n}_i \delta_{\epsilon} \left(\mathbf{r} - \mathbf{R}_i - \frac{L}{2} \mathbf{n}_i \right) - F\mathbf{n}_i \delta_{\epsilon} \left(\mathbf{r} - \mathbf{R}_i + \frac{L}{2} \mathbf{n}_i \right). \tag{2.57}$$

We now expand each term using a Taylor expansion around $\mathbf{r} = \mathbf{R}_i$ (assuming L is small)

$$\delta_{\epsilon} \left(\mathbf{r} - \mathbf{R}_{i} \pm \frac{\mathbf{L}}{2} \mathbf{n}_{i} \right) = \delta_{\epsilon} (\mathbf{r} - \mathbf{R}_{i}) \pm \frac{\mathbf{L}}{2} \mathbf{n}_{i} \cdot \nabla \delta_{\epsilon} (\mathbf{r} - \mathbf{R}_{i}) + \mathcal{O}(\mathbf{L}^{2}). \tag{2.58}$$

Substituting equation (2.58) into the force density (equation (2.57))

$$\mathbf{f}(\mathbf{r}) \approx \operatorname{F}\mathbf{n}_{i} \left[\delta_{\epsilon}(\mathbf{r} - \mathbf{R}_{i}) - \frac{\operatorname{L}}{2}\mathbf{n}_{i} \cdot \nabla \delta_{\epsilon}(\mathbf{r} - \mathbf{R}_{i}) \right]$$

$$- \operatorname{F}\mathbf{n}_{i} \left[\delta_{\epsilon}(\mathbf{r} - \mathbf{R}_{i}) + \frac{\operatorname{L}}{2}\mathbf{n}_{i} \cdot \nabla \delta_{\epsilon}(\mathbf{r} - \mathbf{R}_{i}) \right]$$

$$= -\operatorname{FL}(\mathbf{n}_{i} \otimes \mathbf{n}_{i}) \cdot \nabla \delta_{\epsilon}(\mathbf{r} - \mathbf{R}_{i}).$$

$$(2.59)$$

In component form

$$f_k(\mathbf{r}) \approx -\text{FL}\nabla_i \left(n_{ik} n_{ij} \delta_{\epsilon} (\mathbf{r} - \mathbf{R}_i) \right).$$
 (2.60)

For a collection of dipoles, we have

$$f_k(\mathbf{r}) \approx -\text{FL}\nabla_j \sum_i n_{ik} n_{ij} \, \delta_\epsilon(\mathbf{r} - \mathbf{R}_i),$$
 (2.61)

where $\delta_{\epsilon}(\mathbf{r} - \mathbf{R}_i)$ is related to the local concentration of the SPPs, denoted as $C(\mathbf{r})$, and we assume that it is constant; thus, equation (2.61) reduces to

$$f_i = -\text{FLC}\nabla_j n_i n_j = \xi \nabla_j n_i n_j, \qquad (2.62)$$

where $\xi = -\text{FLC}$ denotes the activity parameter proportional to the strength of the force dipoles, the SPP length and the concentration. Hence, the active stress tensor is given explicitly as

$$\sigma_{ij}^a = \xi n_i n_j. \tag{2.63}$$

2.5 Ericksen–Leslie equations for active nematics

This section summarises the Ericksen–Leslie equations for active nematics [114,115,202, 238]. In the presence of an orienting field, the conservation of mass and the balance of

angular and linear momentum are given explicitly by

$$\frac{\partial v_i}{\partial x_i} = 0, (2.64)$$

$$\frac{\partial}{\partial x_i} \left(\frac{\partial w_F}{\partial (\partial_i \theta_\alpha)} \right) - \frac{\partial w_F}{\partial \theta_\alpha} - \frac{\partial \mathcal{D}}{\partial \dot{\theta}_\alpha} + \frac{\partial \Psi_m}{\partial \theta_\alpha} = 0 \quad (\alpha = 1, 2), \tag{2.65}$$

$$\frac{\partial}{\partial x_j} \left(\frac{\partial \mathcal{D}}{\partial (\partial_j v_i)} + \xi n_i n_j \right) - \frac{\partial \mathcal{D}}{\partial \dot{\theta_\alpha}} \frac{\partial \theta_\alpha}{\partial x_i} - \frac{\partial \tilde{p}}{\partial x_i} = \rho \frac{D v_i}{D t} \quad (i = 1, 2, 3, \ \alpha = 1, 2), \quad (2.66)$$

where $\tilde{p} = p + w_F$ is the modified pressure, defined in terms of the isotropic pressure p and free elastic energy w_F and Ψ_m is the orienting field given in equation (2.25). The coupling term $(\partial \mathcal{D}/\partial \dot{\theta}_{\alpha})(\partial \theta_{\alpha}/\partial x_i)$ in the momentum equation (2.66) is responsible for backflow mechanism. It represents the force density exerted on the fluid by changes in the director field, coupling the rate of director reorientation $\dot{\theta}_{\alpha}$ to its spatial gradient $\partial \theta_{\alpha}/\partial x_i$. This feedback from director dynamics to flow induces fluid motion as the director evolves, capturing the essence of backflow in nematic liquid crystals.

In the static case, the dissipation function and activity are absent, and the Ericksen– Leslie equations reduce to

$$\frac{\partial}{\partial x_i} \left(\frac{\partial w_F}{\partial (\partial_i \theta_\alpha)} \right) - \frac{\partial w_F}{\partial \theta_\alpha} + \frac{\partial \Psi_m}{\partial \theta_\alpha} = 0. \tag{2.67}$$

Equation (2.67) is the Euler-Lagrange equilibrium equation of static theory or the minimisation of the energy density for the angles θ_{α} .

Having described the governing equation in the bulk of the system, in the following section, we will discuss the relevant boundary conditions for this research, including the classical no-slip and no-penetration conditions for velocity and the infinite director anchoring.

2.6 Boundary conditions

Boundary conditions play an essential role in determining both the orientation of the nematic director and the hydrodynamic response of the suspension. In classical nematic liquid crystals, two common types of anchoring are typically considered at the boundary: planar anchoring, in which the director **n** aligns parallel to the surface, and homeotropic anchoring, in which the director aligns perpendicularly to the surface [127, 202].

In continuum models, these conditions are often expressed by fixing the director field ${\bf n}$ at the boundary $\partial\Omega$

Planar anchoring:
$$\mathbf{n} \cdot \hat{\mathbf{z}} = 0$$
, (2.68)

Homeotropic anchoring:
$$\mathbf{n} \times \hat{\mathbf{z}} = 0$$
, (2.69)

where $\hat{\mathbf{z}}$ is the surface normal. More generally, one can model anchoring via a Rapini–Papoular surface energy term [177],

$$F_s = \frac{W}{2} \int_{\partial\Omega} \left[1 - (\mathbf{n} \cdot \mathbf{n}_0)^2 \right] dS, \tag{2.70}$$

where \mathbf{n}_0 is the preferred anchoring direction, W is the anchoring strength, and dS is the surface element.

In passive liquid crystals, both planar and homeotropic anchoring can be achieved experimentally by mechanical rubbing, surface patterning, or chemical treatments [33, 100, 184]. However, in *active nematics*, controlled anchoring of the director field at solid boundaries remains an open challenge. Unlike passive systems, active nematics are typically realised in microtubule–kinesin or actomyosin mixtures, where the active stresses and continuous creation/annihilation of defects prevent stable, long-lived anchoring [40, 184].

Besides director anchoring, the choice of hydrodynamic boundary conditions is equally important. The most common include the (i) no-slip and no-penetration $\mathbf{v}|_{\partial\Omega} = 0$, which enforces vanishing tangential and normal velocity at solid boundaries, (ii) free-slip / stress-free: $v_{\perp}|_{\partial\Omega} = 0$ and $\sigma_{\perp\parallel}|_{\partial\Omega} = 0$, where \perp and \parallel denote components normal and tangential to the boundary, respectively, and σ is the stress tensor, (iii) periodic boundaries, where both velocity \mathbf{v} and director field \mathbf{n} repeat identically across opposite

sides of the simulation domain. These different velocity boundary conditions have been employed depending on the geometry and intended flow regime [40, 238, 240].

Several numerical studies have shown that imposed director anchoring conditions dramatically affect defect dynamics and emergent flows in confined active nematics. In channels with planar anchoring, active nematics often exhibit spontaneous unidirectional flow at low activity, which transitions to oscillatory and eventually turbulent regimes as activity increases; in such cases, defects tend to align with the walls, leading to extended shear bands [18, 187]. By contrast, homeotropic anchoring typically induces bend instabilities near the walls, driving stronger defect nucleation and enhanced turbulence in confined geometries [28, 138, 172, 240]. In domains with periodic boundary conditions, the active nematic generally evolves toward the well-known active turbulence state, characterised by motile $\pm 1/2$ defects and mesoscale vortices. Here, no preferred alignment exists, and defect dynamics are governed solely by the interplay of activity and elastic stresses [40,59]. Thus, while strong anchoring remains a mathematically convenient assumption in models, it must be emphasised that such conditions are not experimentally achievable in active nematics. Nevertheless, simulations employing planar or homeotropic boundary conditions remain useful for probing how confinement and wall alignment would influence defect dynamics and collective flows.

In our study, we apply the infinite planar and homeotropic anchoring conditions for the director and the no-slip and no-penetration boundary conditions for the velocity ($\mathbf{v} = 0$ on the boundaries).

2.7 Summary

In summary, we have considered the Frank-Oseen and Ericksen-Leslie dynamic theory of nematic liquid crystals. The Frank-Oseen elastic theory was formulated based on the six components of the curvature strains described by the splay, twist, and bend configurations, while the Ericksen-Leslie theory was formulated using the conservation laws of mass, linear, and angular momentum. The dissipation function is written in

terms of the director and the rate of strain tensor, with an additional term that models the internal energy production in an active nematic fluid. We also summarised the derivation of the active stress tensor based on Newton's third law of motion, using selfpropelling particles as an example of living matter. We concluded this chapter with the concept of some necessary boundary conditions for both the director and the fluid velocity.

In Chapters 1 and 2, we have provided the historical background on passive and active fluids, with a particular focus on active nematics, as well as the theoretical framework based on the Ericksen-Leslie theory to set the stage for our study.

Chapter 3

Effects of Activity on

Kickback/Backflow in a

One-dimensional Geometry

3.1 Introduction

As previously mentioned in Chapter 2, the kickback mechanism occurs when a strong enough field (beyond the critical field strength) is applied, causing the director to reorient rapidly. When the field is suddenly removed, the director overshoots, temporarily aligning at $\theta > \pi/2$, before relaxing to its equilibrium state. In active nematics, flow also arises due to director distortions. However, the influence of activity on the kickback mechanism and the interplay between activity and the orienting field remain an open question.

In this chapter, we investigate the combined effects of the activity and an orienting field on the active nematic. We formulate a one-dimensional model of active nematics using a planar or homeotropic initial alignment. Activity can be seen as an internal orienting field because there is a critical value of activity, below which the director is uniform/undistorted, and above which there is director distortion. We investigate how

applying an orienting field will affect this transition.

To understand the system's behaviour at early times, we solve the governing equations analytically by linearising around a uniform director. We first examine the effect of activity in the absence of an orienting field for planar alignment. For extensile nematics, the director remains close to its initial configuration with minimal distortion. In contrast, for contractile nematics, the director undergoes a reorientation, resulting in sustained flow, a situation that is now well known [236]. When an orienting field is applied, the system is characterised by a critical orienting field below which the elastic forces resist director orientation and remain in their original state. However, if the field is much greater than the critical threshold, the director realigns more closely with the field. This phenomenon is called "Fréedericksz transitions" as mentioned earlier.

To capture how activity affects kickback, we start with an initial homeotropic alignment and then set H=0. For $\xi=0$, the system exhibits the classical kickback effect, where the director initially starts at $\theta=\pi/2$ rad and overshoots as time progresses before gradually relaxing to the uniform equilibrium state. However, for extensile nematics, the kickback effect diminishes as the activity parameter increases, whereas for contractile nematics, it remains sustained.

Next, we explore the nonlinear behaviour of the system at later times by solving the governing equations numerically using a finite difference method. Our results show that the system exhibits either a uniform, symmetric, or antisymmetric state. It is worth noting that for extensile systems, the transition from a trivial to a non-trivial state occurs above a critical field strength. In contrast, for contractile nematics, the transition occurs below a critical field strength. Interestingly, for weakly contractile systems, the director exhibits an overshoot and tends to align at $\theta \approx \pi$ rad, leading to complex flow. This finding has implications for sensor design applications.

Finally, we examine a nonlinear model of activity in a hybrid-aligned nematic (HAN) geometry. The results indicate that the system exhibits bistability in contractile systems due to different director profiles, whereas in extensile systems, the director remains con-

stant at approximately 1.24 rad in the bulk of the channel. This difference in behaviour highlights the fundamental asymmetry between contractile and extensile systems in the HAN channel, arising due to antagonistic boundary conditions.

We begin by formulating the model in Section 3.2, followed by a linear analysis for planar alignment in the absence and presence of an orienting field to examine the effect of activity and an orienting field on the backflow mechanism in Sections 3.3.1 and 3.3.2, respectively. We finish our linear analysis by examining homeotropic alignment in the absence of an orienting field in Section 3.3.3. Section 3.4 presents our nonlinear analysis under planar alignment, employing a series of computations to identify the transitions between different types of solutions. This is followed by a nonlinear analysis of activity in a Hybrid Aligned Nematic (HAN) cell in Section 3.5. We finish with concluding remarks in Section 3.6.

3.2 Model formulation

We consider the effect of a combination of activity and orienting field between two parallel plates, at z = 0 and z = d, subject to infinite planar anchoring for the director and no-slip conditions on the boundaries of the channel as shown in Figure 3.1.

We now seek the solutions to the governing equations (2.64)–(2.66) in one dimension, and with a director that remains in the x-z-plane so that $\theta_2=0$ in (2.52). In particular, the director $\mathbf{n}=\mathbf{n}(z,t)$, the velocity $\mathbf{v}=\mathbf{v}(z,t)$ and the orienting field \mathbf{H} take the form

$$\mathbf{n} = (\cos \theta(z, t), 0, \sin \theta(z, t)), \tag{3.1}$$

$$\mathbf{v} = (v(z, t), 0, 0), \tag{3.2}$$

$$\mathbf{H} = (0, 0, H), \quad H = |\mathbf{H}|,$$
 (3.3)

where $\theta(z,t)$ is the director angle measured with respect to the x-direction and v(z,t) is the flow velocity. We also specify that the orienting field **H** is applied along the

z-direction. This choice is compatible with the assumed director orientation in the x-z-plane and the geometry of the problem.

Substituting equations (3.1) and (3.2) into equation (2.35), we find the Frank-Oseen elastic free energy, w_F , given by

$$w_F = \frac{1}{2}\theta_z^2 \left(K_1 \cos^2 \theta + K_3 \sin^2 \theta \right),$$
 (3.4)

and from (2.36), the dissipation function, \mathcal{D} , is

$$\mathcal{D} = \frac{1}{2}g(\theta)v_z^2 + m(\theta)v_z\theta_t + \frac{1}{2}\gamma_1\theta_t^2,$$
(3.5)

where γ_1 is the rotational viscosity, $g(\theta)$ is the effective shear viscosity of the liquid crystal, and $m(\theta)$ is the viscosity term, which are expressed in terms of Leslie viscosities as follows:

$$g(\theta) = \frac{1}{2} \left[\alpha_4 + (\alpha_5 - \alpha_2) \sin^2 \theta + (\alpha_3 + \alpha_6) \cos^2 \theta \right] + \alpha_1 \sin^2 \theta \cos^2 \theta, \tag{3.6}$$

$$m(\theta) = \alpha_3 \cos^2 \theta - \alpha_2 \sin^2 \theta. \tag{3.7}$$

Substituting equation (3.1) into (2.24), we obtain the orienting field term

$$\Psi_m = \frac{1}{2} \chi_{m_{\perp}} H^2 + \frac{1}{2} \chi_a H^2 \sin^2 \theta. \tag{3.8}$$

The balance of angular momentum, equation (2.65), using the Frank-Oseen elastic free energy (3.4) and dissipation function (3.5), becomes

$$\gamma_1 \theta_t - \left(K_1 \cos^2 \theta + K_3 \sin^2 \theta \right) \theta_{zz} - \left(K_3 - K_1 \right) \sin \theta \cos \theta \,\,\theta_z^2$$
$$+ m(\theta) v_z + \chi_a H^2 \sin \theta \cos \theta = 0. \tag{3.9}$$

Similarly, we obtain the linear momentum equations from (2.66) using (3.2) and (3.5),

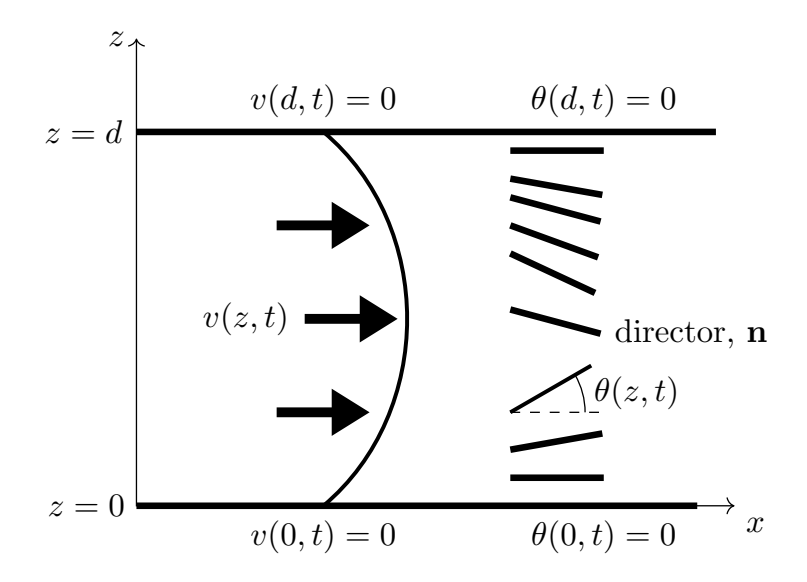


Figure 3.1: Active nematic in a channel between two solid plates at z=0 and z=d with flow parallel to the x-direction. The black solid rods show the director orientation.

in the low-Reynolds-number approximation [26, 115, 167] as follows

$$0 = (g(\theta)v_z + m(\theta)\theta_t + \xi \sin\theta \cos\theta)_z - \tilde{p}_x, \tag{3.10}$$

$$0 = \tilde{p}_y, \tag{3.11}$$

$$0 = (\xi \sin(2\theta) - m(\theta)v_z - \gamma_1 \theta_t) \theta_z - \tilde{p}_z, \tag{3.12}$$

where $\tilde{p} = p + w_F - \Psi_m$. Since p is translationally invariant in the x-direction, then by equation (3.12), we have that p = p(z,t). This implies that $\tilde{p} = \tilde{p}(z,t)$, and hence the full pressure p = p(z,t), since w_F and Ψ_m also depend only on z and t. To deduce that $p_x = 0$ from the x-momentum equation (3.10), we require an additional assumption of no externally applied pressure gradient along the channel. In the absence of such a gradient, we set $p_x = 0$.

Hence, from equations (3.10)–(3.12), we obtain

$$p(z,t) = \int (\xi \sin(2\theta) - m(\theta)v_z - \gamma_1 \theta_t) \theta_z dz - w_F + \Psi_m.$$
 (3.13)

From equation (3.10), we now have

$$(g(\theta)v_z + m(\theta)\theta_t + \xi \sin\theta \cos\theta)_z = 0. \tag{3.14}$$

We will subsequently solve the nonlinear coupled governing dynamical equations given by equations (3.9) and (3.14).

We impose infinite planar anchoring and a no-slip condition on the wall of the parallel plates, giving rise to the following boundary conditions

$$\theta(0,t) = 0, \quad \theta(d,t) = 0,$$
(3.15)

$$v(0,t) = v(d,t) = 0. (3.16)$$

It is important to note that equations (3.9) and (3.14) remain unchanged via the transformations $\theta(z,t) \to -\theta(d-z,t)$ and $v(z,t) \to v(d-z,t)$.

3.3 Linear analysis for activity-driven channel flow

To simplify the problem, we linearise about the uniform alignment state in the absence and presence of an orienting field, assuming that θ is close to its initial state in the early stages of the dynamics. We consider a initial state of the form $\theta = \Phi$ and v = 0, where Φ is a constant.

We now explore the stability of the system by considering small perturbations about this initial state. Let

$$\theta(z,t) = \Phi + \epsilon \hat{\theta}(z,t),$$
(3.17)

$$v(z,t) = \epsilon \hat{v}(z,t), \tag{3.18}$$

where $\epsilon \ll 1$ and $\hat{\theta}$ is the linearised perturbation. This notation will be used consistently throughout the linear analysis. We denote $\theta(z,t)$ as the director angle and $\hat{\theta}(z,t)$ as its

perturbation about the initial state.

Substituting into equations (3.17) and (3.18) equations (3.9) and (3.14), and applying a Taylor expansion, we obtain

$$\left(\epsilon g(\Phi)\hat{v}_z + \epsilon m(\Phi)\hat{\theta}_t + \xi \sin\Phi\cos\Phi + \epsilon\xi\hat{\theta}\cos(2\Phi)\right)_z + \mathcal{O}(\epsilon^2) = 0, \tag{3.19}$$

$$\epsilon \gamma_1 \hat{\theta}_t - \epsilon \left(K_1 \cos^2 \Phi + K_3 \sin^2 \Phi \right) \hat{\theta}_{zz} - \epsilon (K_3 - K_1) \sin \Phi \cos \Phi (\hat{\theta}_z)^2$$

$$+\epsilon m(\Phi)\hat{v}_z + \epsilon \chi_a H^2 \hat{\theta} \cos(2\Phi) + \mathcal{O}(\epsilon^2) = 0. \tag{3.20}$$

At zeroth order, we require $\sin \Phi \cos \Phi = 0$ only when $H \neq 0$ due to the presence of the orienting field term. In the case where H = 0, no such condition arises, and the only constraint on Φ comes from the boundary condition. Since we are linearising about a steady state that satisfies $\theta(0,t) = \theta(d,t) = 0$, we set $\Phi = 0$. Retaining only the $\mathcal{O}(\epsilon)$ terms, we obtain the linearised system

$$\left(g(\Phi)\hat{v}_z + m(\Phi)\hat{\theta}_t + \xi\hat{\theta}\cos(2\Phi)\right)_z = 0, \tag{3.21}$$

$$\gamma_1 \hat{\theta}_t - \left(K_1 \cos^2 \Phi + K_3 \sin^2 \Phi \right) \hat{\theta}_{zz} + m(\Phi) \hat{v}_z$$

$$-(K_3 - K_1)\sin\Phi\cos\Phi\hat{\theta}_z^2 + \chi_a H^2\hat{\theta}\cos(2\Phi) = 0.$$
 (3.22)

We now consider the solutions to equations (3.21) and (3.22) for possible combinations of $\Phi = 0$ when H = 0 or $H \neq 0$ and $\Phi = \pi/2$ when H = 0. We consider the case $\Phi = \pi/2$ when $\hat{\theta}(0) = 0 = \hat{\theta}(d)$ because it is similar to the system relaxation from a switched-on state $\hat{\theta} \approx \pi/2$ towards an equilibrium state.

3.3.1 Linearising about planar alignment in the absence of an orienting field

In this section, we consider switch-on dynamics in active systems akin to the situation where the Fréedericksz transition occurs in planar to homeotropic alignment when the orienting field is suddenly switched on, with the orienting field much greater than the threshold value. In active nematics, the activity effectively acts as an orienting field because the active stresses couple to the director, driving spontaneous flow and reorientation. This means that activity itself provides a symmetry-breaking mechanism that aligns the director field, as discussed previously. When the activity is sufficiently strong, it can drive a transition similar to the Fréedericksz transition, leading to pronounced flow effects. Although this section outlines previously known results, it establishes the procedure for introducing an orienting field.

In the absence of the orienting field (H = 0) and setting $\Phi = 0$ in equations (3.21) and (3.22), we obtain a coupled linear system of partial differential equations given by

$$\eta_1 \frac{\partial^2 \hat{v}}{\partial z^2} + \alpha_3 \frac{\partial^2 \hat{\theta}}{\partial z \partial t} + \xi \frac{\partial \hat{\theta}}{\partial z} = 0, \tag{3.23}$$

$$K_1 \frac{\partial^2 \hat{\theta}}{\partial z^2} - \gamma_1 \frac{\partial \hat{\theta}}{\partial t} - \alpha_3 \frac{\partial \hat{v}}{\partial z} = 0, \tag{3.24}$$

where $\eta_1 = \frac{1}{2}(\alpha_3 + \alpha_4 + \alpha_6)$ is a Miesowicz viscosity [202]. As expected, when the activity strength $\xi = 0$, we revert to the passive nematic linearised partial differential equations given in Stewart [202, p. 226]. Multiplying equation (3.24) by η_1 , differentiating with respect to z and adding the result to (3.23) multiplied by α_3 , we obtain an equation for $\hat{\theta}$ only

$$\frac{\partial^3 \hat{\theta}}{\partial z^3} + \beta_1 \frac{\partial \hat{\theta}}{\partial z} + \beta_2 \frac{\partial^2 \hat{\theta}}{\partial z \partial t} = 0, \tag{3.25}$$

where

$$\beta_1 = \frac{\xi \alpha_3}{\eta_1 K_1}, \quad \beta_2 = \frac{1}{\eta_1 K_1} (\alpha_3^2 - \eta_1 \gamma_1).$$
 (3.26)

3.3.1.1 Characteristic length and time scales

The dynamics of $\theta(z,t)$ in the active system is described by equation (3.25), where the coefficients β_1 and β_2 encapsulate the physical properties of the system. Specifically,

the intrinsic active length scale

$$l_a = \frac{1}{\sqrt{|\beta_1|}} = \sqrt{\frac{\eta_1 K_1}{|\xi \alpha_3|}},$$
 (3.27)

sets the characteristic spatial extent over which active stresses deform the nematic director. This active length scale is consistent with [81]. Physically, l_a measures the size of the region driven by activity before elasticity dominates and suppresses further distortions.

The coefficient $\beta_2 = (1/\eta_1 K_1) (\alpha_3^2 - \eta_1 \gamma_1)$, together with $\beta_1 = \xi \alpha_3/\eta_1 K_1$, defines the active time scale,

$$\tau_a = \frac{\beta_1}{\beta_2} = \frac{\gamma}{|\xi|}, \quad \text{with } \gamma = \frac{\alpha_3^2 - \eta_1 \gamma_1}{\alpha_3}, \tag{3.28}$$

which characterises how quickly the director field responds to active forcing. Together, l_a and τ_a capture the essential scales governing the onset and evolution of activity-driven patterns in active nematics.

We now discuss the implications of these scales using the parameters in Table 1.1, for the smallest and largest activity values. In this Chapter, we consider a channel height of $d=200~\mu\mathrm{m}$ for capturing general flow behaviour. In our system, the active length scale is $l_a\approx 11.4/\sqrt{|\xi|}\mu\mathrm{m}$. For the smallest activity, $\xi=0.001\mathrm{Pa}$, $l_a\approx 360~\mu\mathrm{m}$, larger than the channel height, indicating almost uniform behaviour and weak distortions. The corresponding active time scale is $\tau_a\approx 2375~\mathrm{s}$. For this situation, we expect no activity-induced distortions because of the large active lengthscale, and we need not run a simulation for the full duration of the active timescale. For the largest activity, $\xi=2~\mathrm{Pa}, l_a\approx 8.06~\mu\mathrm{m}$, much smaller than the channel height, which produces strongly localised distortions. The corresponding active time scale is $\tau_a\approx 1.19~\mathrm{s}$. For this situation, the suggested active lengthscale suggests distortion will occur, and we must ensure we run the simulation for greater than the active timescale to ensure we observe the full behaviour of the system.

Simulation times of 200 s are therefore sufficient to capture both slow and fast dynamics: for the smallest activity, this corresponds to only about 0.08 active response times, while for the largest activity it spans over 400 active response times, ensuring that both nearly uniform behaviour and rapid, localized responses are fully resolved. Thus, varying ξ from very small to very large changes both the length scale of active distortions and the time scale of their evolution, from almost uniform, slowly-evolving systems at low ξ to highly localized, rapidly-evolving dynamics at high ξ .

3.3.1.2 Solution of the linearised system

We now solve equation (3.25) using a separation of variables approach. Let us assume a solution of the form

$$\hat{\theta}(z,t) = \tilde{\theta}(z)e^{-t/\tau},\tag{3.29}$$

where τ is a decay timescale to be determined. Substituting equation (3.29) into equation (3.25) gives

$$\tilde{\theta}'''(z) + \left(\beta_1 - \frac{\beta_2}{\tau}\right)\tilde{\theta}'(z) = 0. \tag{3.30}$$

This is a third-order ODE for $\tilde{\theta}(z)$ and thus requires three boundary conditions. Two of these are provided by the anchoring conditions

$$\hat{\theta}(0,t) = \hat{\theta}(d,t) = 0 \quad \Rightarrow \quad \tilde{\theta}(0) = \tilde{\theta}(d) = 0. \tag{3.31}$$

The third condition arises from the no-slip boundary condition on the velocity field v, which is coupled to $\hat{\theta}$ through equation (3.23). Substituting the ansatz (equation (3.29)) into (3.23) and integrating, we impose the condition

$$\hat{v}(0,t) = \hat{v}(d,t) = 0. \tag{3.32}$$

These constraints on \hat{v} yield an effective third boundary condition for $\tilde{\theta}$, ensuring a well-posed eigenvalue problem.

A particular solution satisfying the boundary conditions can be written as

$$\hat{\theta}(z,t) = \bar{\theta} \left[\cos \left(q - \frac{2q}{d}z \right) - \cos(q) \right] e^{-t/\tau}, \tag{3.33}$$

where $\bar{\theta}$ and q are constants.

To determine the associated velocity, we differentiate (3.33) with respect to t and z and substitute into equation (3.23), giving

$$\frac{\partial^2 \hat{v}}{\partial z^2} = -\frac{2q\bar{\theta}}{\eta_1 d} \left(\frac{\alpha_3}{\tau} - \xi\right) \sin\left(q - \frac{2q}{d}z\right) e^{-t/\tau}.$$
 (3.34)

Integrating equation (3.34) twice and using the no-slip conditions $\hat{v}(0,t) = \hat{v}(d,t) = 0$, we obtain

$$\hat{v}(z,t) = \bar{v} \left[\sin \left(q - \frac{2q}{d}z \right) + \left(\frac{2}{d}z - 1 \right) \sin(q) \right] e^{-t/\tau}, \tag{3.35}$$

where

$$\bar{v} = -\frac{\bar{\theta}d}{2\eta_1 q} \left(\frac{\alpha_3}{\tau} - \xi\right). \tag{3.36}$$

In the passive case ($\xi=0$), equation (3.36) reduces to the known result for passive nematics [202, p. 227]

$$\bar{v} = -\frac{\bar{\theta}d\alpha_3}{2\eta_1 q\tau}. (3.37)$$

To determine the admissible values of q, we substitute equations (3.33) and (3.35) into the original system (3.24)–(3.23) and use (3.36), yielding the following pair of

transcendental equations

$$\frac{\gamma_1}{\tau}\cos q - \frac{1}{\eta_1 q} \left(\frac{\alpha_3^2}{\tau} - \xi \alpha_3\right) \sin q = 0, \tag{3.38}$$

$$\frac{\gamma_1}{\tau} - \frac{4K_1q^2}{d^2} - \left(\frac{\alpha_3}{\tau} - \xi\right) = 0. \tag{3.39}$$

Solving equation (3.39) for τ gives

$$\tau = \alpha \gamma_1 \left(\frac{4K_1 q^2}{d^2} - \frac{\alpha_3 \xi}{\eta_1} \right)^{-1}, \quad \text{where} \quad \alpha = 1 - \frac{\alpha_3^2}{\gamma_1 \eta_1}. \tag{3.40}$$

The positivity of the dissipation function means that $\eta_1 > 0$ and $\eta_1 \gamma_1 - \alpha_3^2 > 0$ hold, which means that $\gamma_1 > \alpha_3^2/\eta_1 \ge 0$. These inequalities mean that $0 < \alpha < 1$ [202]. When $\xi = 0$, equation (3.40) reverts to the passive nematic problem.

Substituting (3.40) into (3.38) and simplifying, we obtain

$$r(q) = q - (1 - \alpha) \tan q + \frac{\alpha_3 \xi \alpha}{\eta_1} \left(\frac{4K_1 q^2}{d^2} - \frac{\alpha_3 \xi}{\eta_1} \right)^{-1} \tan q = 0.$$
 (3.41)

Equation (3.41) has a countable set of solutions q_n , referred to as mode numbers, ordered by their real parts satisfying $\Re(q_0) \leq \Re(q_1) \leq \Re(q_2) \leq \ldots$ The index n denotes the mode number. The corresponding τ_n values are referred to as the time constants.

The time constants, τ_n with positive real parts, correspond to decaying modes, while those with negative real parts represent exponentially growing modes. The mode with the most negative real part dominates at long times, which we call the dominant growing mode, and which we denote as τ_{min} .

Figure 3.2 illustrates the behaviour of the function r(q) as a function of q, together with the first few solutions of the equation r(q) = 0 that satisfy the condition $\Re(q) > 0$, and for $\xi = 0$ no admissible root exists. Note that the asymptotes of r(q) coincide either with the asymptotes of $\tan(q)$ or the solutions of $4K_1q^2/d^2 - \alpha_3\xi/\eta_1 = 0$.

To determine τ_n , we first solve for q_n . However, since the equation for q has both

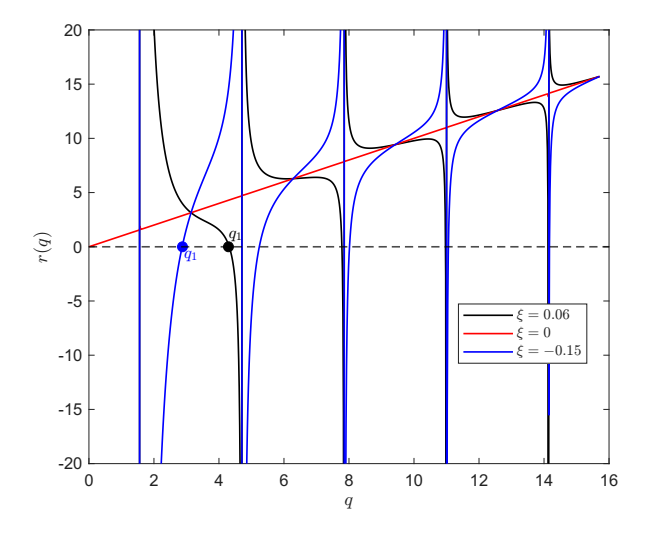


Figure 3.2: Plot of the function r(q) as a function of q for $\xi = [-0.15, 0, 0.06]$ Pa. The blue and black markers indicate the values of q_1 corresponding to $\xi = -0.15$ Pa and $\xi = 0.06$ Pa, respectively.

polynomial and trigonometric components, it is a transcendental equation with no solution that can be written in terms of a finite combination of standard functions. Therefore, we solve for q_n numerically and use the obtained solutions to compute τ_n .

To determine the transition from a uniform state to an unstable state, we need to solve for the critical value of the activity, denoted by ξ_c . This transition occurs when $4K_1q^2/d^2 - \alpha_3\xi/\eta_1 = 0$. The critical activity occurs at the first mode, n = 1, also known as the (fundamental mode), and is given explicitly as

$$\xi_c = \frac{4K_1 q_1^2 \eta_1}{d^2 \alpha_3},\tag{3.42}$$

where q_1 represents the mode number associated with the first mode. We note that all the parameters in the definition of critical activity ξ_c are positive, except the viscosity α_3 [202]. So, when $\alpha_3 < 0$, we have $\xi_c < 0$, which is the usual case when the active nematic is rod-like. On the other hand, when $\alpha_3 > 0$, then $\xi_c > 0$, which is associated with disc-like active nematics [238].

From equation (3.26), the expression for the parameter, β_1 , together with equation (3.42) can be written as $\beta_1 = 4q_1^2/d^2$. Introducing the non-dimensional parameter $\xi = \beta_1 d^2$,

the corresponding critical activity is then given by

$$\xi_c = \beta_1 d^2 = (2q_1)^2. (3.43)$$

To then find the solutions for $\hat{\theta}(z,t)$ and $\hat{v}(z,t)$, we employ the superposition principle

$$\hat{\theta}(z,t) = \sum_{n=1}^{\infty} \bar{\theta}_n \left[\cos \left(q_n - \frac{2q_n}{d} z \right) - \cos(q_n) \right] \exp \left(-\frac{t}{\tau_n} \right), \tag{3.44}$$

$$\hat{v}(z,t) = \sum_{n=1}^{\infty} \bar{v}_n \left[\sin \left(q_n - \frac{2q_n}{d} z \right) + \left(\frac{2z}{d} - 1 \right) \sin(q_n) \right] \exp\left(-\frac{t}{\tau_n} \right), \qquad (3.45)$$
with
$$\bar{v}_n = -\frac{\bar{\theta}_n d}{2\eta_1 q_n} \left(\frac{\alpha_3}{\tau_n} - \xi \right),$$

where $\bar{\theta}_n$ are the constant coefficients chosen to satisfy the initial conditions

$$\hat{\theta}(z,0) = \hat{\theta}_0(z),\tag{3.46}$$

$$\hat{v}(z,0) = 0, (3.47)$$

where $0 \le z \le d$ and $\hat{\theta}_0(z)$ describes the initial director configuration. For our analysis, we specify $\hat{\theta}_0(z) = \Theta \sin(\pi z/d)$, with $\Theta = 0.0001$, which satisfies the boundary conditions and provides a physically realistic small perturbation.

We choose $\hat{\theta}_0(z)$ to satisfy equation (3.46)

$$\hat{\theta}_0(z) = \sum_{n=1}^{\infty} \bar{\theta}_n \left[\cos \left(q_n - \frac{2q_n}{d} z \right) - \cos(q_n) \right]. \tag{3.48}$$

To determine $\bar{\theta}_n$, let

$$f_m(z) = \cos\left(q_m - \frac{2q_m}{d}z\right) - \cos(q_m). \tag{3.49}$$

Multiplying both sides of equation (3.48) by f_m and integrating with respect to z from

0 to d yields

$$\int_0^d \hat{\theta}_0(z) f_m(z) = \int_0^d \sum_{n=1}^\infty \bar{\theta}_n f_n(z) f_m(z) dz.$$
 (3.50)

Since f_m is not orthogonal, this problem does not have an analytical solution, so we resort to determining $\bar{\theta}_n$ numerically. Since f_n and f_m are known functions, evaluation of the left-hand side of equation (3.50) will give constants for m = 1, 2, 3... and integration of $f_n f_m$ will give us a positive semidefinite matrix, while the $\bar{\theta}_n$ are unknown variables that will be determined. To achieve this, we use the parameter values listed in [202] to first compute q_n and τ_n numerically, and then use these results to evaluate $\bar{\theta}_n$. Our numerical calculations were performed using Maple [88], Version 2018.

Since equation (3.48) involves an infinite sum, we must truncate the series in practice to compute a numerical approximation of the initial condition. Specifically, we consider the truncated expansion

$$\hat{\theta}_0(z) \approx \sum_{n=1}^N \bar{\theta}_n f_n(z), \tag{3.51}$$

where $f_n(z)$ is defined in equation (3.49), and N is chosen such that increasing it further has a negligible impact on the accuracy of the reconstructed initial condition.

The truncation effectively reduces the infinite-dimensional system (3.50) to a finite-dimensional linear system of the form

$$A\bar{\boldsymbol{\theta}} = \mathbf{b},\tag{3.52}$$

where the entries of the matrix $A \in \mathbb{R}^{N \times N}$ are given by

$$A_{mn} = \int_0^d f_n(z) f_m(z) \, dz,$$
 (3.53)

and the entries of the right-hand side vector $\mathbf{b} \in \mathbb{R}^N$ are

$$b_m = \int_0^d \hat{\theta}_0(z) f_m(z) \, dz.$$
 (3.54)

In practice, we select N large enough to ensure convergence of the solution for $\hat{\theta}_0(z)$. The actual initial condition used in simulations is this truncated reconstruction, evaluated numerically using the computed coefficients.

Regarding the possibility of deriving an orthogonality condition using an adjoint formulation, while such an approach might in principle lead to an appropriate basis with orthogonal functions, in our case, the functions $f_n(z)$ depend on parameters q_n that are not linearly spaced, and the functional form of f_n does not naturally lend itself to a Sturm-Liouville framework. Therefore, finding a self-adjoint operator that yields f_n as eigenfunctions with guaranteed orthogonality is non-trivial and lies outside the scope of this work. Instead, we treat the system numerically, using the fact that f_n and f_m are explicitly known functions, which allows us to compute all necessary integrals and solve the resulting linear system efficiently using standard numerical tools in Maple [88].

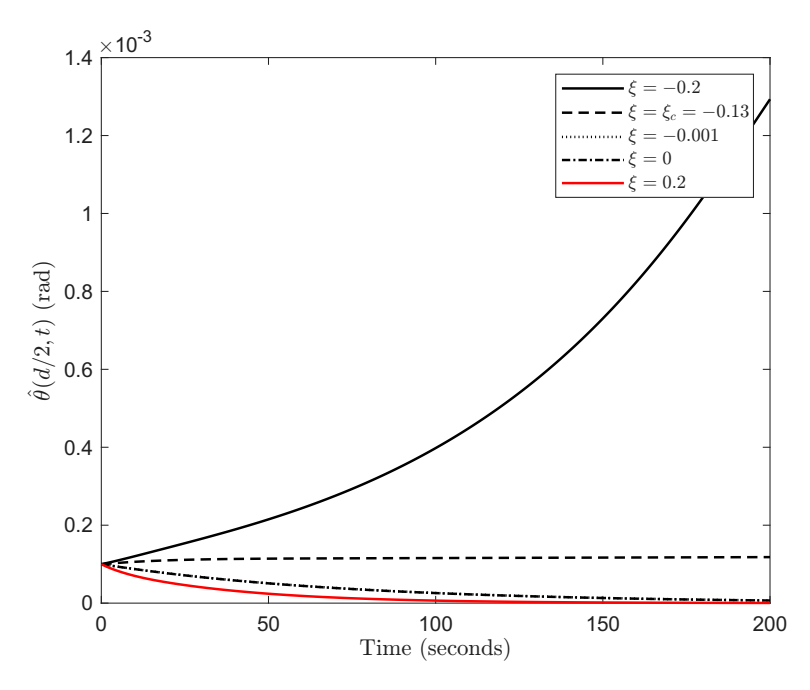


Figure 3.3: Plot of the director angle perturbation as a function of t at z=d/2 for $\xi=[-0.2,-0.13,-0.001,0,0.2]$ Pa.

In Figure 3.3, we plot the director angle perturbation at the center of the channel as a function of time for different values of the activity parameter ξ . For positive activity ($\xi = 0.2 \text{ Pa}$), the perturbation decreases over time and relaxes towards the undistorted state. When the activity parameter is reduced to zero, the perturbation also decays, consistent with the passive case. For weak negative activity ($\xi = -0.13 \text{ Pa}$), the perturbation again decreases in time, corresponding to the regime $\xi < \xi_c$. At the critical activity $\xi = \xi_c \approx -0.13 \text{ Pa}$, the system is marginally stable, and for values of ξ below this threshold (e.g., $\xi = -0.2 \text{ Pa}$), the perturbation grows with time as the higher activity drives instability and distortion.

It should be noted that the curves shown are obtained from a linear theory. Within this framework, the system does not evolve to a steady state; instead, the solutions continue to grow or decay in time without saturating. Consequently, even at extended simulation times, the curves do not reach a steady state, which is inherent to the theoretical approach rather than a limitation of the simulation duration.

For weak activity, the system decays from its uniform state. However, as the magnitude of the activity increases, the director undergoes significant reorientation, leading to sustained flow. These behaviours align with the classical scenario studied by [1,45,236], where the system exhibits flow.

In the next sections, we will introduce an orienting field, and examine how the coupling between the activity and the orienting field affects the dynamics of the system's flow and director orientation.

3.3.2 Linearising about planar alignment in the presence of an orienting field

As mentioned in the introduction, in passive nematics, the system is characterised by a critical orienting field when an orienting field is applied. For an applied field below this critical threshold, the elastic forces resist the director's reorientation, and the system

remains in its original undistorted state. However, when the applied field exceeds the critical threshold, the director undergoes a reorientation, aligning more closely with the direction of the field. This transition is referred to as the "Fréedericksz transition". This reveals the balance between elastic resistance and external field-induced alignment.

Here, we extend the above analysis by introducing an orienting field in addition to the activity strength parameter. This allows us to investigate how the presence of an external orienting field modifies the critical activity threshold and the resulting director configurations. This is crucial for understanding the combined effects of activity and the applied orienting field, which is relevant in understanding the dynamics of active systems.

Specifically, by letting $\Phi = 0$ and $H \neq 0$, equations (3.21) and (3.22) become

$$\eta_1 \frac{\partial^2 \hat{v}}{\partial z^2} + \alpha_3 \frac{\partial^2 \hat{\theta}}{\partial z \partial t} + \xi \frac{\partial \hat{\theta}}{\partial z} = 0, \tag{3.55}$$

$$\gamma_1 \frac{\partial \hat{\theta}}{\partial t} - K_1 \frac{\partial^2 \hat{\theta}}{\partial z^2} + \alpha_3 \frac{\partial \hat{v}}{\partial z} - \chi_a H^2 \hat{\theta} = 0.$$
 (3.56)

As expected, when the orienting field H=0, we revert to equations (3.24) and (3.23), which are the activity-driven state. Introducing the dimensionless parameters $\Lambda_1 = K_1/\chi_a H^2$, $\Lambda_2 = \gamma_1/\chi_a H^2$ and $\Lambda_3 = \alpha_3/\chi_a H^2$, equations (3.55) and (3.56) can be rewritten as

$$\Lambda_1 \frac{\partial^2 \hat{\theta}}{\partial z^2} + \hat{\theta} - \Lambda_2 \frac{\partial \hat{\theta}}{\partial t} - \Lambda_3 \frac{\partial \bar{v}}{\partial z} = 0, \tag{3.57}$$

$$\eta_1 \frac{\partial^2 \hat{v}}{\partial z^2} + \alpha_3 \frac{\partial^2 \hat{\theta}}{\partial z \partial t} + \xi \frac{\partial \hat{\theta}}{\partial z} = 0. \tag{3.58}$$

We again search for solutions of the form of equations (3.33) and (3.35) and obtain

$$\hat{\theta}(z,t) = \bar{\theta} \left[\cos \left(q - \frac{2q}{d}z \right) - \cos(q) \right] \exp \left(-\frac{t}{\tau} \right), \tag{3.59}$$

$$\hat{v}(z,t) = \bar{v} \left[\sin \left(q - \frac{2q}{d}z \right) + \left(\frac{2}{d}z - 1 \right) \sin(q) \right] \exp\left(-\frac{t}{\tau} \right), \tag{3.60}$$

where $\bar{\theta}$ and \bar{v} are non-zero constants and $\tau = \beta_6/(\beta_5 - (2q/d)^2)$ with $\beta_5 = (\eta_1 + \xi \Lambda_2)/\eta_1 \Lambda_1$ and $\beta_6 = (\Lambda_3 \alpha_3 - \Lambda_2 \eta_1)/\eta_1 \Lambda_1$.

Substituting (3.59) and (3.60) into equation (3.58) shows that the condition

$$\bar{v} = -\frac{\bar{\theta}d}{2\eta_1 q} \left(\xi - \frac{\alpha_3}{\tau} \right), \tag{3.61}$$

must hold to ensure consistency.

In order to determine τ and q, we substitute equations (3.59) and (3.60) together with (3.61) into the linearised form of equation (3.58), and obtain

$$\tau = \alpha \gamma_1 \left(\frac{4K_1 q^2}{d^2} - \frac{\alpha_3 \xi}{\eta_1} - \chi_a H^2 \right)^{-1}, \tag{3.62}$$

$$q - (1 - \alpha) \tan q + \frac{1}{\gamma_1} \left(\frac{\alpha_3 \xi}{\eta_1} \tan q + \chi_a H^2 q \right) \tau = 0.$$
 (3.63)

If H=0, we resort to (3.40), and whenever $\xi=0$, we obtain

$$\tau = \alpha \Lambda_2 \left(1 - 4 \frac{q^2 H_c^2}{\pi^2 H^2} \right)^{-1}. \tag{3.64}$$

For a detailed explanation of the Fréedericksz transition in the planar to homeotropic alignment, refer to Stewart [202]. Again, if $\xi = H = 0$, we revert to the passive nematic liquid crystal problem.

Setting $\xi = 0$ and $H \neq 0$, equation (3.63) reduces to equation (3.41), in which case we get back to the equation for the passive nematic liquid crystal, given explicitly by

$$\frac{4q^2}{\pi^2} \left[\frac{\tan q - q/(1-\alpha)}{\tan q - q} \right] = \left(\frac{H}{H_c} \right)^2, \tag{3.65}$$

where H_c is the critical field strength, define as $H_c = (\pi/d)(\sqrt{K_1/\chi_a})$.

Next, we analyse the critical activity, ξ_c , when a field is applied. For planar alignment,

the critical activity ξ_c occurs at the first mode, n=1, and is given by

$$\xi_c = \frac{\eta_1}{\alpha_3} \left[\frac{4K_1 q_1^2 \eta_1}{d^2} - \chi_a H^2 \right]. \tag{3.66}$$

For $\chi_a > 0$, the orienting field **H** tends to align the director **n** parallel to **H** [202]. In the definition of critical activity, all parameters are positive except the viscosity α_3 , which can be positive for rod-like active nematics or negative for disc-like active nematics. For case the $\alpha_3 > 0$, then $\xi_c > 0$ if and only if $4K_1q_1^2\eta_1/\alpha_3d^2 > \chi_aH^2$, or $\xi_c < 0$ if and only if $4K_1q_1^2\eta_1/\alpha_3d^2 < \chi_aH^2$. For $\alpha_3 < 0$, then $\xi_c < 0$ if $4K_1q_1^2\eta_1/\alpha_3d^2 > \chi_aH^2$, or $\xi_c > 0$ if $4K_1q_1^2\eta_1/\alpha_3d^2 > \chi_aH^2$.

From equations (3.62) and (3.62), we get a new version of equation (3.41) given as

$$q - (1 - \alpha) \tan q + \frac{1}{\gamma_1} \left(\frac{\alpha_3 \xi}{\eta_1} \tan q + \chi_a H^2 q \right) \left(\frac{4K_1 q^2}{d^2} - \frac{\alpha_3 \xi}{\eta_1} - \chi_a H^2 \right)^{-1} = 0, \quad (3.67)$$

which will be solved numerically.

We introduce the magnetic field in dimensionless form by writing H in terms of the critical field H_c , such that $H = \varrho H_c$, where H_c is defined in Table 1.1. So that if $\varrho = 1$, we have $H = H_c$, which corresponds to the Fréedericksz transition. The general solution for the velocity amplitude in dimensionless form can then be expressed as

$$\bar{v}_n^* = \left[-\frac{2\alpha_3 \hat{q}_n}{\eta_1 \alpha \gamma_1} + \frac{\alpha_3 \hat{\xi}}{2\eta_1^2 \alpha \gamma_1 \hat{q}_n} + \frac{\hat{\xi}}{2\eta_1 \hat{q}_n} - \frac{\alpha_3}{2\eta_1 \alpha \gamma_1 \hat{q}_n} \right] \bar{\theta}_n^*, \tag{3.68}$$

where $\hat{q}_n = q_n d$ is the dimensionless wavenumber, $\varrho = H/H_c$ dimensionless magnetic field, $\hat{\xi} = \xi d^2/\pi^2 K_1 \varrho^2$ is the dimensionless activity and \bar{v}_n^* and $\bar{\theta}_n^*$ are dimensionless amplitudes, corresponding to \bar{v}_n and $\bar{\theta}_n$.

We now examine the behaviour of the director angle perturbation $\hat{\theta}(z,t)$ in the presence of an orienting field. We first determine $\bar{\theta}_n$ numerically, using the initial conditions specified in equations (3.46) and (3.47) and choose $\varrho = [0.5, 1, 3, 5]$.

In Figure 3.4, we present the director angle perturbation as a function of time for different values of the activity parameter and orienting field strengths. For activity magnitudes below the critical value ($\xi > \xi_c$, e.g., $\xi = -0.001$ Pa), the perturbation decays over time, relaxing toward the undistorted state. At the critical activity $\xi = \xi_c \approx -0.13$ Pa, the perturbation is marginally stable for $H < H_c$, and begins to decay in time as the orienting exceeds the threshold field. For magnitude of activity above the critical value ($\xi < \xi_c$, e.g., $\xi = -0.2$ Pa), the perturbation grows over time. When orienting fields are applied, the perturbation grows for $H < H_c$ whenever the activity magnitudes below the critical value, and decays for activity magnitudes above the critical value (see Figure 3.4(a)–(b)), while for $H > H_c$ (e.g., $\varrho = 3$ and $\varrho = 5$), the field suppresses the activity effect, resulting in decay, as shown in Figure 3.4(c)–(d).

The physical intuition behind the stability of extensile systems ($\xi > 0$) compared to the instability of contractile systems ($\xi < 0$) arises from the coupling between director distortions and the flows they generate under planar boundary conditions. For an initially planar orientation, small bend perturbations in the director field tend to orient toward the channel walls. In extensile systems, it tries to create a flow towards the walls, but since the walls are impermeable, this cannot happen. In contrast, small splay perturbations in contractile systems drive flow along the channel, reinforcing the perturbation and causing instability. When an orienting field is applied ($H > H_c$), the director tends to align with the field, which suppresses the growth of splay perturbations, stabilising the system.

In conclusion, the evolution of the director over time is governed by the interplay between activity and orienting fields. For activity magnitudes below the critical value, perturbations decay, consistent with the behaviour of passive nematics. Above the critical activity, contractile systems exhibit growth in perturbations, while extensile systems remain stable due to boundary constraints. The introduction of an orienting field $(H > H_c)$ suppresses activity-induced instabilities by aligning the director with the field, stabilising the system and limiting perturbation growth. These results underscore

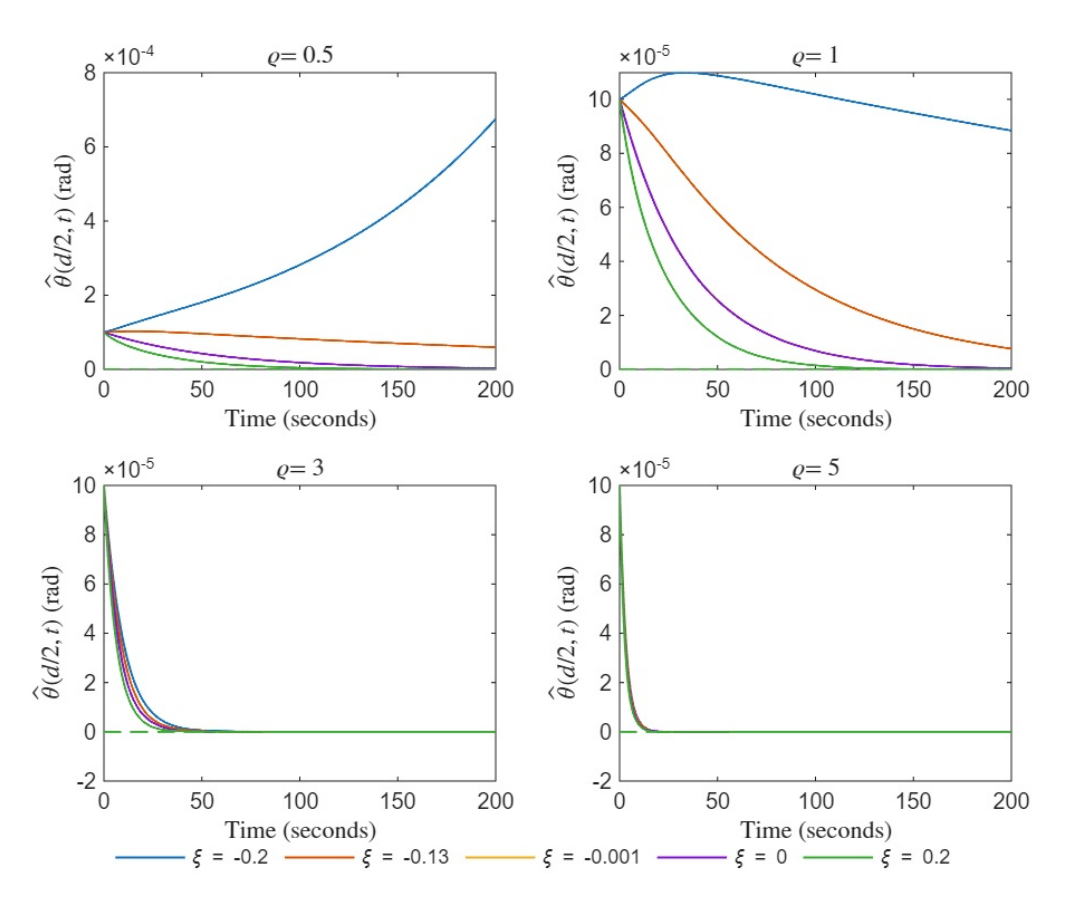


Figure 3.4: The director angle perturbation $\hat{\theta}$ and flow velocity perturbation \hat{v} as a function of t: (a) $\varrho = 0.5$ (b) $\varrho = 1.0$, (c) $\varrho = 3.0$ and (d) $\varrho = 5.0$, for $\xi = [-0.2, -0.13, -0.001, 0, 0.2]$ Pa.

the competing effects of activity-driven dynamics and orienting fields in determining the temporal evolution of the director.

In the following section, we will analyse how the activity affects the kickback subject to homeotropic alignment, characterised by an anchoring angle of $\theta = \pi/2$ rad. This investigation will help in understanding how activity affects the kickback response.

3.3.3 Linearsing about homeotropic alignment in the absence of an orienting field

In contrast to the initial planar alignment considered in the last section, we now consider an initial homeotropic alignment so that the initial director alignment is orthogonal to the substrate. It is therefore assumed that $\theta \approx \pi/2$ rad. This situation is similar to the

classical kickback situation where it is assumed that for t < 0, an orienting field has aligned the director to $\theta \cong \pi/2$ rad and that the orienting field is removed at t = 0. We now examine the system's behaviour by setting H = 0 and $\Phi = \pi/2$ rad with t > 0 into equations (3.21) and (3.22), and we obtain a coupled linear system of partial differential equations given by

$$\eta_2 \frac{\partial^2 \hat{v}}{\partial z^2} - \alpha_2 \frac{\partial^2 \hat{\theta}}{\partial z \partial t} - \xi \frac{\partial \hat{\theta}}{\partial z} = 0, \tag{3.69}$$

$$\gamma_1 \frac{\partial \hat{\theta}}{\partial t} - K_3 \frac{\partial^2 \hat{\theta}}{\partial z^2} - \alpha_2 \frac{\partial \hat{v}}{\partial z} = 0, \tag{3.70}$$

where $\eta_2 = \frac{1}{2}(\alpha_4 + \alpha_5 - \alpha_2)$ is a Miesowicz viscosity.

Note that the linearised system in initial planar alignment is associated with the splay deformation elastic constant K_1 , and the viscosities α_3 and η_1 , while initial homeotropic alignment is associated with the bend deformation elastic constant K_3 , and the viscosities α_2 and η_2 . The equations are identical following the transformation $K_1 \mapsto K_3$, $\alpha_2 \mapsto -\alpha_3$, $\eta_1 \mapsto \eta_2$ and $\xi \mapsto -\xi$.

Solving for τ and q, we obtain the new time constant τ and an equation for q given by

$$\tau = \alpha \gamma_1 \left(\frac{4K_3 q^2}{d^2} - \frac{\alpha_2 \xi}{\eta_2} \right)^{-1},\tag{3.71}$$

$$r(q) = q - (1 - \alpha) \tan q + \frac{\alpha_2 \xi \alpha}{\eta_2} \left(\frac{4K_3 q^2}{d^2} + \frac{\alpha_2 \xi}{\eta_2} \right)^{-1} \tan q = 0.$$
 (3.72)

For $\xi = 0$ Pa (see Figure 3.5), we revert to the case of a passive nematic liquid crystal, where the system behaves according to the classical dynamics of passive nematics. In this scenario, the perturbation $\hat{\theta}$ undergoes the "classical kickback effect." Initially, after the orienting field is removed, the perturbation $\hat{\theta}$ is greater than $\pi/2$. This is because the director initially tries to align with the field, but once the field is removed, the director undergoes a relaxation process where the director tends to return to its equilibrium state, but the high-order modes decay quickly, leaving the low mode, which pushes the director above $\pi/2$ in the center of the cell [202].

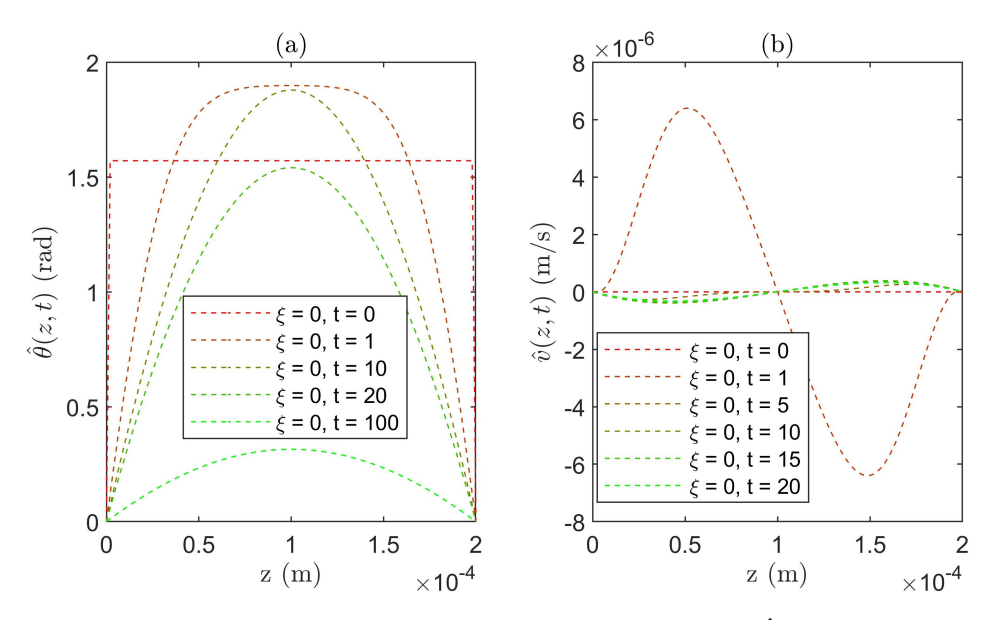


Figure 3.5: Plot showing the (a) director angle perturbation $\hat{\theta}$ and (b) flow velocity perturbation \hat{v} as a function of z for various time when the director is initially aligned at $\theta = \pi/2$ rad.

Next, we turn our attention to the impact of activity on this behaviour. As the activity parameter value, ξ is introduced, we expect the director's relaxation dynamics to be altered. The activity introduces a new term into the governing equations, which can lead to deviations from the classical passive nematic behaviour, causing realignment and overshooting the director angle. We examine the behaviour of the system for various activity parameter values.

We present the behaviour of the system for active contractile and extensile nematics in Figure 3.6, showing the director angle perturbation at the channel center as a function of time for various activity parameters. For $\xi = 0$, the system exhibits the classical kickback behaviour of passive nematics, where the perturbation initially aligns at $\hat{\theta} = \pi/2$ rad, increases, and then decays over time (Figure 3.6(a)). As the activity increases to $\xi = 0.01$ Pa, the kickback diminishes (Figure 3.6(b)), and at $\xi = 0.2$ Pa, the kickback disappears entirely, with $\hat{\theta} \approx 1.53$ rad initially and the perturbation immediately relaxing to the equilibrium state (Figure 3.6(c)). In contrast, for contractile activity $\xi = -0.0095$ Pa, the kickback persists with $\hat{\theta} \approx 3.33$ rad (Figure 3.6(d)).

We further investigate the behaviour system by plotting the director angle perturbation

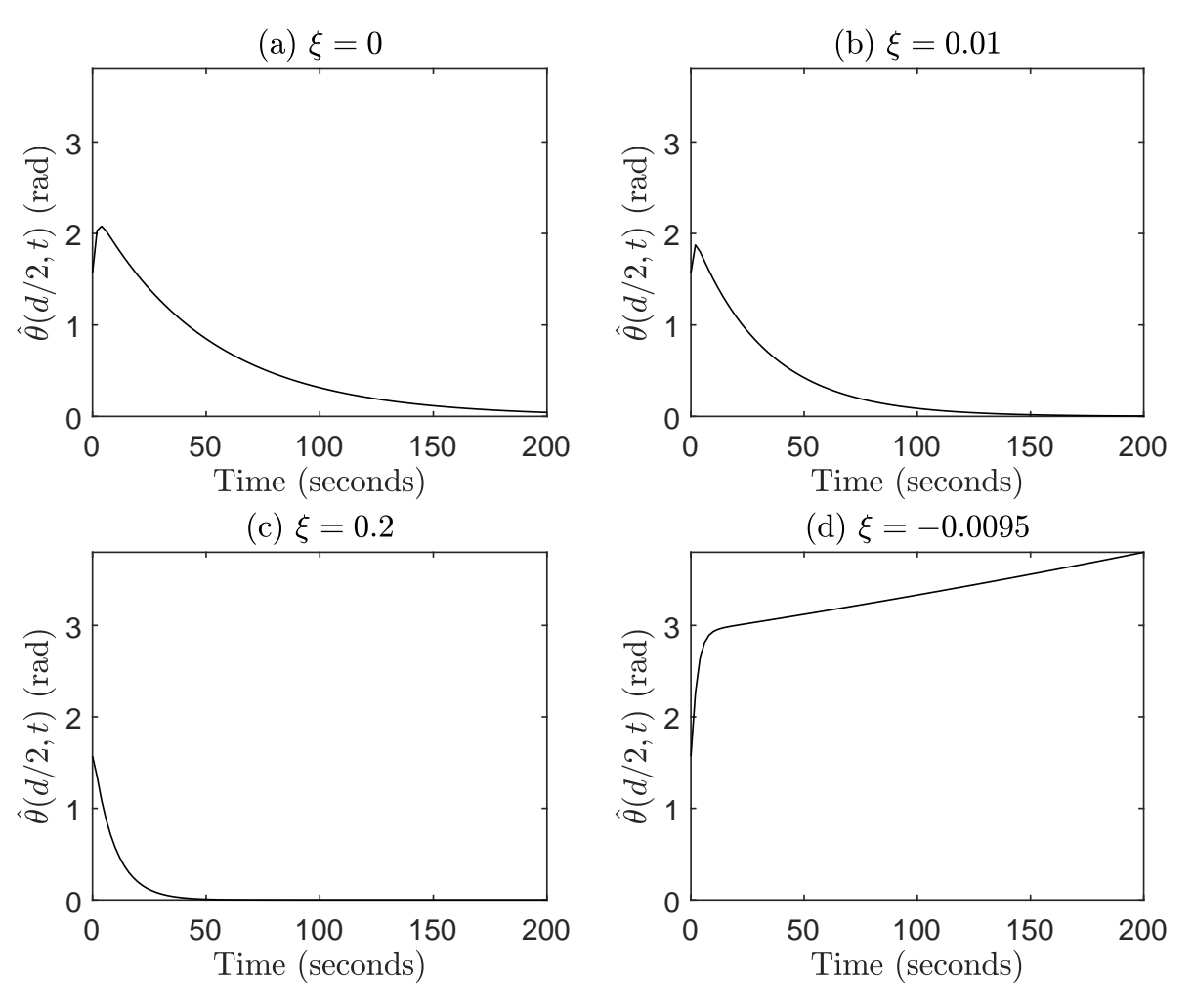


Figure 3.6: Plot of the director angle perturbation in the center of the channel as a function of time, t, for (a) $\xi = 0$ Pa, (b) $\xi = 0.01$ Pa, (c) $\xi = 0.2$ Pa, and (d) $\xi = -0.0095$ Pa under homeotropic alignment.

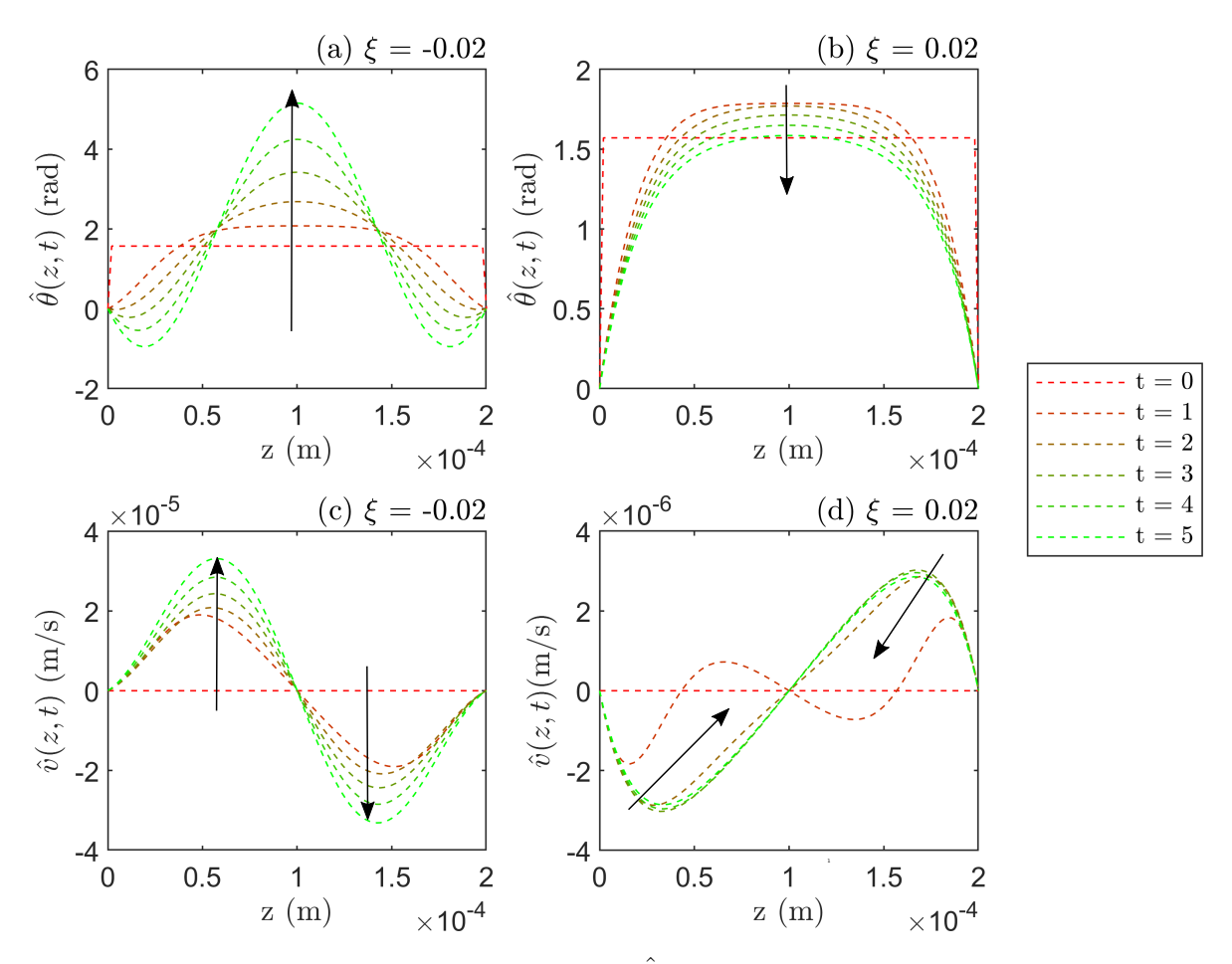


Figure 3.7: The director angle perturbation $\hat{\theta}$ and the flow velocity perturbation \hat{v} in the absence of a field for various time t when $\xi = -0.02$ Pa and $\xi = 0.02$ pa, for homeotropic alignment, respectively. For clarity, we use the arrow-headed lines to indicate the direction of increasing time.

and flow velocity perturbation as a function of z for various times. Figure 3.7 illustrates the evolution of the perturbation of the director angle and flow velocity for $\xi = -0.02$ Pa and $\xi = 0.02$ Pa, respectively. For the case of negative activity, the perturbation begins at $\pi/2$ rad, indicating the initial alignment, and increases over time, as shown in Figure 3.7(a).

For extensile systems, the director angle perturbation is initially at $\hat{\theta} = \pi/2$ rad, then increases before finally decreasing to the non-zero equilibrium state, as observed in Figure 3.7(b). This behaviour suggests that positive activity suppresses any initial director orientation, driving the director smoothly toward its non-zero equilibrium state. Figures 3.7(c) and 3.7(d) depict the evolution of perturbed flow velocity under the same conditions. For both contractile and extensile nematics, the flow velocity shows distinct profiles with respect to time, influenced by director distortions.

These results are consistent with those reported in [238]. In particular, the study showed that in active nematic liquid crystals subject to a uniform orienting field, the presence of sufficient activity can suppress the transient overshoot of the director angle, known as kickback. For symmetric director configurations, the director may exhibit kickback only for activity below a critical value, whereas for anti-symmetric configurations, kickback is generally absent. Similarly, in our simulations of extensile active nematics with activity exceeding the critical value, we observe that the director relaxes smoothly to its pre-switched configuration upon removal of the field, with no evidence of kickback.

Throughout Section 3.3, we investigated the short-time behaviour of active nematics across three distinct scenarios. These included planar alignment in both the absence and presence of an orienting field, where the dynamics involved the Fréedericksz transition. Additionally, we analysed the system under homeotropic alignment in the absence of an orienting field. In these cases, the system is characterised by kickback when $\xi = 0$ and low activity strengths. However, for extensile nematics, the kickback effect diminishes as the activity increases. These studies provide an understanding of the short-time behaviour of the system, capturing Fréedericksz transition and kickback effects, which

reveal the sensitivity of active nematics to both activities and applied orienting fields.

Building on this, the next section will extend the analysis by examining the longer-time behaviour of the system under planar alignment in the presence of an orienting field. By solving the governing equations numerically, we aim to characterise the solution transitions for various activity parameter values and orienting fields to provide a more comprehensive understanding of the interplay between activity and orienting fields.

3.4 Nonlinear analysis under planar alignment subject to an orienting field

In the previous section, we analysed the system using linear stability theory to identify key transitions and gain insight into the initial dynamics. These results provide valuable context for understanding the mechanisms that govern the system's response and establish a foundation for the more complex behaviour observed in the nonlinear regime.

Building on this foundation, we now extend our investigation to the long-term dynamics by numerically solving the full nonlinear equations of motion. This approach allows us to explore the emergence of distinct transition states and capture the asymptotic behaviour that cannot be accessed through linear analysis alone.

Specifically, we aim to investigate how variations in the activity parameter and orienting fields affect flow regimes, director distortions, active energy dissipation and elastic energy. The results obtained will allow us to identify the different solution regimes. Additionally, investigating the contribution of active energy dissipation will help us understand how changes in the orienting field and activity affect the system.

3.4.1 Finite difference approximation for Ericksen-Leslie equations

In this section, we present the details of the finite difference approximations in Section (3.4). The nonlinear coupled governing dynamical equations (3.9) and (3.14), together with the infinite planar anchoring and a no-slip condition, can be reformulated as

$$\dot{\theta} = A_1 \theta_{zz} + B_1 \theta_z^2 - C_1 v_z + D_2 \sin \theta \cos \theta, \tag{3.73}$$

$$0 = B_3 \theta_{zzz} + \left(g(\theta) - C_4 \right) v_{zz} + \left(A_2 + A_3 + 2B_4 \right) \theta_z \theta_{zz}$$

$$+ \left(\Lambda_1 v_z - 2C_2 v_z + D_2 \sin \theta \cos \theta + E_1 + E_2 \right) \theta_z + \left(B_2 + C_3 \right) \theta_z^3, \tag{3.74}$$

and

$$\theta(0,t) = \theta(d,t) = \Phi_b, \tag{3.75}$$

$$v(0,t) = v(d,t) = 0, (3.76)$$

where $\dot{\theta}$ is a material derivative of θ , which is the as the d/dt, and

$$A_{1} = f_{1}/\gamma_{1}, \quad B_{1} = f_{2}/\gamma_{1}, \quad C_{1} = m/\gamma_{1}, \quad \Phi_{b} = 0 \text{ or } \pi/2,$$

$$A_{2} = A_{1}\Lambda_{2}, \quad B_{2} = B_{1}\Lambda_{2}, \quad C_{2} = C_{1}\Lambda_{2}, \quad A_{3} = C_{1}\Lambda_{3},$$

$$B_{3} = A_{1}m, \quad B_{4} = B_{1}m, \quad C_{3} = C_{1}\Lambda_{4}, \quad C_{4} = C_{1}m, \quad D_{2} = \chi_{a}(\varrho H_{c})^{2}/\gamma_{1},$$

$$E_{1} = (\chi_{a}(\varrho H_{c})^{2})\Lambda_{2}m/\gamma_{1}) \left(\cos^{2}\theta - \sin^{2}\theta\right), \quad E_{2} = \xi \left(\cos^{2}\theta - \sin^{2}\theta\right), \quad (3.77)$$

and

$$f_{1} = K_{1} \cos^{2} \theta + K_{3} \sin^{2} \theta$$

$$f_{2} = (K_{3} - K_{1}) \sin \theta \cos \theta$$

$$\Lambda_{1} = \left[(\alpha_{5} - \alpha_{2}) - (\alpha_{6} - \alpha_{3}) + 2\alpha_{1} \cos^{2} \theta - 2\alpha_{1} \sin^{2} \theta \right] \sin \theta \cos \theta$$

$$\Lambda_{2} = (-2\alpha_{3} - 2\alpha_{2}) \sin \theta \cos \theta$$

$$\Lambda_{3} = (-2K_{1} + 2K_{3}) \sin \theta \cos \theta$$

$$\Lambda_{4} = -(K_{3} - K_{1}) \sin^{2} \theta + (K_{3} - K_{1}) \cos^{2} \theta.$$
(3.78)

We now define the discretisation used in the finite difference scheme in the following steps.

Step one: We divide the domain into a series of discrete nodes:

Here, h = d/N is the distance between nodes, N is the number of intervals, and d is the domain size. We refer to j index as the global index, which is useful for defining the full discretised system, particularly when imposing boundary conditions. The index k is used only for the interior points, excluding the boundaries, which is convenient when solving the governing equations. The interior points are indexed from k = 1 to k = N - 1, mapping onto the global indices $j = 2, \ldots N$.

We create a solution vector, denoted by y with index i such that the entries from i = 1 to i = N - 1 are given by $\theta_1, \theta_2, \ldots, \theta_{N-1}$ and the entries from i = N to i = 2(N-1) are given by $v_1, v_2, \ldots, v_{N-1}$. The index j represents all discrete points in the domain, including the boundary nodes at j = 1 and j = N + 1.

The solution vector is therefore given by

$$y = (\theta_1, \ \theta_2 \dots, \theta_{N-1}, \ v_1, \ v_2, \ v_{N-1})^{\mathrm{T}}.$$
 (3.79)

Step two: We approximate the spatial gradients using a second-order accurate finite difference approximation. In our case, we have used central or skewed finite difference approximations for the interior θ equations, but because the boundary conditions enter the equations for the outer nodes at j = 1 and j = N + 1, this will result in different cases. We need five possible cases for the v equations because of the third-order derivative that appears in equation (2.50). We now discretise the various derivatives as follows. We approximate θ''' using the following discretisation:

$$\theta_{j}^{""} = \begin{cases} (-\Phi_{b} + 3\theta_{1} - 3\theta_{2} + \theta_{3})/h^{3} & \text{for } j = 2, \\ (-\Phi_{b} + 2\theta_{1} - 2\theta_{3} + \theta_{4})/2h^{3} & \text{for } j = 3, \\ (-\theta_{(j-3)} + 2\theta_{(j-2)} - 2\theta_{j} + \theta_{(j+1)})/2h^{3} & \text{for } 4 \leq j \leq N - 2, \\ (-\theta_{(N-4)} + 2\theta_{(N-3)} - 2\theta_{(N-1)} + \Phi_{b})/2h^{3} & \text{for } j = N - 1, \\ (-\theta_{(N-3)} + 3\theta_{(N-2)} - 3\theta_{(N-1)} + \Phi)/h^{3} & \text{for } j = N. \end{cases}$$
(3.80)

Similarly, we approximate θ'' using the following discretisation:

$$\theta_{j}'' = \begin{cases} \left(\theta_{2} - 2\theta_{1} + \Phi_{b}\right)/h^{2} & \text{for } j = 2, \\ \left(\theta_{j} - 2\theta_{(j-1)} + \theta_{(j-2)}\right)/h^{2} & \text{for } 3 \leq j \leq N - 1, \\ \left(\Phi_{b} - 2\theta_{(N-1)} + \theta_{(N-2)}\right)/h^{2} & \text{for } j = N. \end{cases}$$
(3.81)

For θ' , we have

$$\theta'_{j} = \begin{cases} (\theta_{2} - \Phi_{b})/2h & \text{for } j = 2, \\ (\theta_{j} - \theta_{(j-2)})/2h & \text{for } 3 \leq j \leq N - 1, \\ (\Phi_{b} - \theta_{(N-1)})/2h & \text{for } j = N. \end{cases}$$

$$(3.82)$$

Similarly, for v'' and v', we have

$$v_j'' = \begin{cases} (v_2 - 2v_1 + 0)/h^2 & \text{for } j = 2, \\ (v_j - 2v_{(j-1)} + v_{(j-2)})/h^2 & \text{for } 3 \le j \le N - 1, \\ (0 - 2v_{(N-1)} + v_{(N-2)})/h^2 & \text{for } j = N. \end{cases}$$
(3.83)

$$v'_{j} = \begin{cases} (v_{2} - 0)/2h & \text{for } j = 2, \\ (v_{j} - v_{(j-2)})/2h & \text{for } 3 \leq j \leq N - 1, \\ (0 - v_{(N-2)})/2h & \text{for } j = N. \end{cases}$$
(3.84)

Next, we substitute equations (3.80) - (3.84) into equations (3.73) and (2.50) and obtain the following discretised differential equations:

$$\dot{\theta}_{j} = A_{1j}\theta_{j}'' + B_{1j}\left(\theta_{j}'\right)^{2} - C_{1j}v_{j}' + D_{2}\sin\theta_{j}\cos\theta_{j},$$

$$0 = B_{3j}\theta_{j}''' + \left(g(\theta_{j}) - C_{4j}\right)v_{j}'' + \left(A_{2j} + A_{3j} + 2B_{4j}\right)\theta_{j}''\theta_{j}'$$

$$+ \left(\left(\Lambda_{1j} - 2C_{2j}\right)v_{j}' + D_{2}\sin\theta_{j}\cos\theta_{j} + \left(E_{1j} + E_{2j}\right)\right)\theta_{j}' + \left(B_{2j} + C_{3j}\right)\left(\theta_{j}'\right)^{3},$$
(3.86)

for j = 2..., N. Here, A_{1j} , B_{1j} , C_{1j} , A_{2j} , B_{2j} , C_{2j} , A_{3j} , B_{3j} , C_{3j} , E_{1j} , E_{2j} are the values of A_1 , B_1 , C_1 , A_2 , B_2 , C_2 , A_3 , B_3 , C_3 , E_1 , E_2 , respectively, where $\theta = \theta_j$ and $v = v_j$.

Step three: We can now write the system in the form of Differential Algebraic Equa-

tions (DAE) or matrix notation as $M\dot{Y} = F(Y)$. The mass matrix, M, the vectors Y and F(Y) are given as follows

$$M = \begin{bmatrix} 1 & 0 & 0 & 0 & 0 & 0 & 0 & \cdots & 0 \\ 0 & 1 & 0 & 0 & 0 & 0 & 0 & \cdots & 0 \\ 0 & 0 & 1 & 0 & 0 & 0 & 0 & \cdots & 0 \\ 0 & 0 & 0 & \ddots & 0 & 0 & 0 & \cdots & 0 \\ 0 & 0 & 0 & 0 & 1 & 0 & 0 & \cdots & 0 \\ 0 & 0 & 0 & 0 & 0 & 0 & \cdots & 0 \\ 0 & 0 & 0 & 0 & 0 & 0 & \cdots & 0 \\ \vdots & \vdots \\ 0 & 0 & 0 & 0 & 0 & 0 & 0 & 0 & 0 \end{bmatrix},$$
(3.87)

$$Y = \begin{pmatrix} \theta_1 \\ \theta_2 \\ \theta_3 \\ \theta_{N-1} \\ v_1 \\ v_2 \\ v_3 \\ \vdots \\ v_{N-1} \end{pmatrix}, \tag{3.88}$$

and

$$F(Y) = \begin{bmatrix} (A/h^2) \left(\theta_2 - 2\theta_1 + \Phi_b\right) - (B/2h) \left(v_2 - 0\right) \\ \vdots \\ (A/h^2) \left(\theta_{N-3} - 2\theta_{N-2} + \theta_{N-1}\right) - (B/2h) \left(v_{N-1} - \theta_{N-3}\right) \\ (A/(h^2) \left(\Phi_b - 2\theta_{N-1} + \theta_{N-2}\right) - (B/2h) \left(0 - v_{N-2}\right) \\ (G/h^3) \left(-\Phi_b + 3\theta_1 - 3\theta_2 + \theta_3\right) + (C/h^2) \left(v_2 - 2v_1 + 0\right) + (\xi/2h) \left(\theta_2 - \Phi_b\right) \\ (G/2h^3) \left(-\Phi_b + 2\theta_1 - 2\theta_3 + \theta_4\right) + (C/h^2) \left(v_3 - 2v_2 + v_1\right) + (\xi/2h) \left(\theta_3 - \theta_1\right) \\ \vdots \\ (G/2h^3) \left(-\theta_{N-5} + 2\theta_{N-4} - 2\theta_{N-2} + \theta_{N-1}\right) + (C/h^2) \left(v_{N-2} - 2v_{N-3} + v_{N-4}\right) + (\xi/2h) \left(\theta_{N-2} - \theta_{N-4}\right) \\ (G/2h^3) \left(-\theta_{N-4} + 2\theta_{N-3} - 2\theta_{N-1} + \Phi_b\right) + (C/h^2) \left(v_{N-1} - 2v_{N-2} + v_{N-3}\right) + (\xi/2h) \left(\theta_{N-1} - \theta_{N-3}\right) \\ (G/h^3) \left(-\theta_{N-3} + 3\theta_{N-2} - 3\theta_{N-1} + \Phi_b\right) + (C/h^2) \left(0 - 2v_{N-1} + v_{N-2}\right) + (\xi/2h) \left(\Phi_b - \theta_{N-2}\right) \end{bmatrix}.$$

Step four: We use the ode15s solver in Matlab (R2022a) Version 9.13 [130] to integrate the non-linear coupled partial differential equations in time using an initial condition $\theta = \Theta\left(\sin(\pi z/d) + 0.5\sin(2\pi z/d)\right)$ at t = 0, where $\Theta = 0.0001$.

To characterise the solution profiles of the director and flow velocity, the simulations were run up to t=500 seconds to capture the subsequent development and saturation of instabilities into fully developed steady state. For transitions in the director angle distortion, the focus is on the asymptotic behaviour at the final simulation time, t=500 seconds. The system typically reaches steady or quasi-steady states well before t=500 seconds, with convergence occurring around $t\sim 100-150$ seconds depending on the activity strength and orienting field.

To gain insight into the underlying physics, the system is analysed for various activity strengths and orienting field values, using N=200 spatial intervals to resolve the director angle and flow velocity profiles. The linear stability results provide an important guide to understanding the onset of instabilities and the early-time dynamics, which in turn inform the interpretation of the fully nonlinear behaviour observed in the simulations. By comparing linear predictions with the nonlinear outcomes, we can identify how initial perturbations evolve, and how activity amplifies or suppresses flow. This approach ensures that the linear analysis is used not in isolation, but as a tool to develop intuition for the more complex nonlinear dynamics. Later in this section, we explicitly compare the numerical and analytical solutions by computing the critical activity, which marks the transition from a homogeneous to a nonhomogeneous director configuration.

An important quantity governing the system response is the active time scale, τ_a , which characterises how quickly the director field responds to active forcing relative to viscous dissipation and elastic relaxation (see equations (3.62) and (3.63)). This timescale, together with the active length scale l_a , captures the essential physics of activity-driven pattern formation in active nematics. For low activity, $\tau_a \approx 2375$ s, indicating extremely slow evolution, whereas for the largest activity considered, $|\xi|=2$ Pa, the corresponding

length and time scales are $l_a \approx 8.06 \ \mu \text{m}$ and $\tau_a \approx 1.19 \ \text{s}$, which shows that active distortions are strongly localised and the system responds quickly to activity.

We discretise the governing equations using the finite difference method, and perform our simulations for different values of the activity parameter values, ξ , and the orienting fields, $\varrho = H/H_c$, where H is the orienting field and H_c is the critical orienting field. Note that the Fréedericksz transition occurs when $H = H_c$, which corresponds to $\varrho = 1$.

Initially, we perform our computations for fixed values of an orienting field and varying values of the activity parameter and observe three distinct solutions: an undistorted uniform solution and symmetric and antisymmetric director distortion solutions. For low values of the activity parameter, the orienting field dictates the behaviour, and the director angle in the center of the channel prefers to align along the field direction. We will find that increasing the activity decreases the director angle in the center of the channel, indicating that the activity is reducing director distortion in the center of the channel and eventually overriding the field effect, giving rise to the antisymmetric solution. Interestingly, for extensile systems, the transition from a trivial state to a nontrivial state occurs at the orienting field above the critical field strength, while for contractile systems, the transition occurs at the orienting field below the critical field strength.

3.4.2 Characterisation of the solution profiles

In this section, we investigate the forms of the director and flow profile, demonstrating the effects on the solution symmetry and critical activity.

We define a solution as "symmetric" if it exhibits even symmetry about the center point of the geometry, meaning the director and flow velocity profiles remain unchanged under reflection across the center. Conversely, a solution is considered "antisymmetric" if it exhibits odd symmetry; in this case, the profiles reverse their sign upon reflection. Note that a symmetric director profile is associated with an antisymmetric flow velocity profile, where the flow changes from positive to negative across the center. Similarly, an

antisymmetric director profile is associated with a symmetric flow velocity profile, where the velocity remains unchanged under reflection, highlighting the inherent coupling between the director and flow fields in the system.

We first consider the classical case where $\varrho = 0$ for different activity parameter values. Specifically, we choose $\xi = [-0.03, 0, -0.24, 0.3]$ Pa, covering passive, weakly and strongly active systems.

We present the director angle and flow velocity as a function of z for $\xi=0.3$ Pa (see Figures 3.8(a) and 3.8(e)). In this activity regime, the director remains undistorted, aligning with the uniform director state, and no flow is generated. This occurs because, under planar anchoring, extensile nematics relax to an equilibrium state. We decrease the activity to $\xi=0$ and plot the director angle and flow velocity as a function of z as shown in Figures 3.8(b) and 3.8(f), respectively. As expected, when $\xi=0$, the system remains undistorted and does not generate flow. This behaviour is similar for a weakly active system ($\xi=-0.03$ Pa), as shown in Figures 3.8(c) and 3.8(g), respectively. However, as the activity decreases to $\xi=-0.24$ Pa (Figures 3.8(d) and 3.8(h)), the system exhibits director distortion, which eventually induces flow due to the coupling between the director and flow. This regime is characterised by an antisymmetric director angle profile and a symmetric flow velocity profile. This suggests that when $\xi=0$ and the activity is below the critical value, the director remains undistorted, and no flow is generated. However, when the activity magnitude exceeds the threshold value ($\xi=-0.126$ Pa), the director becomes distorted, leading to flow generation.

We now vary the orienting field to examine its influence on the system's behaviour. We choose $\varrho = [0.5, 1, 1.5, 2, 2.5]$, covering values below, at, and above the critical field. Note that the orienting field reaches the critical value when $\varrho = 1$. This is to characterise the director and the flow velocity profile as the orienting field increases above zero.

For weak orienting fields such as $\varrho = 0.5$, the system exhibits a similar behaviour as the base case ($\varrho = 0$), as shown in Figures 3.9(a)–3.9(h). This occurs because the orienting field remains below the threshold value ($\varrho = 1$). Increasing the orienting

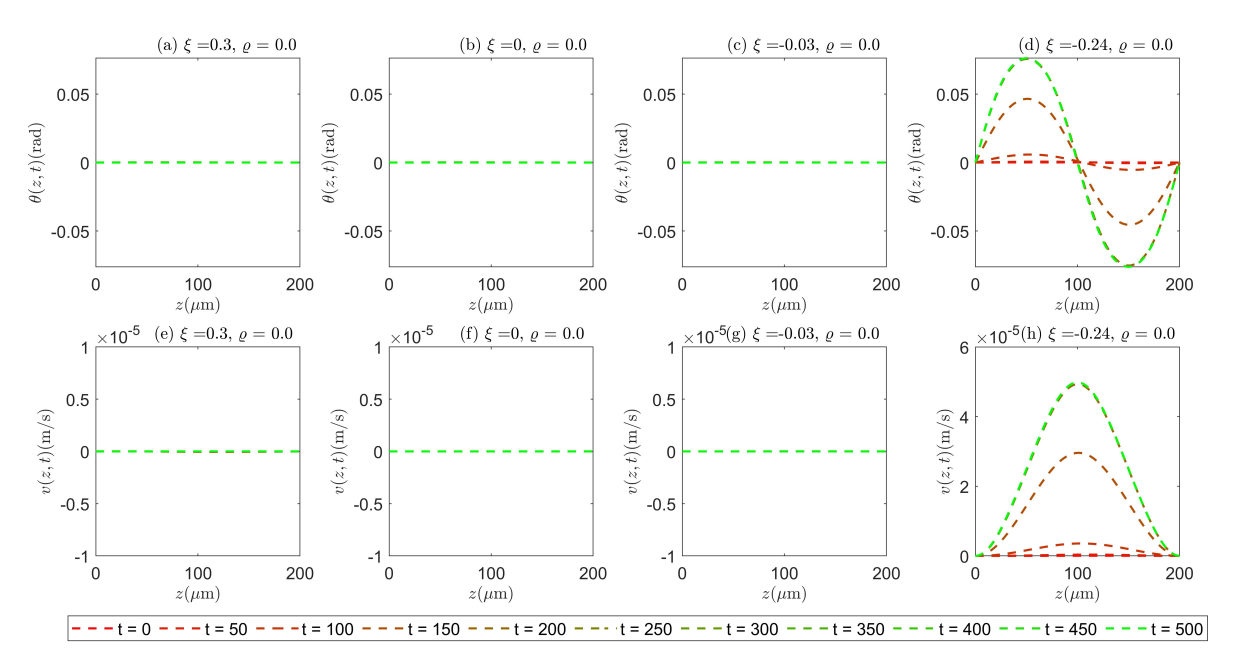


Figure 3.8: Director angle and flow velocity plots for an orienting field, $\varrho = 0$, and for $\xi = [0.3, 0, -0.03, -0.24]$ Pa.

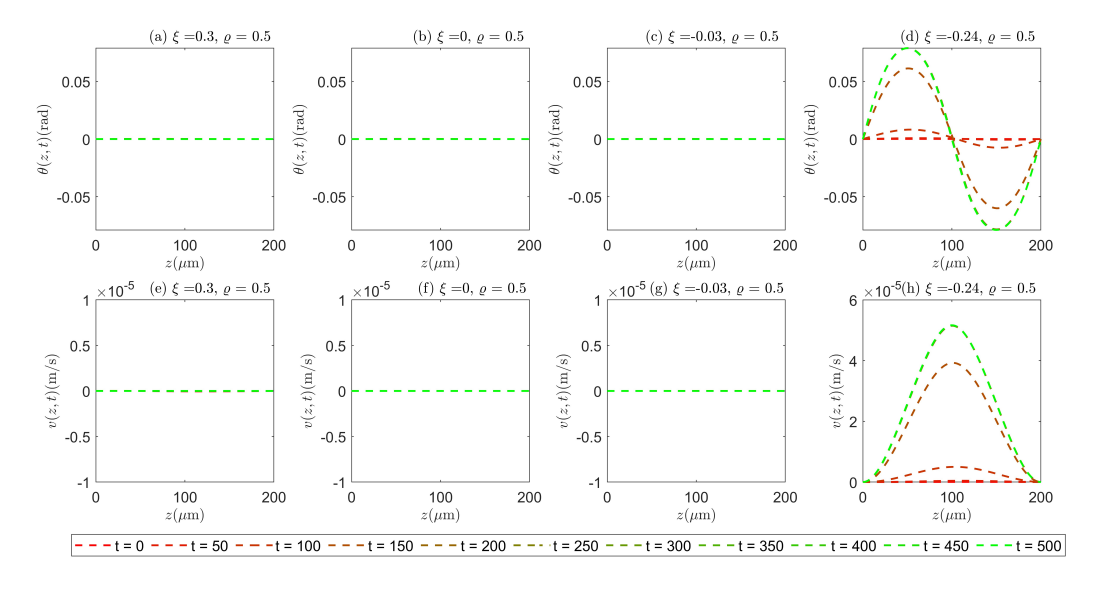


Figure 3.9: Director angle and flow velocity plots for an orienting field, $\varrho=0.5$, and for $\xi=[0.3,0,-0.03,-0.24]$ Pa.

field to $\varrho = 1$ (a classical critical field value, corresponding to Fréedericksz transitions) results in behaviour similar to the cases of $\varrho = 0$ and $\varrho = 0.5$, but above the critical field, we begin to see director distortion, leading to flow, and giving rise to various solution states.

In Figure 3.10, we present the director angle and flow velocity for an orienting field $\varrho = 1.5$, and for $\xi = [-0.03, -0.24, 0, 0.3]$ Pa. For extensile nematics ($\xi = 0.3$ Pa), the

system remains in a uniform state, like the case when $\varrho < 1$, as depicted in Figures 3.10(a) and 3.10(e). Decreasing the activity to $\xi = 0$, the director becomes distorted, leading to flow because the field orienting exceeds the critical value, as shown in Figures 3.10(b) and 3.10(f). This occurs because the director tends to align with the field direction for field strengths greater than the critical field and activity strength zero. For $\xi = -0.03$ Pa (Figures 3.10(c) and 3.10(g)), we observe increased director distortion and enhanced flow, resulting in a symmetric director angle profile and an antisymmetric velocity profile. For activity strength above the critical value ($\xi = -0.24$ Pa), these profiles reverse, leading to antisymmetric director angle and symmetric velocity profiles, as shown in Figures 3.10(d) and 3.10(h).

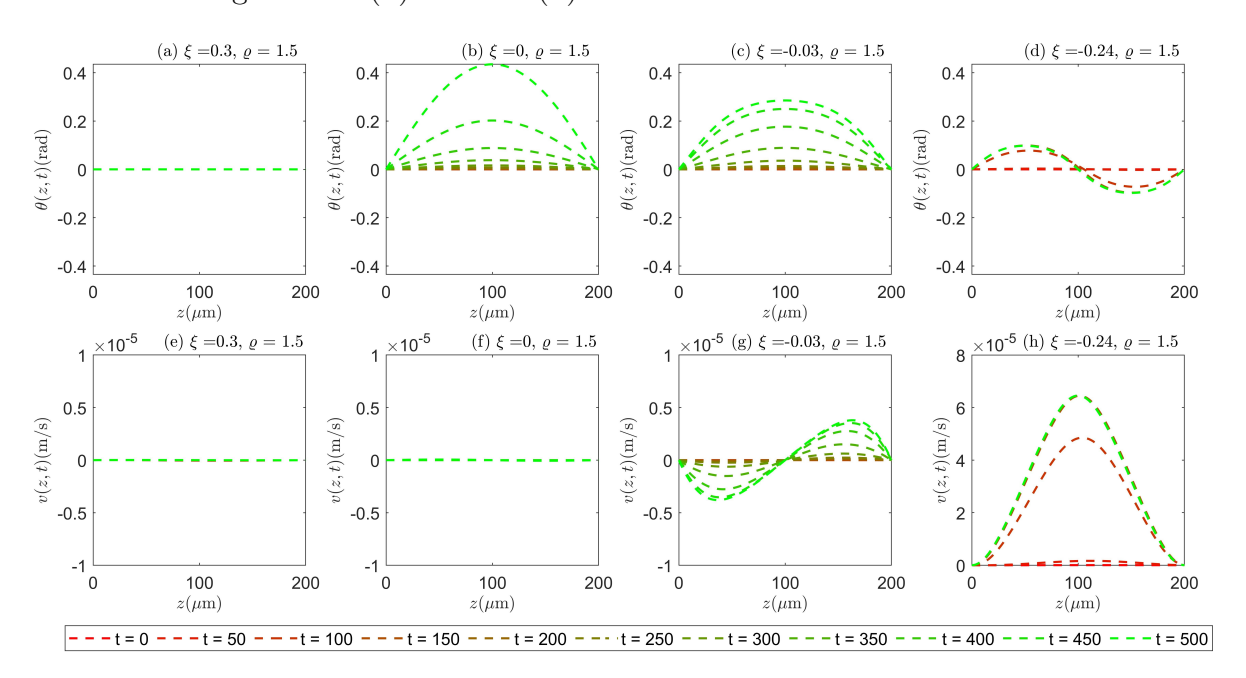


Figure 3.10: Director angle and flow velocity plots for an orienting field, $\varrho = 1.5$, and for $\xi = 0.3$ Pa, $\xi = 0$ Pa, $\xi = -0.03$ Pa and $\xi = -0.24$ Pa.

We further increased the orienting field to $\varrho = 2$ and plot the director angle and flow velocity for the same activity values, as shown in Figure 3.11. For $\xi = 0.3$ Pa, the director becomes distorted and reorients to align $\theta = \pi/2$, leading to flow generation (Figure 3.11(a) and 3.11(e)). In this case, the field is strong enough to align the director at $\theta = \pi/2$ rad, which shows the field effect overrides the activity effect. Decreasing the activity to $\xi = 0$, the director still wants to align in the field direction but with a different structure and low flow (Figures 3.11(b) and 3.11(f)). For $\xi = -0.03$ Pa, the

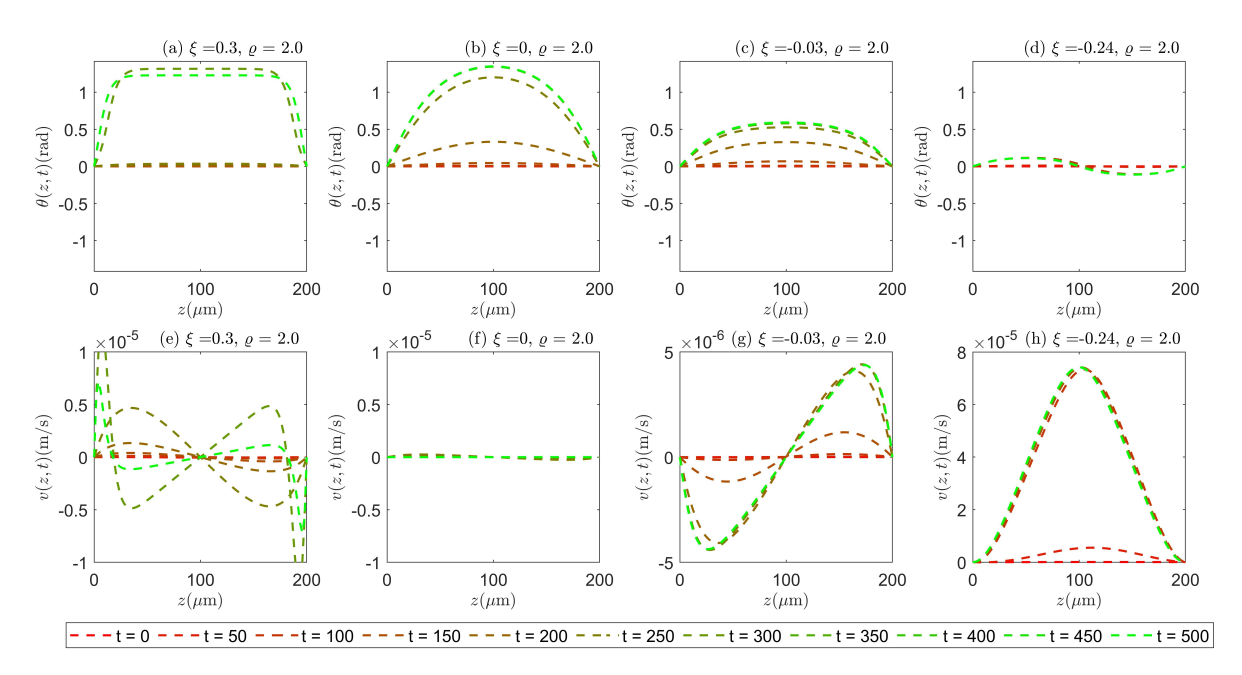


Figure 3.11: Director angle plot and flow velocity plots for an orienting field, $\varrho=2$, and for $\xi=0.3$ Pa, $\xi=0$ Pa, $\xi=-0.03$ Pa and $\xi=-0.24$ Pa.

activity suppresses the field effect, reducing the director angle, leading to the emergence of an antisymmetric velocity profile (Figures 3.11(c) and 3.11(g)). This indicates a competition between activity and the orienting field effects. For $\xi = -0.24$ Pa, the director angle and flow velocity exhibit a similar structure to the case where $\varrho = 1.5$, as shown in Figures 3.11(d) and 3.11(h)).

Finally, we further increased the orienting field to $\varrho=2.5$ and plot the director angle and flow velocity in Figure 3.12. We focus on Figures 3.12(c) and 3.12(g) since the solution profiles for the other values of ξ have already been observed in previous cases. A different behaviour emerges for $\xi=-0.03$ Pa, where the director increases above $\pi/2$ and tends align at $\theta\approx0.8\pi$ rad, as shown in Figures 3.12(c) and 3.12(g). This can cause a significant optical effect, and so may be useful for a sensor. This leads to distinct director angles and flow velocity profiles, highlighting a new regime. In contrast to the works of Voituriez et al. [236] and Edwards and Yeomans [45], who considered how activity alone can destabilize the uniform state and lead to spontaneous flows, our study demonstrates that the solution states are further tuned by the strength of an external orienting field in addition to the activity strength.

As observed in Figures 3.9–3.12, the system exhibits a range of behaviours depending on the orienting field and activity strength. For weaker fields ($\varrho \leq 1$), the director largely remains in the undistorted or slightly distorted states, while increasing activity leads to symmetric or antisymmetric distortions. As the field is strengthened beyond the critical value, a crossover emerges: the director and flow profiles transition between different solution states, sometimes reversing the symmetry of the director angle and flow velocity. This crossover behaviour is already hinted at in Figures 3.10 and 3.11, where small changes in activity induce significant shifts in the flow and director profiles. We note that these observations foreshadow the more precise characterisation of critical activities and behavioural reversals that will be discussed later in this chapter (Figures 3.17–3.19), where we systematically determine the critical activities ξ_{c1} , ξ_{c2} , ξ_{c3} , and ξ_{c4} and show how transitions between symmetric and antisymmetric states occur as a function of activity and orienting field. This approach allows us to understand not only the qualitative crossover, but also the quantitative thresholds at which the system behaviour changes.

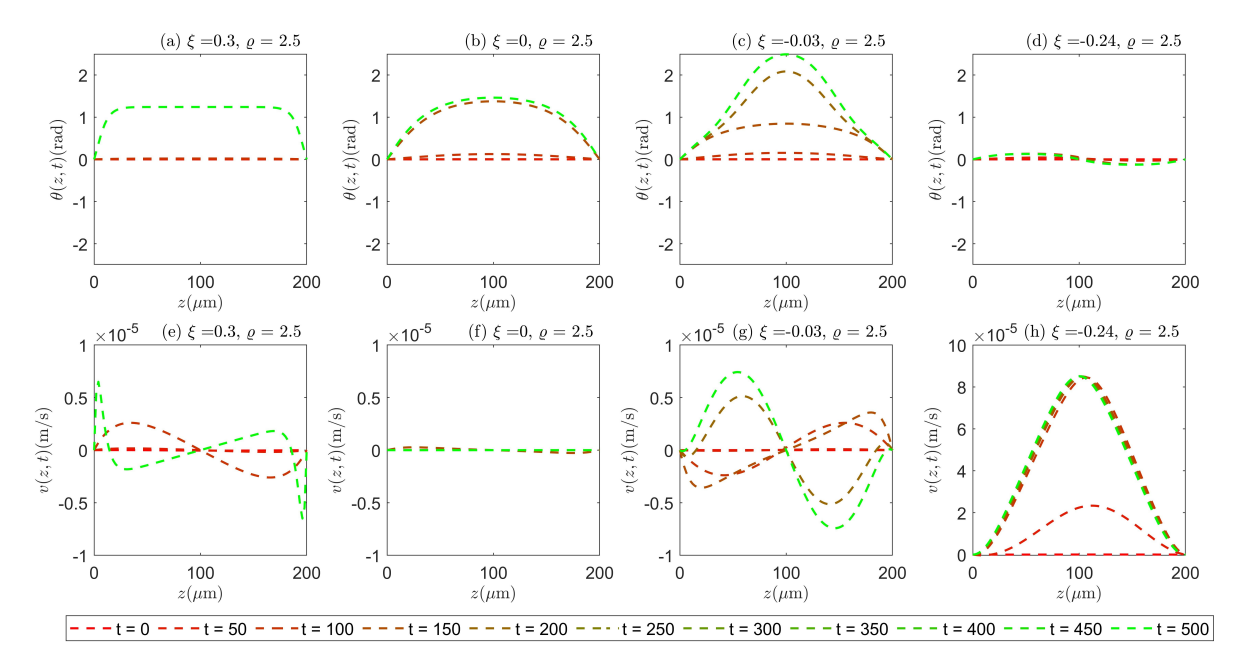


Figure 3.12: Director angle and flow velocity plots for an orienting field, $\varrho=2.5$, and for $\xi=0.3$ Pa, $\xi=0$ Pa, $\xi=-0.03$ Pa and $\xi=-0.24$ Pa.

In the following section, we will summarise these results by analysing the director angle solution at the middle, quarter, and three-quarter positions of the channel to identify different types of director distortions. These measures allow us to systematically determine how different critical activities emerge as the orienting field increases.

3.4.2.1 Summary of transitions in the director distortion solutions

We summarise the effects of the orienting field and activity on the director, by plotting the late-time director angle value at the middle, quarter and third quarter of the channel, denoted as $\theta(d/2)$, $\theta(d/4)$ and $\theta(3d/4)$ for varying activity parameter values, ξ , and fixed values of the orienting field, ϱ . In this way, we can understand the various transition states of the system as activity varies. We compute these measures for various activity values and $\varrho = [0, 0.5, 1, 1.025, 1.5, 2, 2.5]$.

In Figures 3.13–3.22, we define four critical activity thresholds, ξ_{c1} – ξ_{c4} , which mark transitions between qualitatively different solution states of the director. These are identified numerically using the classification tests based on the integrals of θ and $|\theta|$. We define ξ_{c1} as the critical activity threshold corresponding to the onset of director distortion, $|\theta(d/4) - \theta(3d/4)| > \epsilon$, with $\varepsilon = 10^{-6}$. This ensures that there is no net tilt and no residual local distortion. The threshold ξ_{c2} , marks the onset of any distortion and is defined by the condition $(1/d) \int_0^d |\theta(z)| dz > \varepsilon$. We define ξ_{c3} and ξ_{c4} as transitions between symmetric states. Within the distorted (even-symmetric) branch, further thresholds are identified by comparing $\theta(d/2)$ when activity is decreasing or decreasing. Specifically, ξ_{c3} is defined as the critical activity reached when decreasing ξ , at which the director angle satisfies $\theta(d/2) > \pi/2$, whereas ξ_{c4} is defined as the critical activity reached when increasing ξ , at which the director angle satisfies $\theta(d/2) < \pi/2$.

The director angles are computed for 101 discrete activity values in the range $\xi \in [-0.3, 0.6]$ Pa. In Figures 3.13–3.16, the horizontal axis is restricted to $\xi \in [-0.3, 0.3]$ Pa for clarity, giving a spacing of $\Delta \xi = 0.006$ Pa and a numerical uncertainty of approximately $\pm \Delta \xi/2 = \pm 0.003$ Pa. For Figures 3.18–3.19, the full range $\xi \in [-0.6, 3.5]$ Pa is used, giving $\Delta \xi = 0.041$ Pa and a numerical uncertainty of approximately $\pm \Delta \xi/2 = \pm 0.0205$ Pa.

Along with these measures, we also include inset plots of the director angle as a function of z to illustrate the profiles of the undistorted uniform state, as well as the symmetric and antisymmetric states. We denote these states as $\theta \equiv 0$ for the uniform state, θ_{even} for the symmetric state, and θ_{odd} for the antisymmetric state.

We first examine the classical case where $\varrho = 0$ and plot the measures $\theta(d/2)$, $\theta(d/4)$ and $\theta(3d/4)$ as a function of activity, as shown in Figure 3.13. The director remains undistorted for $\xi_{c1} \leq \xi$, where $\xi_{c1} = \xi_c \approx -0.13$ Pa, corresponding to the undistorted uniform state ($\theta \equiv 0$) as illustrated by the inset plot on the right of the Figure 3.13. As the activity decreases, in the range $\xi \leq \xi_{c1}$, a transition occurs, leading to an antisymmetric state, as depicted in the inset plot on the left of Figure 3.13. This demonstrates that activity drives a transition from the undistorted uniform state to the antisymmetric state.

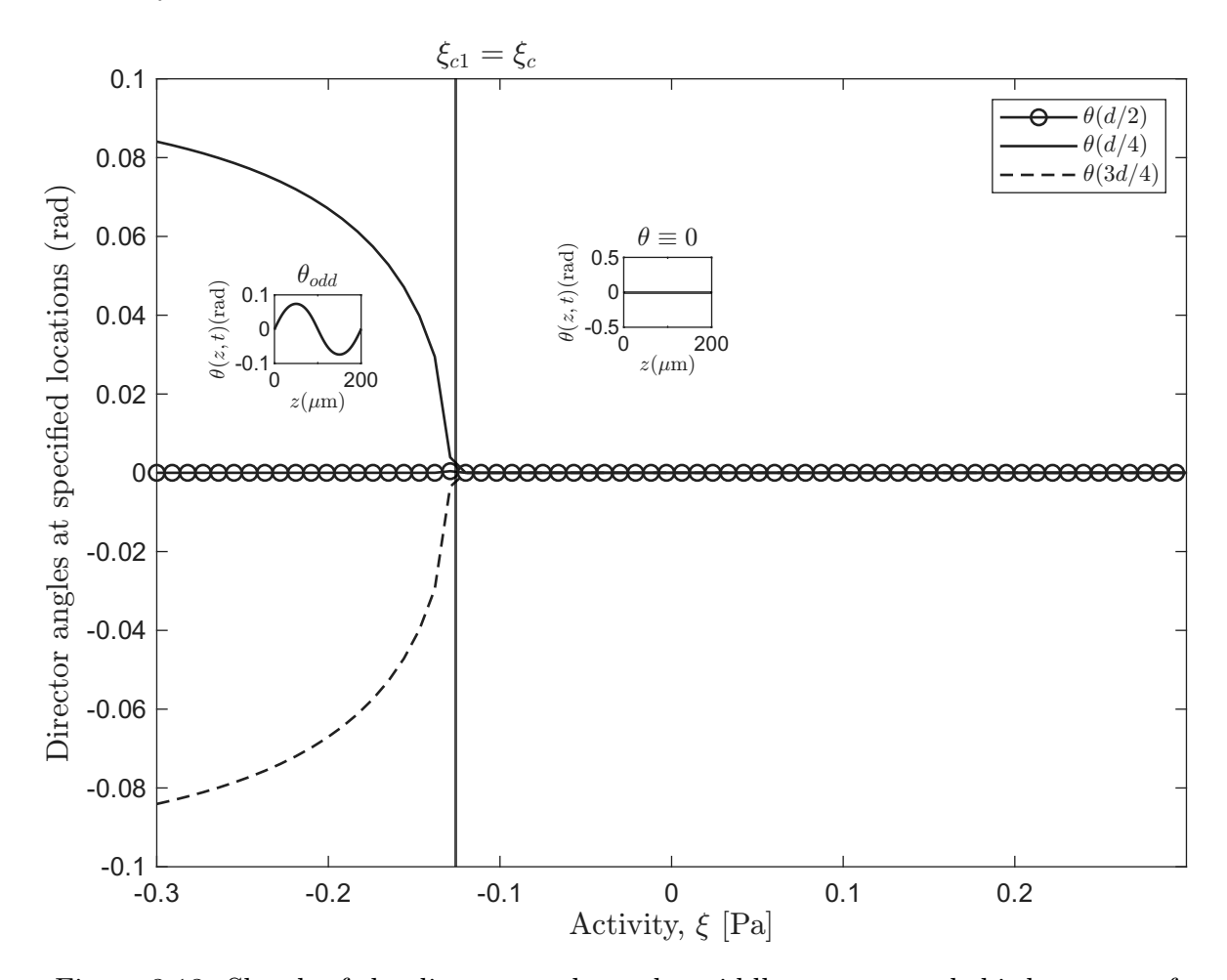


Figure 3.13: Sketch of the director angle at the middle, quarter and third quarter of the channel for $\varrho = 0$, with $\xi_{c1} = \xi_c - 0.13$ Pa.

We now examine the effect of orienting fields on these transitions, starting from weak field values and increasing beyond the critical field value. Figure 3.14 presents the director angle at the middle, quarter, and third-quarter positions of the channel for $\varrho = 0.5$. On the right side of Figure 3.14, we observe an undistorted uniform state $(\theta \equiv 0)$ for $\xi_{c2} \leq \xi$, where $\xi_{c2} \approx -0.102$ Pa marks a new critical activity value at which a transition occurs. We classify this transition to a symmetric state (θ_{even1}) , as illustrated by the inset plot in the region between ξ_{c1} and ξ_{c2} , indicated by the red dashed arrowhead line. Additionally, the critical activity value associated with the change to an antisymmetric distortion shifts to $\xi_{c1} = -0.138$ Pa, indicating that the critical activity value changes as the orienting field increases.

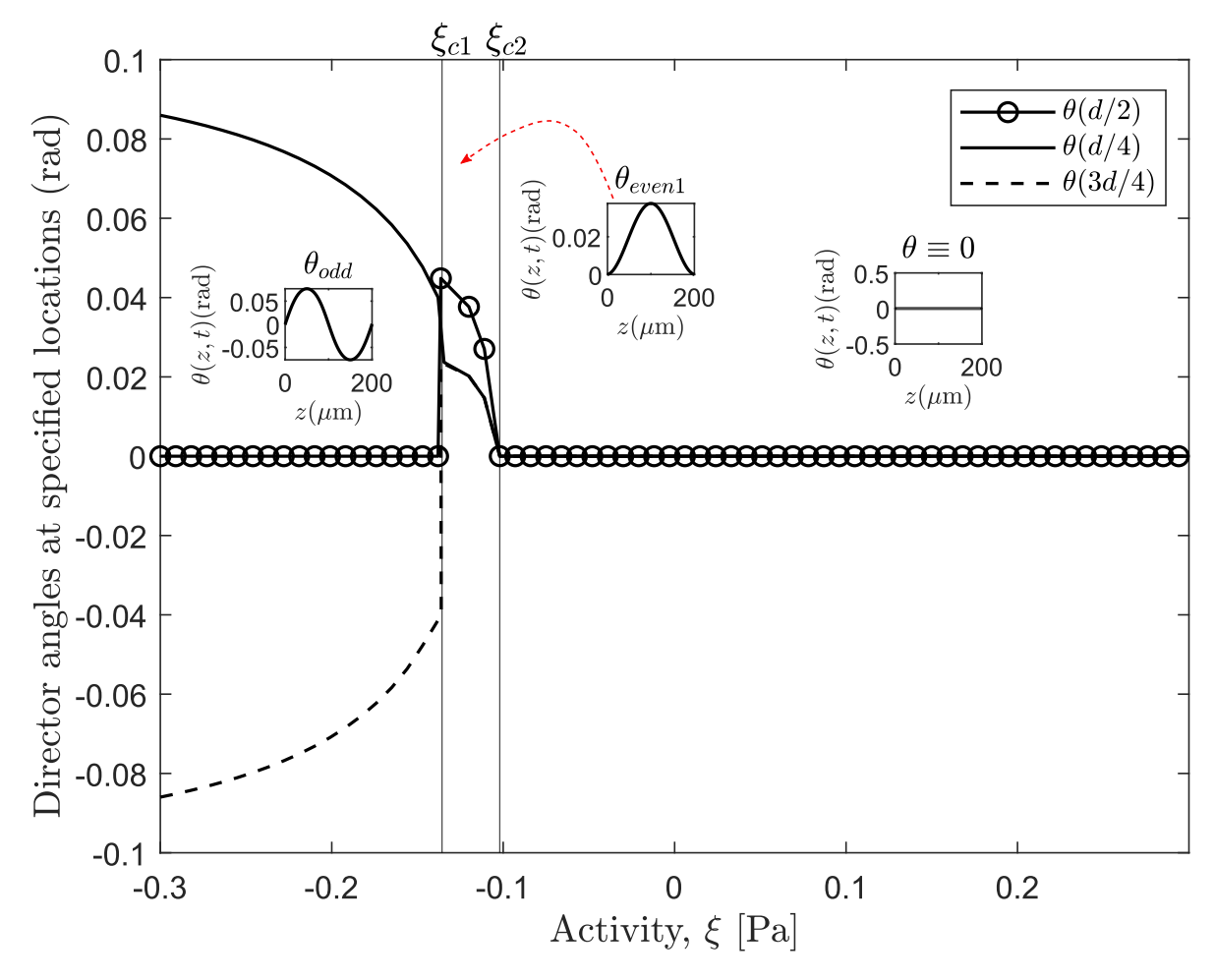


Figure 3.14: Sketch of the director angle at the middle, quarter and third quarter of the channel for $\varrho = 0.5$, with $\xi_{c1} = -0.138$ Pa and $\xi_{c2} = -0.102$ Pa. The red dashed arrowhead line indicates the region where the symmetric state (θ_{even1}) occurs.

We increase the orienting field to $\varrho = 1$, the critical field value where the classical

Fréedericksz transition occurs, and plot the measures $\theta(d/2)$, $\theta(d/4)$ and $\theta(3d/4)$ as a function of ξ , as shown in Figure 3.15. The undistorted uniform state ($\theta \equiv 0$) now occurs for $\xi_{c2} \leq \xi$, where ξ_{c2} reduces to approximately 0 (see the inset plot in the right side of 3.15). The symmetric state (θ_{even1}) now falls in the range $\xi_{c1} \leq \xi \leq 0$, where ξ_{c2} has shifted to -0.003 Pa, indicating that the orienting field effect dominates the activity effect. We choose $\varrho = 1.025$ and plot Figure 3.16 just to show how a new solution evolves.

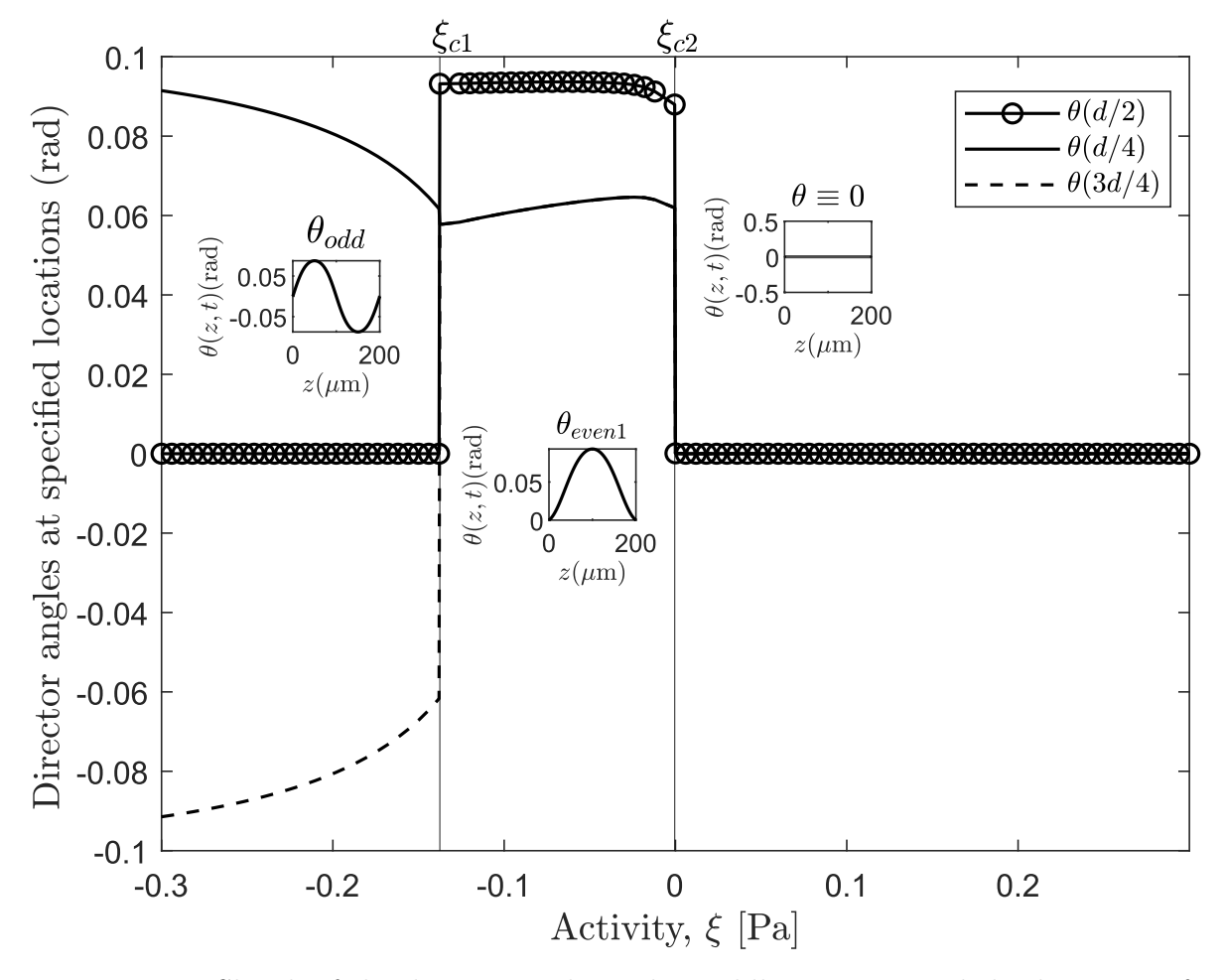


Figure 3.15: Sketch of the director angle at the middle, quarter, and third quarter of the channel for $\varrho = 1$, with $\xi_{c1} = -0.138$ Pa and $\xi_{c2} = -0.003$ Pa.

Increasing the orienting field to $\varrho = 1.5$ leads to the emergence of a new distorted symmetric solution, denoted by θ_{even2} , as shown in the inset of Figure 3.17 for the range $\xi_{c2} \leq \xi \leq -0.0001$. This results in two different director profile: one where the director tends to align approximately at $\pi/2$ rad, and other where the director aligns below $\pi/2$ rad. The appearance of this new director structure can be attributed to the stronger

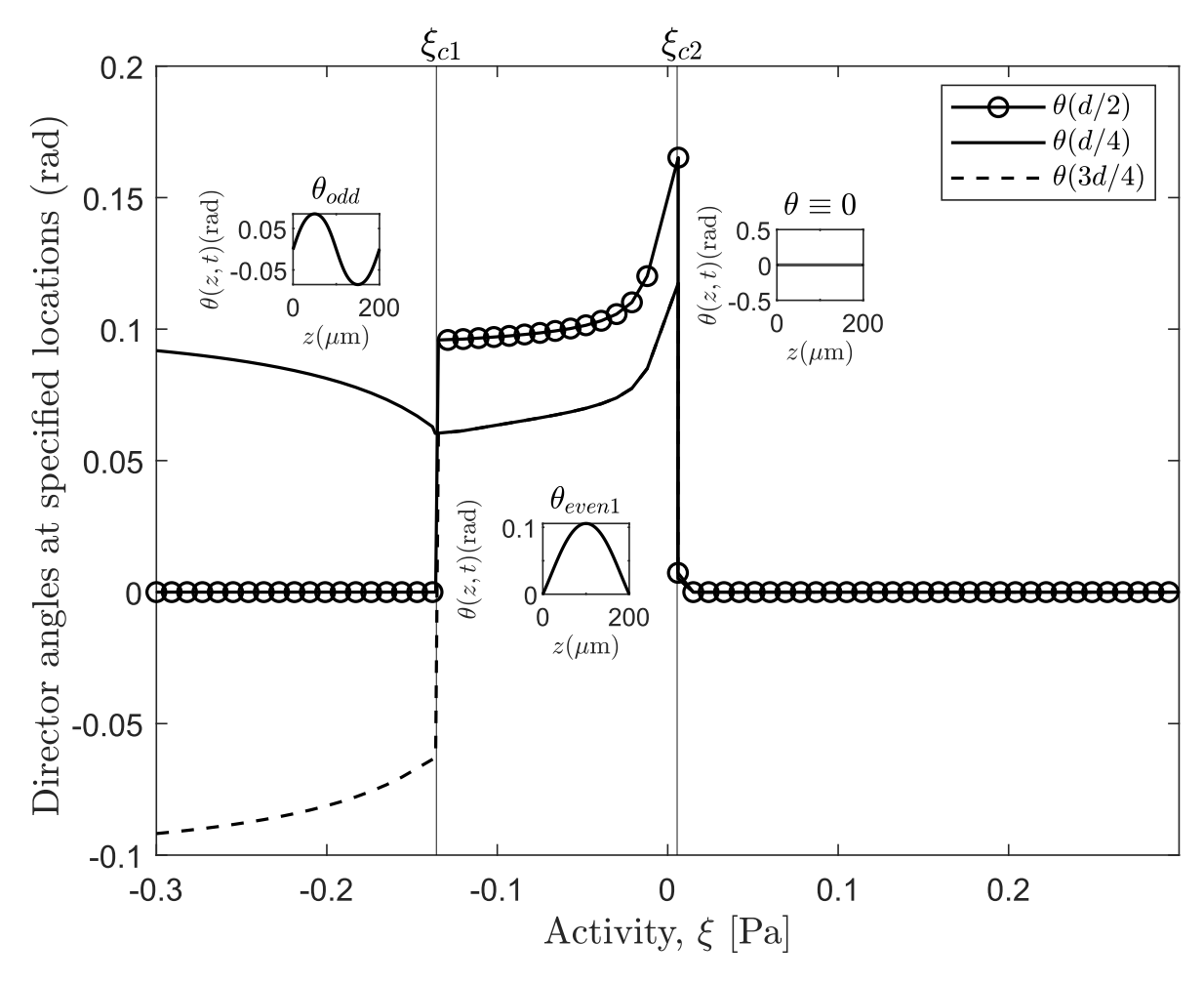


Figure 3.16: Sketch of the director angle at the middle, quarter, and third quarter of the channel for $\varrho = 1.025$, with $\xi_{c1} = -0.138$ Pa and $\xi_{c2} = 0.006$ Pa.

orienting field, which enhances the coupling between the elastic distortions and activity.

Further increasing the ϱ from 1.5 to 2.0, we observe the range of activity for this new state growing, as shown in Figure 3.18. This change in the critical activity value suggests that stronger activity is required to counterbalance the increasing effect of the orienting field.

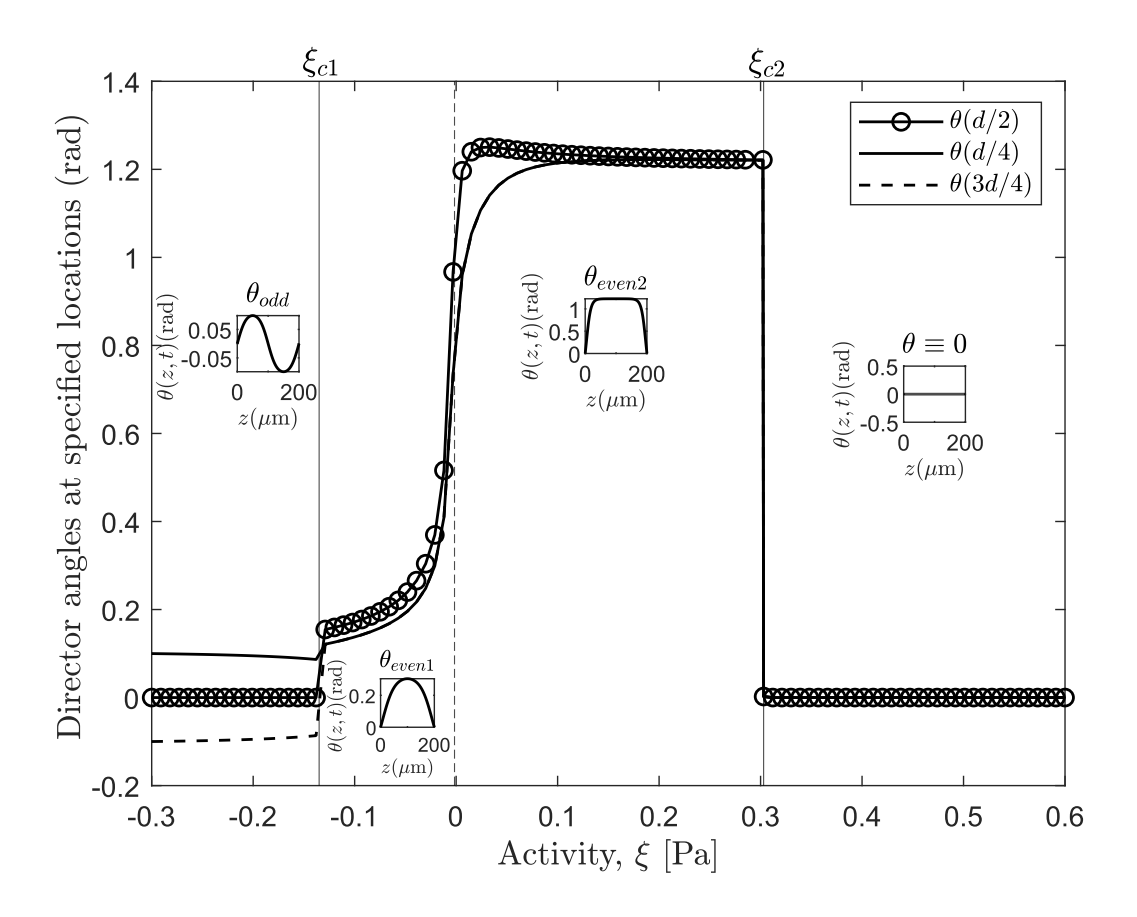


Figure 3.17: Sketch of the director angle at the middle, quarter, and third quarter of the channel for $\varrho = 1.5$, with $\xi_{c1} = -0.138$ Pa and $\xi_{c2} = 0.31$ Pa. The vertical dashed line separates the two types of director profiles, distinguishing those that tend to align near $\pi/2$ rad from those that align below it.

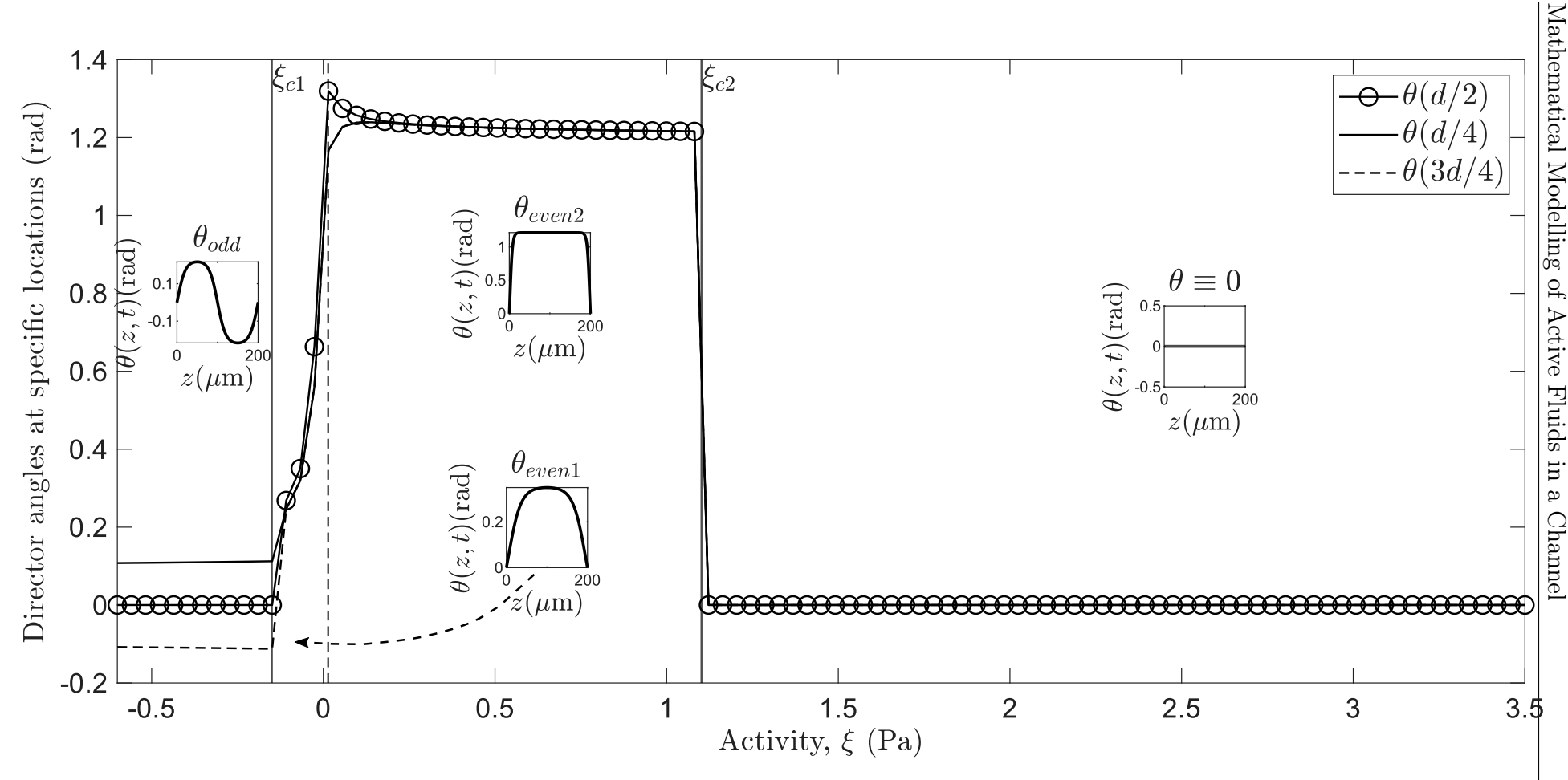


Figure 3.18: Sketch of the director angle at the middle, quarter, and third quarter of the channel, for $\varrho = 2.0$. The region between $\xi_{c1} = -0.15$ Pa and $\xi = 0.015$ Pa corresponds to the first symmetric solution, denoted as θ_{even1} , as indicated by the black dashed arrowhead line. Here, ξ_{c1} shifted to $\xi_{c2} = 1.1$ Pa. The dashed vertical line separates the two types of director profiles, distinguishing those that tend to align near $\pi/2$ rad from those that align below it.

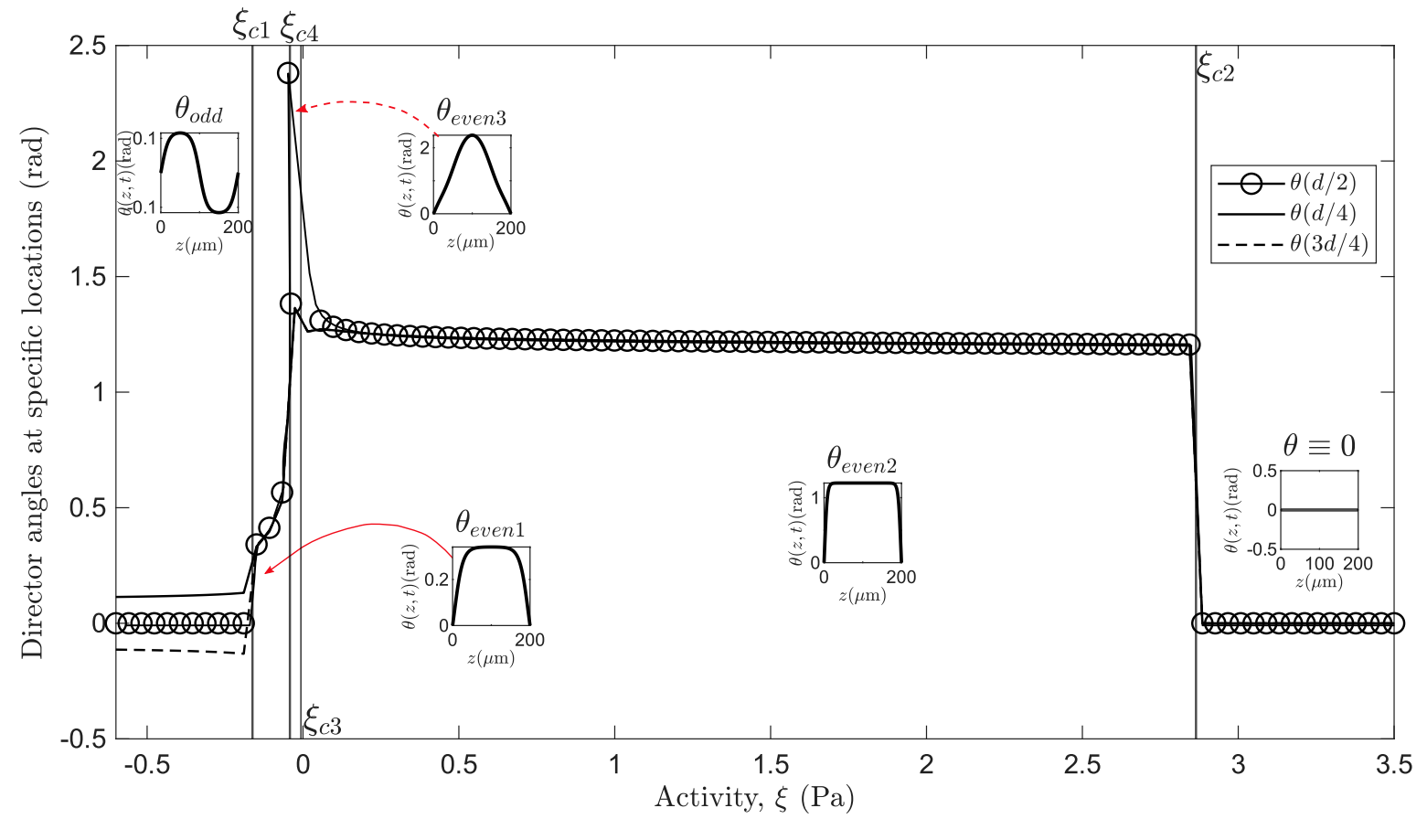


Figure 3.19: Sketch of the director angle at the middle, quarter, and third quarter of the channel, for $\varrho = 2.5$. The region between $\xi_{c1} = 0 - .15$ Pa and $\xi_{c4} = -0.04$ Pa corresponds to the first symmetric solution, denoted as θ_{even1} , as indicated by the solid red arrowhead line. The region between $\xi_{c3} = -0.006$ Pa and ξ_{c4} corresponds to the new symmetric solution, denoted as θ_{even3} , as indicated by the red dashed arrow-headed line. Here, the critical activity ξ_{c2} now becomes 2.84 Pa.

Finally, we increased ϱ to 2.5 and observed the emergence of two new symmetric states, marked by ξ_{c3} and ξ_{c4} , as shown in Figure 3.19. At the critical activity $\xi_{c3} = -0.006$ Pa, reached by decreasing ξ , the director angle rises above $\pi/2$ rad and tends towards $\theta \approx 0.8\pi$ rad, as illustrated in the inset plot labelled θ_{even3} . In contrast, $\xi_{c4} = -0.04$ Pa marks the transition obtained by increasing the magnitude of activity, where the director angle falls below $\pi/2$ rad and approaches $\theta \approx 0.5\pi$, as shown in the inset plot labelled θ_{even1} . This behaviour is similar to what we previously observed in Figure 3.12(b) for $\varrho = 2.5$ and $\xi \approx -0.03$ Pa, and is characterised by complex flow dynamics in which the director structure exhibits a "kink" profile arising from the kickback effect. This kink arises due to the kickback effect, whereby the director field cannot relax smoothly. Such overshoot phenomena are interesting for sensing applications, as even small changes can lead to significant distortions and flow in the system.

In conclusion, our results indicate that the system exhibits one of three solution states: symmetric, antisymmetric, and uniform states, with several subclassifications of symmetric solutions. The uniform state corresponds to a uniform alignment of the director parallel to the boundaries of the channel. For field strengths greater than a critical value, the uniform state is replaced by the symmetric director distortion solution. This is essentially the Fréedericksz transition, where the trivial solution is unstable above a critical field strength. However, the value of the critical field changes as we increase the magnitude of the activity. For contractile systems, the orienting field is below the classical field strength, and for extensile systems, the orienting field is above the classical field strength.

For antisymmetric solutions, there is a reorientation in the middle of the layer for high elastic energy. For low activity parameter values, the orienting field dictates the behaviour, and the director angle in the middle of the layer prefers to align along the field direction. However, increasing the activity increases flow, which tends to align the directors to the $\pm \theta_L$, flow alignment angles also referred to as Leslie angles, hence reducing the director angle in the center and overriding the field effect, giving rise to the antisymmetric solution.

We can summarise the behaviour of the system with a sketch of the boundaries between the various late-time solutions in the ϱ - ξ parameter space. We use a 201×201 grid in both the orienting field, ϱ , and activity, ξ , with $\varrho \in [0,3]$ and $\xi \in [-0.3,0.3]$ Pa. Figure 3.20 displays this information with a sketch of the critical activities, showing the regions where the various solutions exist. We see uniform solutions for $\xi > \xi_{c2}$ (displayed in the region above the solid red line). As the orienting field exceeds a critical value, three different symmetric director distortion solutions emerge: going down Figure 3.20, we get a distorted symmetric solution for $\xi_{c2} < \xi < \xi_{c3}$, where the solid cyan line marks a critical activity value (ξ_{c3}) for which another state emerges. In this solution regime, the director angle tends to align approximately at $\pi/2$ rad. For $\xi_{c3} < \xi < \xi_{c4}$, a new symmetric solution corresponds to a situation where the director tends to align at an angle above $\pi/2$ rad (see the region between solid blue and green lines), where the solid green marks new critical activity (ξ_{c4}) . For $\xi_{c4} < \xi < \xi_{c1}$, we get another symmetric distorted state, which corresponds to a case where the director wants to align at an angle below $\pi/2$ rad. Lastly, for $\xi < \xi_{c1}$, where the solid purple line marks a critical activity (ξ_{c1}) , there is a transition from a symmetric to an antisymmetric state. Below the critical activity ξ_{c1} , activity overrides the field effect, resulting in an antisymmetric solution, as shown by the inset plot labelled θ_{odd} .

Our results show that the critical field strength depends strongly on the activity type. For contractile systems, the critical field lies below the classical Freedericksz threshold, whereas for extensile systems, it lies above this value. This indicates that contractile activity facilitates director alignment, while extensile activity resists alignment. From the perspective of applications such as sensors, this distinction is significant. Contractile systems reach alignment under weaker external fields, making them more responsive and energy-efficient in detecting small perturbations. Extensile systems, on the other hand, require stronger applied fields and therefore exhibit lower sensitivity. Consequently, contractile active nematics offer a clear advantage for sensing applications, as they

enhance sensitivity and reduce the energy cost of operation.

Essentially, for $\xi=0$, a classical field strength occurs at $\varrho=1$, corresponding to the Fréedericksz transition. Interestingly, for extensile systems, the transition from a uniform state to a symmetric state occurs above the critical field strength. For the contractile system, the transition occurs below the critical field strength. This asymmetry implies that negative activity facilitates reaching the reorientation threshold at a smaller field due to contractile effects enhancing alignment more efficiently than extensile effects. At higher-magnitude of negative activities, there is no critical activity because the activity effect dominates the field effect, resulting in an antisymmetric solution.

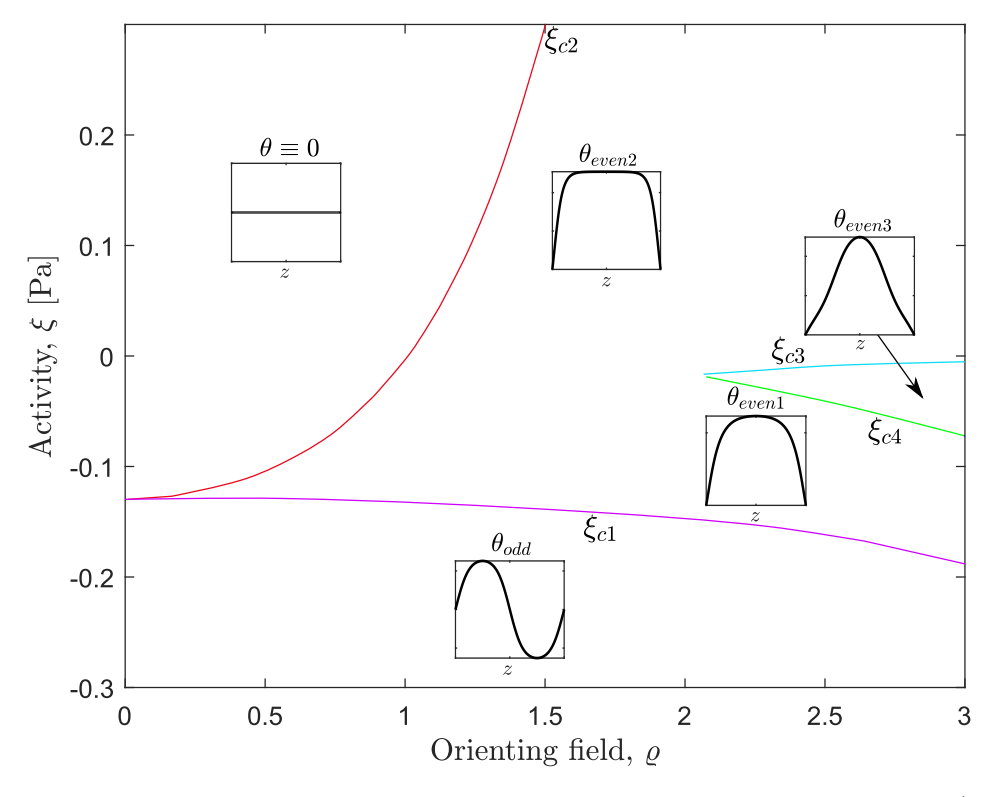


Figure 3.20: The boundaries between the various late-time solutions in (ϱ, ξ) parameter space, where, ξ_{c1} to ξ_{c4} are the different critical activities. The various lines represent the boundaries where transitions between different states occur. The black arrow-headed line points to the region where the symmetric state (θ_{even3}) occurs.

It is useful to investigate the effects that changes in the orienting field and activity have on the system. To achieve this, we consider a measure of how activity induces changes in the system, specifically the total active dissipation in terms of the director and the strain rate tensor, given by

$$D_a = \int_0^d |\xi n_i A_{ij} n_j| d\mathbf{z} = \int_0^d |\xi \sin \theta \cos \theta| d\mathbf{z}.$$
 (3.90)

Note that active dissipation can be positive or negative, so we integrate the modulus to avoid $D_a = 0$ for the odd solutions, and the total nematic elastic energy denoted by ω_d and defined by

$$\omega_d = \int_0^d w_F dz. \tag{3.91}$$

We present the total active dissipation and the total elastic energy in the contour plots of Figure 3.21 and 3.22, respectively. For these figures, the data are computed on a 201×201 grid in both the orienting field ϱ and activity ξ directions. This corresponds to step sizes $\Delta \varrho = 0.015$, $\Delta \xi = 0.003$, with $\varrho \in [0,3]$ and $\xi \in [-0.3,0.3]$ Pa, ensuring high resolution in capturing the variations of total active dissipation and elastic energy across the parameter space.

These figures clearly mimic the behaviour observed in Figure 3.20. High values of ϱ , result in high total elastic energy, and when both ϱ and ξ are large, the total active dissipation increases significantly. The total active dissipation is low whenever $\xi < 0$. However, as $\xi \ll 0$, the total active dissipation starts to grow while the total elastic energy remains small. This is because, in the antisymmetric state, the director angle stabilises at $\pm \theta_L$, where θ_L is small.

3.4.3 Prediction of critical activity, ξ_{c2}

We now determine the critical activity at which the solution transitions from a homogeneous to a nonhomogeneous state, denoted by ξ_{c2} . According to equation (3.59), the most unstable solutions occur when $\tau \ll 0$, while for $\tau > 0$, the solutions become stable. However, in the limit $\tau \to \infty$, the solution becomes independent of time t, which indicates a transition from an undistorted director solution to a distorted director

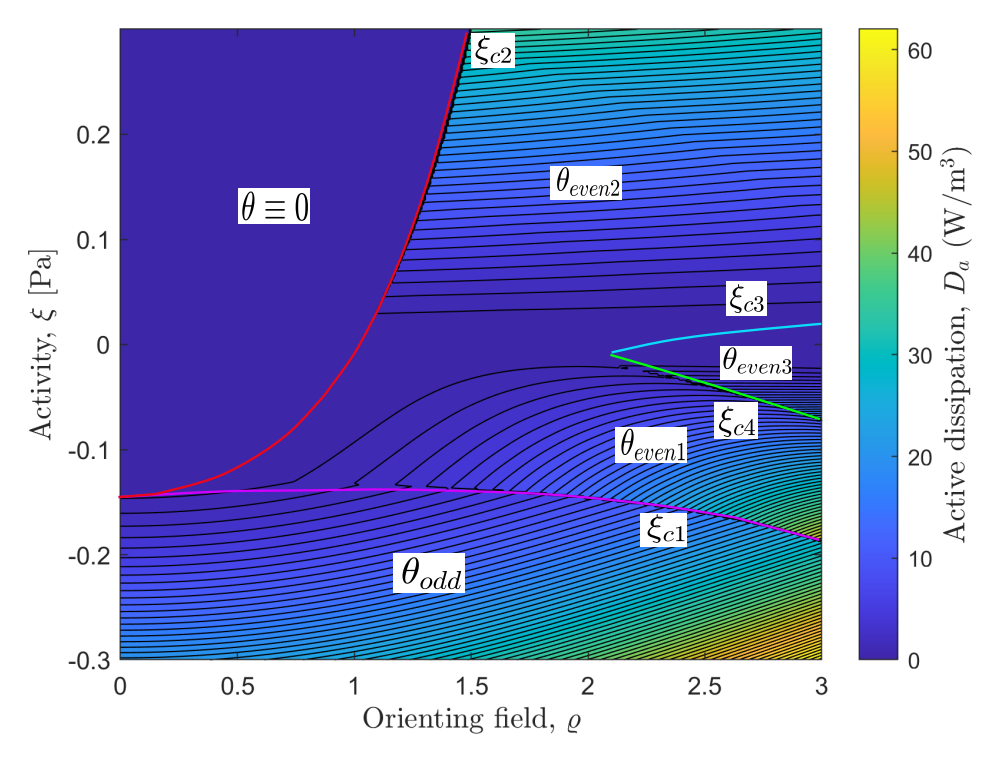


Figure 3.21: Contour plot of total active dissipation, D_a against the orienting field and activity. In the region ξ_{c2} and ξ_{c3} , the system exhibits a symmetric solution (θ_{even2}) , between ξ_{c3} and ξ_{c4} , a different symmetric solution (θ_{even3}) , and in the region ξ_{c4} to ξ_{c1} , another symmetric solution (θ_{even1}) and antisymmetric solution (θ_{odd}) for activities below ξ_{c1} . These are the solutions shown in Figure 3.20.

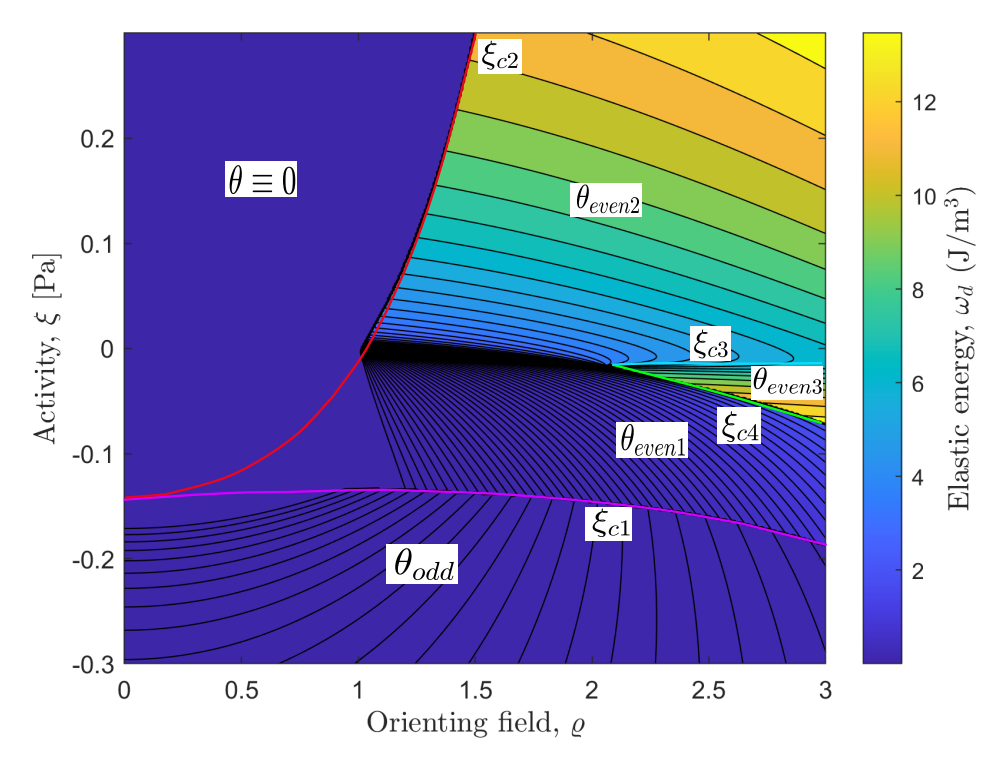


Figure 3.22: Contour plot of total nematic elastic energy, ω_d against the orienting field and activity. The dark region appears due to the high density of contour lines. In the region ξ_{c2} and ξ_{c3} , the system exhibits a symmetric solution (θ_{even2}) , between ξ_{c3} and ξ_{c4} , a different symmetric solution (θ_{even3}) , and in the region ξ_{c4} to ξ_{c1} , another symmetric solution (θ_{even1}) and antisymmetric solution (θ_{odd}) for activities below ξ_{c1} .

solution.

To identify this transition point, we use equations (3.62) and (3.63). From equation (3.62), we see that $\tau \to \infty$ precisely when the denominator vanishes. This gives

$$\frac{4K_1q^2}{d^2} - \frac{\alpha_3\xi}{\eta_1} - \chi_a H^2 = 0. {(3.92)}$$

Next, substituting this condition into equation (3.63), and taking the limit $\tau \to \infty$, the equation can remain finite only if the coefficient of τ vanishes. This leads to the second condition

$$\frac{\alpha_3 \xi}{\eta_1} \tan q + \chi_a H^2 q = 0. \tag{3.93}$$

Equations (3.92) and (3.93) therefore provide two simultaneous relations linking ξ , q, and H. Solving these equations together, and recalling that $H = \varrho_2 H_c$ with $H_c = \varrho_2 H_c$

 $(\pi/d)\sqrt{K_1/\chi_a}$, we obtain

$$\xi_{c2} = \frac{4\eta_1 K_1 q^3 \cot q}{\alpha_3 d^2 (q \cot q - 1)},\tag{3.94}$$

$$\varrho_2 = \frac{4q^2}{\pi^2 (q \cot q - 1)}. (3.95)$$

Equations (3.94) and (3.95) are transcendental equations, and so cannot be solved analytically. To proceed, we find the approximate solution by applying the Taylor series expansion around $q \approx 0$ and $q \approx \pi$, and we obtain

$$\xi_{c2} = -\frac{12\eta_1 K_1}{\alpha_3 d^2} - \frac{6\eta_1 K_1 (-12 + \pi^2 \varrho_2^2)}{\alpha_3 d^2}, \text{ for } q \approx 0,$$

$$\xi_{c2} = \frac{4\eta_1 K_1 \pi^2}{\alpha_3 d^2} + \frac{12\eta_1 K_1 \pi \left(-\pi + \frac{\pi}{4} \left(3 + \sqrt{1 - 2\varrho_2^2}\right)\right)}{\alpha_3 d^2} + \frac{12\eta_1 K_1 \left(-\pi + \frac{\pi}{4} \left(3 + \sqrt{1 - 2\varrho_2^2}\right)\right)^2}{\alpha_3 d^2}, \text{ for } q \approx \pi,$$

$$(3.96)$$

respectively. Equations (3.96) and (3.97) approximate the critical activities when $q \approx 0$ and $q \approx \pi$, respectively, indicating a transition from a uniform state to a distorted state. For validation, we compare the analytical and numerical results, as illustrated in Figure 3.23. The two approaches show a good agreement, especially at $q \approx 0$ and $q \approx \pi$, which confirms the accuracy of the analytical forms. In addition, we include the numerical plot ξ_{c2} as a function of the orienting field, ϱ_2 . This comparison further demonstrates a strong match between the two methods, reinforcing the reliability of the analytical expressions used to describe the onset of the distortion transition.

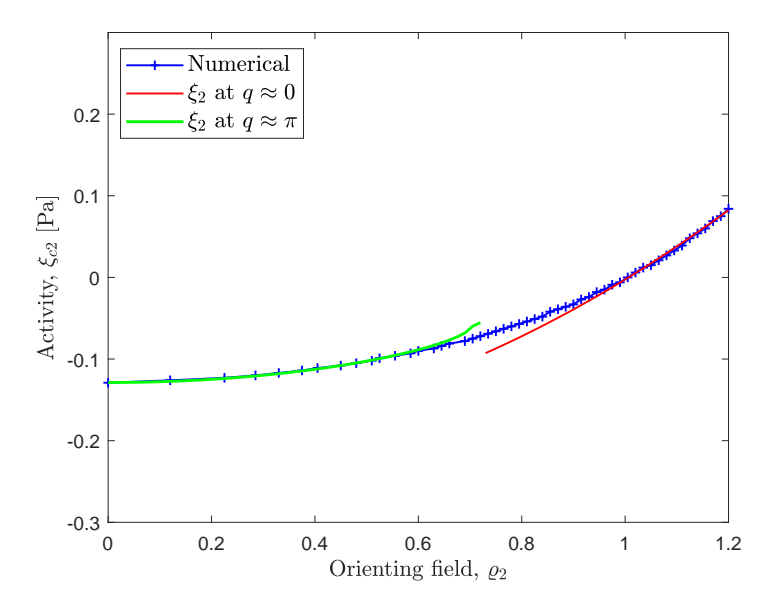


Figure 3.23: Comparison of analytical and numerical solutions for the transition from an undistorted to a distorted state. The red and green lines represent the analytical solution, while the solid blue line denotes the numerical solution.

3.5 Nonlinear analysis of activity in a hybrid aligned nematic Channel

In this section, we explore the distortion-driven active flow for a channel in which there is antagonistic anchoring, by which we mean planar anchoring on the lower substrate and homeotropic anchoring on the upper substrate—the so-called hybrid aligned nematic (HAN) system. The motivation for considering a HAN cell is that the quantity to be sensed may alter the anchoring condition at the top boundary. It is therefore instructive to examine a configuration where the two boundaries impose different anchoring types, with one planar and one homeotropic. The HAN state represents an extreme case chosen to test the largest possible effect of such boundary changes; in a more general situation, the top boundary might instead exhibit a smaller deviation from planar anchoring. We characterise the behaviour of the system for various activity parameters, and concentrate on the flow that occurs because of the antagonistic boundary conditions rather than on the aligning field, so we set $\varrho = 0$. This work will inform the study in the next chapter, where we will look at the situation where part of the channel involves

planar conditions and part involves HAN anchoring conditions.

3.5.1 Mathematical model

In a HAN geometry, the director is anchored parallel to the substrate at z = 0 and perpendicular to the substrate at z = d, as shown in Figure 3.24.

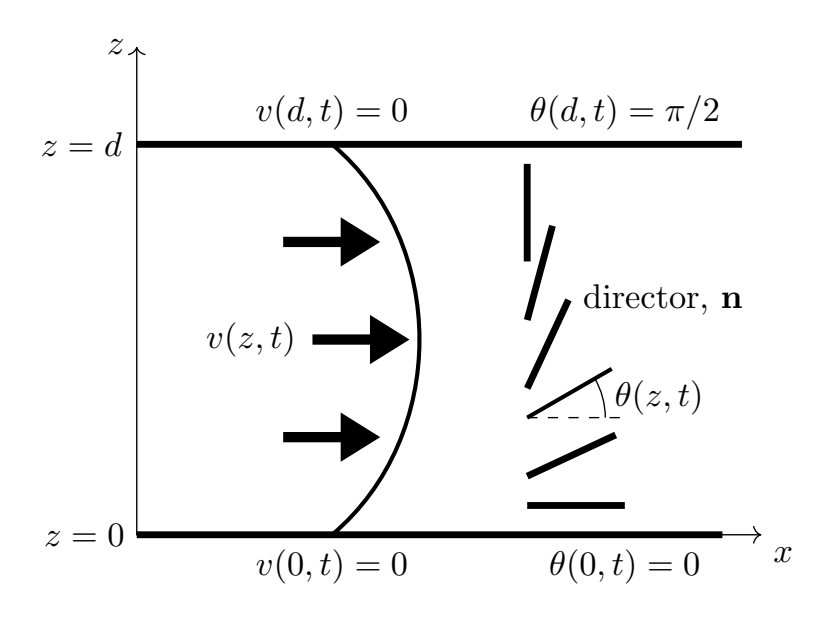


Figure 3.24: Active nematic in a channel between two solid plates at z=0 and z=d/2 with flow parallel to the x-direction. The rods show director orientation.

In the absence of an orienting field, equations (3.9) and (3.14) reduce to

$$(g(\theta)v_z + m(\theta)\theta_t + \xi \sin\theta \cos\theta)_z = 0, \quad (3.98)$$

$$\gamma_1 \theta_t - (K_1 \cos^2 \theta + K_3 \sin^2 \theta) \theta_{zz} - (K_3 - K_1) \sin \theta \cos \theta (\theta_z)^2 + m(\theta) v_z = 0, \quad (3.99)$$

and the new boundary conditions are

$$\theta(0,t) = 0, \quad \theta(d,t) = \pi/2,$$
 (3.100)

$$v(0,t) = v(d,t) = 0. (3.101)$$

Again, we use the ode15s solver in Matlab (R2022a) Version 9.13 [130] to integrate the nonlinear coupled partial differential equations in time using an appropriate initial

condition $\theta_0 = \pi z/2d$ at t = 0, which corresponds to uniform distortion between the two boundaries. The initial flow velocity condition, given by $v_0 = 0$. As before, we set d = 200 microns to ensure consistency with previous sections. We examine the effects of activity in the range $\xi \in [-2, 2]$ Pa and run our simulations for a maximum of t = 200 seconds to ensure a steady state has been reached.

3.5.2 Solution regimes for contractile and extensile active nematics

In a similar way to the previous section, Figure 3.25 illustrates the sketch of the solution profiles of the director angle and flow velocity for contractile and extensile nematics. In particular, we plot the values of the director angle in the center of the channel to examine the symmetry of the solutions. In these simulations, we vary activity incrementally and use the previously obtained solution (for a similar value of the activity) as the initial conditions. We use this continuation method as we increase the activity (blue line) and then as we decrease the activity (black line).

For positive activity values ($0 \le \xi \le 2$) Pa, we see that the director ranges from 0 to $\pi/2$ in line with the boundary conditions, but in the bulk of the cell, the director aligns at a constant angle $\theta \approx 1.24$ rad. As the magnitude of the activity reduces, moving towards the left of Figure 3.25, we see that the system goes through a transition at $\xi = 0$, and two different director solutions are possible. For negative activities ($-2 \le \xi \le 0$), the flow tends to align the director at $n\pi + \theta_L$ ($n \in \mathbb{Z}$) for positive flow gradients, where θ_L is the Leslie angle (flow alignment angle) and $n\pi - \theta_L$ ($n \in \mathbb{Z}$) for negative flow gradients (see the inset plots on the left-hand side of Figure 3.25). There are two possible solutions: one with a negative flow velocity and another with a positive flow velocity, indicating that bistability is present in this system. In one solution, the director goes from θ_L to $\pi - \theta_L$, and we see significant director distortion characterised by a large gradient in θ . However, for the other solution, the director goes from $-\theta_L$ to the positive value θ_L , and there is a small director distortion characterised by a small

gradient in θ .

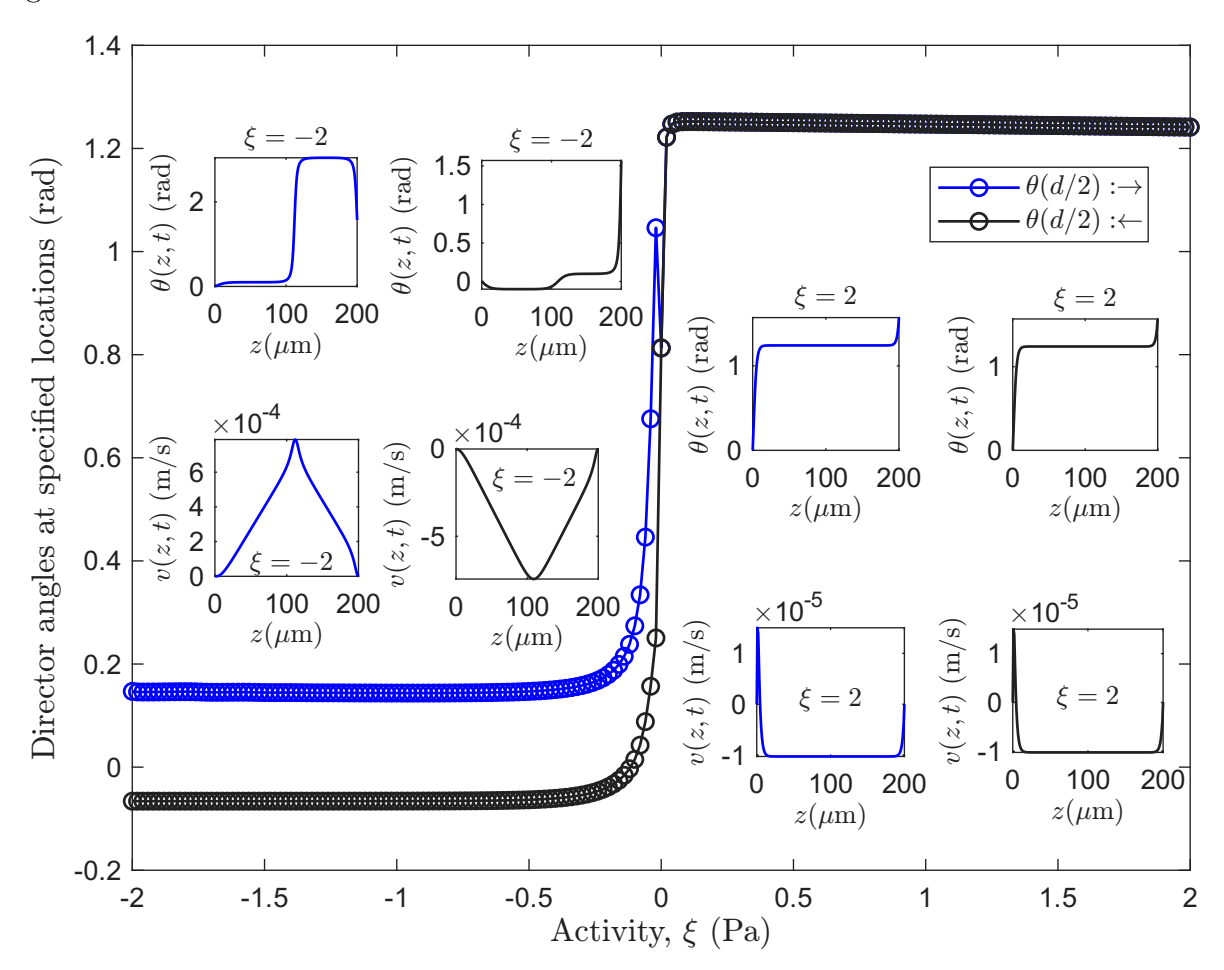


Figure 3.25: Sketch of the director angle at the middle of the channel for $-2 \le \xi \le 2$ Pa.

Our results correspond to the study by Marenduzzo et al. [127] on active nematics in a HAN geometry using lattice Boltzmann simulations of the hybrid lattice, where spontaneous flow was observed for both extensile and contractile nematics. Rorai et al. [184] also shows that active nematics in a quasi-one-dimensional channel geometry with a HAN alignment have nonzero flow velocity for relatively low activities.

To investigate the potential of active nematics for sensing applications, in Section 3.5 we explored how increasing and decreasing the activity induces a hysteresis-like behaviour (Figure 3.25). We note that a similar procedure of increasing and decreasing activity was also performed in Section 3.4 (Figures (3.13)-(3.19)). However, under the conditions considered there, bistability was not observed. In contrast, the hysteresis study in Section 3.5 is designed to understand how changes in activity interact with the

HAN anchoring to produce distortion-driven active flows, concentrating on the effect of antagonistic boundary conditions rather than the external orienting field.

3.6 Conclusions

3.6.1 Linear analysis

We investigated the effects of activity and orienting fields on active nematics with a director between two parallel plates in a 1D geometry, subject to infinite planar anchoring and non-slip conditions on the channel boundaries. In the linear analysis, we investigated three cases, including planar alignment in the absence and presence of an orienting field and homeotropic alignment in the absence of an orienting field.

We first examined the effect of activity in the absence of an orienting field for planar alignment. For extensile nematics, the director remains close to its initial configuration with minimal distortion. For contractile nematics, the director undergoes reorientation, resulting in a sustained flow.

Next, we examined the system's behaviour when an orienting field is applied. In this case, the system exhibits a critical threshold for the orienting field strength. For fields weaker than this critical value, elastic forces oppose the realignment of the director, causing it to remain in its initial configuration. However, when the field strength exceeds the critical threshold, the director realigns more closely with the direction of the applied field, which is characteristic of the Fréedericksz transition.

For homeotropic initial alignment in the absence of an orienting field and when $\xi = 0$, the system initially experiences an overshoot, aligning at $\theta > \pi/2$ rad, before relaxing to the equilibrium state, also known as the kickback effect. However, for extensile nematics, the kickback effects gradually diminish as the activity strength increases. In contrast, for contractile nematics, the kickback effect remains even as the magnitude of activity increases.

3.6.2 Nonlinear analysis

We first explored the longer-time behaviour of active systems under planar alignment.

Our findings show that the system exhibits either undistorted uniform states or symmetric and antisymmetric distorted states.

The uniform state corresponds to a uniform alignment of the director parallel to the boundaries of the channel. For field strengths greater than a critical value, the uniform state is replaced by the symmetric director distortion solution. This is essentially the Fréedericksz transition, where the trivial solution is unstable for a field greater than the critical field. However, the value of the critical field changes as we increase the magnitude of the activity. For contractile systems, the orienting field is below the classical field strength, and for extensile systems, the orienting field is above the classical field strength. For antisymmetric solutions, there is a reorientation in the middle of the layer for high elastic energy. For low activity parameter values, the orienting field dictates the behaviour, and the director angle in the middle of the layer prefers to align along the field direction. However, increasing the activity increases flow, which tends to align the directors at the Leslie angle, hence reducing the director angle in the center of the channel and overriding the field effect, which gives rise to the antisymmetric solution.

Additionally, an analysis of total active dissipation and elastic energy provides further insight into solution transitions. Higher orienting field values lead to increased elastic energy, while large activity values enhance active dissipation. Active dissipation grows for strongly negative activity, whereas elastic energy remains low. These findings contribute to a broader understanding of how external fields influence the behaviour of active systems.

We also examined active nematics in a one-dimensional HAN cell in order to inform work in the next chapter. For positive activity values, the director stabilises at approximately 1.24 rad in the bulk of the channel, but as activity decreases, a transition occurs at

zero activity, leading to two possible director solutions: one with negative flow velocity and the other with positive flow velocity.

A key finding in both the linear and nonlinear analysis is that in weakly contractile systems, the director increase above $\pi/2$ rad and tends to align to $\theta \approx 0.8\pi$ rad, resulting in complex flow, which has implications for sensor design.

Chapter 4

Activity and Geometric Effects in a Two-Dimensional Model in a Channel

4.1 Introduction

Various studies have investigated the flow patterns of active nematics in 2D regions, including rectangular domains, using planar or hybrid-aligned nematic (HAN) anchoring [63,184,211]. However, little attention has been paid to the two-dimensional analysis of systems combining planar and HAN anchoring. To address this gap, we investigate the interplay of these two anchoring conditions, which may be beneficial in the design of sensors, where small changes in alignment can lead to pronounced effects. To do so, we present a 2D theoretical and computational study that involves the mathematical modelling of active nematics in a channel, using a modified form of the Ericksen-Leslie equations for active nematics.

In this Chapter, we examine a model under two types of inlet/outlet boundary conditions: normal flow, which is a model of a single HAN region and periodic, which is a model of a periodic array of HAN regions. We explore the resulting flow regimes for both contractile and extensile nematics under both types of boundary conditions. Under normal flow and periodic conditions, we perform a spectral analysis to examine the

oscillatory behaviour for a high magnitude of activity. For extensile nematics, we also find that the system exhibits both unidirectional and bidirectional flow. We have shown that local disturbances in the director orientation influence the global flow, which may be useful for potential applications in sensor design.

Under periodic conditions, we also analyse the flow regimes for contractile and extensile active nematics by considering the effects of varying both the activity strength and the width of the HAN region. The system exhibits behaviour similar to that observed under normal flow conditions for both contractile and extensile nematics. Furthermore, we examine the effect of the splay-to-bend ratio, which plays a vital role in determining the director orientation in the HAN region, and how the flux changes from negative to positive. Our analysis shows that the ratio of splay and bend elastic constants influences the preferred director orientation and causes the flux to transition from positive to negative for lower positive activity values and all negative activities, while remaining positive for higher positive activity.

4.2 Model formulation

We present a 2D theoretical and computational model of an active nematic sandwiched in a channel, with normal flow or periodic conditions at the ends of the channel. The channel has width w and height d. We again use θ to denote the director angle, which is the angle the director makes with a fixed x-axis [202], as shown in Figure 4.1. We apply planar anchoring of the director everywhere except for the region between coordinates (-l/2, d/2) and (l/2, d/2), where we apply homeotropic anchoring. This means that $\theta = \pi/2$ for -l/2 < x < d/2, z = d/2, and $\theta = 0$ elsewhere on z = -d/2 and z = d/2. For the velocity, we impose the no-slip and no-penetration boundary conditions at $z = \pm d/2$. The flow is driven by activity, and we do not apply a pressure gradient to drive the flow. That is, the flow and any pressure variations result from internal activity or director distortion.

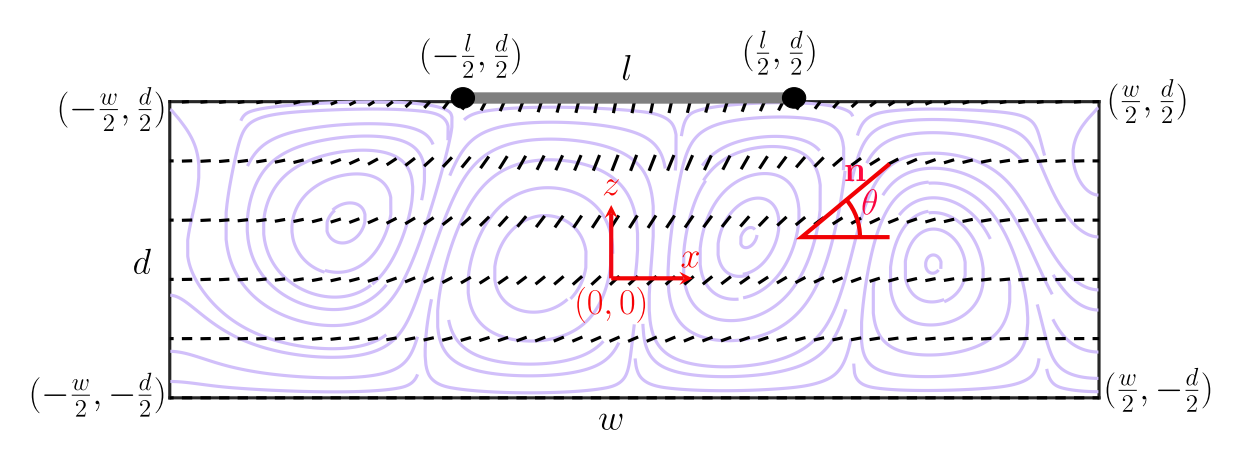


Figure 4.1: Active nematic sandwiched between two solid plates at z = -d/2 and z = d/2. The gray solid line between the points (-l/2, d/2) and (l/2, d/2) represents the region of homeotropic anchoring. The black solid lines represent the director. The background lilac lines represent the streamlines.

4.2.1 Governing equations

We now seek solutions of the governing equations for the director $\mathbf{n} = \mathbf{n}(x, z, t)$ and the velocity field $\mathbf{v} = \mathbf{v}(x, z, t)$ in the form

$$\mathbf{n} = (\cos \theta(x, z, t), 0, \sin \theta(x, z, t)), \tag{4.1}$$

$$\mathbf{v} = (u(x, z, t), \ 0, \ v(x, z, t)), \tag{4.2}$$

$$\tilde{p} = p(x, z, t), \tag{4.3}$$

where θ is the director angle, (x, z) are the Cartesian coordinates and t denotes time [202]. The flow speeds in the x and z directions are u(x, z, t) and v(x, z, t), respectively.

Using this director and velocity, the Ericksen-Leslie equations for active nematics based on the conservation of mass, and the balance of linear and angular momentum [114,

115, 202, 238], as given in Chapter 2, are given by

$$0 = \frac{\partial u}{\partial x} + \frac{\partial v}{\partial z},\tag{4.4}$$

$$0 = \frac{\partial}{\partial x} \left(\frac{\partial D}{\partial u_x} \right) + \xi \frac{\partial}{\partial x} \left(\cos^2 \theta \right) + \frac{\partial}{\partial z} \left(\frac{\partial D}{\partial u_z} \right) + \xi \frac{\partial}{\partial z} \left(\sin \theta \cos \theta \right) - \frac{\partial D}{\partial \dot{\theta}} \theta_x - \tilde{p}_x, \quad (4.5)$$

$$0 = -\tilde{p}_y, \tag{4.6}$$

$$0 = \frac{\partial}{\partial x} \left(\frac{\partial D}{\partial v_x} \right) + \xi \frac{\partial}{\partial x} \left(\sin \theta \cos \theta \right) + \frac{\partial}{\partial z} \left(\frac{\partial D}{\partial v_z} \right) + \xi \frac{\partial}{\partial z} \left(\sin^2 \theta \right) - \frac{\partial D}{\partial \dot{\theta}} \theta_z - \tilde{p}_z, \quad (4.7)$$

$$0 = \frac{\partial}{\partial x} \left(\frac{\partial w_F}{\partial \theta_x} \right) + \frac{\partial}{\partial z} \left(\frac{\partial w_F}{\partial \theta_z} \right) - \frac{\partial w_F}{\partial \theta} - \frac{\partial D}{\partial \dot{\theta}}, \tag{4.8}$$

where the subscripts x and z in θ_x , θ_z , u_x , u_z , v_x and v_z represent partial derivatives with respect to the respective variable. To complete equations (4.5)–(4.8), we need two quantities - the elastic free energy w_F and the dissipation function D [202].

By substituting equations (4.1) and (4.2) into equation (2.36), and simplifying, we obtain the Frank-Oseen elastic free energy w_F , given explicitly as

$$w_{F} = \frac{1}{2} \left[\theta_{x}^{2} \left(K_{1} \sin^{2} \theta + K_{3} \cos^{2} \theta \right) + \theta_{z}^{2} \left(K_{1} \cos^{2} \theta + K_{3} \sin^{2} \theta \right) + (K_{3} - K_{1}) \sin(2\theta) \theta_{x} \theta_{z} \right].$$

$$(4.9)$$

Using equations (4.1) - (4.2) together with equation (2.55) and simplifying, we get

$$\mathcal{D} = \alpha_{1} \left[u_{x} \left((-u_{z} - v_{x}) h_{11} \sin^{2}\theta + (u_{z} + v_{x}) h_{11} - v_{z} \sin^{4}\theta + \sin^{2}\theta v_{z} \right) \right. \\ + u_{z} \left(h_{11} \sin^{2}\theta v_{z} - v_{x} \sin^{4}\theta + \sin^{2}\theta v_{x} \right) + h_{11} \sin^{2}\theta v_{z} v_{x} \right] \\ + \alpha_{2} \left[u_{x} \left(-\frac{1}{4}u_{z} + \frac{1}{4}v_{x} - \frac{1}{2}\theta_{t} \right) h_{11} + u_{z} \left(\frac{1}{4}v_{x} + \frac{1}{4}h_{11}v_{z} - \frac{1}{2} \sin^{2}\theta\theta_{t} - \frac{1}{4}\theta_{t} \right) \right. \\ + v_{x} \left(-\frac{1}{4}h_{11}v_{z} - \frac{1}{2} \sin^{2}\theta\theta_{t} + \frac{3}{4}\theta_{t} \right) + \frac{1}{2}h_{11}v_{z}\theta_{t} - \frac{1}{2}\theta_{t}^{2} \right] \\ + \alpha_{3} \left[u_{x} \left(-\frac{1}{4}u_{z} + \frac{1}{4}v_{x} - \frac{1}{2}\theta_{t} \right) h_{11} + u_{z} \left(-\frac{1}{4}v_{x} + \frac{1}{4}h_{11}v_{z} - \frac{1}{2} \sin^{2}\theta\theta_{t} + \frac{3}{4}\theta_{t} \right) \right. \\ + v_{x} \left(-\frac{1}{4}h_{11}v_{z} - \frac{1}{2} \sin^{2}\theta\theta_{t} - \frac{1}{4}\theta_{t} \right) + \frac{1}{2}h_{11}v_{z}\theta_{t} + \frac{1}{2}\theta_{t}^{2} \right] \\ + \alpha_{5} \left[u_{x} \left(\frac{3}{4}u_{z} + \frac{1}{4}v_{x} + \frac{1}{2}\theta_{t} \right) h_{11} + u_{z} \left(\frac{1}{4}v_{x} + \frac{1}{4}h_{11}v_{z} + \frac{1}{2} \sin^{2}\theta\theta_{t} - \frac{1}{4}\theta_{t} \right) \right. \\ + v_{x} \left(\frac{3}{4}h_{11}v_{z} + \frac{1}{2} \sin^{2}\theta\theta_{t} - \frac{1}{4}\theta_{t} \right) - \frac{1}{2}h_{11}v_{z}\theta_{t} \right] \\ + \alpha_{6} \left[u_{x} \left(\frac{1}{4}u_{z} + \frac{3}{4}v_{x} - \frac{1}{2}\theta_{t} \right) h_{11} + u_{z} \left(\frac{1}{4}v_{x} + \frac{3}{4}h_{11}v_{z} - \frac{1}{2} \sin^{2}\theta\theta_{t} + \frac{1}{4}\theta_{t} \right) \right. \\ + v_{x} \left(\frac{1}{4}h_{11}v_{z} - \frac{1}{2} \sin^{2}\theta\theta_{t} + \frac{1}{4}\theta_{t} \right) + \frac{1}{2}h_{11}v_{z}\theta_{t} \right] \\ + v_{x} \left(\frac{1}{4}h_{11}v_{z} - \frac{1}{2} \sin^{2}\theta\theta_{t} + \frac{1}{4}\theta_{t} \right) + \frac{1}{2}h_{11}v_{z}\theta_{t} \right] \\ + \left. \frac{1}{2}v_{x}u_{z}\alpha_{4} + g_{3}u_{x}^{2} + g_{1}u_{z}^{2} + g_{2}v_{x}^{2} + g_{4}v_{z}^{2} \right. \\ + \left. \xi \left[\cos^{2}\theta u_{x} + h_{11} (v_{x} + u_{y}) + \sin^{2}\theta v_{y} \right],$$

$$(4.10)$$

where

$$g_1(\theta) = \frac{1}{2} \left[\alpha_4 + (\alpha_3 + \alpha_6) \cos^2 \theta + \sin^2 \theta (\alpha_5 - \alpha_2) \right] + \alpha_1 \sin^2 \theta \cos^2 \theta, \tag{4.11}$$

$$g_2(\theta) = \frac{1}{2} \left[\alpha_4 + (\alpha_6 - \alpha_3) \cos^2 \theta + (\alpha_5 + \alpha_2) \sin^2 \theta \right] + \alpha_1 \sin^2 \theta \cos^2 \theta, \tag{4.12}$$

$$g_3(\theta) = \frac{1}{2}\alpha_1 \cos^4 \theta + \frac{1}{2}\alpha_4 + \frac{1}{2}(\alpha_5 + \alpha_6)\cos^2 \theta, \tag{4.13}$$

$$g_4(\theta) = \frac{1}{2}\alpha_1 \sin^4 \theta + \frac{1}{2}\alpha_4 + \frac{1}{2}(\alpha_5 + \alpha_6)\sin^2 \theta, \tag{4.14}$$

$$h_{11}(\theta) = \sin \theta \cos \theta. \tag{4.15}$$

For a detailed derivation of the rate of dissipation, refer to Appendix A. The equations describing the conservation of mass, linear and angular momentum are therefore

$$0 = u_x + v_z,$$

$$0 = \frac{\partial}{\partial x} \left[u_z h_1 + v_x h_2 - \gamma_2 h_8 h_{11} - \frac{1}{4} \alpha_1 \cos(2\theta) v_z + \frac{1}{4} \xi \left(\cos(2\theta) + 2h_{13} u_x \right) \right]$$

$$+ \frac{\partial}{\partial z} \left[u_x h_1 + v_z h_3 + \frac{1}{4} v_x h_4 + \gamma_2 h_8 \cos^2 \theta + \frac{1}{2} h_{11} \gamma_1 h_8 + \frac{1}{2} \gamma_2 h_8 + 2g_1 u_z \right]$$

$$+ \frac{\partial \theta}{\partial x} \left[\alpha_3 u_z \cos(2\theta) + \alpha_2 v_x \cos(2\theta) + \gamma_2 \left(v_z - u_x \right) h_{11} + \gamma_1 h_8 \right] + \xi h_9 - \tilde{p}_x, \quad (4.17)$$

$$0 = -\tilde{p}_y, \tag{4.18}$$

$$0 = \frac{\partial}{\partial x} \left[u_x h_5 + \frac{1}{2} h_{10} u_z + v_z h_6 - \frac{1}{2} \gamma_1 h_8 h_{12} - \frac{1}{2} \gamma_2 h_8 \cos^2 \theta + \frac{1}{2} \left(\xi h_{11} + 2g_3 v_x \right) \right]$$

$$+ \frac{\partial}{\partial z} \left[u_z h_7 + v_x h_6 + \alpha_1 h_{11}^2 u_x + h_{14} v_z + \gamma_2 h_8 h_{11} + \alpha_1 u_x \sin^4 \theta \right]$$

$$+ \frac{\partial \theta}{\partial z} \left[u_z h_{12} \alpha_2 - \gamma_1 \sin^2 \theta v_x + \gamma_1 h_8 h_{12} - \gamma_2 \left(u_x - v_z \right) h_{11} \right]$$

$$+ \xi \left[2 \sin \theta \cos \theta \theta_z + \theta_x \cos^2 \theta \right] - \tilde{p}_z,$$

$$(4.19)$$

$$\gamma_{1}\theta_{t} = 2\theta_{x}\theta_{z}\left((K_{1} - K_{3})\sin^{2}\theta + K_{3} - K_{1}\right) - \gamma_{1}(u + \theta_{z}v) - \frac{1}{2}u_{z}\left(\gamma_{1} + \gamma_{2}\cos(2\theta)\right) - \frac{1}{2}v_{x}\left(-\gamma_{1} + \gamma_{2}\cos(2\theta)\right) + \left(K_{1}(\theta_{x}^{2} - \theta_{z}^{2}) + K_{3}(\theta_{z}^{2} - \theta_{x}^{2})\right)\sin\theta\cos\theta + (u_{x} - v_{z})\gamma_{2}\sin\theta\cos\theta + f_{2}\theta_{xx} + f_{3}\theta_{xz} + f_{1}\theta_{zz},$$
(4.20)

where

$$f_1(\theta) = K_1 \sin^2 \theta + K_3 \cos^2 \theta, \tag{4.21}$$

$$f_2(\theta) = K_1 \cos^2 \theta + K_3 \sin^2 \theta, \tag{4.22}$$

$$f_3(\theta) = (K_3 - K_1)\sin\theta\cos\theta,\tag{4.23}$$

$$h_1(\theta) = \sin \theta \cos \theta \left[\alpha_1 \cos(2\theta) - \alpha_5 - \alpha_1 \sin \theta \cos^3 \theta \right], \tag{4.24}$$

$$h_2(\theta) = \sin \theta \cos \theta \left[\alpha_1 \cos(2\theta) + \alpha_6 - \alpha_1 \sin \theta \cos^3 \theta \right], \tag{4.25}$$

$$h_3(\theta) = \sin \theta \cos \theta \left[\alpha_1 \cos(2\theta) - \alpha_1 \cos^2 \theta + \alpha_6 \right], \tag{4.26}$$

$$h_4(\theta) = \alpha_1 \sin^2 \theta + \alpha_5 + \alpha_6 - \gamma_1 + 2\alpha_4, \tag{4.27}$$

$$h_5(\theta) = \sin \theta \cos \theta \left[\alpha_1 \cos^2 \theta + \alpha_6 + \alpha_1 \cos \theta \sin^3 \theta \right], \tag{4.28}$$

$$h_6(\theta) = \alpha_5 \sin \theta \cos \theta + \alpha_1 \cos \theta \sin^3 \theta, \tag{4.29}$$

$$h_7(\theta) = \alpha_6 \sin \theta \cos \theta + \alpha_1 \cos \theta \sin^3 \theta, \tag{4.30}$$

$$h_8(\theta, u, v) = \theta_t + u\theta_x + v\theta_z, \tag{4.31}$$

$$h_9(\theta) = \theta_z \cos(2\theta) - 2\cos\theta \sin\theta\theta_x, \tag{4.32}$$

$$h_{10}(\theta) = \left[(\alpha_5 + \alpha_6)\sin^2\theta + 1 \right] - \gamma_1 \left(\sin^2\theta + 1\right) + 2\alpha_1 \sin^2\theta + \alpha_4, \tag{4.33}$$

$$h_{12}(\theta) = \sin^2 \theta + 1,$$
 (4.34)

$$h_{13}(\theta) = \alpha_1 \cos \theta \sin^3 \theta + \alpha_6 \cos \theta \sin \theta, \tag{4.35}$$

$$h_{14}(\theta) = \alpha_1 \sin \theta \cos^3 \theta + \alpha_6 \cos \theta \sin \theta. \tag{4.36}$$

(4.37)

4.2.2 Boundary conditions

To solve equations (4.16)–(4.19), we need appropriate boundary conditions for θ , u, v and \tilde{p} . For components u and v of the velocity, we impose no-slip and no-penetration boundary conditions on the solid walls at z = -d/2 and z = d/2. Specifically, the appropriate

boundary conditions are

$$u(x, -d/2) = 0, \ v(x, -d/2) = 0,$$
 (4.38)

$$u(x, d/2) = 0, \ v(x, d/2) = 0.$$
 (4.39)

For the director angle, we use a combination of planar and homeotropic anchoring conditions. We imposed planar anchoring $(\theta = 0)$ everywhere on the solid walls except in the region defined by the coordinates (-l/2, d/2) to (l/2, d/2). Within this specific region, we impose homeotropic anchoring $\theta = \pi/2$ rad.

Both the left- and right-hand boundaries are modelled as open, and we choose two different possible sets of boundary conditions. The first we called normal flow, which models the large distance from the HAN region, so that there is no variation in the director and the flow is normal. The appropriate boundary conditions are then,

$$\theta_x = 0 \text{ at } x = \pm w/2, \tag{4.40}$$

$$v = 0 \text{ at } x = \pm w/2.$$
 (4.41)

For the horizontal velocity u, we apply the *stress-free* boundary condition on the lateral walls, which requires that the tangential (shear) stress vanishes. This condition is written as

$$\boldsymbol{\sigma} \cdot \hat{\mathbf{x}} = 0 \quad \text{at } x = \pm \frac{w}{2},$$
 (4.42)

where σ is the stress tensor and $\hat{\mathbf{x}}$ is the outward unit normal to the wall. In a twodimensional x-z configuration, this gives

$$\sigma_{xz}|_{x=\pm\frac{w}{2}} = 0, \tag{4.43}$$

The second situation is periodic conditions, so that

$$\theta(-w/2, z) = \theta(w/2, z), \tag{4.44}$$

$$v(-w/2, z) = v(w/2, z). (4.45)$$

4.3 Numerical calculations I: normal flow conditions

To numerically solve equations (4.16)–(4.20) together with boundary conditions (4.38)–(4.45), we use the COMSOL Multiphysics® Software Version 6.1 to perform our calculations [31]. To solve for the velocity field in COMSOL, we adopt the incompressible creeping flow model to solve the linear momentum equations (4.17) and (4.19). The active nematic elements of these equations are used as input for a volume force node added to the Newtonian system.

To solve for the director angle, we first rewrite equation (4.20) in COMSOL's general PDE form

$$e_a \frac{\partial^2 \theta}{\partial t^2} + d_a \frac{\partial \theta}{\partial t} + \nabla \cdot \Gamma = f, \tag{4.46}$$

where $\nabla = [\partial/\partial x, \partial/\partial z]$ and $\Gamma = [-f_2(\theta)\theta_x, -f_1(\theta)\theta_z]$ is the conservative flux. In this formulation, d_a is the damping coefficient, here identified with the rotational viscosity as $d_a = \gamma_1$, and e_a is the mass coefficient. Although, $e_a = 0$ in our system, we retain it in the equation because COMSOL's PDE interface requires the standard form to include both mass and damping terms. Writing the director equation in this form therefore makes the implementation straightforward and consistent with COMSOL's framework, while still preserving the original physical variables. The forcing term f is given by

$$f = -2f_3\theta_x^2 + f_3\theta_{xz} + (K_3 - K_1)\cos(2\theta)\theta_x\theta_z + \gamma_2(u_x - v_z)\sin\theta\cos\theta - \frac{1}{2}(\gamma_2\cos(2\theta) + \gamma_1)u_z - \frac{1}{2}(\gamma_2\cos(2\theta) - \gamma_1)v_x - \gamma_1v\theta_z - \gamma_1u\theta_x,$$
(4.47)

where γ_1 is the rotational viscosity, which governs the relaxation of the director angle, and γ_2 is the torsion viscosity.

We choose an appropriate initial condition to satisfy approximately the anchoring for the director angle, given explicitly by

$$\theta_0(x,z) = \frac{\pi}{2} \left[\tanh\left(\frac{(x+l/2)}{\epsilon}\right) - \tanh\left(\frac{(x-l/2)}{\epsilon}\right) \right] \left[\frac{z+l/2}{d}\right], \tag{4.48}$$

and appropriate initial velocities $u_0 = v_0 \equiv 0$, where ϵ is the size of the transition from planar to HAN anchoring. We choose $\epsilon = 1 \mu m$ throughout this thesis to closely match the boundary conditions with the initial conditions. For reference, the domain width is $w = 20 \mu m$, so that $\epsilon/w \ll 1$, to ensure a rapid transition to the HAN region compared with the lateral size of the system. In this Chapter, we revert to the more standard $d = 2 \mu m$, since we are considering a sensor device.

To interpret the results, we divide the channel into different subregions: the left planar region, the HAN region, the right planar region and the transition regions, as shown in Figure 4.2. In order to investigate the flow dependence on the geometry, we first consider the case where the HAN channel width is fixed and then vary the channel width. This is to verify that a small channel width does not significantly impact the flow or the overall dynamics of the system. Next, we vary the activities and fix the channel width and the HAN channel length. We also consider changing the activity parameter value and the HAN channel width for both contractile and extensile nematics.

4.3.1 Effects of varying channel width

In this section, we fix the HAN region width, l, and activity, ξ , and vary the channel width, w. The goal is to understand how the channel width affects the system's behaviour under weak activity, which is vital for applications where the geometry of the environment significantly impacts system behaviour, such as in microfluidic devices and biological systems. The simulation is run for 2 seconds (in model time) to allow the

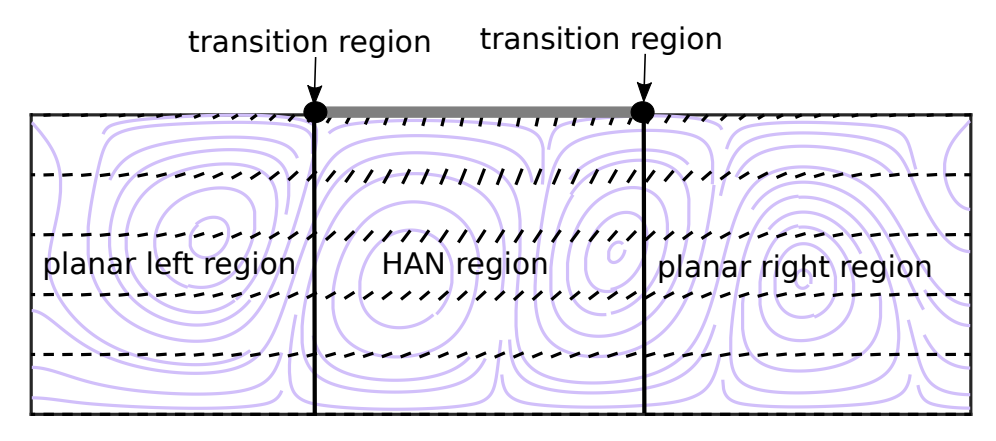


Figure 4.2: A schematic showing the division of the channel into planar left, HAN, planar right and transition regions.

initial changes in the system to stabilise, and so captures the long-term behaviour.

We first present a summary of the simulations for weakly active systems, both contractile and extensile, for various channel width. Specifically, we choose w=20, w=40, w=60, and w=80 microns, with $l=6.667\,\mu\text{m}$, and $\xi=\pm0.001$ Pa, although we present the results for only $\xi=-0.001$ Pa because the results are very similar for weakly active systems. The apparent symmetry breaking arises from the choice of initial director field $\theta(x,z)$. In particular, the imposed orientation leads to different behaviours in the left and right regions of the system, so the initial condition itself introduces the asymmetry.

Figure 4.3 shows a plot of the director for various values of channel widths. Note that in this plot, we have scaled the x-axis. We use the background colour to represent the director angle, black lines to represent the streamlines, white rods to represent the director, and black arrows to represent the flow direction.

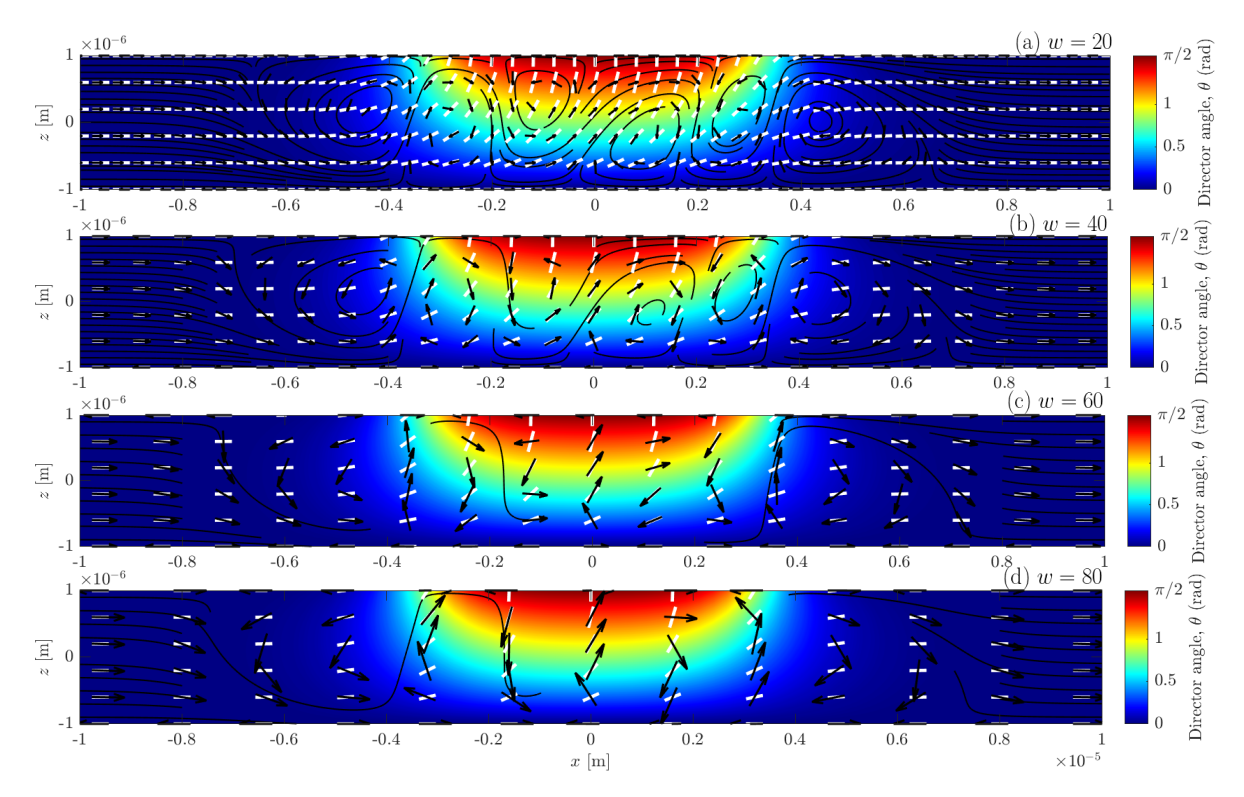


Figure 4.3: Plot of the director angle for different region widths at $\xi = -0.001$ Pa and t = 2 s for: (a) $w = 20 \,\mu\text{m}$, (b) $w = 40 \,\mu\text{m}$, (c) $w = 60 \,\mu\text{m}$, and (d) $w = 80 \,\mu\text{m}$. Each panel shows streamlines (black lines), the director (white rods), flow direction (black arrows), and the director angle (background colour). Horizontal velocity profiles for the different channel widths are included, with the x-axis fixed to $[-1,1] \times 10^{-5} \,\text{m}$ in all cases to facilitate comparison. The HAN region width used in the simulations is $l = 6.667 \,\mu\text{m}$.

For all chosen values of channel width, the director in both left and right planar regions remains undistorted, indicating a uniform solution aligned to planar anchoring. However, in the transition and HAN regions, the director is distorted because of the boundary conditions, leading to flow even for this very low activity strength (see Figures 4.3 (a)–(d)). In addition, the system is characterised by an approximately rectilinear flow in the left and right planar regions and a circulatory flow where there are localised distortions in the HAN and transition regions. The system has almost the same flow for all the chosen values of channel width.

The minimal dependence of the flow on the channel width, w, allows us to choose w = 20 microns in the following work to aid computation efficiently.

Before we proceed, it is pertinent to discuss the characteristic length and time scales

of the 2D model. We use equations (3.27) and (3.28), together with the parameters in Tables 1.1 and 1.2. For example, we choose $\xi = 0.0001$ Pa and $\xi = 150$ Pa, as these represent the smallest and largest activity values considered in this thesis. The channel spans a height $d=2~\mu\mathrm{m}$ and a width $w=20~\mu\mathrm{m}$. The active length scale evaluates to $l_a\approx 11.4/\sqrt{|\xi|}~\mu\mathrm{m}$. For a small activity, $|\xi|=0.0001$ Pa, this gives $l_a\approx 11400~\mu\mathrm{m}$, which is much larger than both the channel height and width, indicating that distortions will be weakly resolved. The corresponding active time scale is $\tau_a\approx 2375$ s, implying extremely slow dynamics.

For large activity, $|\xi|=150$ Pa, the active length scale is $l_a\approx 0.93~\mu\text{m}$, which is smaller than the channel height, so distortions are strongly confined and well-resolved. The active time scale is $\tau_a\approx 0.016$ s, meaning the system evolves very rapidly, and a short simulation of a few seconds captures multiple active response times.

This means that the channel dimensions and simulation duration relative to the active scales lead to distinct regimes. For very small activity, we have $d, w \ll l_a$ and $t \ll \tau_a$, indicating that the system is effectively uniform and evolves extremely slowly, so the natural activity-driven patterns cannot develop due to high level of spatial confinement, compared to the active length scale.

In contrast, for very large activity, we have $d, w \gg l_a$ and $t \gg \tau_a$, meaning that the system dimensions can contain activity-induced distortions and evolves rapidly, allowing simulations to capture the relevant dynamics within short times.

In the thin channel of $d=2~\mu\mathrm{m}$, relevant for sensor design, even small local perturbations can generate significant director distortions and flow across the channel, which allows the system to effectively "sense" changes in boundary conditions or the presence of objects. The channel height is therefore chosen to match the spatial scale of active distortions and optimize sensitivity for potential active nematic sensors.

4.3.2 Effects of varying activity strength and HAN region width for contractile nematics

This section focuses on contractile active nematics, where we examine the solution profiles for varying HAN region width and activity strength values. We begin by exploring the solution profiles for varying activity while keeping the HAN region width fixed, revealing how the director angle and flow patterns evolve under different activity magnitudes. We observe distinct behaviours, including the reduction of circulations and changes in the flow direction as activity increases. In particular, at high activity values, oscillations become apparent in both the HAN and planar regions.

Next, we analyse the systems by varying both the width of the HAN region and the activity strength. To measure the effects, we calculate the flux on the left boundary. We find that larger HAN region widths and higher activity magnitudes result in a higher flux into the system.

Finally, we investigate the oscillatory nature of the flow, particularly at high activities. By performing a spatial frequency analysis via the Fast Fourier Transform (FFT), we assess the oscillations in both the left and right planar regions, as well as in the HAN region in Section 4.3.2.3.

4.3.2.1 Solution profiles for a fixed HAN region width and varying activity strengths

In this section, we vary the activity parameter while keeping the HAN region width fixed. Figure 4.4 presents the director and streamlines for w = 20 microns, l = 20/3 microns and $\xi = [0, -0.1, -1, -10, -100]$ Pa. For the activity strength $\xi = 0$, the system is characterised by very small flow ($u = 9.7 \times 10^{-8}$ m/s), which is simply due to the small elastic relaxation to an equilibrium state since the initial condition for the director structure is not exactly the same as the equilibrium structure. For $\xi = -0.1$ Pa, the director remains largely undistorted in both the left and right planar regions

with maximum flow velocity of $u = 1.6 \times 10^{-6}$ m/s, as shown in Figures 4.4(a)–(b). In addition, the system is characterised by a rectilinear flow moving to the right-hand side of the channel. In the HAN region, the system exhibits flow distortions, characterised by four distinct circulations. For $\xi = -1$ Pa and $\xi = -10$ Pa, the circulations reduce to two distinct loops and one large loop, respectively. In this regime of activity strength, the flow is in fact in a reversed direction with a lower maximum velocity of 10^{-5} m/s (see Figures 4.4(c)–(d)), suggesting that circulation in the HAN region decreases with increasing activity strength. At all these orders of activity, the director distortion leads to the generation of bulk flow in the system.

In Figure 4.4(e), where the activity has increased to $\xi = -100$ Pa, the director angle is seen to oscillate in the planar regions. Similar results were seen for extensile active nematics using planar anchoring [63, 126, 187]. Thampi [211] also observes oscillatory behaviour accompanied by distorted streamlines for high values of activity parameters using periodic anchoring.

Our results suggest that increasing the magnitude of the activity eventually results in oscillations in the system accompanied by high flow in most of the region.

4.3.2.2 Flux measurement for varying activity strength and HAN region width

To measure the flux of fluid into the system, we explore our results by numerically integrating the velocity u at the inlet/outlet with respect to z for $\xi \in [-100, 0]$ Pa and for $l \in [w/1000, w/3]$ microns. Since both left and right boundaries are modelled as open boundaries, so that no flux is lost, $\int u_L dz \equiv \int u_R dz$, where u_L and u_R denote the flow velocity at the left and right boundaries, respectively. This equality reflects the inherent left-right symmetry of the governing equations and boundary conditions. However, this symmetry is broken by the choice of initial conditions, in particular the initial theta configuration in the HAN region, which can bias the system towards flow in a preferred direction. As a result, although the equations are symmetric, the system

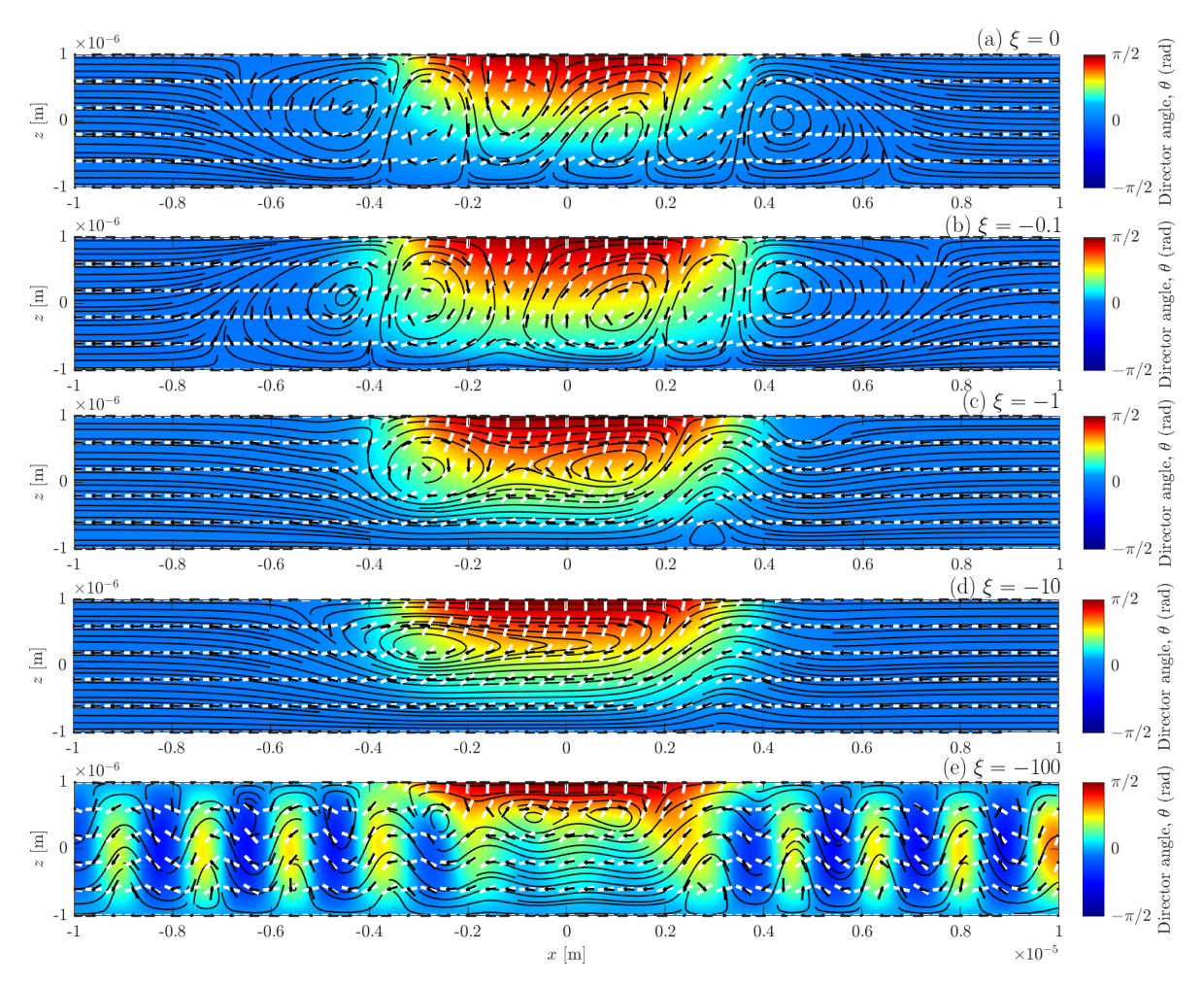


Figure 4.4: Plot of the director angle for (a) $\xi = 0$ Pa, (b) $\xi = -0.1$ Pa, (c) $\xi = -1$ Pa, (d) $\xi = -10$ Pa, (d) and (e) $\xi = -100$ Pa with w = 20 microns and t = 2 seconds, seconds, depicting the streamlines (black lines), director (white rods), flow direction (black arrows) and the director angle (background colour).

dynamically evolves with a flow pattern that breaks left-right symmetry. Therefore, in this section, we present only the results for the left boundary.

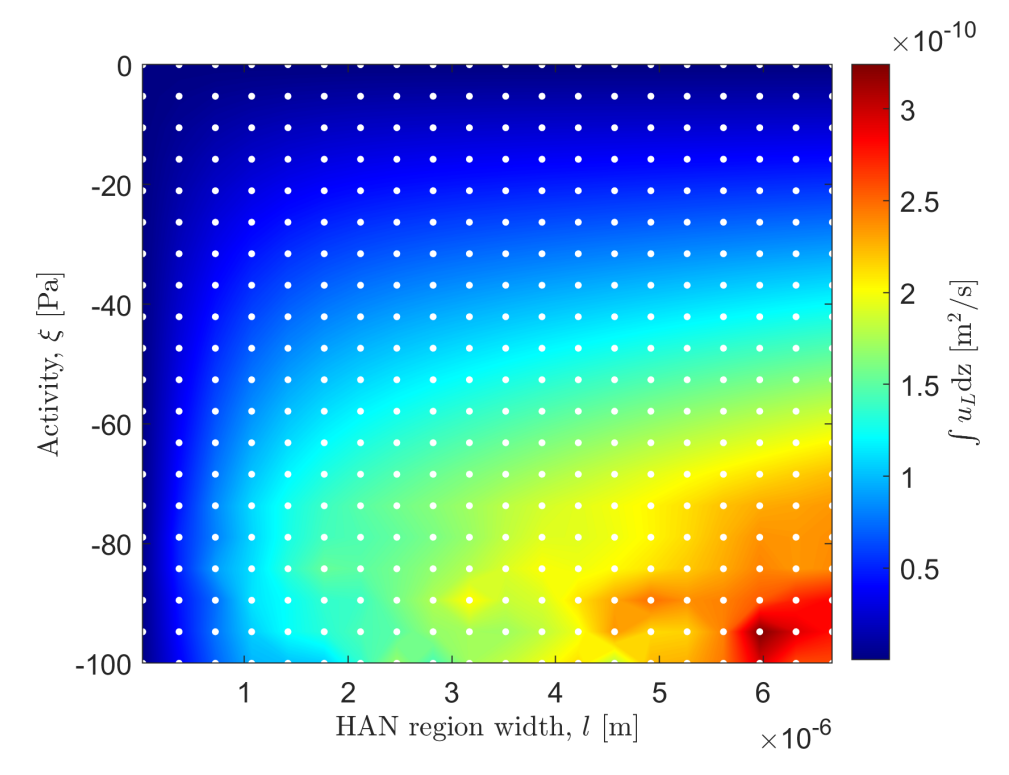


Figure 4.5: Plot of $\int u_L dz$ against activity and HAN region width, l. The dots represent the parameter values that have been simulated, and the background colour is interpolated between the values at the dots.

Figure 4.5 presents $\int u_L dz$ for varying ξ and l for contractile active nematics. We see that the flux decreases, indicating a greater flow out of the region on the left boundary, as both the activity, ξ and HAN region width, l, increase. Thus, larger HAN region width and activity strength lead to more fluid leaving the system at the left boundary.

4.3.2.3 Oscillatory flow for a fixed HAN region width

To fully understand the nature of the oscillations observed in Section 4.3.1, we explore the results at higher magnitudes of the activity. To achieve this, we perform both temporal and spatial spectral analyses of the director angle. We show only the results for the spatial analysis because the temporal analysis shows that after a short time, the system does not oscillate in time.

The FFT transforms the space into a frequency domain, which we use to perform a

spatial frequency analysis for the entire domain in each of the subregions. First, we provide an example plot of the director angle along the centre of the channel, z = 0, for the entire region and the sub-regions.

Figure 4.6 displays the director angle as a function of x at z=0 (that is, along the center of the channel) for the entire channel, the planar regions left and right and the HAN region. We observe relatively uniform oscillations in both the left and right hand planar regions and less regular oscillations in the HAN region.

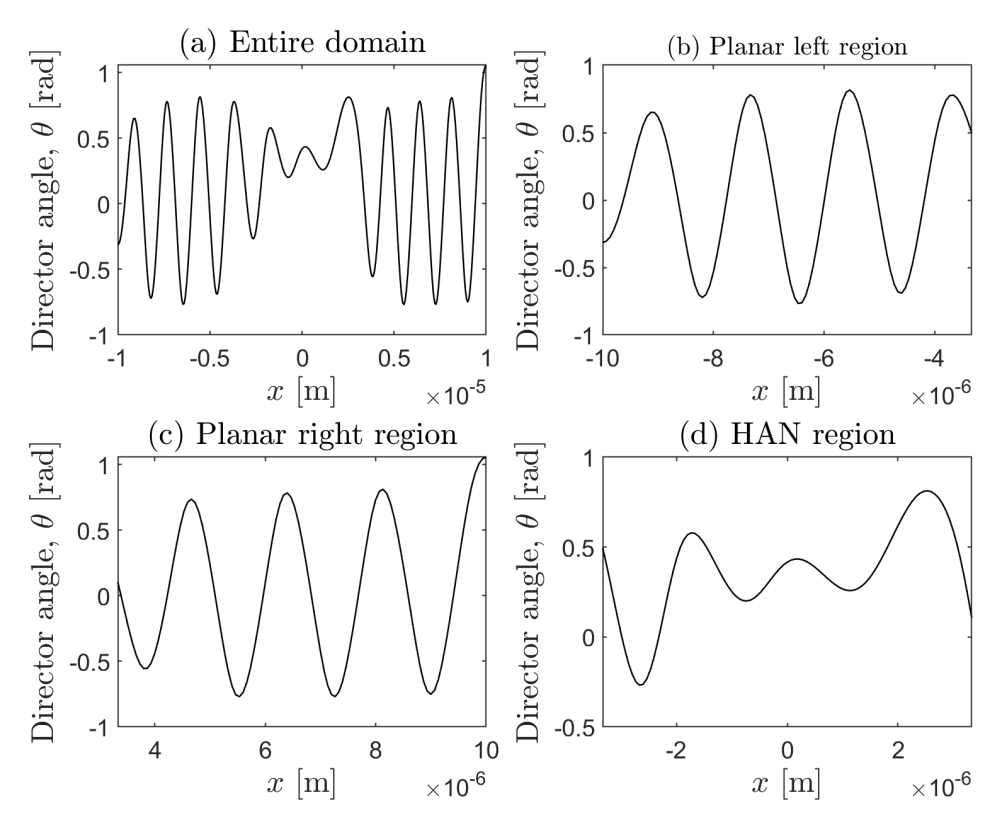


Figure 4.6: The director angle as a function along the centreline z = 0 across the (a) whole region, (b) planar left region, (c) planar right region, and (d) HAN region.

We present the results of our spatial analysis in Figure 4.7. We plot the magnitude of the Fourier mode against the wavenumber k (spatial frequency) for the entire domain, the two planar regions, and the HAN region to characterize the nature of the oscillations in each region. The wavenumber k is scaled in μ m⁻¹, corresponding to lengths $L = 2\pi/k$.

Figure 4.7(a) shows the magnitude of the mode versus k for the entire domain. The dominant peak occurs at $k_{\rm peak} \approx 5.98~\mu {\rm m}^{-1}$, corresponding to a wavelength $L \approx 1.051~\mu {\rm m}$. The left and right planar regions feature similar peak wavenumbers, $k_{\rm peak} \approx 5.94~\mu {\rm m}^{-1}$,

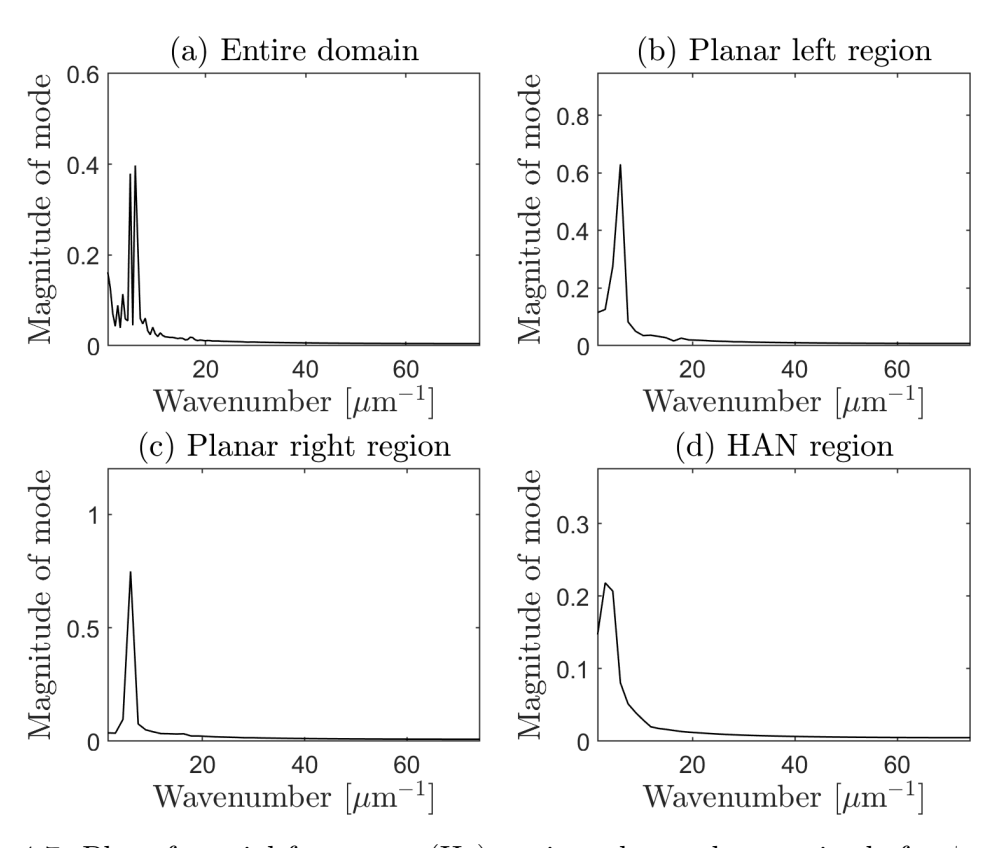


Figure 4.7: Plot of spatial frequency (Hz) against the mode magnitude for $\xi = -100$ Pa: (a) entire region ($k \approx 5.98 \ \mu \text{m}^{-1}$), (b) planar left region ($k \approx 5.94 \ \mu \text{m}^{-1}$), (c) planar right region ($k \approx 5.94 \ \mu \text{m}^{-1}$), and (d) HAN region ($k \approx 2.97 \ \mu \text{m}^{-1}$).

corresponding to $L \approx 1.058~\mu\text{m}$, but with differing magnitudes of the modes: approximately 31.81 for the left region and 37.81 for the right region (Figures 4.7(b) and (c)). The HAN region exhibits a dominant peak at $k_{\text{peak}} \approx 2.97~\mu\text{m}^{-1}$, corresponding to a larger wavelength $L \approx 2.116~\mu\text{m}$, with a smaller mode magnitude of 11.02 (Figure 4.7(d)).

The differences in magnitude between the left and right planar regions are noteworthy. Although the peak wavenumbers are similar, which indicates comparable spatial scales of oscillations, the differing mode magnitudes suggest that the director distortions are stronger on one side than the other. This asymmetry arises from the HAN region, where the director tilt is positive rather than negative, which breaks the symmetry between the planar regions. For the HAN region, the lower k_{peak} and smaller magnitude indicate that oscillations are longer in wavelength and weaker, which reflects the more complex and diffuse nature of director variations under hybrid alignment conditions.

Overall, the Fourier analysis reveals that the planar regions support fine-scale, high-magnitude oscillations, whereas the HAN region supports broader, lower-amplitude oscillations. This information give an intuition into the characteristic spatial patterns that may influence active flow and potential sensing applications.

It is interesting to note that, although the system exhibits spatial fluctuations for sufficiently high magnitudes of activity, no time-dependent oscillations are observed. Similar flow patterns were reported by Samui et al. [187], who examined flow transitions in active nematics and their length scales in a confined 2D geometry under planar anchoring conditions. Their study reveals flow transitions in extensile active nematics, ranging from unidirectional flow to fully developed active turbulence as the activity strength increases. In contrast, our study applies a combination of planar and homeotropic anchoring, and oscillations were observed in contractile rather than extensile nematics.

4.3.2.4 Oscillatory flow measure for varying activity and HAN region width

In this Section, using the above methodology, we examine how the oscillations change with respect to the HAN region width and the activity strength. We consider $\xi \in [-100, 0]$ Pa and $l \in [w/1000, w/3]$ microns, and perform a spatial frequency analysis of the director angle for the entire domain as well as for subregions, including the planar left, HAN, and planar right regions. However, we present detailed results only for the planar left and right regions, as the oscillations in the HAN region are more complex and difficult to characterise.

After computing the Fourier transform of the director angle $\theta(x)$ for the entire domain and subregions, the peak magnitudes and corresponding frequencies are identified using the findpeaks function in MATLAB. For each subregion, the Fourier transform is computed as $\tilde{\theta}(k) = \text{FFT}[\theta(x) - \langle \theta(x) \rangle]$, where $\langle \theta(x) \rangle$ is the mean director angle along the x-direction. The fftshift function is applied to center the zero frequency.

The peaks of the Fourier spectrum are then identified for frequencies exceeding a threshold $T_f = 10^5$ and magnitudes exceeding $T_m = 0.15$. Specifically, for each set of peaks, the largest peak above these thresholds is selected as the dominant oscillatory mode. Denoting the peak frequency and magnitude as p_f and p_m , respectively, a region is classified as oscillatory if $|p_f| > T_f$ and $|p_m| > T_m$.

The uncertainty in the peak frequency, δp_f , is estimated from the frequency resolution of the Fourier transform, $\delta p_f = 1/L_x$, where L_x is the number of spatial points in the subregion. The uncertainty in the peak magnitude, δp_m , is estimated from the noise floor of the Fourier spectrum. These uncertainties are reported for all peak measurements to ensure the reliability of the oscillation classification.

In Figure 4.8, we present plots of the spatial frequencies as a function of ξ and l for the left- and right-planar regions. We use red dots to represent oscillations and cyan dots to represent non-oscillations. Figure 4.8(a) shows the results for the planar left region, which suggests that the system oscillates for a high magnitude of activity parameter

values and all HAN region widths. However, for the planar right region, the system oscillates for intermediate- and high-magnitude activity parameter values, as shown in Figure 4.8(b). Overall, it was found that oscillations are likely seen in the planar right region. The sudden jump in the frequency plots occurs because, for certain parameter values, the peak at zero frequency becomes dominant. However, as the parameters change, the peak shifts, and the non-zero frequency becomes dominant. This switch between dominant peaks creates the appearance of a sudden jump in the plot.

4.3.3 Effects of varying activity strength and HAN region width for extensile nematics

This section explores the solution profiles for extensile active nematics. Using the same analysis framework as in Section 4.3.2, we examine the solution profiles under varying activity strength and HAN region widths. This includes observing changes in the director angle and flux patterns, as well as the flow measure for varying activity and the HAN region width. The behaviour of the system is studied for activity magnitudes ranging from low values, where the system behaves in a similar way to contractile active nematics, to high activity values, where a more complex bidirectional flow regime emerges. For these simulations, we chose $\xi \in [0, 150]$ Pa because the bidirectional flow regime is captured within this activity strength range, and we chose l = w/3 microns.

4.3.3.1 Solution profiles for a fixed HAN region width and varying activity strength

In this section, we present results for varying positive activity parameter values. Figure 4.9 shows a plot of the director angle $\xi = [0.1, 1, 10, 100]$ Pa. For activities $\xi = 0.1$ and 1, extensile active nematics behave similarly to contractile active nematics, with an undistorted director angle in both the left and right planar regions and localised flow in the HAN and transition regions. This is because the activity strength values are too weak to generate significant flow. In this flow regime, the system is characterised

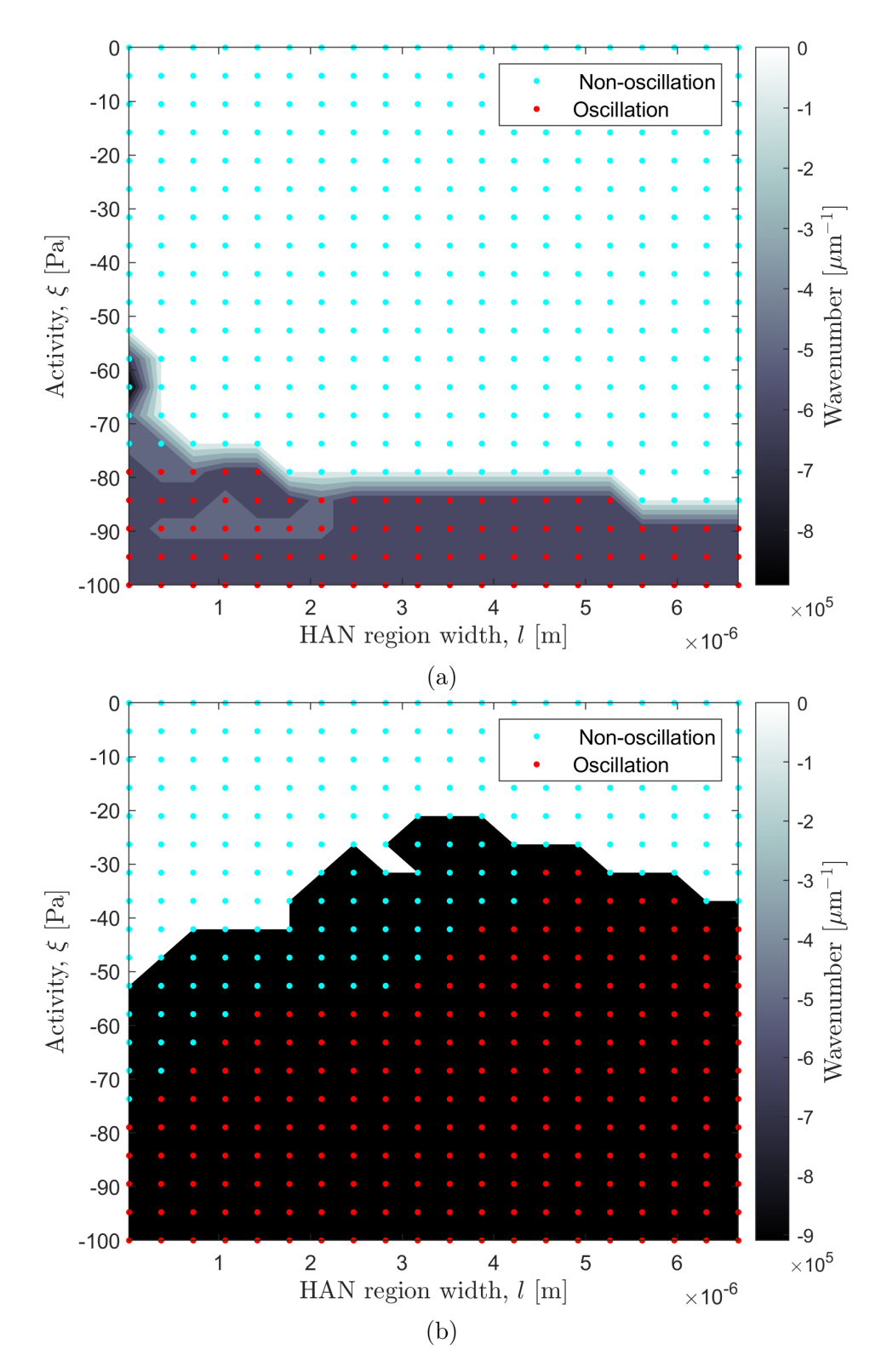


Figure 4.8: Sketches showing oscillations for planar left and planar right regions spanning (ξ, l) . (a) Sketch showing oscillations for the planar left region. (b) Sketch showing oscillations for the planar right region. The red dots represent oscillatory flow and the cyan dots represent non-oscillatory flow. The black region indicates significant frequency, and the cyan dots within this black region represent very low-amplitude oscillations that are not classified as oscillations.

by approximately rectilinear flow in both planar regions, with a maximum velocity of the order of 10^{-7} m/s, as shown in Figures 4.9(a)–(b). In the HAN region, the system is characterised by circulatory flow with director distortion. Increasing activity to 10 retains the flow structure but with a maximum velocity of the order of 10^{-5} m/s (see Figure 4.9(c)). The flow direction also remains unchanged, unlike in the case of contractile nematics, for which the flow changes direction for $\xi = -1$ Pa. For higher activity strengths, the system displays bidirectional flow at the inlet and outlet, with a maximum velocity of the order of 10^{-4} m/s (see Figure 4.9(d)). This flow is characterised by a significant change in the form of velocity induced by the HAN region.

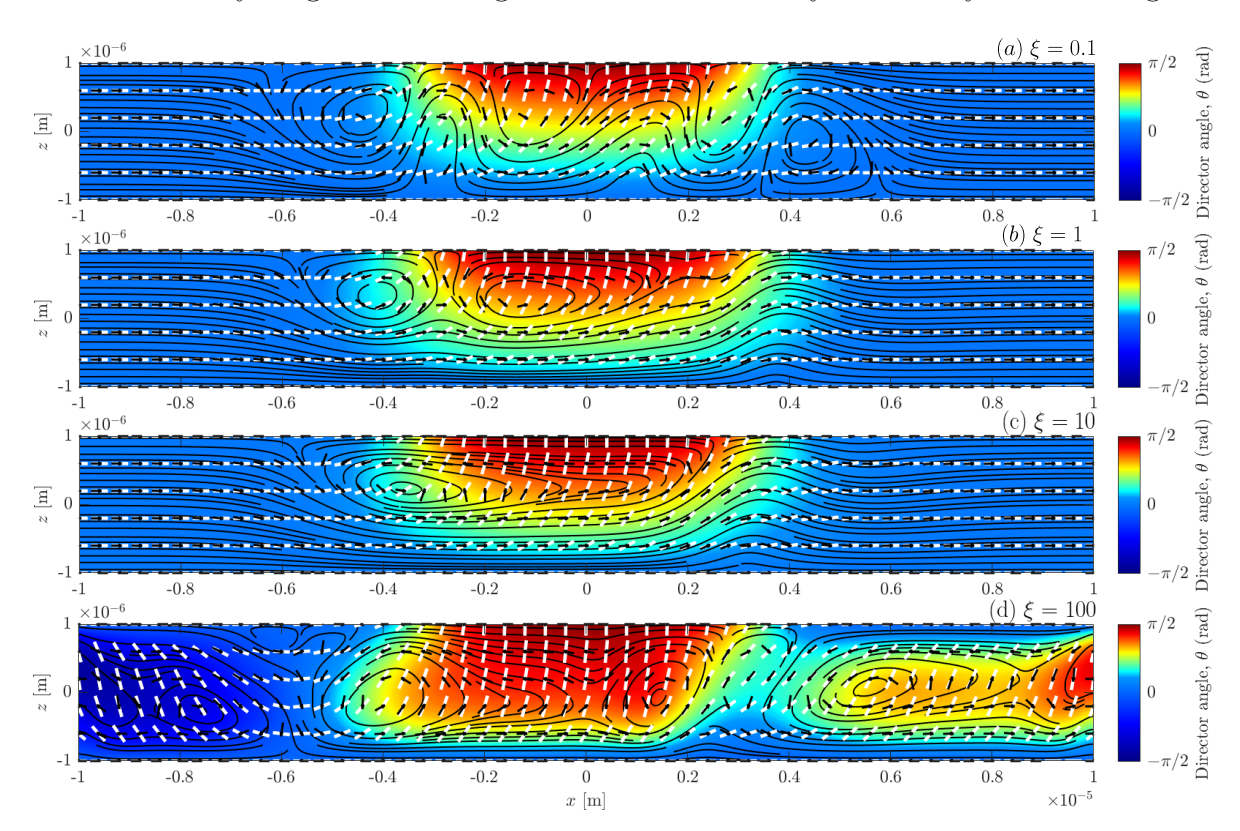


Figure 4.9: Plot of the director angle in region (x, z) for (a) $\xi = 0.1$ Pa, (b) $\xi = 1$ Pa, (c) $\xi = 10$ Pa, (d) $\xi = 100$ Pa with w = 20 microns and at t = 2 seconds. The panels display the streamlines (black lines), director (white rods), flow direction (black arrows), and the director angle (background colour).

4.3.3.2 Flow measure for varying activity and fixed HAN region width

To fully assess the nature of the flow in the left and right planar regions, we numerically integrate u and |u| at the left and right boundaries. We denote the velocity on the left

and right boundaries with u_L and u_R , respectively. For a unidirectional flow, we expect $\int u dz = \int |u| dz$ and for a bidirectional flow, we expect $\int u dz \neq \int |u| dz$.

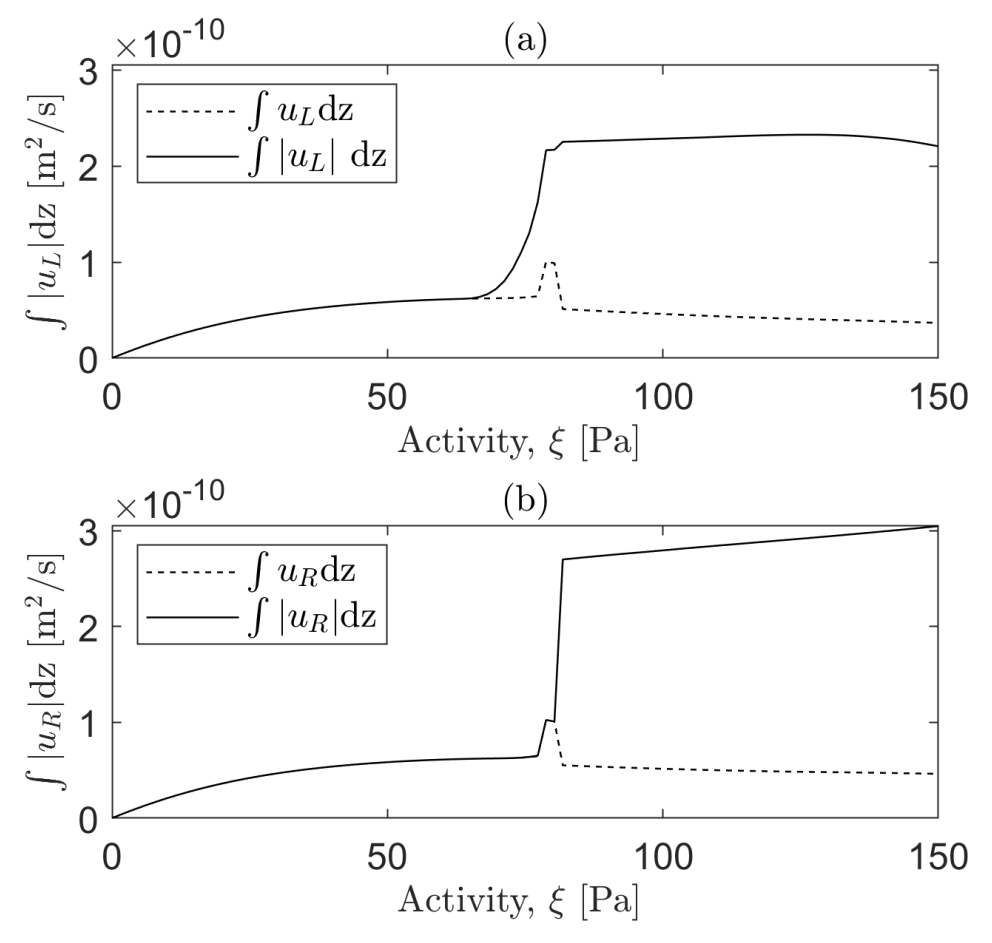


Figure 4.10: (a) $\int u_L dz$ and $\int |u_L| dz$, (b) $\int u_R dz$ and $\int |u_R| dz$ as a function of activity for l = w/3 microns.

Figure 4.10 shows that the system exhibits two different types of flow for extensile active nematics. In Figure 4.10(a), for the left boundary, we observe a unidirectional flow for approximately $\xi \in [0, 67]$ Pa, since $\int u_L dz = \int |u_L| dz$, and for approximately $\xi > 67$ Pa, we have a bidirectional flow. On the right boundary, we observe unidirectional flow for approximately $\xi \in [0, 80]$ Pa and bidirectional flow for approximately $\xi > 80$ Pa as shown in Figure 4.10(b).

Our results reveal the emergence of bidirectional flow in the planar regions at sufficiently high activity values. By integrating the velocity along the left and right boundaries, we find that the flow transitions from unidirectional at low activity to bidirectional at higher activity, with $\int u \, dz \neq \int |u| \, dz$. On the left boundary, bidirectional flow appears

for $\xi \gtrsim 67$ Pa (see Figure 4.10(a)), while on the right boundary it appears for $\xi \gtrsim 80$ Pa (Figure 4.10(b)). This behaviour is consistent with observations in [211], where bidirectional flows arise in sufficiently wide channels due to hydrodynamic instabilities of extensile active nematics. Similar to the review by Thampi, our bidirectional flow is anti-parallel with zero velocity at the channel centerline and maxima near the boundaries. However, unlike the review by Thampi, which employed periodic or circular channels to facilitate unidirectional flow, our simulations use standard flow conditions with fixed boundaries, leading naturally to a transition from unidirectional to bidirectional flow. This shows the influence of boundary anchoring and channel confinement on the symmetry and threshold of the flow transition.

The significant change in flux, with a sharp transition, results from symmetry breaking driven by the interaction between activity and boundary conditions. This phenomenon is crucial for applications like controlling fluid transport in microfluidic devices, where precise flow measurement is essential. Additionally, it holds potential for sensing technologies, as such large-scale transitions can be used to detect small changes in system parameters.

4.3.3.3 Flow profiles for varying activity and HAN region width

One of the objectives of this research is to explore the potential application of sensor design. Active nematics can cause long-range effects in the orientation and flow of active fluids through small changes in their alignment. This could potentially be useful in the development of sensors. To investigate whether geometric parameters can change the system from unidirectional flow to bidirectional flow, we consider a range of HAN region widths from w/1000 to w/3 microns.

To classify the solution, we use four Boolean tests based on a threshold parameter

 $\epsilon = 0.1$. Each test returns either true or false:

UU:
$$\left[\left| \frac{\int |u_L| \, dz - |\int u_L| \, dz}{|\int u_L| \, dz} \right| < \epsilon \right] \text{ and } \left[\left| \frac{\int |u_R| \, dz - |\int u_R| \, dz}{|\int u_R| \, dz} \right| < \epsilon \right], \tag{4.49}$$

BB:
$$\left[\left| \frac{\int |u_L| \, dz - |\int u_L| \, dz}{|\int u_L| \, dz} \right| > \epsilon \right] \text{ and } \left[\left| \frac{\int |u_R| \, dz - |\int u_R| \, dz}{|\int u_R| \, dz} \right| > \epsilon \right], \tag{4.50}$$

UB:
$$\left[\left| \frac{\int |u_L| \, dz - |\int u_L| \, dz}{|\int u_L| \, dz} \right| < \epsilon \right] \text{ and } \left[\left| \frac{\int |u_R| \, dz - |\int u_R| \, dz}{|\int u_R| \, dz} \right| > \epsilon \right], \tag{4.51}$$

BU:
$$\left[\left| \frac{\int |u_L| \, dz - |\int u_L| \, dz}{|\int u_L| \, dz} \right| > \epsilon \right] \text{ and } \left[\left| \frac{\int |u_R| \, dz - |\int u_R| \, dz}{|\int u_R| \, dz} \right| < \epsilon \right]. \tag{4.52}$$

The notations UU, BB, UB, and BU represent different flow patterns. UU is used to represent unidirectional flow in both the planar left and planar right regions, UB is used to represent unidirectional flow in the planar left region and bidirectional flow in the planar right region, BU is used to represent bidirectional flow in the planar left region and unidirectional flow in the planar right region, and BB is used to represent bidirectional flow in both regions.

Explicitly, we get unidirectional-unidirectional flow (UU) if UU = true, bidirectional-bidirectional flow (BB) if BB = true, unidirectional-bidirectional flow (UB) if UB = true, and bidirectional-unidirectional flow (BU) if BU = true.

Figure 4.11 shows the different solution states of the system for various values of the activity strength and HAN region width. By analysing this figure, we can capture the system's behaviour across the bulk of the channel and better understand the different solution states. The green dots represent bidirectional flow throughout the region triggered by high activity parameter values. The cyan dots correspond to the flow regime BU, which indicates asymmetric behaviour for the flow in the planar left region and symmetric behaviour for the flow in the planar right region. The red dots represent UU, indicating unidirectional flow throughout the region, which occurs for lower and intermediate values of the activity strength. It is interesting to note that the transition from UU to BB depends on both the HAN region width and the activity strength.

Bidirectional flow is due to the HAN distortion, which includes bend and splay distor-

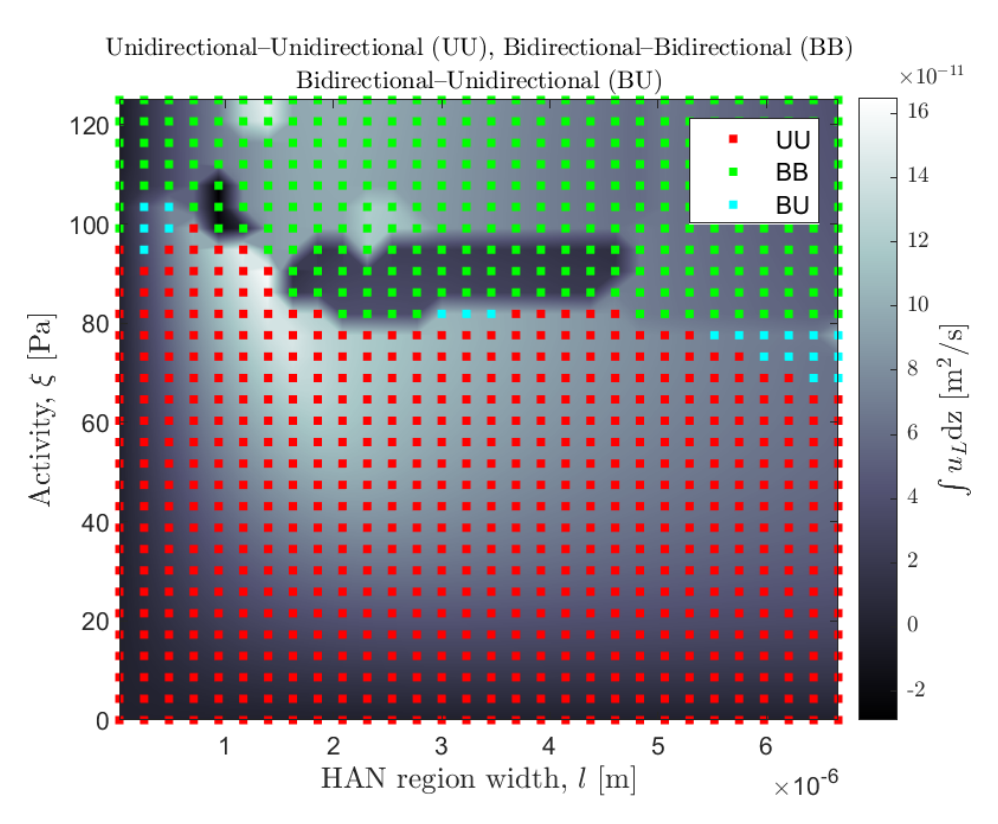


Figure 4.11: Plot showing the different solutions states as ξ and l vary. The green dots represent unidirectional-unidirectional (UU), the red dots represent bidirectional-bidirectional (BB), and the cyan dots represent bidirectional-unidirectional (BU) flow. The background colour is the flux at the left-hand boundary.

tions, but it is mostly bend in one region (left edge of HAN-planar boundary and splay in another (right edge of HAN-planar boundary), so these might affect where flow is initiated, which might cause two types of flow, and so bidirectional flow happens.

4.3.4 Numerical calculations II: periodic conditions

In this section, we study the flow of active nematics in a channel under periodic conditions. Additionally, we consider the effect of different elastic constants on the director orientation and flow velocity.

The normal flow condition in the previous section was a model of an infinite region and an isolated HAN region. The periodic condition models multiple HAN regions, all a distance w apart. So, here we consider how multiple HAN regions interact with each other.

We consider the model in Section 4.3 by applying periodic conditions at the left- and right-hand side boundaries $x = \pm w/2$, keeping the Dirichlet boundary conditions at the top and bottom walls. This means that $\theta_L = \theta_R$, $\theta_{xL} = \theta_{xR}$ and $u_L = u_R$, $u_{xL} = u_{xR}$, where θ_L and θ_R represent the director angle at the left-hand and right-hand boundaries, respectively, and u_L and u_R denote the velocity at the left-hand and right-hand boundaries, respectively. To ensure convergence of the solution, we enforce the pressure-point condition at a single point (x, z) = (-d/2, 0). Our simulations are conducted for 2 seconds, again using the COMSOL Multiphysics® Software Version 6.1 [31], for contractile and extensile active nematics. In the case of contractile active nematics, we choose $\xi \in [-100, 0]$ Pa, whereas for extensile active nematics, we choose ξ from the range [0, 150] Pa, and we choose $\xi \in [w/1000, w/3]$ microns.

4.3.4.1 Investigation of flow profiles for contractile nematics

Our results show that, similar to the normal flow boundary condition case, the system is characterised by unidirectional flow, recirculation, and oscillatory flow as the magnitude of the activity parameter values increases from low to high values. Here, we present only the results for high activity strengths, since other results are very similar to the normal flow scenario.

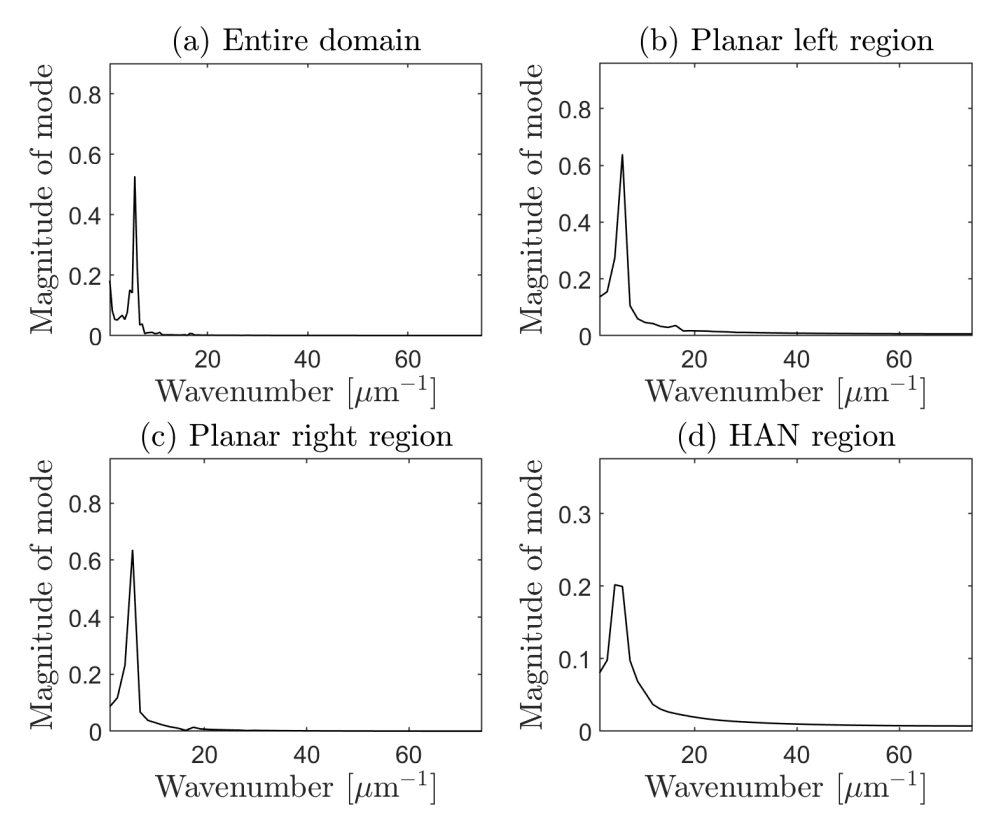


Figure 4.12: Plot of the mode magnitude versus the spatial frequency for $\xi = -100$: (a) entire region, (b) left planar region, (c) right planar region (d) HAN region.

Figure 4.12 displays the mode magnitude against the spatial frequency for the entire domain, the two planar regions, and the HAN region. The system is characterised by an oscillatory flow, which is dominant in the left and right planar regions, each with a magnitude of mode of approximately 32 and spatial frequency of approximately 5.94 μ m⁻¹ for each of the planar regions, as shown in Figures 4.12(b) and 4.12(c), respectively. The HAN region (see Figure 4.12(d)), is more difficult to characterise since the frequency spectrum is broader and has a lower peak value. The results are similar to those we obtained when we applied normal flow conditions.

As in the normal flow scenario, we performed a spectral frequency analysis for contractile nematics, considering varying the activity strength values and HAN region widths. Figure 4.13 is similar to Figure 4.7, and so, for the contractile nematics, the boundary condition does not seem to significantly affect the flow and the behaviour of the

director.

4.3.4.2 Investigation of flow profiles for extensile nematics

We now perform our computation for a fixed value of the width of the HAN region, l, and vary the value of the activity parameter, ξ , for extensile nematics. Since we use periodic boundary conditions, $u_L = u_R$, and so, we need only examine the flux at the left-hand boundary.

As in the normal flow case, the solutions are characterised by two distinct scenarios: unidirectional and bidirectional flow. The transition between these states is marked by a value of a critical activity parameter $\xi \approx 67$ Pa, below which the system exhibits unidirectional flow, and above, which we get bidirectional flow (see Figure 4.14). In the current case, the bidirectional flow is characterised by two different forms, as shown in the inset plots in Figure 4.14. This differs slightly from the system behaviour under normal flow conditions in that solutions using normal flow conditions are characterised by critical activity $\xi \approx 67$ Pa on the left boundary and $\xi \approx 80$ Pa on the right boundary. To examine the two transition points illustrated in Figure 4.16, we generate a velocity plot of the region (Figure 4.15), in which the velocity is represented by the background colour. We investigate the flow before the first transition at $\xi \approx 33$ Pa. The system exhibits a unidirectional flow characterised by circulations in the HAN region (see Figure 4.15(a)). As activity increases to $\xi \approx 83$ Pa, the flow becomes bidirectional, characterised by more circulation, with $u_L < 0$ on the lower half on the left-hand side of the channel and $u_L > 0$ on the upper half of the right-hand side (see Figure 4.15(b)). Increasing further the activity strength to $\xi \approx 86$ Pa, we observe that the change in the circulation region has caused a different kind of bidirectional flow, characterised by $u_L > 0$ in the upper half and $u_L < 0$ in the lower half of the channel with reduced circulation as shown in Figure 4.15(c).

Next, we perform simulations by varying the activity and the HAN region width. We chose $\xi \in [0, 100]$ Pa and l = [w/1000, w/3] microns and simulated for 2 seconds. We

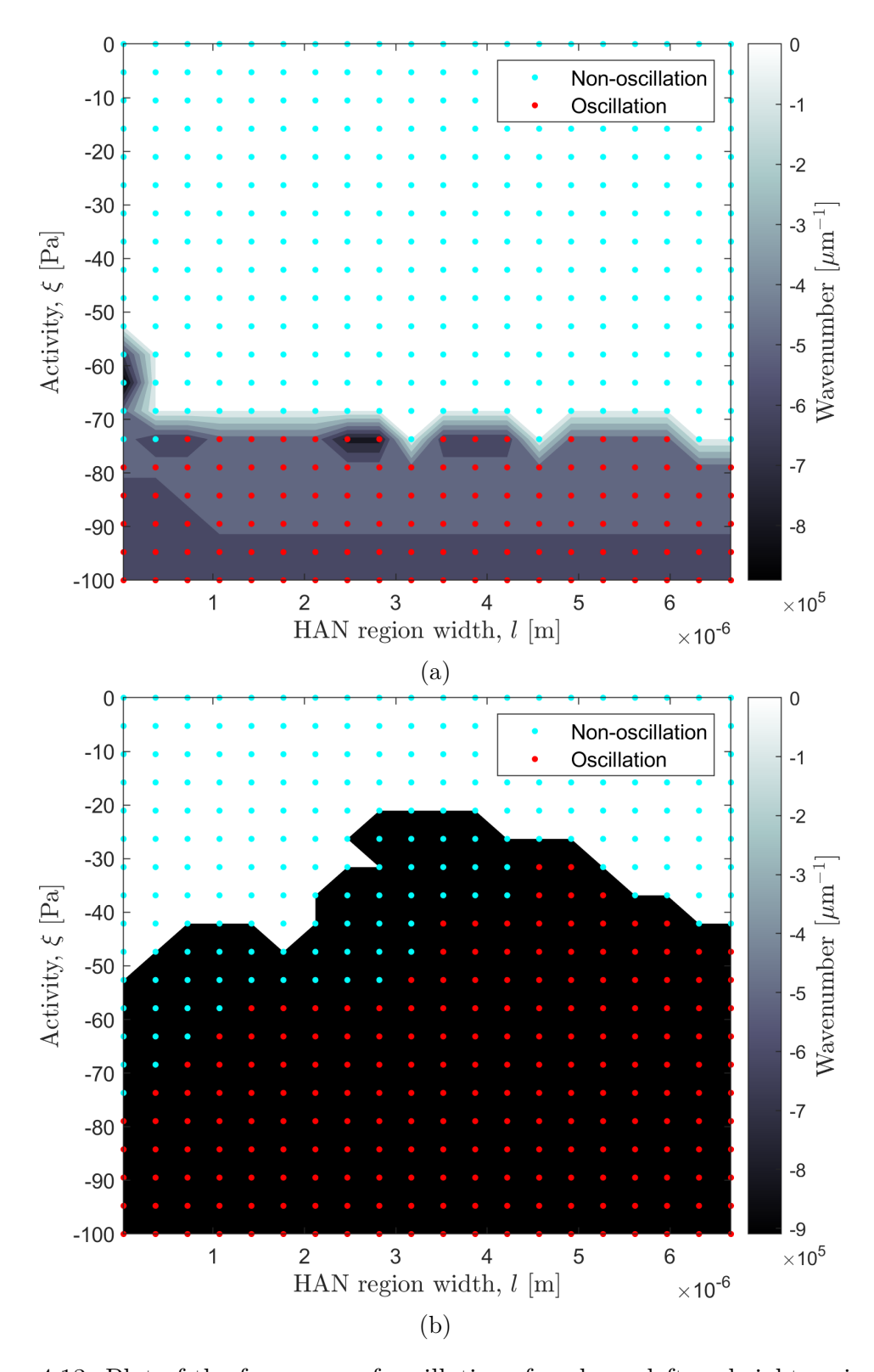


Figure 4.13: Plot of the frequency of oscillations for planar left and right regions as functions ξ and l, respectively. The red dots represent systems we classify as having oscillatory flow and the cyan dots represent systems with non-oscillatory flow. The black region indicates significant frequency, and the cyan dots within this black region represent very low-amplitude oscillations that are not classified as oscillations.

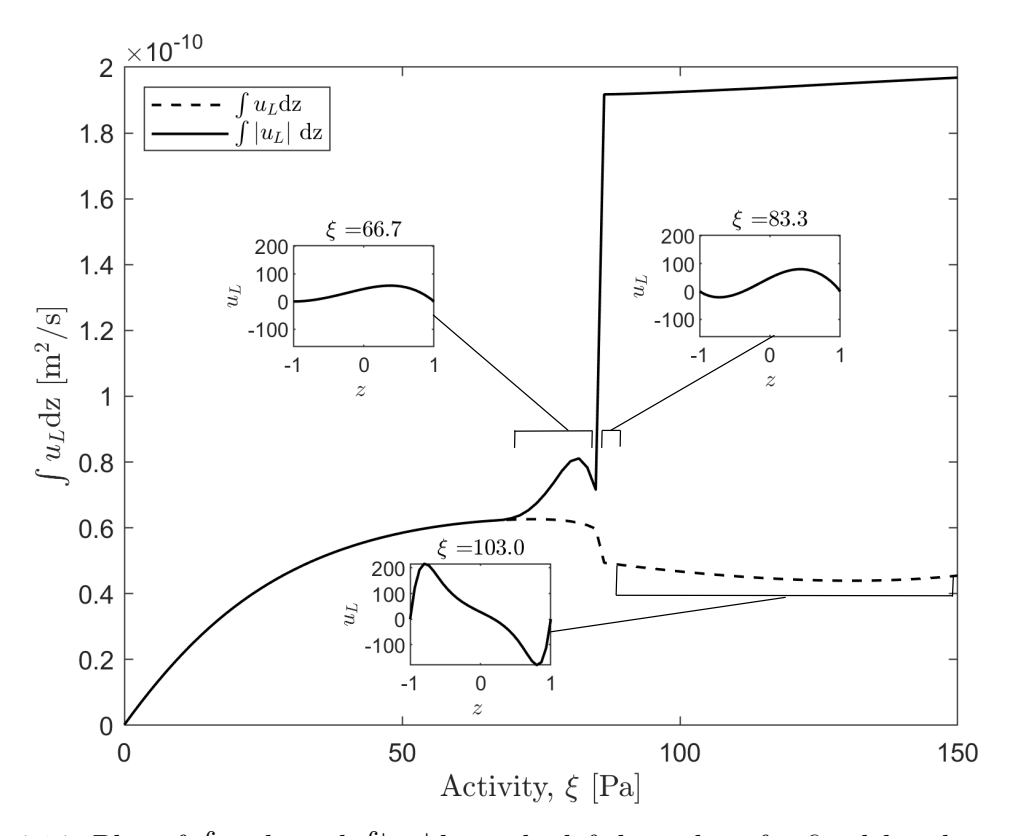


Figure 4.14: Plot of $\int u_L dz$ and $\int |u_L| dz$ at the left boundary for fixed l and varying ξ .

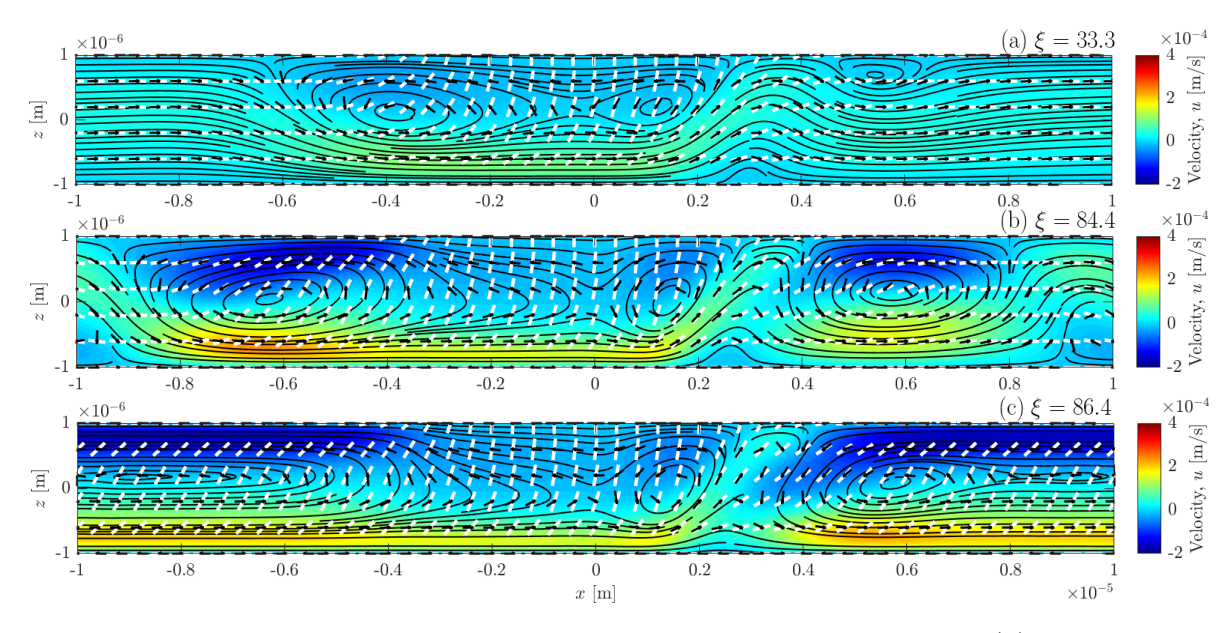


Figure 4.15: Plot of the velocity in the region spanned by x and z for (a) $\xi = 33.3$ Pa, (b) $\xi = 83.3$ Pa, and (c) $\xi = 86.4$ Pa. Streamlines (black lines), director (white rods), flow direction (black arrows) and (background colour) flow velocity

•

then apply the test functions defined in equations (4.50)–(4.50) to determine the nature of the flow. Since the boundary condition is periodic, we know that $\int u_L dz = \int u_R dz$. Therefore, we have only two possibilities UU and BB. In essence, when compared to the normal flow case, the BU solution is replaced by UU for small and high values of l, but for intermediate values of l, the BU solution is replaced by BB, as shown in Figure 4.16.

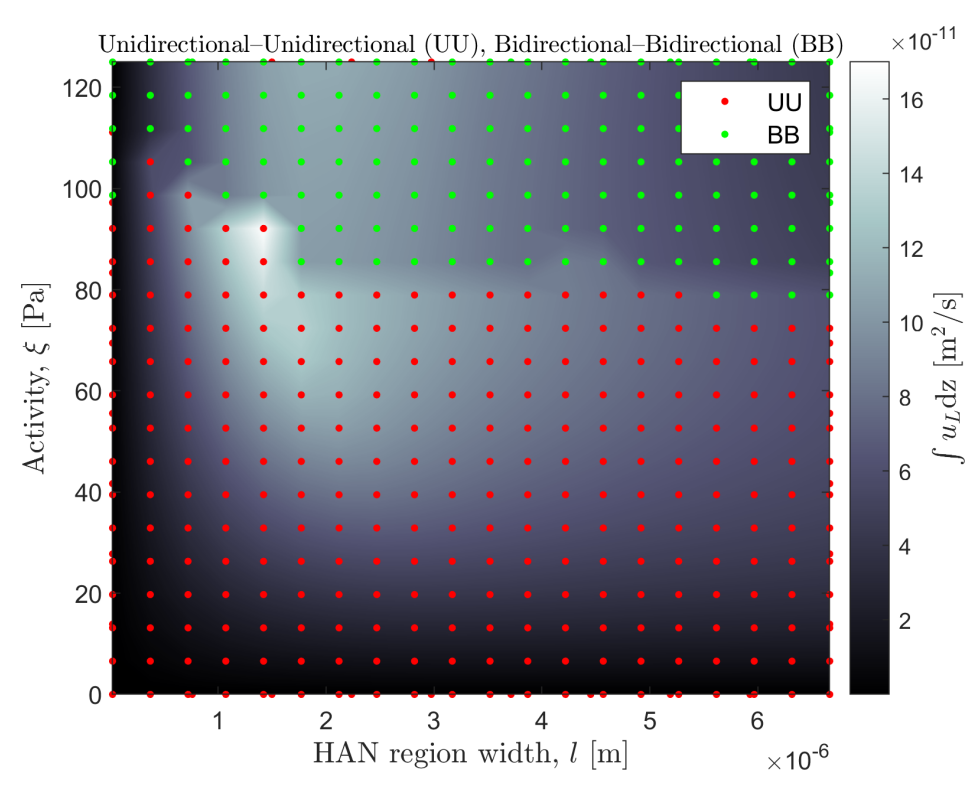


Figure 4.16: Plot showing the different solutions states as ξ and l vary. The green dots represent unidirectional-unidirectional (UU), and the red dots represent bidirectional-bidirectional (BB) flow. The background colour is the flux at the left-hand boundary.

4.3.5 Effect of the elastic constant ratio on director orientation and flow velocity

In this section, we investigate how the ratio of splay and bend elastic constants influences the behaviour of the system, particularly the flow and director orientation. The motivation for this study stems from the fact that distortions in the director field generate flow in active nematics: extensile systems are unstable to bend distortions, while contractile systems are unstable to splay distortions. Therefore, the relative amounts of splay and bend in the system are expected to have a critical impact on the resulting flow patterns.

To systematically study this effect, we vary the elastic constants K_1 (splay) and K_3 (bend) while keeping the elastic energy of a simple HAN state unchanged. This approach ensures that changes in the flow behaviour are due to the relative anisotropy of the elastic constants rather than changes in the overall elastic energy.

For the simple HAN state, the director profile is given by $\theta(z) = \pi/4 + \pi z/2d$. Using the expression for the elastic free energy density, the total elastic energy of this configuration is given as

$$E_{\tau} = \frac{\pi^2}{16d} \left(K_1 + K_3 \right), \tag{4.53}$$

where E_{τ} represents the elastic energy associated with the HAN distortion. To systematically vary the elastic constants from reference MBBA values [202], we introduce scaling factors α and β such that $K_1 \to \alpha K_1$ and $K_3 \to \beta K_3$. Substituting into equation (4.53) gives the elastic energy explicitly in terms of the free energy and the scaling parameters

$$E_{\tau} = \frac{\pi^2}{16d} \left(\alpha K_1 + \beta K_3 \right). \tag{4.54}$$

This formulation allows us to independently control the splay-to-bend ratio while monitoring its effect on flow generation, providing insight into how elastic anisotropy shapes active nematic dynamics. Next, we define $\alpha K_1/\beta K_3 = \kappa$. If we require the free energies (4.53) and (4.54) to remain equal as we change the elastic constant, then equating the right-hand side of equation (4.53) to the right-hand side of equation (4.54), gives

$$\beta = \frac{(K_1 + K_3)}{K_3(\kappa + 1)}. (4.55)$$

The definition of κ then gives

$$\alpha = \frac{(K_1 + K_3)}{K_1(\kappa + 1)}\kappa. \tag{4.56}$$

Substituting the values α and β in equation (4.54) will automatically leave the free energy unchanged as we change κ .

We again perform our simulations until t = 2 seconds using the COMSOL Multiphysics® Software Version 6.1 [31] to analyse the behaviour of both contractile and extensile active nematics. We choose $\kappa \in [0.03, 16]$, and initially consider the activity values of $\xi = \pm 0.0001$ Pa. We chose the range of κ to ensure that the splay and bend elastic constants fall within the range of experimental data [202]. The values of K_1 and K_3 as functions of κ are shown in Figure 4.17. These values (see Table 6) fall within the range of elastic constants reported experimentally for nematics. For instance, Kemkemer et al. [97] measured splay and bend elastic moduli in the range $K_{11} \approx (1.3 (2.6) \times 10^{-13} \text{ N}$ and $K_{33} \approx (1.3 \times 10^{-13} - 1.04 \times 10^{-12}) \text{ N}$, which are consistent with the values adopted here. These values are also in agreement with the results of [109], where the orientational elastic constant of a bulk nematic liquid crystal was found to be 0.5×10^{-14} N. The special case exists where $\kappa = 1$, when $K_1 = K_3 = 6.75 \times 10^{-12}$ N. For reference, in previous sections we used $K_1 = 6 \times 10^{-12} \text{ N}$ and $K_3 = 7.5 \times 10^{-12} \text{ N}$. By varying κ over this range, we explore elastic constants that extend below and above the values used in previous sections, while remaining within experimentally reported ranges.

In Figure 4.18, we present a plot showing the director orientation in relation to the scaling ratio κ . Below $\kappa = 1$, the director tends to favour the splay configuration because $K_3 > K_1$ as shown by the first two sketches in Figure 4.18, while above $\kappa = 1$, the director tends to favour the bend configuration because $K_3 < K_1$. At $\kappa = 1$, the director's orientation balances, resulting in a linear transition from planar orientation at z = -d/2 to homeotropic orientation at z = d/2.

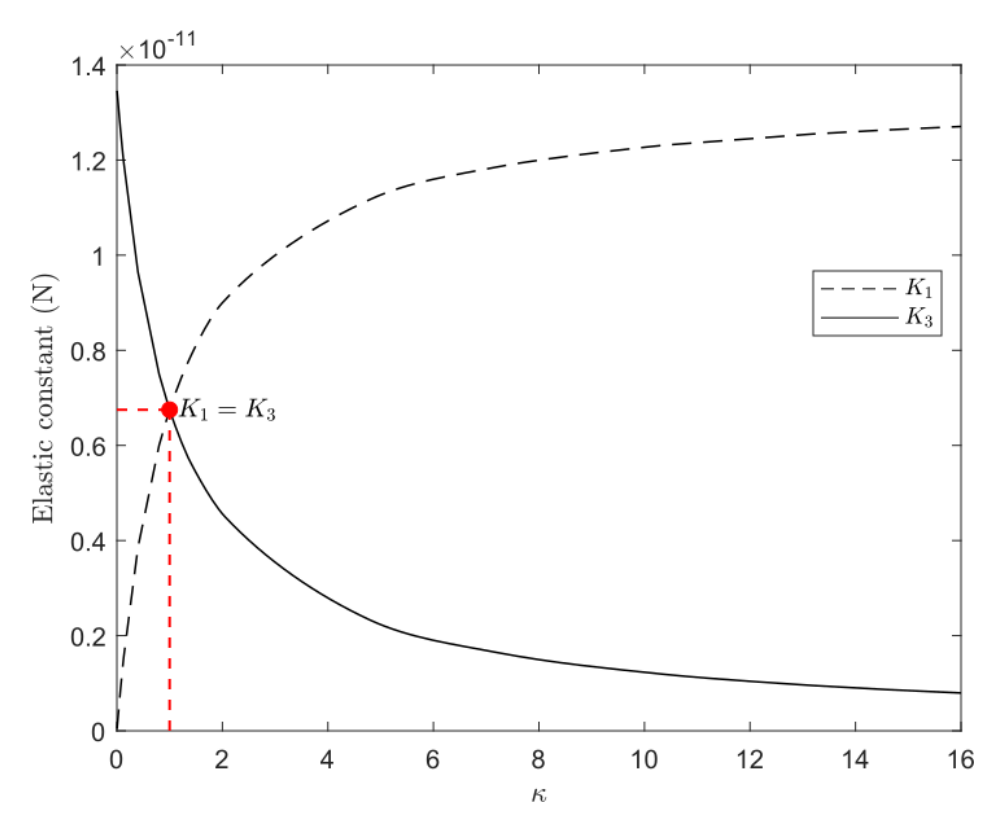


Figure 4.17: Plot illustrating the variation of splay and bend elastic constants with respect to the scaling ratio. The intersection point of the dashed and solid lines occurs when $K_1 = K_3$, indicating $\kappa = 1$, as depicted by the red dashed line. Additionally, the dashed black line represents the behaviour of the splay elastic constant, while the black solid line represents the behaviour of the bend elastic constant.

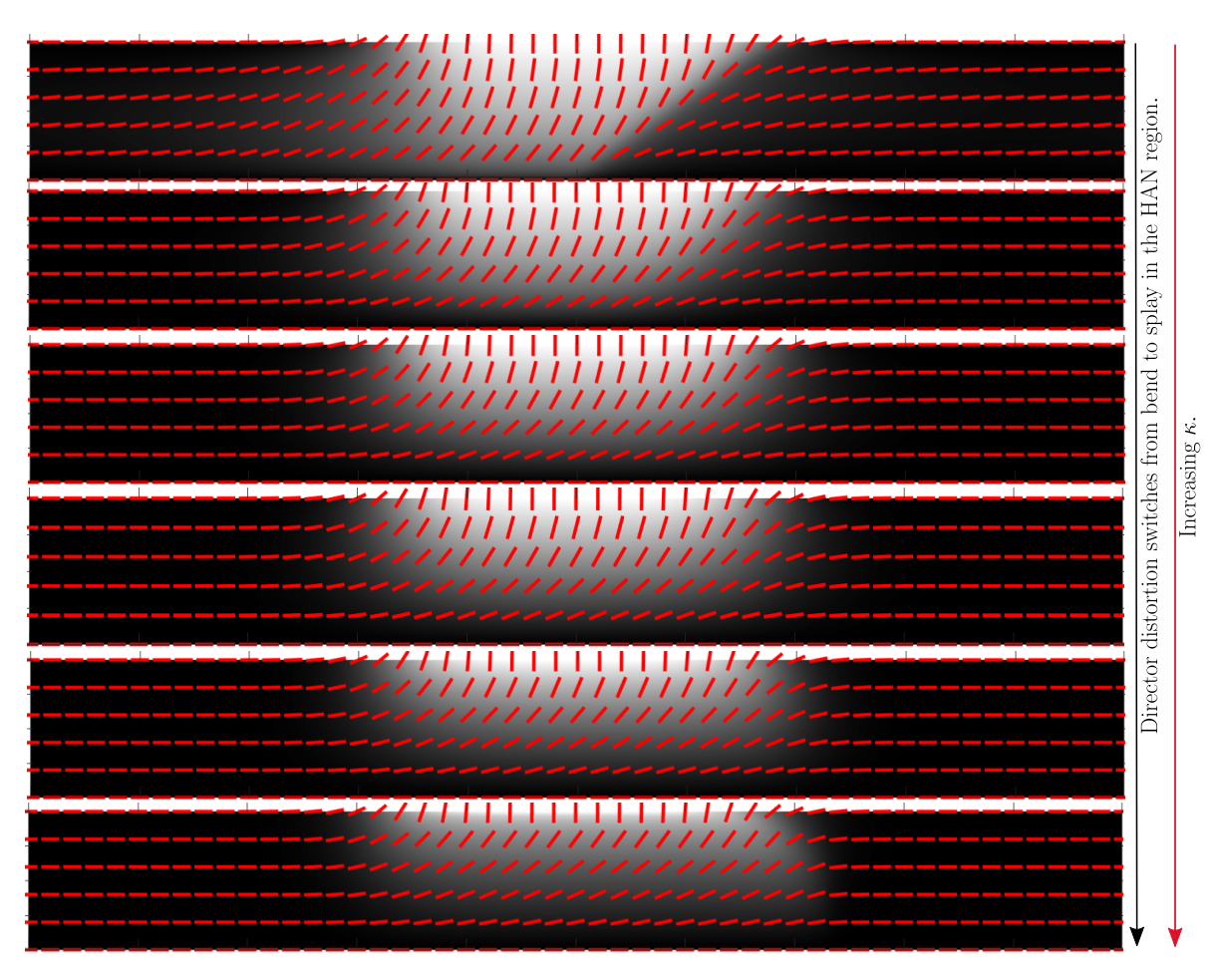


Figure 4.18: Schematic showing the director distortion from homeotropic to planar anchoring as κ increases for $\xi \pm 0.0001$ Pa, w=20 microns, l=w/3 microns and $\kappa = [0.04,\ 0.4,\ 0.8,\ 1,\ 2.31,14.4]$, respectively. Going down the plots, K_1 increases, while K_3 decreases.

We then explored the impact of the elastic constants on the flow velocity. Our observations reveal that the flow is the same regardless of whether it is contractile or extensile when the value of the activity parameter is very small. To investigate what happens when the value of the activity parameter increases, we consider the effects of varying both the splay and bend scaling ratio, κ , and the value of the activity strength. We choose $\xi \in [0, \pm 0.5]$ Pa and $\kappa \in [0.03, 16]$.

In Figure 4.19, we plot the director angle, in the center of the channel, that is, for (x,z)=(0,0), as a function of the scaling ratio κ . As expected, the director angle decreases as the scaling ratio κ increases. Bend configuration is induced for the higher values of κ , while the splay configuration K_1 is induced for lower values of κ . The director angles at the centre of the HAN region are consistent across the different activity strengths.

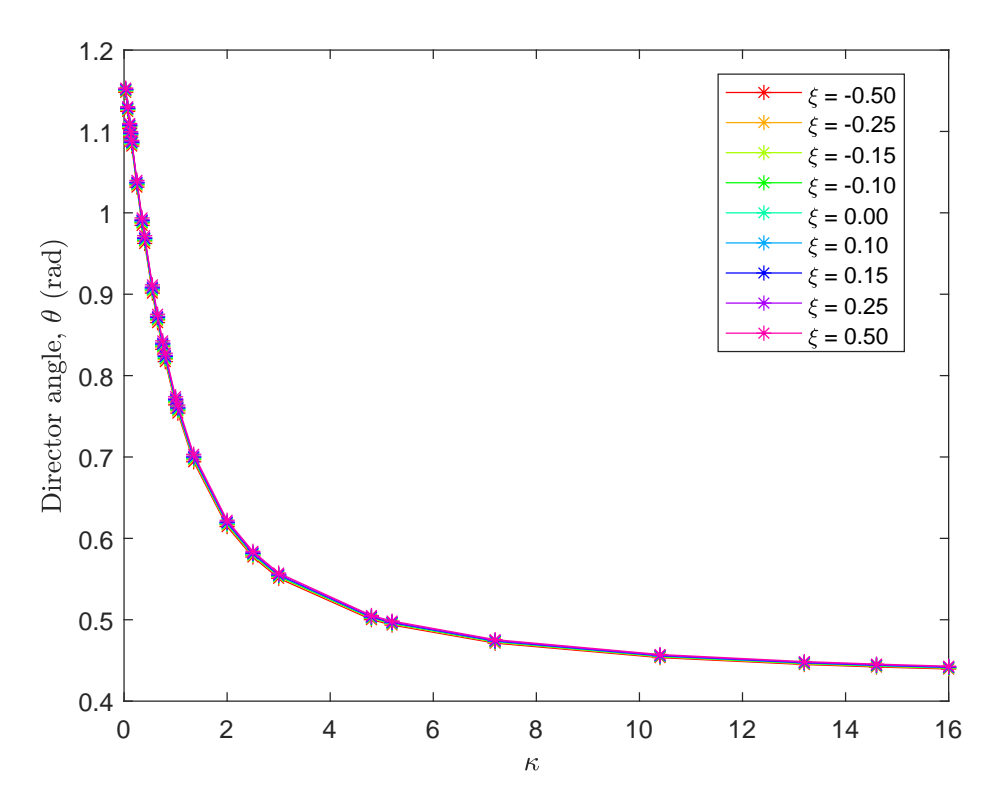


Figure 4.19: Plot of director angle in the centre of the channel as function of κ for $\xi = [0 \pm 0.1, \pm 0.15, \pm 0.25, \pm 0.5]$ Pa.

4.3.5.1 Flux measurement for varying splay/bend scaling ratio

We also analyse the flux at the left-hand side boundary, as a function of the splay/bend scaling ratio κ for $\xi = [0, \pm 0.1, \pm 0.15, \pm 0.25, \pm 0.5]$ Pa. Figure 4.20 shows flux as a function of κ for the chosen values of activity. For negative and very small (both negative and positive) values of ξ , the flux transitions from positive to negative as the splay/bend scaling ratio κ increases, as indicated by the green, red, cyan and black curves. However, for sufficiently extensile systems, the flux remains positive for all values of κ . Therefore, for contractile and weakly extensile systems, elasticity can determine the direction of flow.

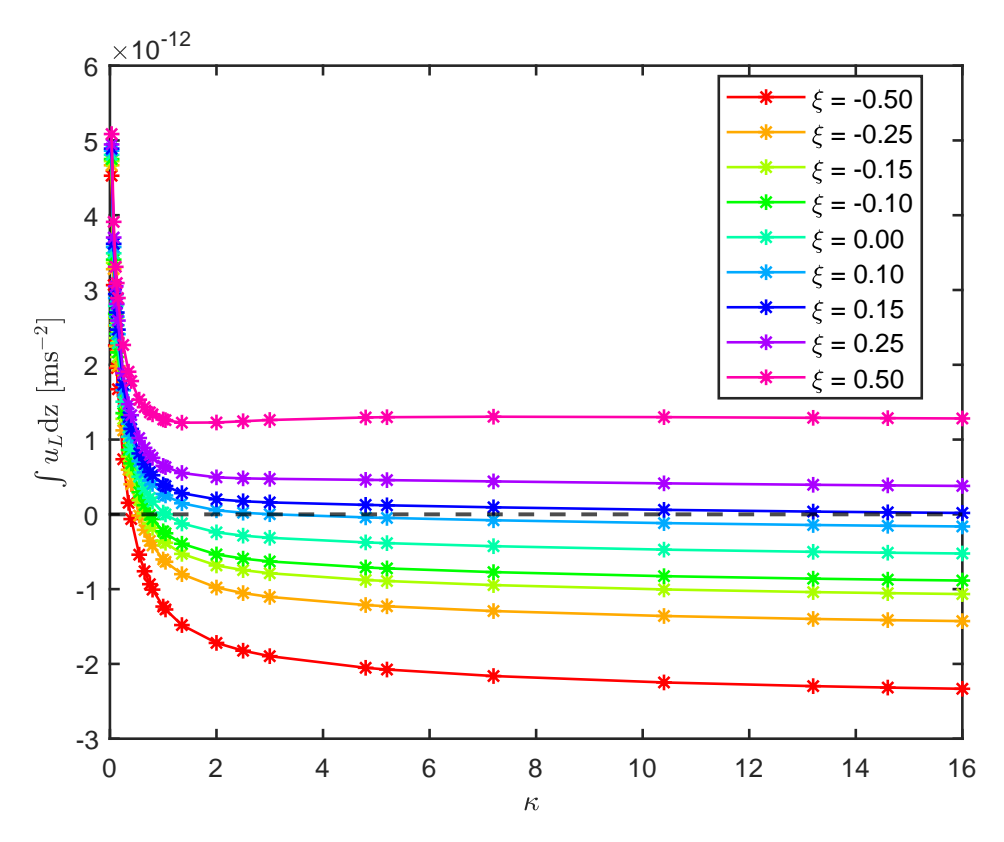


Figure 4.20: Plot of the flux on the left boundary as a function of κ for $\xi = [0 \pm 0.1, \pm 0.15, \pm 0.25, \pm 0.5]$ Pa.

4.3.5.2 Tracking circulation relative to the splay/bend scaling ratio

We also track the circulation in the system and analyse the flow profile for $0.03 \le \kappa \le$ 16. Based on the observed behaviour, we categorise the following contour plots into three groups: $\kappa = 0.03$ to $\kappa = 0.35$, $\kappa = 0.4$ to $\kappa = 1.04$, and $\kappa = 1.10$ to $\kappa = 16$.

In the first category, we present velocity plots for $\kappa = 0.03$, $\kappa = 0.15$, $\kappa = 0.25$, and $\kappa = 0.35$, as shown in Figure 4.21. For $\kappa = 0.03$, the system exhibits a relatively high flow in the HAN region, along with circulations near the bottom wall around the right transition region, accompanied by noticeable director distortion (Figure 4.21(a)). As the splay/bend scaling ratio increases to $\kappa = 0.15$ and $\kappa = 0.25$, new circulation emerges near the top wall of the planar left and right regions, as shown in Figures 4.21(b) and 4.21(c). When κ increases further to 0.35, additional circulation appears near the bottom wall of the planar right region (Figure 4.21(d)), while the circulation in the right transition region decreases in size. This occurs because bend distortion becomes more difficult over splay distortion, leading to distortions in the director field at the bottom of the HAN region. Essentially, the system favours the splay configuration when $K_1 \ll K_3$, and splay distortion does not lead to flow in an extensile system.

Next, we examine the velocity profile and circulation in the second category considering $\kappa = 0.40$, 0.65, 1.00, and 1.04, where $\kappa = 1.04$ represents a special case where the flux is nearly zero. For $\kappa = 0.40$ and 0.65, we observe a more pronounced circulation in the transition and HAN regions, with a high flow across the center of the region moving toward the right-hand side (Figures 4.22(a) and (b)). When κ increases to 1.00, which is equal to the ratio of the standard MBBA nematic elastic constant for the splay and bend configurations, four distinct loops appear in the HAN region, along with one loop in each planar region (Figure 4.22(c)). Interestingly, for $\kappa = 1.04$, the integral of u_L with respect to z, denoted by $\int u_L dz$, is approximately zero, and the loops in the planar regions extend to the left and right-hand side boundaries, indicating no overall flux (Figure 4.22(d)).

Upon increasing κ to 1.35, the flow becomes negative, indicating a reversal in the velocity direction, as shown in Figure 4.23(a). Additionally, the number of loops in the HAN region is reduced to three. When κ increases to 1.55, the circulation in the planar left and right regions begins to diminish in size, along with the loops in the HAN region, as shown in Figure 4.23(b). Increasing κ further to 2.0, the loops in the

HAN region evolve into two distinct circulations (see Figure 4.23(c)). At a sufficiently high value of κ , specifically $\kappa = 4.8$ (see Figure 4.23(d)), circulation in the HAN region disappears, while circulation in the planar regions further diminishes. This indicates that for $\kappa < 1.04$, the circulation evolves as κ increases, whereas for $\kappa > 1.04$, the circulation decreases.

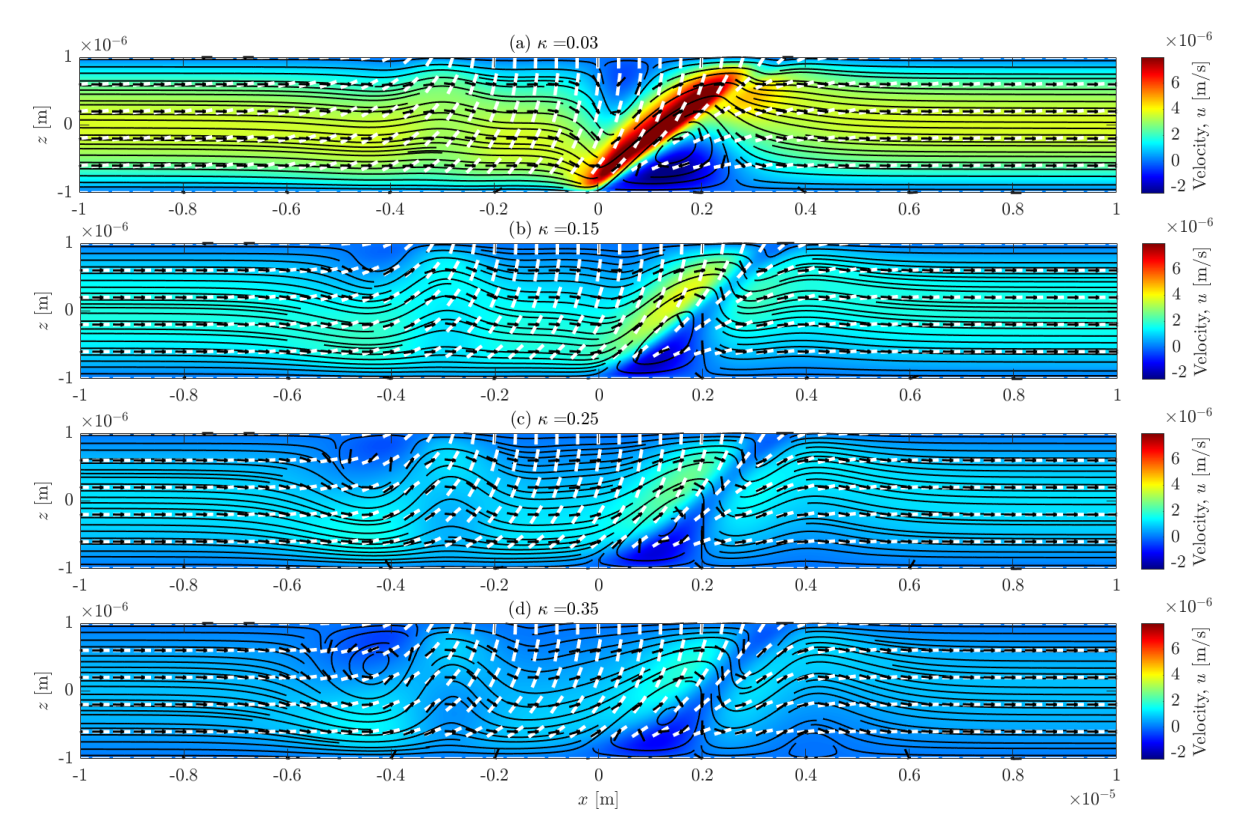


Figure 4.21: Plot of the velocity in the x-direction for $\kappa = 0.03$, $\kappa = 0.15$, $\kappa = 0.25$ and $\kappa = 0.35$, and t = 2 seconds. The panels depict the streamlines (black lines), director (white rods), flow direction (black arrows) and velocity (background colour).

Finally, we consider cases where the splay/bend scaling ratio is significantly greater than $\kappa=0.8$ where we select $\kappa=2.00$, $\kappa=4.80$, $\kappa=14.60$, and $\kappa=16.00$. This is illustrated in Figure 4.23, which again depicts the behaviour of the system in terms of its flow velocity. Within this range of κ values, the system displays similar behaviour, demonstrating negative flow in the bulk of the region, significant distortions of the director around the transition regions, and single circulations in the left and right-hand side transition regions, as well as a singular circulation in the right-hand side planar region, which diminishes as κ increases.

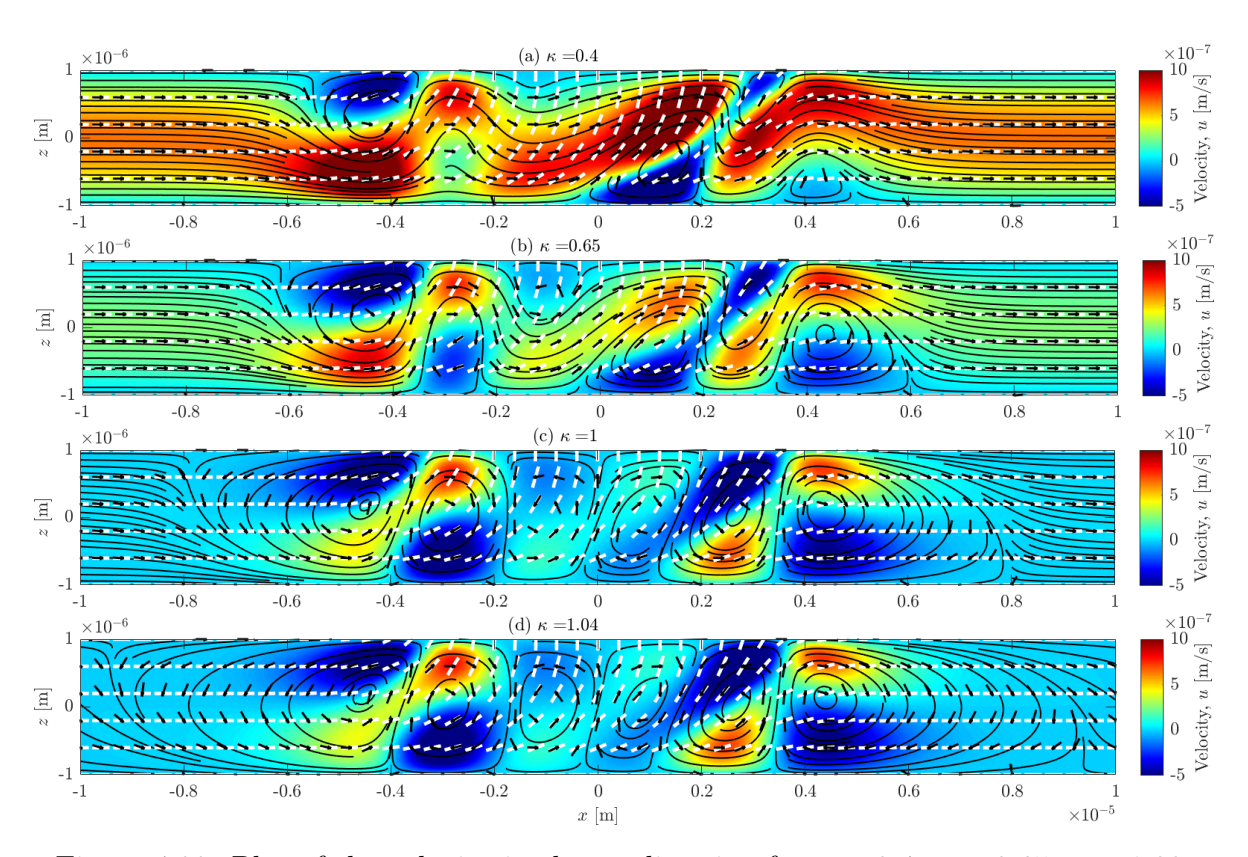


Figure 4.22: Plot of the velocity in the x-direction for $\kappa = 0.4$, $\kappa = 0.65$, $\kappa = 1.00$, and $\kappa = 1.04$, and t = 2 seconds. The panels depict the streamlines (black lines), director (white rods), flow direction (black arrows) and velocity (background colour).

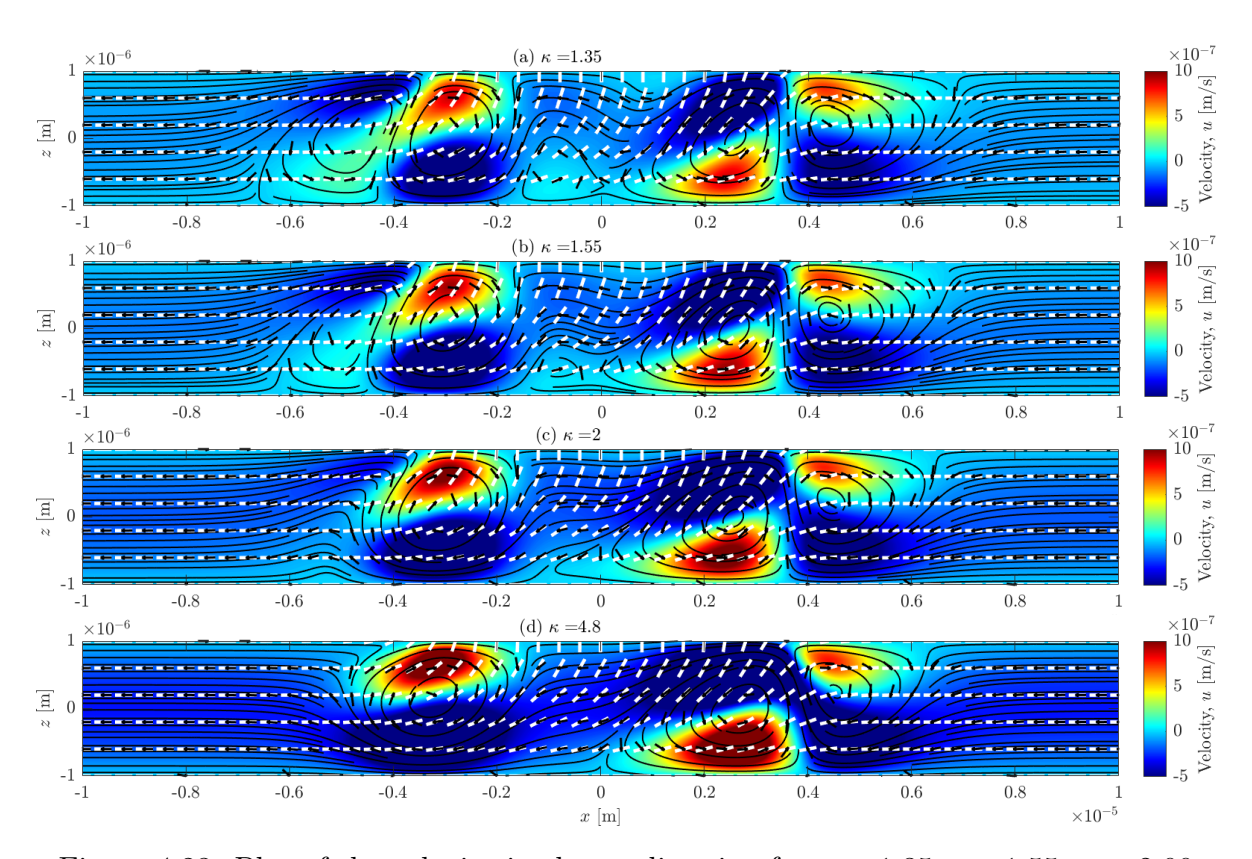


Figure 4.23: Plot of the velocity in the x-direction for $\kappa = 1.35$ $\kappa = 1.55$, $\kappa = 2.00$ and $\kappa = 4.80$, and t = 2 seconds. The panels depict the streamlines (black lines), director (white rods), flow direction (black arrows) and velocity (background colour).

Our findings reveal that as the splay/bend ratio increases, i.e. the bend elastic constant decreases and/or the splay increases, causing significant changes to the flow. For $\kappa < 1$, the system behaves more like a regional flow with reduced recirculations. In this case, the system prefers the splay configuration to minimise energy since $K_1 < K_3$. Since flow distortion reduces the flow in an extensile nematic, the flow is of low magnitude. However, for $\kappa > 1$, the bend configuration is preferred, indicating that $K_1 \ll K_3$, and as extensile nematic in a bend distortion is unstable, increased flow occurs.

4.3.6 Conclusion

In this Chapter, we have examined active nematics in a 2D channel using a mixture of planar and HAN anchoring. Using normal flow and periodic boundary conditions, we characterise the range of flow profiles for varying magnitudes of the activity at a fixed channel width for both contractile and extensile active nematics. We summarised our findings as follows.

4.3.6.1 Normal flow boundary conditions

For low-magnitude activities, both contractile and extensile systems exhibit approximately rectilinear flow in the planar regions. In the HAN and transition regions, the flow is circulatory and is associated with the director distortion. Further increasing the activity strength, the system exhibits more localised flow, reduced circulation, and director distortion. The system exhibits spatial fluctuation for sufficiently high magnitudes of activities for the contractile system, although there are no time-dependent oscillations in the system. In the regime of lower activities for extensile nematics, we observed unidirectional flow, whereas, for high activity strengths, we observed bidirectional flow characterised by an antisymmetric distorted state in the center of the channel. Varying both the activity and the HAN region width, the extensile nematic is characterised by three solutions: UU, BU, and BB. The transition from UU to BB is influenced by both the value of the activity strength and the width of the HAN region. The transition from UU to BB is largely dependent on the activity strength.

We have seen that local disturbances in the director orientation influence the global flow in the system. This suggests that the local dynamics of the system significantly affect the overall behaviour of the system. Since global flow is induced by HAN anchoring, it is plausible to consider its potential use in sensor design.

4.3.6.2 Periodic boundary conditions

For contractile active nematics, the system largely displays behaviour reminiscent of previous observations when subjected to the normal flow condition. Varying both the activity and the length of the HAN region, we observed that extensile active nematics exhibit only unidirectional-unidirectional (UU) flow for both low and intermediate values of activities and all HAN region widths; and bidirectional-bidirectional (BB) flow for higher values of activities and the HAN region width. Bidirectional flow is categorised into two distinct patterns. The first type is characterised by $u_L < 0$ on the lower half on the left-hand side of the channel and $u_L > 0$ on the upper half on the right-hand side. The second type is characterised by $u_L > 0$ in the upper half and $u_L < 0$ in the lower half of the channel.

We also investigated the effects of the ratio between the splay and bend elastic constants on the director orientation and flow behaviour. By varying the splay/bend scaling ratio scaling factor, κ , we observed distinct changes in the elastic properties of the system and their impact on the flow.

Our analysis revealed that the ratio of the splay and the bend elastic constants plays a significant role in determining the preferred director distortion, which leads to a role in determining the flow profile. The system undergoes a transition from positive to negative flux, which indicates a change in the system's flow dynamics at a critical value of elastic constant ratio κ .

At κ above the critical value the flow transitions to a negative flux with more pronounced circulation in the HAN region, emphasizing the interaction between the elastic constants of splay and bend. However, as the activity parameter increases, significant changes

emerge. For lower values of positive activities and all negative activities, the flux changes from positive to negative at a critical value of κ , indicating a change in the dominance of active stress over elastic forces. However, for higher positive activities, the system is characterised by a unidirectional flow with a positive flux, revealing that activity always dominates the elastic forces.

Chapter 5

Two-Dimensional Transient Flow during HAN State Formation

5.1 Introduction

In studying active nematics, the anchoring conditions at the boundaries play a crucial role in determining the flow patterns and the director orientation within the system. In previous chapters, we examined the behaviour of such a system with a focus on static boundary conditions, which reveal that activity strength and the width of the HAN region affect the flow and director orientation. However, real-world applications of active nematics, such as sensors, will involve dynamic boundary conditions that evolve when a disturbance affects the boundary of a layer of liquid crystal. Understanding how localised disturbances and time-dependent changes affect subsequent dynamics is, therefore, essential to envisioned applications, for example, in the conceptual design of sensors. Of particular importance are the timing and mechanism of the system's response to changes in anchoring. In particular, quantifying the response time for characteristic changes to occur following a change in anchoring can help predict the behaviour of the system in real-world applications.

In this chapter, we explore the effects of localised and evolving changes in anchoring by

introducing a time-dependent boundary condition that mimics changes to anchoring in a sensor. In doing so, we aim to capture the transient dynamics and flow evolution in the formation of the HAN state. For contractile nematics, we show how the system evolves in time in the HAN region for different activity strengths and boundary effects. For low activity strengths, the system exhibits behaviours consistent with previous models in Section 4.3.4.1. For high activity strengths, the system exhibits rectilinear flow for early times and oscillatory flow characterised by travelling waves at later times. Our calculations show that the waves travel from right to left in the channel. A temporal frequency analysis demonstrates that the system oscillates in time but later disappears when the HAN state is fully formed, which was not seen in Section 4.3.2.4.

Similar transient effects are observed at low activity strengths for extensile nematics. For high activity strengths, changes in anchoring induce transitions from bidirectional flow to unidirectional flow. These transitions demonstrate how dynamic boundary conditions can significantly change the behaviour of an active nematic.

The results provide crucial insights into the transient dynamics of active nematics under time-dependent boundary conditions. By examining how the HAN state forms and evolves, this investigation lays the groundwork for optimising the design of active nematic systems for practical applications, such as sensors. Furthermore, understanding the interplay between activity and boundary effects can deepen our understanding of active nematics, which might be a guide for better control of their complex behaviours.

The Chapter is structured as follows. We begin by formulating the model in Section 5.2, followed by a series of numerical computations to quantify transient dynamics in Section 5.3. We finish with concluding remarks in Section 5.4.

5.2 Model formulation

To determine the system's response time to a stimulus or a change in anchoring, we investigate the transient dynamics as the director at the upper surface reorients from

planar to homeotropic. We consider the model in Section 4.3.4, where we imposed periodic boundary conditions for the director and flow at the channel inlet and outlet. However, we modify the model by introducing a time-dependent function describing the director orientation at the upper surface in the central region to mimic a change that is to be sensed. Below, we provide a detailed explanation of its implementation and usage.

We solve equations (4.16)–(4.20) numerically, using COMSOL Multiphysics® Software Version 6.1 [31] with a modified boundary condition on the top wall, given in terms of a new ramp function $r_f(t) = 0$ for $t < L_{rf}$ and $r_f(t) = S_{rf}(t - L_{rf})$ for $L_{rf} \le t \le 1/S_{rf} + L_{rf}$ and $r_f(t) = 1$ for $t > 1/S_{rf} + L_{rf}$, where L_{rf} and S_{rf} are the location and slope of the ramp function, respectively, and t is time. The location and slope of the ramp function have units of seconds and inverse seconds, respectively. This function involves a user-defined slope for a linear increase that starts at a specified time, which is determined by the location of the ramp function, L_{rf} [31]. We reformulate the boundary condition at the top wall to incorporate the time-dependent change of anchoring in terms of the ramp function by setting

$$\theta(x) = \frac{\pi r_f(t)}{4} \left[\tanh\left(\frac{(x+l/2)}{\epsilon}\right) - \tanh\left(\frac{(x-l/2)}{\epsilon}\right) \right], \tag{5.1}$$

When $r_{rf}(t) \equiv 1$, we reduce to the model of Chapter 4.

The initial conditions used for all simulations in this chapter are given as

$$u = 0, (5.2)$$

$$v = 0, (5.3)$$

$$\theta(x,z) = \frac{\pi}{4} \left[\tanh\left(\frac{x+l/2}{\epsilon}\right) - \tanh\left(\frac{x-l/2}{\epsilon}\right) \right] \left[\frac{z+d/2}{d}\right], \tag{5.4}$$

representing a quiescent fluid with a spatially varying initial director that smoothly transitions across the region of interest.

In our model, the ramp function $r_f(t)$ prescribes how the director at the upper surface transitions from planar to homeotropic, with the slope S_{rf} controlling the rate of change. The duration of this transition is $\Delta t_{rf} = 1/S_{rf}$, which can be compared to the system's intrinsic active timescale, $\tau_a = \gamma/|\xi|$, to form the dimensionless ramp time $\hat{t}_{rf} = |\xi|/\gamma S_{rf}$.

This dimensionless measure quantifies whether the boundary forcing is slow or fast relative to the system's natural response. For small S_{rf} ($\hat{t}_{rf} \gg 1$), the boundary changes gradually compared to τ_a , so the director evolves slowly and the system effectively follows the ramp quasi-statically. In particular, for small activities where τ_a is very long, a slow ramp delays the development of flows and transient patterns. Conversely, for large S_{rf} ($\hat{t}_{rf} \ll 1$), the boundary is forced rapidly relative to τ_a , and the director may be unable to traverse intermediate configurations. Therefore, the relative speed of the ramp compared to the active timescale determines whether the system has sufficient time to respond fully to the boundary change, which links the ramp slope directly to the observed "switch-on" time.

We perform simulations for contractile and extensile active nematics for activity strengths that capture bidirectional flow behaviour for extensile nematics and oscillatory flow behaviour for contractile nematics.

We consider the effects of changing the slope of the ramp function and the value of the activity parameter on both extensile and contractile active nematics. We choose values of the activity parameter $\xi \in [0, \pm 100]$ Pa and set the location of the ramp function to be $L_{rf} = 0.5$ seconds. We present results for slopes in the interval $S_{rf} \in [0.1, 15]$ s⁻¹ as we find that the influence of the ramp function on the system is weak for $S_{rf} > 15$ s⁻¹.

5.2.1 Transient flow for contractile active nematics

In this section, we explore the effect of the ramp slope, focusing on low and high activity strengths for contractile nematics. We have previously established that the system oscillates spatially, and we now proceed by examining transient dynamics following a change in anchoring, reflected by properties of the ramp function. To achieve this, we first consider $S_{rf} \in [0.1, 2]$ s⁻¹ and $\xi \in [-10, -100]$ Pa. We simulate for 2 seconds, setting the width of the HAN region to be l = w/3 microns, as before.

In Figure 5.1, we present the velocity field at different times to illustrate the evolution of the flow and the transition of the director from planar to homeotropic alignment at the upper surface for weakly active systems, specifically, for $\xi = -0.1$ Pa and $S_{rf} = 1$ s⁻¹. The black lines represent streamlines, the white rods represent the director, the black arrows represent the flow direction, and the background colour reflects the flow velocity.

The plots correspond to times t = [0, 0.52, 1.10, 1.50] seconds. Initially, the director is planar everywhere, from which it follows that the system does not exhibit flow. As the anchoring changes after $t = L_{rf} = 0.5$ seconds, flow and director distortion begin to appear. When $t = L_{rf} + 1/S_{rf} = 1.5$ seconds, the director at the upper surface in the HAN region is fully switched to homeotropic alignment. It is interesting to note that the introduction of the ramp function eliminates the circulations in the planar regions whenever $L_{rf} \leq t \leq 1/S_{rf} + L_{rf}$.

Figure 5.2 displays the velocity field for t = [0, 0.52, 0.60, 1.10, 1.50] seconds, a ramp slope $S_{rf} = 1 \text{ s}^{-1}$ and a higher activity of $\xi = -100 \text{ Pa}$. At t = 0 (Figure 5.2(a)), as expected, the flow velocity is zero. At t = 0.52 seconds (Figure 5.1(b)), as the director at the upper boundary starts to switch away from planar anchoring, we begin to observe a flow. At t = 0.6 seconds (Figure 5.2(c)), oscillations appear with travelling waves moving from left to right in the channel. When t = 1.1 seconds (Figure 5.2(d)), the system continues to oscillate, with larger magnitude velocity but now with the travelling wave in the opposite direction. At t = 1.5 seconds and beyond (Figure 5.2(e)), the oscillations are fully formed, and the travelling waves continue to move from right to left.

Given our interest in the HAN region, we observe the director angle in the center of

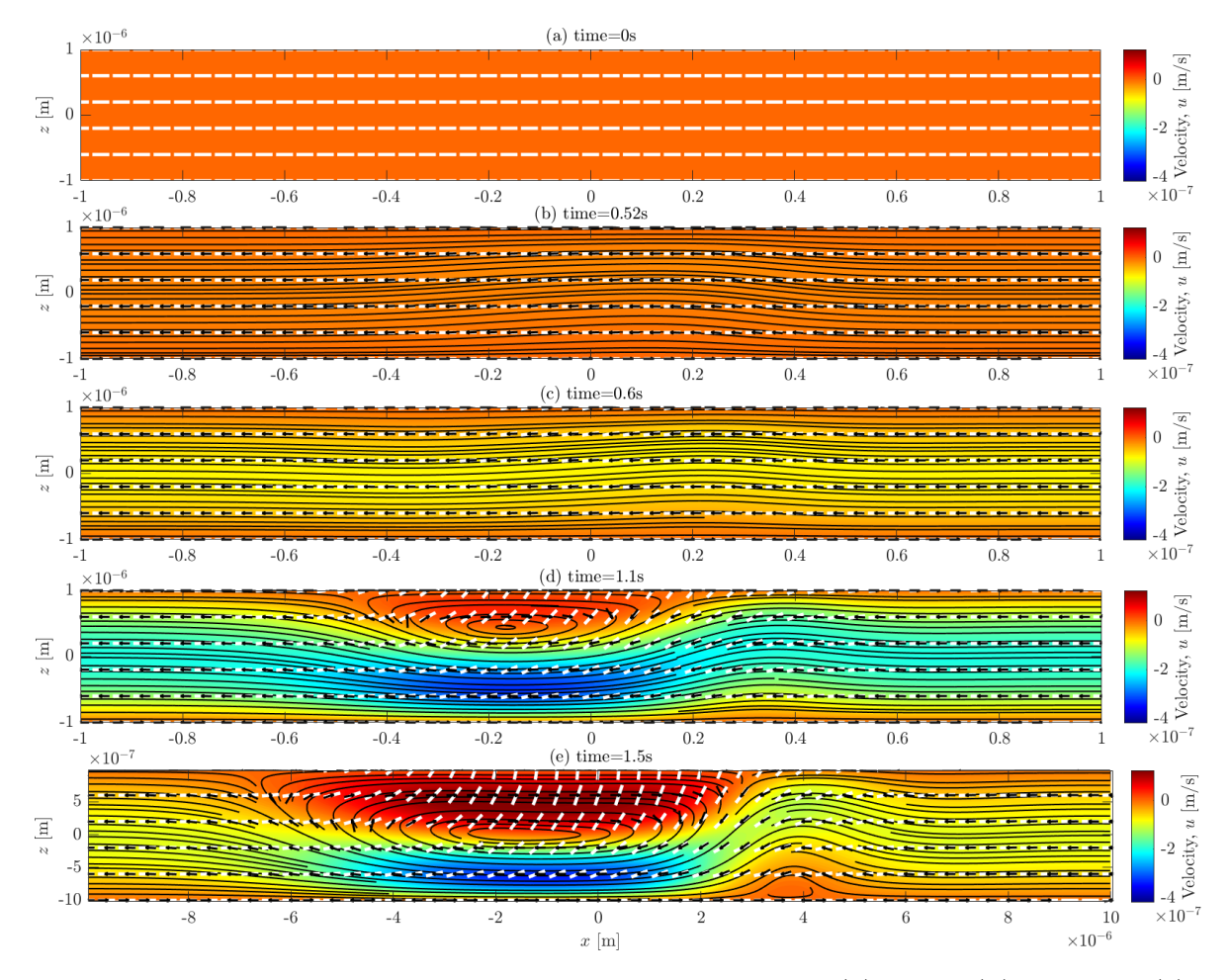


Figure 5.1: Plots of the flow velocity for $\xi = -0.1$ Pa and (a) t = 0, (b) t = 0.52, (c) t = 1.1 and (d) t = 1.5 seconds. The panels depict streamlines (black lines), white rods represent the director, black arrows represent the flow direction, and the background colour reflects the flow velocity.

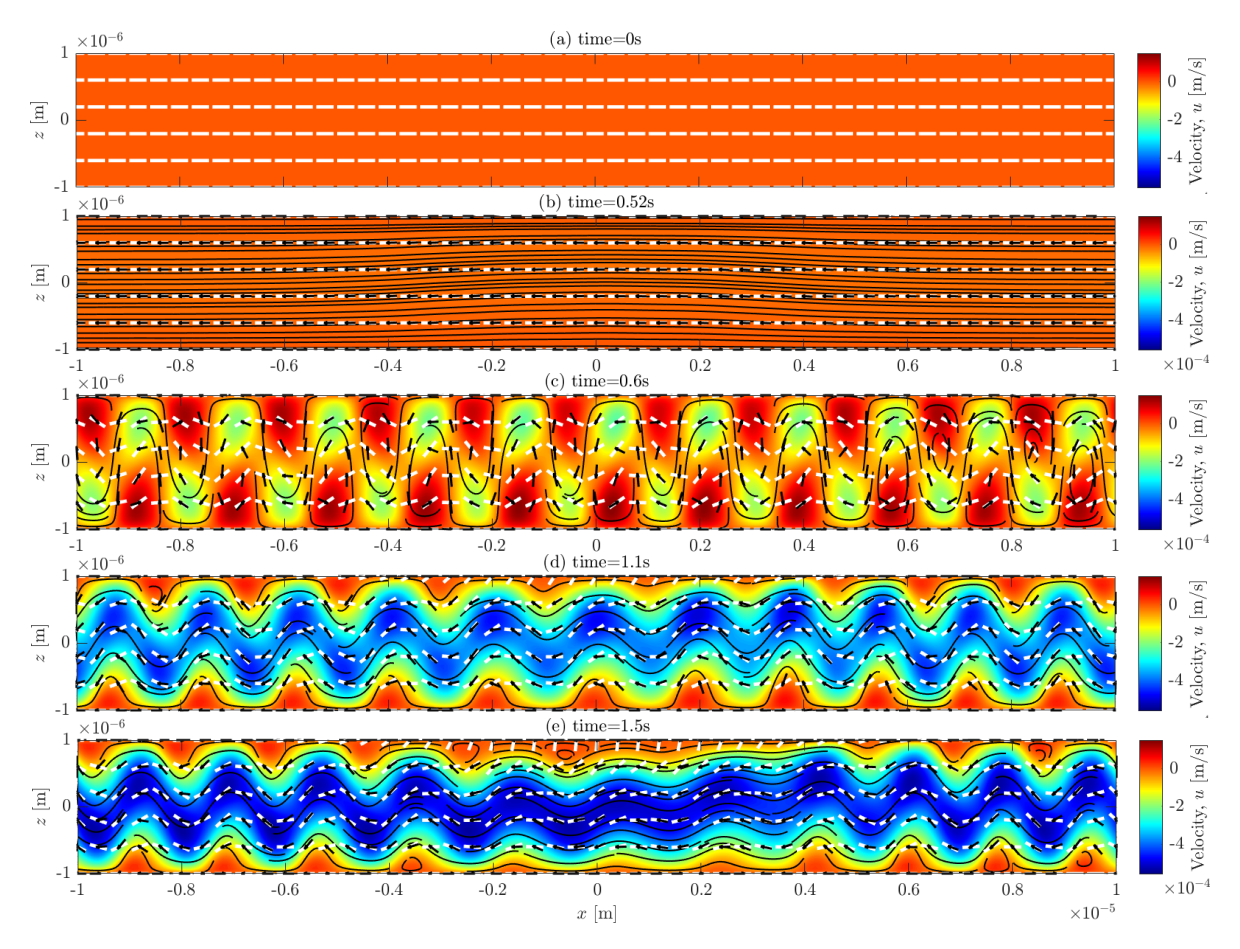


Figure 5.2: Plots of the flow velocity for $\xi=-100$ Pa and (a) t=0, (b) t=0.52, (c) t=0.6, (d) t=1.1 and (e) t=1.5 seconds. The panels depict streamlines (black lines), white rods represent the director, black arrows represent the flow direction, and the background colour reflects the flow velocity.

the channel (x, z) = (0, 0), for $\xi = -100$ Pa and $S_{rf} = 1$ s⁻¹, and perform a temporal frequency analysis.

Figure 5.3 displays the magnitude of the Fourier modes against the temporal frequency of the director angle. The spectrum shows a clear dominant peak at 18.28 Hz, corresponding to a characteristic oscillation period of approximately $T \approx 0.055 \, \mathrm{s}$. This main timescale reflects the natural oscillation of the director field in response to the balance between active stresses and elastic restoring forces. Physically, it represents the fundamental "heartbeat" of the system's temporal dynamics, where the director undergoes coherent periodic reorientations.

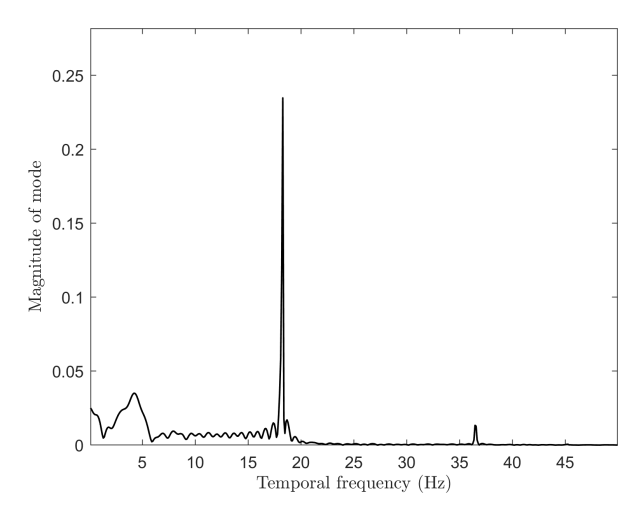


Figure 5.3: Plot of magnitude of mode against the temporal frequency of the director angle in the centre of the channel for $\xi = -100$ Pa, $S_{rf} = 1$ s⁻¹ and t = 2 seconds.

In addition to this dominant peak, smaller peaks are visible at both lower and higher frequencies. The lower-frequency peaks correspond to slower oscillations, with timescales in the range of $0.1\text{--}0.3\,\mathrm{s}$. These capture longer modulation effects or envelope oscillations in the signal, likely linked to slow relaxation processes or energy redistribution across modes. The higher-frequency peaks, by contrast, correspond to shorter timescales ($\sim 0.01\text{--}0.03\,\mathrm{s}$) and are interpreted as higher harmonics of the main oscillation. Their presence arises from nonlinearities in the active nematic dynamics, which generate additional frequency content beyond the fundamental mode.

From this analysis, we learn that while the system has a well-defined dominant oscillation period, the dynamics are not purely periodic. Instead, they are enriched by multiple interacting timescales: slower modulations at low frequency and nonlinear harmonics at higher frequency. This richer temporal structure would be difficult to discern from the time-domain signal alone but is revealed clearly by the frequency-domain analysis.

To understand the nature of oscillations in the system with respect to changes in activity and slope, we perform a spectral frequency analysis using the test function and assumptions in Section 4.3.3.3. Figures 5.4 and 5.5 show the oscillation frequency in the $S_{rf} - \xi$ parameter space for the left planar region and the HAN region, respectively. We consider only the left planar region because the results are very similar to those of the planar right region. For the left planar region, oscillations were observed for $\xi \leq -80$ Pa and all values of the slope, which aligns with the findings of Section 4.3.4.1 (see Figure 4.13(a)), where oscillations start from $\xi = -80$ Pa for l = w/3 microns. Moving to the HAN region, part of the parameter region for which there were oscillations in the left planar region becomes non-oscillatory. Specifically, for $S_{rf} > 0.31 \text{ s}^{-1}$ and $\xi \approx -80$ Pa, oscillations are not observed in the HAN region, even though they are observed in the left planar region. High-magnitude frequencies are classified as non-oscillatory because they are very low-amplitude oscillations.

5.2.2 Quantification of travelling waves

Previously, we observed oscillatory behaviour in the system, characterised by travelling waves. These waves play a significant role in the transient dynamics of active nematics, particularly in determining the spatial-temporal evolution of the director orientation. To gain a deeper understanding of the dynamics, we quantify and analyse the properties of these travelling waves.

To this end, we further analyse the direction and behaviour of these travelling waves by plotting the director angle along z=0 and tracking the locations of the peaks at each point in time. This approach allows us to visualise the wave propagation and identify key features such as directionality.

Figure 5.6 displays the director angle at z = 0 as a function of x and t, where the black

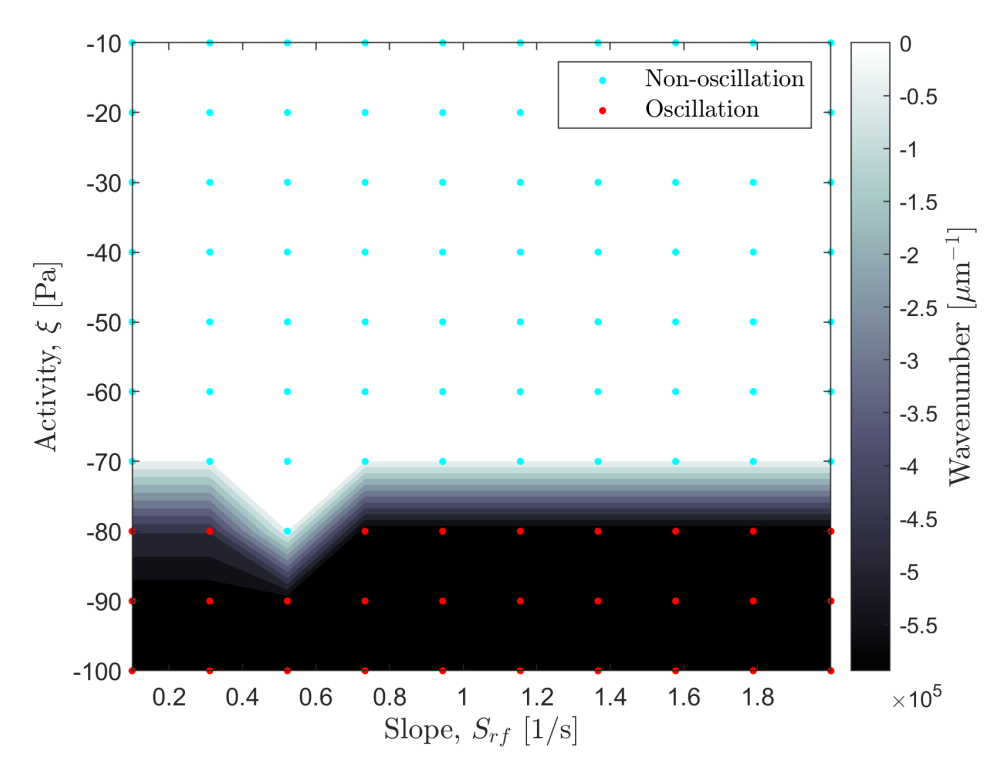


Figure 5.4: Plot of spatial frequency for the planar left region. The red dots represent systems categorised as exhibiting oscillatory flow, and the cyan dots represent systems with non-oscillatory flow. The black region depicts significant frequency, and the cyan dots within this black region represent very low-amplitude oscillations that are not classified as oscillations. The criteria used to distinguish oscillatory from non-oscillatory flow are defined in Section 4.3.2.4, where a system is classified as oscillatory if both the peak frequency and magnitude satisfy $|p_f| > T_f$ and $|p_m| > T_m$, with thresholds $T_f = 10^5$ and $T_m = 0.15$.

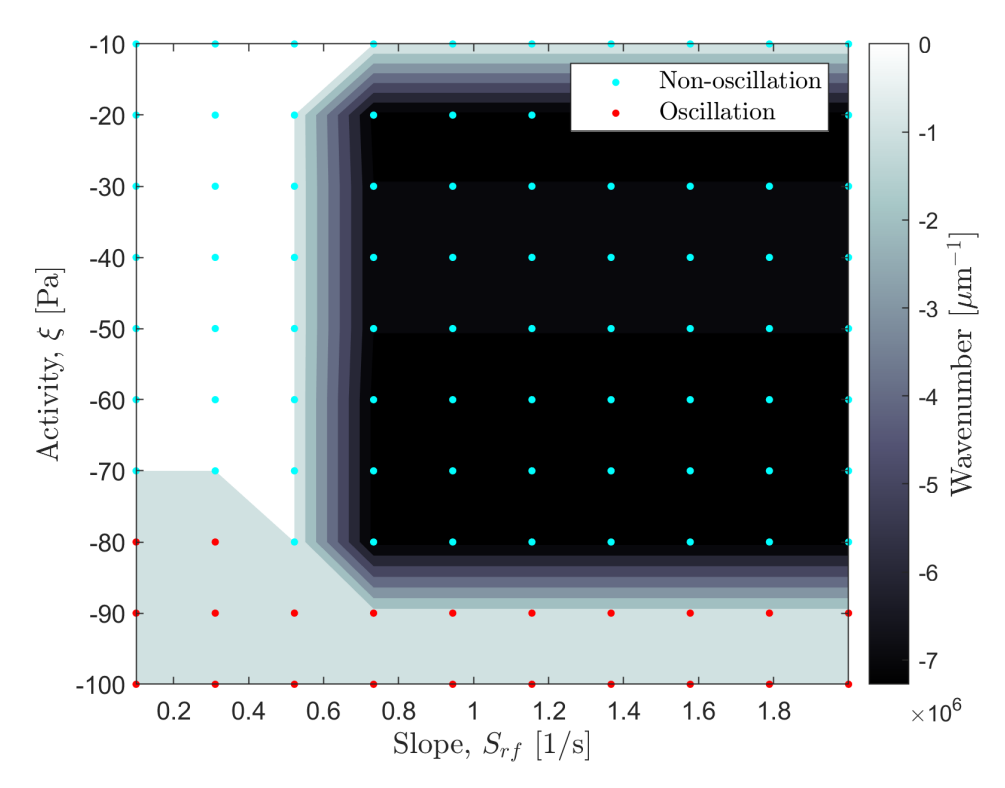


Figure 5.5: Plot of spatial frequency in the HAN region. The red dots represent systems categorised as exhibiting oscillatory flow, and the cyan dots represent systems with non-oscillatory flow. The black region depicts significant frequency, and the cyan dots within this black region represent very low-amplitude oscillations that are not classified as oscillations. The criteria used to distinguish oscillatory from non-oscillatory flow are defined in Section 4.3.2.4, where a system is classified as oscillatory if both the peak frequency and magnitude satisfy $|p_f| > T_f$ and $|p_m| > T_m$, with thresholds $T_f = 10^5$ and $T_m = 0.15$.

circles represent peaks. For $t \leq 0.5$ seconds, the upper anchoring condition is $\theta = 0$, and thus the director orientation is uniform, corresponding to no flow. However, for t > 0.5, director distortion and oscillations emerge, resulting in travelling waves moving to the right in the planar regions but to the left in most of the HAN region, as indicated by the black circles. We find that the travelling wave reverses direction at t = 0.575 seconds, as highlighted in Figure 5.6, where the black circles start travelling to the left throughout the channel.

Our observations can be placed in the broader context of the work of Saintillan and Shelley [185], who analysed instabilities and pattern formation in suspensions of contractile active particles. Their linear stability analysis revealed that for pushers ($\xi < 0$), low-wavenumber shear stress fluctuations possess a positive growth rate, while at higher wavenumbers the fluctuations oscillate and eventually damp. This dispersion relation predicts the coexistence of exponentially growing long-wave modes and oscillatory finite-wavelength modes, which naturally leads to the emergence of travelling waves. In our simulations, the dominant oscillation frequency identified by Fourier analysis (Figure 5.3) can be interpreted as the analogue of these unstable oscillatory modes, selected by the interplay between active driving, elastic restoring forces, and confinement.

Beyond the linear regime, Saintillan and Shelley demonstrated that initially isotropic suspensions evolve into states characterised by coherent travelling waves, band formation, and quasiperiodic oscillations of the shear stress. High-wavenumber modes decay, but nonlinear mode coupling generates low-wavenumber structures that dominate the long-time dynamics. This mirrors our finding that the director field undergoes coherent oscillations at a well-defined frequency, enriched by secondary peaks at lower and higher harmonics. Their simulations further revealed the emergence of concentration bands that fold, break, and reform, driving quasiperiodic dynamics and oscillations in the global input power. While our system does not explicitly track particle concentration, the reversal of wave direction observed at t=0.575 seconds is consistent with this broader picture of nonlinear mode interactions and temporal modulation. Impor-

tantly, their instabilities spontaneously selected low-wavenumber modes permitted by the system size. Our mixed anchoring geometry modifies the propagation direction of travelling waves and introduces a reversal not seen in periodic domains.

Thus, our results not only confirm the generality of the shear-stress-driven travelling waves predicted by Saintillan and Shelley but also extend their framework to confined active nematics with heterogeneous boundary conditions, revealing new dynamical features such as wave reversals.

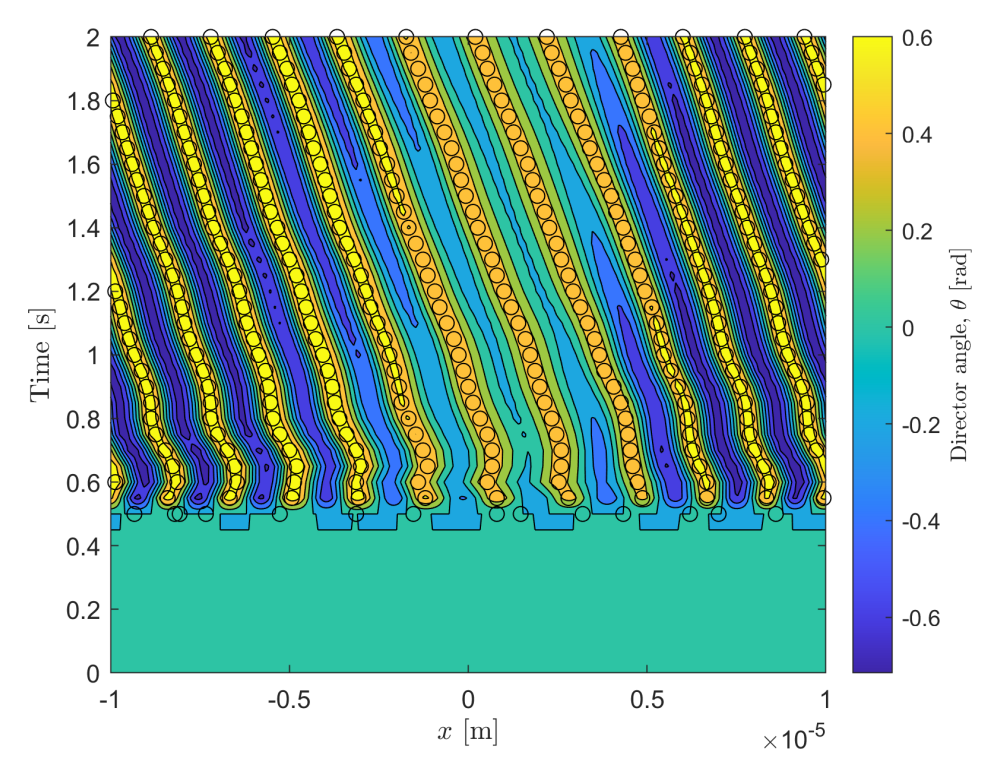


Figure 5.6: Plot of the director angle along z = 0, for x and t > 0, $\xi = -100$ Pa and $S_{rf} = 15$. The black circles indicate the position of the director angle maxima, and eventually indicate the direction of the travelling waves, while the background colour depicts the director angle.

5.3 Transient flow for extensile active nematics

We now examine transient flow dynamics for extensile systems. In Section 4.3.4.2, we found that the flow transitions from unidirectional to bidirectional as the activity strength changes. With the introduction of the ramp function, the flow transitions from bidirectional to unidirectional for higher activity strengths.

In this section, I extend the simulation time from 2 seconds to 5 seconds for the chosen activity $\xi = |100|$ Pa. Here, the active length scale evaluates to $l_a \approx 1.14~\mu\text{m}$, which is smaller than the channel height, so distortions are strongly confined and well resolved. The corresponding active time scale is $\tau_a \approx 0.024$ s, meaning the system evolves extremely rapidly, and the essential response occurs within a fraction of a second. Nevertheless, extending the simulation to 5 seconds is important for assessing the flow regime. In particular, it allows us to determine whether the bidirectional flow observed at earlier times persists once the ramp has fully developed, or whether it relaxes into a unidirectional configuration. Thus, the longer duration provides a more reliable picture of the stability and persistence of bidirectional flow under strong activity forcing.

To demonstrate the flow transition from BB to UU as the slope of the ramp function increases, we use the test functions in equations (4.49)–(4.52) to determine if the flow is unidirectional—unidirectional (UU) or bidirectional—bidirectional (BB). We calculate the times when the flow transitions between BB and UU, and refer to these times as transition times.

Figure 5.7 displays the transition times from BB to UU with respect to the slope of the ramp function and activity parameter, where the numerical values (other than those indicated by 5) represent the transition times from BB to UU and 5 indicates that there is no transition for t < 5 seconds. For lower values of the slope, the bidirectional flow takes longer to transition to unidirectional flow, whereas for higher values of the slope of the ramp function, the bidirectional flow transitions to unidirectional flow more quickly. Interestingly, increasing the slope weakens the effects of activity, resulting in the switch from BB to UU.

Figure 5.8 provides a zoomed-in view of the transition times from bidirectional (BB) to unidirectional (UU) flow in the region $S_{rf} < 1$, which corresponds to the most dynamically interesting regime. Similar to Figure 5.7, the numerical values indicate the transition times from BB to UU, while the value 5 denotes that no transition occurs for t < 5 seconds. This zoomed figure highlights that, in this low-slope region, the BB

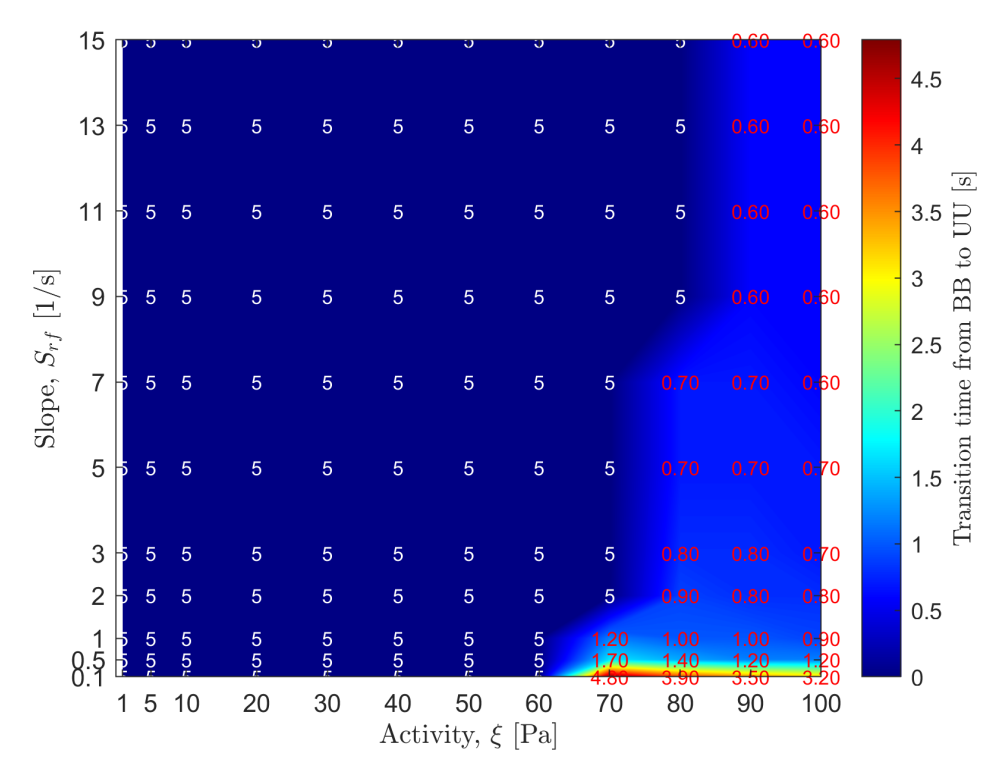


Figure 5.7: Plot of transition times from BB to UU in parameter ξ and S_{rf} space. The red dots represent flow we classify as bidirectional, and the cyan dots represent non-unidirectional flow, while 5 indicates there are no transitions after t > 5 seconds.

flow generally takes longer to transition to UU flow compared to higher slopes, and the effect of activity is more pronounced. By focusing on $S_{rf} < 1$, Figure 5.8 shows more detail in the region where the interplay between ramp slope and activity strongly influences the transition dynamics, which provides a clearer picture of the underlying flow behaviour.

5.4 Conclusions

In this Chapter, we examined the transient response of the system as the director at the upper boundary of the HAN region transitions from planar to homeotropic anchoring. We introduced a ramp function to control the boundary condition at the upper wall and mimic the introduction of an object that we wish to sense. We investigated the impact of the time for the director to change from planar to homeotropic alignment on the system's behaviour for various activity strengths.

Weakly active systems exhibit rectilinear flow with few circulations as the director re-

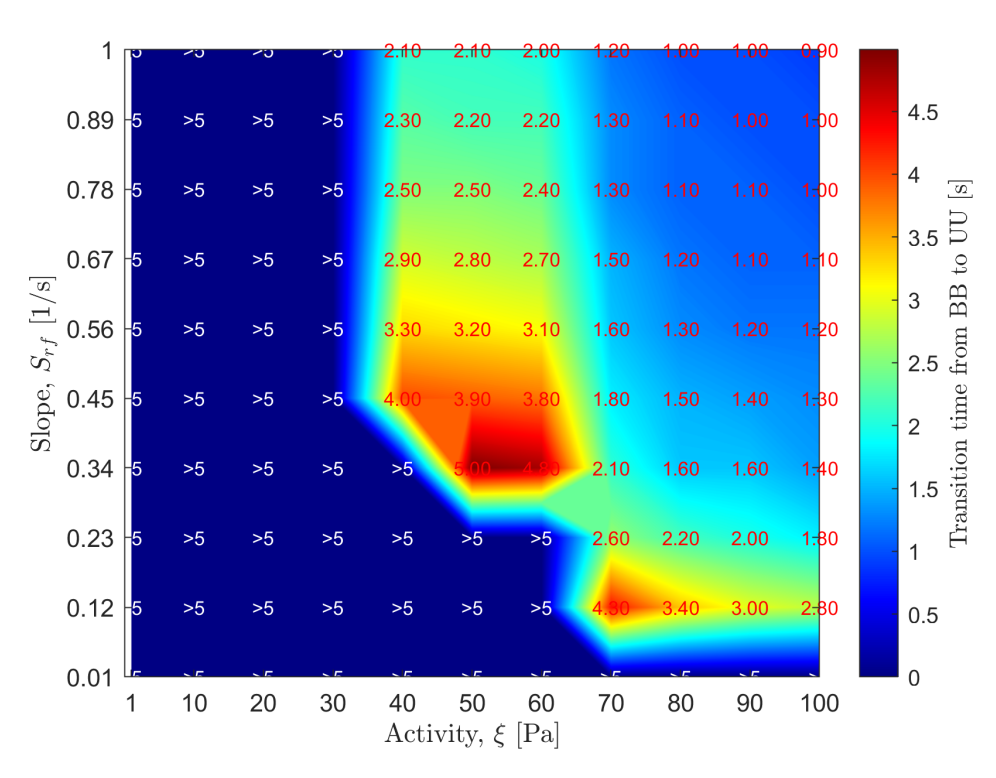


Figure 5.8: Transition times from bidirectional (BB) to unidirectional (UU) flow in the ξ - S_{rf} parameter space. Red dots indicate cases classified as bidirectional flow, cyan dots indicate non-unidirectional flow, and a value of 5 denotes that no transition occurs within t > 5 seconds. The figure focuses on the interesting region for $S_{rf} < 1$, where the transition dynamics are most sensitive to the slope of the ramp function and the activity parameter.

orients from planar to homeotropic as time evolves. For higher activity strengths, contractile nematics exhibit oscillatory flow characterised by travelling waves, which are prominent at slow anchoring changes and decrease for faster anchoring changes. The travelling waves travel to the left, indicating that the flow is in the negative x-direction. For extensile nematics, we observed bidirectional flow for higher activities but transitioned to unidirectional flow as we increased the slope of the ramp function.

Our results suggest that the flow is sensitive to how fast the anchoring changes at the top boundary. A slower transition from planar to homeotropic delays the system's switch-on time and weakens the effect of activity. In contrast, the steepest slopes lead to faster switching, ultimately leading to the disappearance of bidirectional behaviour. These findings underscore the importance of the boundary effects in the HAN region in controlling the system's transient response and highlight how activity and boundary conditions interact to drive complex behaviours in active nematic systems.

Our findings on time-dependent boundary anchoring in active nematics provide a physical framework for understanding wound healing dynamics. In particular, the sensitivity of the system to the rate of boundary change parallels how the speed of cytoskeletal remodelling and adhesion turnover at wound edges dictates collective migration efficiency. Slow reorganisation of anchoring in our model leads to delayed and weakened flows, resembling impaired or inefficient wound closure, while rapid anchoring changes drive strong, directed flows similar to the coordinated migration of epithelial sheets during efficient repair. Furthermore, the emergence of oscillatory, wave-like flows in contractile nematics at high activity strengths mirrors the pulsatile actomyosin contractions and travelling mechanical waves observed experimentally at wound margins. The transition between bidirectional and unidirectional flows in extensile nematics also reflects how tissues dynamically switch between competing migration fronts and consolidated directional closure. Thus, by quantifying how localised, time-dependent boundary changes propagate into large-scale flows, our study provides mechanistic insight into how wounds convert local edge dynamics into coherent collective migration, bridging active nematic

physics and biological tissue repair.

Chapter 6

Summary and Future Work

6.1 Summary

In this thesis, we have examined active nematics in channels, using the planar and homeotropic anchoring conditions for the director, along with no-slip and non-penetration boundary conditions for the velocity field. We adopted the Ericksen-Leslie continuum theory of active nematics and considered 1D and 2D approximations. The summary of the key findings is as follows.

In Chapter 3, we examined the activity and orienting field effects on kickbacks and backflow. We solved the system analytically and numerically using planar or homeotropic alignment, both with and without an orienting field. As is well known, the solution for the planar alignment case in the absence of the orienting field is characterised by a critical activity. Below this critical activity, the system exhibits a no-flow state with an undistorted director state, and above which the director is distorted, leading to flow. When an orienting field is present and $\xi = 0$, the system undergoes a classical Fréedericksz transition once the field strength exceeds a certain threshold. In scenarios where both activity and the orienting field are present, the system exhibits a feedback mechanism due to the competition between the activity and the orienting field. For relaxation from an initial homeotropic alignment, the system exhibits a kickback mechanism in the

absence of an orienting field. However, when an orienting field is applied, the kickback effect disappears if the field strength exceeds a certain threshold for extensile nematics, while kickback persists for contractile nematics.

To investigate long-time nonlinear behaviour, we used a finite difference approximation to solve the one-dimensional model. The nonlinear solutions include director angle and velocity profiles for various combinations of activity parameter values and orienting fields. These solutions exhibit uniform, symmetrically distorted, or antisymmetrically distorted states. We also measured active dissipation and elastic energy. Our results show that higher orienting field values increased elastic energy, while large activity values enhanced active dissipation. Active dissipation grows for strongly negative activity, whereas elastic energy remains low. For the HAN cell, the director stabilises at approximately 1.24 rad in the bulk of the channel for extensile systems. As activity becomes more negative, a transition occurs, leading to bistability in contractile systems. A key finding from both the linear and nonlinear analyses is that in a weakly contractile system, the director exhibits an overshoot, resulting in complex flow behaviour, which has implications for sensor design.

In Chapter 4, we examined a two-dimensional study of active nematics in a channel by considering the effects of changing the activity and geometric effects.

Under the normal flow condition, which mimics a single area of homeotropic anchoring on the upper substrate, the contractile active nematics are characterised by unidirectional uniform flow and localised circulatory flow for low activity strengths and for all HAN region widths. For sufficiently high magnitudes of activities, the system is characterised by spatial fluctuation, although there are no time-dependent oscillations in the system. For extensile active nematics, the system exhibits UU, BU, and BB flow patterns depending on the magnitude of the activity. The notations UU, BB, UB, and BU represent different flow patterns. UU is used to represent unidirectional flow in both the planar left and planar right regions, UB is used to represent unidirectional flow in the planar left region and bidirectional flow in the planar right region, BU is used

to represent bidirectional flow in the planar left region and unidirectional flow in the planar right region, and BB is used to represent bidirectional flow in both regions. The transition from UU to BB is largely determined by the value of the activity strengths, while the BU solution arises from the changes to the width of the HAN region.

For periodic boundary conditions which mimic a periodic array of homeotropic alignments, we examined how multiple HAN regions interact with each other. The findings are reminiscent of findings using the normal flow conditions, except that BU solutions no longer exist. From the flux measurements, we observed two distinct critical activities within the bidirectional solution regime. We also examined the effect of the elastic constant deformation on the director orientation and flow. Increasing the ratio of the splay and bend elastic constants, the flux changes from positive to negative for contractile nematics and remains positive for extensile active nematics. The key finding in this Chapter is that local disturbances in the director orientation influence the global flow in the system.

Chapter 5 explored two-dimensional transient dynamics in the HAN state formation by controlling the top boundary at the center of the channel. For contractile nematics, the system exhibits circulatory flow characterised by director distortion in weakly active nematics and oscillatory flow with travelling waves at higher activity strengths. In extensile nematics, the behaviour is similar to that of contractile nematics at low activity strengths. The results showed that flow dynamics are highly sensitive to the rate of anchoring change at the top boundary. A slower transition from planar to homeotropic anchoring delays the system's switch-on time and weakens the effect of activity. In contrast, a steeper transition leads to faster switching, ultimately eliminating bidirectional behaviour.

In conclusion, we have shown that local director distortions generate global flow. This finding is crucial for sensing applications and provides valuable insights into controlling the behaviour of active fluids. Additionally, it improves our understanding of biological processes such as biofilm formation and morphogenesis.

6.2 Future work

Building on the findings of this thesis, several directions can be pursued to extend and deepen the understanding of active nematic systems. In this work, we have focused exclusively on wet active fluids with nematic symmetry, assuming constant concentration, low Reynolds number, no defects, perfectly strong anchoring, and short simulation times. While these assumptions allow for analytical and numerical tractability, they also impose limitations on the generality of the results. Below, we outline potential extensions and critically discuss their motivations and significance.

6.2.1 Extensions to other active matter systems

One natural extension is to consider active dry fluids, such as schools of fish [52] and vibrated granular particles [213], where momentum is dissipated primarily through friction with the surrounding medium or substrate, rather than through viscous stresses in a continuous fluid. Incorporating dry active matter would allow exploration of collective motion in regimes where hydrodynamics plays a minor role, broadening the applicability of this framework to a wider class of active systems. This is particularly interesting because it can reveal how frictional damping, rather than viscosity, influences pattern formation, defect dynamics, and flow instabilities.

Another extension involves relaxing the assumption of constant concentration by including dynamic concentration fields and particle interactions. This can be achieved by introducing stochastic partial differential equations, such as Fokker-Planck equations [125, 170], to account for noise and fluctuations in particle positions and orientations. The motivation here is to capture emergent phenomena, such as clustering or spontaneous flow instabilities, that arise due to concentration heterogeneities, which are absent in the current constant-concentration framework.

6.2.2 Higher-dimensional and complex geometries

In Chapter 3, we studied kickback and backflow in a one-dimensional channel with splay and bend geometries. Extending these analyses to two or three dimensions would provide a more realistic representation of experimental systems, where director orientations and flow patterns are not confined to a single plane. Specifically, incorporating twist geometries, with the twist elastic constant K_2 in the free energy, would allow us to study how three-dimensional distortions influence backflow dynamics. This is significant because many real-world nematic systems exhibit complex director deformations that cannot be captured in one-dimensional models.

Similarly, the HAN problem can be extended to include the effect of an external orienting field. Investigating how this field modifies the HAN state could provide insights into controlling director alignment and flow patterns in devices, which is crucial for applications in active materials and microfluidics.

6.2.3 Geometric and activity-driven effects

Chapter 4 considered two-dimensional geometries and the effects of activity on director and flow patterns. Several extensions are particularly promising:

- I. Three-dimensional simulations: Extending the model to three dimensions and to a Q-tensor formulation would allow for the study of defect lines, complex flow structures, and interactions between multiple defects. This is motivated by experimental observations that active nematics in confined geometries often exhibit three-dimensional structures that cannot be captured in two dimensions. Including 3D effects is therefore essential for quantitative comparisons with experiments.
- II. **Designing responsive materials and sensors:** Experimental studies suggest that active nematics are highly sensitive to external stimuli such as pressure, electrostatic and light. Exploring this sensitivity can lead to the design of activity-

driven sensors, where small changes in the environment trigger measurable responses in the nematic configuration. This is an interesting avenue because it bridges fundamental physics with potential technological applications.

III. Applications to biophysical systems: Active nematic models can be applied to cytoskeletal networks, tissue dynamics, or biofilm formations. Extending the model to capture the mechanical and dynamical properties of these biological systems would enhance its relevance and allow for predictions about processes such as cell migration, division, and collective motion. This is particularly compelling because it connects soft matter physics with biological function, offering opportunities for interdisciplinary research.

6.2.4 Transient dynamics and switch-on/off states

In Chapter 5, we focused on the transient dynamics of the switch-on state, where the director transitions from planar to homeotropic alignment. A natural extension is to study the switch-off scenario, where the director returns from homeotropic to planar alignment. Understanding both transitions is crucial for potential sensor applications, as real devices must operate under repeated cycles of alignment changes.

6.2.5 Critical assumptions and limitations

Throughout this thesis, several simplifying assumptions were made for analytical and computational tractability. These include:

- I. Low-Reynolds number: Neglecting inertia is reasonable for microfluidic systems, but at higher flow speeds or larger scales, inertial effects could modify defect motion and flow patterns.
- II. No defects: The absence of defects simplifies analysis, but in practice, defects often dominate the dynamics of active nematics. Including defects in simulations would provide a more realistic description.

- III. Constant scalar order parameter: Relaxing this assumption could capture variations in nematic order due to activity, confinement, or temperature gradients.
- IV. **Perfectly strong anchoring:** Real surfaces may exhibit weak or patterned anchoring, influencing director alignment and flow near boundaries.
- V. **Absence of noise:** Including thermal or active fluctuations would make the model more robust and allow exploration of stochastic effects on defect nucleation and collective motion.

Addressing these limitations in future work would strengthen the connection between simulations, theory, and experiments, and enhance the predictive power of active nematic models.

Appendices

A Derivation of the 2D versions of the elastic free energy and dissipation function

In this section, we derive the Frank-Oseen elastic free energy, w_F (equation (4.9)) in (4.2.1) and the dissipation function (equation (4.10)) as follows.

To derive the Frank-Oseen elastic free energy, we substitute equations (4.1) and (4.2) into equation (2.35), and calculate each term on the right-hand side. Simplifying, we obtain the following equations:

$$(n_{i,i})^2 = \theta_x^2 \sin^2 \theta - 2\sin \theta \cos \theta \theta_x \theta_z + \theta_z^2 \cos^2 \theta, \tag{A.1}$$

$$n_{i,j}n_{i,j} = \theta_x^2 \sin^2 \theta - \theta_x^2 \cos^2 \theta + \theta_z^2 \sin^2 \theta + \theta_z^2 \cos^2 \theta, \tag{A.2}$$

$$n_{i,j}n_{j,i} = \theta_x^2 \sin^2 \theta - 2\theta \cos \theta \theta_x \theta_z + \theta_z^2 \cos^2 \theta, \tag{A.3}$$

$$n_{j}n_{i,j}n_{k}n_{i,k} = \theta_{x}^{2}\sin^{2}\theta\cos\theta^{2} + \theta_{x}^{2}\cos^{4}\theta + 2\theta_{x}\theta_{z}\sin^{3}\theta\cos\theta + 2\theta_{x}\theta_{z}\cos^{3}\theta\cos\theta + \theta_{z}^{2}\sin^{2}\theta\cos^{2}\theta + \theta_{z}^{2}\sin^{4}\theta.$$
(A.4)

Using equations (A.1)-(A.4) into equation (2.35) and simplifying, we obtain the elastic

free energy as

$$w_{F} = \frac{1}{2} \left[\theta_{x}^{2} \left(K_{1} \sin^{2} \theta + K_{3} \cos^{2} \theta \right) + \theta_{z}^{2} \left(K_{1} \cos^{2} \theta + K_{3} \sin^{2} \theta \right) + (K_{3} - K_{1}) \sin(2\theta) \theta_{x} \theta_{z} \right]. \tag{A.5}$$

In a similar way, we derive the rate of dissipation in Subsection (4.2.1). To achieve this, we first compute the rate of strain tensor (symmetry velocity tensor): $A_{ij} = \frac{1}{2} (v_{i,j} + v_{j,i})$, and vorticity tensor (anti-symmetry velocity tensor): $W_{ij} = \frac{1}{2} (v_{i,j} - v_{j,i})$. Using equations (4.1) and (4.9), we get the components of the rate of strain tensor and vorticity tensor, given explicitly as

$$A_{11} = u_x, \tag{A.6}$$

$$A_{12} = \frac{1}{2} (u_z + v_x), \qquad (A.7)$$

$$A_{21} = A_{12} = \frac{1}{2} (u_z + v_x), \qquad (A.8)$$

$$A_{22} = v_z, \tag{A.9}$$

$$A_{13} = A_{23} = A_{33} = 0, (A.10)$$

and

$$W_{11} = W_{13} = W_{22} = W_{23} = W_{33} = 0, (A.11)$$

$$W_{12} = \frac{1}{2} (u_z - v_x), \qquad (A.12)$$

$$W_{21} = \frac{1}{2} \left(v_x - u_z \right). \tag{A.13}$$

The co-rotational time flux: $N_i = \dot{n}_i - W_{ij}n_j$, i, j = 1, 2, 3, where \dot{n}_i is the material

derivatives. So that

$$N_1 = \dot{n}_i - \frac{1}{2} (u_z - v_x) \sin \theta, \tag{A.14}$$

$$N_2 = \dot{n}_i - \frac{1}{2} (v_x - u_z) \cos \theta,$$
 (A.15)

$$N_3 = 0, (A.16)$$

where $\dot{n}_x = \sin \theta \dot{\theta}$ and $\dot{n}_z = \cos \theta \dot{\theta}$, and $\dot{\theta} = \theta_t + u\theta_x + v\theta_z$.

Next, we compute each term on the left hand side of equation (2.55). So that

$$(n_{i}A_{ij}n_{j})^{2} = \cos^{4}\theta u_{x}^{2} + 2\cos^{3}\theta \sin\theta v_{x}u_{x} + 2\cos^{3}\theta \sin\theta u_{x}u_{z} + \sin^{4}\theta v_{z}^{2}$$

$$+ 2\cos^{2}\theta \sin^{2}\theta u_{x}v_{z} + \cos^{2}\theta \sin^{2}\theta v_{x}^{2} + 2\cos^{2}\theta \sin^{2}\theta v_{x}u_{z}$$

$$+ 2\cos\theta \sin^{3}\theta v_{x}v_{z} + \cos^{2}\theta \sin^{2}\theta u_{z}^{2} + 2\cos\theta \sin^{3}\theta u_{z}v_{z}, \qquad (A.17)$$

$$\begin{split} N_{i}A_{ij}n_{j} = & u_{x}\cos\theta\,\dot{n}_{x} - \frac{1}{2}u_{x}u_{z}\cos\theta\sin\theta + \frac{1}{2}u_{x}v_{x}\cos\theta\sin\theta + \frac{1}{2}\cos\theta v_{x}\,\dot{n}_{z} \\ & - \frac{1}{4}\cos\theta^{2}v_{x}^{2} + \frac{1}{2}\cos\theta u_{z}\,\dot{n}_{z} + \frac{1}{4}\cos\theta^{2}u_{z}^{2} + \frac{1}{2}\sin\theta v_{x}\,\dot{n}_{x} + \frac{1}{4}\sin\theta^{2}v_{x}^{2} \\ & + \frac{1}{2}\sin\theta u_{z}\,\dot{n}_{x} - \frac{1}{4}\sin\theta^{2}u_{z}^{2} + v_{z}\sin\theta\,\dot{n}_{z} - \frac{1}{2}v_{z}\sin\theta\cos\theta v_{x} \\ & + \frac{1}{2}v_{z}u_{z}\sin\theta\cos\theta, \end{split} \tag{A.18}$$

$$A_{ij}A_{ij} = u_x^2 + \frac{1}{2}v_x^2 + (v_x)u_z + \frac{1}{2}u_z^2 + v_z^2,$$
(A.19)

$$n_{i}A_{ij}A_{jk}n_{k} = \cos^{2}\theta u_{x}^{2} + \cos\theta u_{x} (v_{x} + u_{z})\sin\theta + \frac{1}{2}\cos^{2}\theta (v_{x} + u_{z})^{2} + \cos\theta (v_{x} + u_{z})v_{z}\sin\theta + \frac{1}{2}\sin^{2}\theta (v_{x} + u_{z})^{2} + \sin^{2}\theta v_{z}^{2},$$
 (A.20)

$$N_{i}N_{i} = \dot{n}_{x}^{2} - \sin\theta u_{z}\dot{n}_{x} + \sin\theta v_{x}\dot{n}_{x} + \frac{1}{4}\sin^{2}\theta u_{z}^{2} - \frac{1}{2}\sin^{2}\theta u_{z}v_{x}$$

$$+ \frac{1}{4}\sin^{2}\theta v_{x}^{2} + \dot{n}_{z}^{2} - \cos\theta v_{x}\dot{n}_{z} + \cos\theta u_{z}\dot{n}_{z} + \frac{1}{4}\cos^{2}\theta v_{x}^{2}$$

$$- \frac{1}{2}\cos^{2}\theta v_{x}u_{z} + \frac{1}{4}\cos^{2}\theta u_{z}^{2}, \tag{A.21}$$

$$A_{ij}n_i n_j = \cos^2 \theta u_x + \cos \theta (v_x + u_z) \sin \theta + \sin^2 \theta v_z.$$
(A.22)

Summing all the terms, we get

$$\mathcal{D} = \alpha_{1} \left[u_{x} \left((-u_{z} - v_{x}) \sin \theta \cos \theta \sin^{2} \theta + (u_{z} + v_{x}) \sin \theta \cos \theta - v_{z} \sin^{4} \theta + \sin^{2} \theta v_{z} \right) \right. \\ + u_{z} \left(\sin \theta \cos \theta \sin^{2} \theta v_{z} - v_{x} \sin^{4} \theta + \sin^{2} \theta v_{x} \right) + \sin \theta \cos \theta \sin^{2} \theta v_{z} v_{x} \right] \\ + \alpha_{2} \left[u_{x} \left(-\frac{1}{4} u_{z} + \frac{1}{4} v_{x} - \frac{1}{2} \theta_{t} \right) \sin \theta \cos \theta + u_{z} \left(\frac{1}{4} v_{x} + \frac{1}{4} \sin \theta \cos \theta v_{z} - \frac{1}{2} \sin^{2} \theta \theta_{t} - \frac{1}{4} \theta_{t} \right) \\ + v_{x} \left(-\frac{1}{4} \sin \theta \cos \theta v_{z} - \frac{1}{2} \sin^{2} \theta \theta_{t} + \frac{3}{4} \theta_{t} \right) + \frac{1}{2} \sin \theta \cos \theta v_{z} \theta_{t} - \frac{1}{2} \theta_{t}^{2} \right] \\ + \alpha_{3} \left[u_{x} \left(-\frac{1}{4} u_{z} + \frac{1}{4} v_{x} - \frac{1}{2} \theta_{t} \right) \sin \theta \cos \theta + u_{z} \left(-\frac{1}{4} v_{x} + \frac{1}{4} \sin \theta \cos \theta v_{z} - \frac{1}{2} \sin^{2} \theta \theta_{t} + \frac{3}{4} \theta_{t} \right) \right. \\ + v_{x} \left(-\frac{1}{4} \sin \theta \cos \theta v_{z} - \frac{1}{2} \sin^{2} \theta \theta_{t} - \frac{1}{4} \theta_{t} \right) + \frac{1}{2} \sin \theta \cos \theta v_{z} \theta_{t} + \frac{1}{2} \theta_{t}^{2} \right] \\ + \alpha_{5} \left[u_{x} \left(\frac{3}{4} u_{z} + \frac{1}{4} v_{x} + \frac{1}{2} \theta_{t} \right) \sin \theta \cos \theta + u_{z} \left(\frac{1}{4} v_{x} + \frac{1}{4} \sin \theta \cos \theta v_{z} + \frac{1}{2} \sin^{2} \theta \theta_{t} - \frac{1}{4} \theta_{t} \right) \right. \\ + v_{x} \left(\frac{3}{4} \sin \theta \cos \theta v_{z} + \frac{1}{2} \sin^{2} \theta \theta_{t} - \frac{1}{4} \theta_{t} \right) - \frac{1}{2} \sin \theta \cos \theta v_{z} \theta_{t} \right] \\ + v_{x} \left(\frac{3}{4} \sin \theta \cos \theta v_{z} + \frac{1}{2} \sin^{2} \theta \theta_{t} - \frac{1}{4} \theta_{t} \right) - \frac{1}{2} \sin \theta \cos \theta v_{z} \theta_{t} \right] \\ + v_{x} \left(\frac{1}{4} \sin \theta \cos \theta v_{z} - \frac{1}{2} \sin^{2} \theta \theta_{t} + \frac{1}{4} \theta_{t} \right) + \frac{1}{2} \sin \theta \cos \theta v_{z} \theta_{t} \right] \\ + v_{x} \left(\frac{1}{4} \sin \theta \cos \theta v_{z} - \frac{1}{2} \sin^{2} \theta \theta_{t} + \frac{1}{4} \theta_{t} \right) + \frac{1}{2} \sin \theta \cos \theta v_{z} \theta_{t} \right] \\ + v_{x} \left(\frac{1}{4} \sin \theta \cos \theta v_{z} - \frac{1}{2} \sin^{2} \theta \theta_{t} + \frac{1}{4} \theta_{t} \right) + \frac{1}{2} \sin \theta \cos \theta v_{z} \theta_{t} \right] \\ + \left. \left(\frac{1}{2} \left[u_{x} \left(\frac{1}{4} u_{x} + \frac{3}{4} v_{x} - \frac{1}{2} \theta_{t} \right) \sin \theta \cos \theta + u_{z} \left(\frac{1}{4} v_{x} + \frac{3}{4} \sin \theta \cos \theta v_{z} - \frac{1}{2} \sin^{2} \theta \theta_{t} + \frac{1}{4} \theta_{t} \right) \right. \\ + \left. \left(\frac{1}{2} \left[u_{x} \left(\frac{1}{4} u_{x} + \frac{1}{2} u_$$

where

$$g_1(\theta) = \frac{1}{2} \left[\alpha_4 + (\alpha_3 + \alpha_6) \cos^2 \theta + \sin^2 \theta (\alpha_5 - \alpha_2) \right] + \alpha_1 \sin^2 \theta \cos^2 \theta, \tag{A.24}$$

$$g_2(\theta) = \frac{1}{2} \left[\alpha_4 + (\alpha_6 - \alpha_3) \cos^2 \theta + (\alpha_5 + \alpha_2) \sin^2 \theta \right] + \alpha_1 \sin^2 \theta \cos^2 \theta, \tag{A.25}$$

$$g_3(\theta) = \frac{1}{2}\alpha_1 \cos^4 \theta + \frac{1}{2}\alpha_4 + \frac{1}{2}(\alpha_5 + \alpha_6)\cos^2 \theta,$$
 (A.26)

$$g_4(\theta) = \frac{1}{2}\alpha_1 \sin^4 \theta + \frac{1}{2}\alpha_4 + \frac{1}{2}(\alpha_5 + \alpha_6)\sin^2 \theta.$$
 (A.27)

B Splay/bend scaling ratio and their corresponding splay and bend elastic constants

Here we present the values of the splay/bend scaling ratio, $\kappa = \alpha K_1/\beta K_3$, and their corresponding elastic constants, K_1 and K_3 shown in Figure 4.17 as follows.

κ	K_1 (N)	K_3 (N)
0.03	4.3062×10^{-14}	1.3457×10^{-11}
0.07	8.9143×10^{-13}	1.2609×10^{-11}
0.11	1.3324×10^{-12}	1.2168×10^{-11}
0.13	1.5404×10^{-12}	1.1960×10^{-11}
0.40	3.8571×10^{-12}	9.6429×10^{-12}
0.80	6.0000×10^{-12}	7.5000×10^{-12}
0.98	6.6742×10^{-12}	6.8258×10^{-12}
1.00	6.7500×10^{-12}	6.7500×10^{-12}
1.04	6.8934×10^{-12}	6.6066×10^{-12}
1.10	7.0782×10^{-12}	6.4218×10^{-12}
1.22	7.4271×10^{-12}	6.0729×10^{-12}
1.23	7.4372×10^{-12}	6.0628×10^{-12}
1.35	7.7580×10^{-12}	5.7420×10^{-12}
2.00	9.0000×10^{-12}	4.5000×10^{-12}
4.80	1.1172×10^{-11}	2.3276×10^{-12}
7.20	1.1854×10^{-11}	1.6463×10^{-12}
10.40	1.2316×10^{-11}	1.1842×10^{-12}
13.20	1.2549×10^{-11}	9.5070×10^{-13}
14.60	1.2635×10^{-11}	8.6538×10^{-13}
16.00	1.2706×10^{-11}	7.9412×10^{-13}

Table 6: Table of splay/bend scaling ratio, κ and their corresponding splay and bend elastic constants.

Bibliography

- S.R. Aditi and S. Ramaswamy. Hydrodynamic fluctuations and instabilities in ordered suspensions of self-propelled particles. *Physical Review Letters*, 89(5):058101, 2002.
- [2] A. Ahmadi, M.C. Marchetti, and T.B. Liverpool. Hydrodynamics of isotropic and liquid crystalline active polymer solutions. *Physical Review E*, 74(6):061913, 2006.
- [3] S. Alam, B. Najma, A. Singh, J. Laprade, G. Gajeshwar, H.G. Yevick, A. Baskaran, P.J. Foster, and G. Duclos. Active fréedericksz transition in active nematic droplets. *Physical Review X*, 14(4):041002, 2024.
- [4] E. Allen, G. McKay, and N.J. Mottram. Constitutive equations for a continuum theory of active nematics. *Unpublished manuscript*, 2020.
- [5] D.W. Allender, G.P. Crawford, and J.W. Doane. Determination of the liquid-crystal surface elastic constant k 24. *Physical Review Letters*, 67(11):1442, 1991.
- [6] H. Andralojc, J. Turley, H. Weavers, P. Martin, I.V. Chenchiah, R.R. Bennett, and T.B. Liverpool. Dynamics of wound closure in living nematic epithelia. arXiv preprint arXiv:2506.04922, 2025.
- [7] D. Andrienko. Introduction to liquid crystals. *Journal of Molecular Liquids*, 267:520–541, 2018.

- [8] B. Bahadur. Liquid Crystals: Applications and Uses, volume 1. World Scientific, 1990.
- [9] A. Baskaran and M. C. Marchetti. Hydrodynamics of self-propelled hard rods. *Physical Review E*, 77(1):011920, 2008.
- [10] A. Baskaran and M. C. Marchetti. Statistical mechanics and hydrodynamics of bacterial suspensions. Proceedings of the National Academy of Sciences, 106(37):15567–15572, 2009.
- [11] J. Bastos-Arrieta, A. Revilla-Guarino, W.E. Uspal, and J. Simmchen. Bacterial biohybrid microswimmers. *Frontiers in Robotics and AI*, 5:97, 2018.
- [12] T. Bera and J. Fang. Polyelectrolyte-coated liquid crystal droplets for detecting charged macromolecules. *Journal of Materials Chemistry*, 22(14):6807–6812, 2012.
- [13] H.C. Berg. Random walks in biology. Princeton University Press, 1993.
- [14] E. Bertin, H. Chaté, F. Ginelli, S. Mishra, A. Peshkov, and S. Ramaswamy. Mesoscopic theory for fluctuating active nematics. New Journal of Physics, 15(8):085032, 2013.
- [15] E. Bertin, M. Droz, and G. Grégoire. Boltzmann and hydrodynamic description for self-propelled particles. *Physical Review E*, 74(2):022101, 2006.
- [16] J.R. Blake. A spherical envelope approach to ciliary propulsion. *Journal of Fluid Mechanics*, 46(1):199–208, 1971.
- [17] C. Blanc, D. Svenšek, S. Žumer, and M. Nobili. Dynamics of nematic liquid crystal disclinations: The role of the backflow. *Physical Review Letters*, 95(9):097802, 2005.
- [18] M.L. Blow, S.P. Thampi, and J.M. Yeomans. Biphasic, lyotropic, active nematics. *Physical Review Letters*, 113(24):248303, 2014.

- [19] R.T. Bonnecaze and J.F. Brady. Dynamic simulation of an electrorheological fluid. *The Journal of Chemical Physics*, 96(3):2183–2202, 1992.
- [20] A.I. Boullerne. The history of myelin. Experimental Neurology, 283:431–445, 2016.
- [21] J.M. Brake, M.K. Daschner, Y. Luk, and N.L. Abbott. Biomolecular interactions at phospholipid-decorated surfaces of liquid crystals. *Science*, 302(5653):2094– 2097, 2003.
- [22] L.N. Carenza, G. Gonnella, A. Lamura, G. Negro, and A. Tiribocchi. Lattice boltzmann methods and active fluids. *European Physical Journal E*, 42:1–38, 2019.
- [23] R.J. Carlton, J.T. Hunter, D.S. Miller, R. Abbasi, P.C. Mushenheim, L.N. Tan, and N.L. Abbott. Chemical and biological sensing using liquid crystals. *Liquid Crystals Reviews*, 1(1):29–51, 2013.
- [24] M.E. Cates and E. Tjhung. Theories of binary fluid mixtures: from phase-separation kinetics to active emulsions. *Journal of Fluid Mechanics*, 836:P1, 2018.
- [25] S. Chandrasekhar. Liquid Crystals. Cambridge University Press, 1992.
- [26] M.G. Clark and F.M. Leslie. A calculation of orientational relaxation in nematic liquid crystals. Proceedings of the Royal Society A, 361(1707):463–485, 1978.
- [27] A.P.B. Clemente, H. Kuang, A.M. Shabana, T.P. Labuza, and E. Kokkoli. Design of an aptamer-amphiphile for the detection of β -lactoglobulin on a liquid crystal interface. *Bioconjugate Chemistry*, 30(11):2763–2770, 2019.
- [28] R.C.V. Coelho, N.A.M. Araújo, and M.M. Telo da Gama. Director alignment at the nematic–isotropic interface: Elastic anisotropy and active anchoring. *Philo-sophical Transactions of the Royal Society A*, 379(2208):20200394, 2021.
- [29] P.J. Collings and J.W. Goodby. *Introduction to liquid crystals: chemistry and physics*. CRC Press, 2019.

- [30] P.J. Collings, M. Hird, and C. Tschierske. Introduction to liquid crystals: Chemistry and physics. *Angewandte Chemie International Edition*, 36(18):2017, 1997.
- [31] COMSOL, Inc. COMSOL Multiphysics Version 6.1. Burlington, MA, USA, 2022.
- [32] M. Courtney, X. Chen, S. Chan, T. Mohamed, P.P. Rao, and C.L. Ren. Droplet microfluidic system with on-demand trapping and releasing of droplet for drug screening applications. *Analytical Chemistry*, 89(1):910–915, 2017.
- [33] J.R.L. Cousins, S.K. Wilson, N.J. Mottram, D. Wilkes, and L. Weegels. Squeezing a drop of nematic liquid crystal with strong elasticity effects. *Physics of Fluids*, 31(8):083107, 2019.
- [34] S. Datta, R. Barua, and J. Das. A review on electro-rheological fluid (er) and its various technological applications. Extremophilic Microbes and Metabolites-Diversity, Bioprospecting and Biotechnological Applications, 2020.
- [35] P.G. De Gennes and J. Prost. *The Physics of Liquid Crystals*. Oxford University Press, 1993.
- [36] P.G. A. De Gennes. Short range order effects in the isotropic phase of nematics and cholesterics. *Molecular Crystals and Liquid Crystals*, 12(3):193–214, 1971.
- [37] J. Denk and E. Frey. Pattern-induced local symmetry breaking in active-matter systems. *Proceedings of the National Academy of Sciences*, 117(50):31623–31630, 2020.
- [38] I. Dierking. Textures of Liquid Crystals. John Wiley & Sons, 2003.
- [39] A. Doostmohammadi, M.F. Adamer, S.P. Thampi, and J.M. Yeomans. Stabilization of active matter by flow-vortex lattices and defect ordering. *Nature Communications*, 7(1):10557, 2016.
- [40] A. Doostmohammadi, J. Ignés-Mullol, J.M. Yeomans, and F. Sagués. Active nematics. *Nature Communications*, 9(1):3246, 2018.

- [41] A. Doostmohammadi, T.N. Shendruk, K. Thijssen, and J.M. Yeomans. Onset of meso-scale turbulence in active nematics. *Nature Communications*, 8(1):15326, 2017.
- [42] A. Doostmohammadi and J.M. Yeomans. Coherent motion of dense active matter.

 European Physical Journal Special Topics, 227(17):2401–2411, 2019.
- [43] K. Drescher, J. Dunkel, L.H. Cisneros, S. Ganguly, and R E. Goldstein. Fluid dynamics and noise in bacterial cell-cell and cell-surface scattering. *Proceedings* of the National Academy of Sciences, 108(27):10940–10945, 2011.
- [44] G. Duclos, C. Blanch-Mercader, V. Yashunsky, G. Salbreux, J.-F. Joanny, J. Prost, and P. Silberzan. Spontaneous shear flow in confined cellular nematics. *Nature Physics*, 14(7):728–732, 2018.
- [45] S.A. Edwards and J.M. Yeomans. Spontaneous flow states in active nematics: a unified picture. *Europhysics Letters*, 85(1):18008, 2009.
- [46] J. Elgeti, M.E. Cates, and D. Marenduzzo. Defect hydrodynamics in 2d polar active fluids. *Soft Matter*, 7(7):3177–3185, 2011.
- [47] J.L. Ericksen. Hydrostatic theory of liquid crystals. Archive for Rational Mechanics and Analysis, 9(1):371–378, 1962.
- [48] C. Esteves, E. Ramou, A.R.P. Porteira, A.J. Moura Barbosa, and A.C.A. Roque. Seeing the unseen: the role of liquid crystals in gas-sensing technologies. *Advanced Optical Materials*, 8(11):1902117, 2020.
- [49] Y. Fan, K. Wu, S.A. Aghvami, S. Fraden, and K.S. Breuer. Effects of confinement on the dynamics and correlation scales in kinesin-microtubule active fluids. *Physical Review E*, 104(3):034601, 2021.
- [50] B.A. Finlayson and L.E. Scriven. Convective instability by active stress. Proceedings of the Royal Society A: Mathematical and Physical Sciences, 310(1501):183– 219, 1969.

- [51] G.A. Flores and J. Liu. Embolization of blood vessels as a cancer therapy using magnetorheological fluids. *Journal of Intelligent Material Systems and Structures*, 13(10):641–646, 2002.
- [52] E. Fodor and M.C. Marchetti. The statistical physics of active matter: From self-catalytic colloids to living cells. *Physica A: Statistical Mechanics and its Applications*, 504:106–120, 2018.
- [53] F.C. Frank. Liquid crystals: On the theory of liquid crystals. *Discussions of the Faraday Society*, 25:19–28, 1958.
- [54] V. Fréedericksz and A. Repiewa. Theoretisches und experimentelles zur frage nach der natur der anisotropen flüssigkeiten. Zeitschrift für Physik, 42(7):532– 546, 1927.
- [55] V. Fréedericksz and V. Zolina. Forces causing the orientation of an anisotropic liquid. *Transactions of the Faraday Society*, 29(140):919–930, 1933.
- [56] G. Friedel. Les états mésomorphes de la matière. In *Annales de Physique*, volume 18, pages 273–474, 1922.
- [57] L. Gattermann and A. Ritschke. Ueber azoxyphenoläther. Berichte der deutschen chemischen Gesellschaft, 23(1):1738–1750, 1890.
- [58] J.L. Geng and L. Song. Accurate modelling of nematic liquid crystal under the combination of microwave signal and applied voltage. *Liquid Crystals*, 47(1):67– 75, 2020.
- [59] L. Giomi. Geometry and topology of turbulence in active nematics. *Physical Review X*, 5(3):031003, 2015.
- [60] L. Giomi, M.J. Bowick, P. Mishra, R. Sknepnek, and C.M. Marchetti. Defect dynamics in active nematics. *Philosophical Transactions of the Royal Society A:* Mathematical, Physical and Engineering Sciences, 372(2029):20130365, 2014.

- [61] L. Giomi, T.B. Liverpool, and M.C. Marchetti. Sheared active fluids: Thickening, thinning, and vanishing viscosity. *Physical Review E*, 81(5):051908, 2010.
- [62] L. Giomi, L. Mahadevan, B. Chakraborty, and M.F. Hagan. Excitable patterns in active nematics. *Physical Review Letters*, 106(21):218101, 2011.
- [63] L. Giomi, L. Mahadevan, B. Chakraborty, and M.F. Hagan. Banding, excitability and chaos in active nematic suspensions. *Nonlinearity*, 25(8):2245, 2012.
- [64] L. Giomi and M.C. Marchetti. Polar patterns in active fluids. *Soft Matter*, 8(1):129–139, 2012.
- [65] L. Giomi, M.C. Marchetti, and T.B. Liverpool. Complex spontaneous flows and concentration banding in active polar films. *Physical Review Letters*, 101(19):198101, 2008.
- [66] L. Gómez-Nava, R. Bon, and F. Peruani. Intermittent collective motion in sheep results from alternating the role of leader and follower. *Nature Physics*, 18(12):1494–1501, 2022.
- [67] G.W. Gray, K.J. Harrison, and J.A. Nash. New family of nematic liquid crystals for displays. *Electronics Letters*, 9(6):130–131, 1973.
- [68] M. Grinfeld, M. Langer, and N.J. Mottram. Nematic viscosity estimation using director kickback dynamics. *Liquid Crystals*, 38(8):981–987, 2011.
- [69] H. Gruler, U. Dewald, and M. Eberhardt. Nematic liquid crystals formed by living amoeboid cells. *The European Physical Journal B*, 11:187–192, 1999.
- [70] E. A. Guggenheim. Thermodynamics: An Advanced Treatment for Chemists and Physicists. North-Holland, Amsterdam, 7 edition, 1985.
- [71] P. Guillamat, J. Ignés-Mullol, and F. Sagués. Control of active liquid crystals with a magnetic field. *Proceedings of the National Academy of Sciences*, 113(20):5498– 5502, 2016.

- [72] P. Guillamat, J. Ignés-Mullol, and F. Sagués. Taming active turbulence with patterned soft interfaces. *Nature Communications*, 8(1):564, 2017.
- [73] P. Guillamat, J. Ignés-Mullol, S. Shankar, M.C. Marchetti, and F. Sagués. Probing the shear viscosity of an active nematic film. *Physical Review E*, 94(6):060602, 2016.
- [74] P. Gulati, S. Shankar, and M.C. Marchetti. Boundaries control active channel flows. *Frontiers in Physics*, 10:675, 2022.
- [75] Y. Han and S. Choi. Force-feedback control of a spherical haptic device featuring an electrorheological fluid. *Smart Materials and Structures*, 15(5):1438, 2006.
- [76] J. Hardoüin. Active Liquid Crystals in Confinement. PhD thesis, Universitat de Barcelona, 2020.
- [77] J. Hardoüin, C. Doré, J. Laurent, T. Lopez-Leon, J. Ignés-Mullol, and F. Sagués. Active boundary layers in confined active nematics. *Nature Communications*, 13(1):6675, 2022.
- [78] J. Hardoüin, R. Hughes, A. Doostmohammadi, J. Laurent, T. Lopez-Leon, J.M. Yeomans, J. Ignés-Mullol, and F. Sagués. Reconfigurable flows and defect land-scape of confined active nematics. *Communications Physics*, 2(1):121, 2019.
- [79] R. Hartmann, P.K. Singh, P. Pearce, R. Mok, B. Song, F. Díaz-Pascual, J. Dunkel, and K. Drescher. Emergence of three-dimensional order and structure in growing biofilms. *Nature Physics*, 15(3):251–256, 2019.
- [80] L.C. Head, C. Doré, R.R. Keogh, L. Bonn, G. Negro, D. Marenduzzo, A. Doost-mohammadi, K. Thijssen, T. López-León, and T.N. Shendruk. Spontaneous self-constraint in active nematic flows. *Nature Physics*, 20(3):492–500, 2024.
- [81] E.J. Hemingway, P. Mishra, M.C. Marchetti, and S.M. Fielding. Correlation lengths in hydrodynamic models of active nematics. Soft Matter, 12(38):7943– 7952, 2016.

- [82] L.W. Honaker, C. Chen, F.M.H. Dautzenberg, S. Brugman, and S. Deshpande. Designing biological microsensors with chiral nematic liquid crystal droplets. ACS Applied Materials & Interfaces, 14(33):37316–37329, 2022.
- [83] W. Horsthemke, C.R. Doering, R. Lefever, and A.S. Chi. Effect of external-field fluctuations on instabilities in nematic liquid crystals. *Physical Review A*, 31(2):1123, 1985.
- [84] J. Hu, M. Yang, G. Gompper, and R.G. Winkler. Modelling the mechanics and hydrodynamics of swimming e. coli. *Soft Matter*, 11(40):7867–7876, 2015.
- [85] C. Huang, L. Lou, and C. Lee. Calibration-free force sensors using liquid crystal arrays. In *SENSORS*, 2012 IEEE, pages 1–4. IEEE, 2012.
- [86] G. Huber, S.A. Koehler, and J. Yang. Micro-swimmers with hydrodynamic interactions. *Mathematical and Computer Modelling*, 53(7-8):1518–1526, 2011.
- [87] T. Ihle. Kinetic theory of flocking: Derivation of hydrodynamic equations. *Physical Review E*, 83(3):030901, 2011.
- [88] Waterloo Maple Inc. Maple 2018: Standard Worksheet Interface. Waterloo Maple Inc., Waterloo, Ontario, Canada, 2018. Build ID 1330573, x86 64, Windows 10. Released March 2018.
- [89] B. Jerome. Surface effects and anchoring in liquid crystals. Reports on Progress in Physics, 54(3):391, 1991.
- [90] J.-F. Joanny, F. Jülicher, K. Kruse, and J. Prost. Hydrodynamic theory for multi-component active polar gels. *New Journal of Physics*, 9(11):422, 2007.
- [91] F. Juelicher, K. Kruse, J. Prost, and J-F. Joanny. Active behavior of the cytoskeleton. *Physics Reports*, 449(1-3):3–28, 2007.
- [92] P. Kalita, S.S. Shukla, R.K. Singh, and A. Bhattacharjee. Potential liquid crystal-based biosensor depending on the interaction between liquid crystals and pro-

- teins. Spectrochimica Acta Part A: Molecular and Biomolecular Spectroscopy, 254:119634, 2021.
- [93] S. Kaluvan, J.H. Park, Y.S. Lee, M.S. Han, and S.B. Choi. A new measurement method for operation mode dependent dynamic behavior of magnetorheological fluid. Proceedings of the Institution of Mechanical Engineers, Part C: Journal of Mechanical Engineering Science, 231(18):3358–3369, 2017.
- [94] B. Kang, B. Kim, D. Jung, and S. Choi. A mathematical model of cavitation behaviour in a single-ended magnetorheological damper: experimental validation. Smart Materials and Structures, 31(3):035012, 2022.
- [95] H. Kelker. History of liquid crystals. *Molecular Crystals and Liquid Crystals*, 21(1-2):1-48, 1973.
- [96] H. Kelker and B. Scheurle. A liquid-crystalline (nematic) phase with a particularly low solidification point. Angewandte Chemie International Edition in English, 8(11):884–885, 1969.
- [97] R. Kemkemer, D. Kling, D. Kaufmann, and H. Gruler. Elastic properties of nematoid arrangements formed by amoeboid cells. *European Physical Journal E*, 1:215–225, 2000.
- [98] J.O. Kessler. Gyrotactic buoyant convection and spontaneous pattern formation in algal cell cultures. In Nonequilibrium cooperative phenomena in physics and related fields, pages 241–248. Springer, 1984.
- [99] J. Kim, J. Kim, S. Choi, and K. Kim. Er inserts for shock wave reduction in structures. *International Journal of Vehicle Design*, 33(1-3):296–308, 2003.
- [100] J. Kim, S. Kumar, and S. Lee. Alignment of liquid crystals on polyimide films exposed to ultraviolet light. *Physical Review E*, 57(5):5644, 1998.
- [101] S. Kim, P. Kim, C. Park, and S. Choi. A new tactile device using magnetorheological sponge cells for medical applications: Experimental investigation. Sen-

- sors and Actuators A: Physical, 239:61–69, 2016.
- [102] A.D. Kiselev. Saddle-splay-term-induced orientational instability in nematicliquid-crystal cells and director fluctuations at substrates. *Physical Review E*, 69(4):041701, 2004.
- [103] J.U. Klamser, S.C. Kapfer, and W. Krauth. Thermodynamic phases in twodimensional active matter. *Nature Communications*, 9(1):5045, 2018.
- [104] M. Kleman and O. Lavrentovich. Soft matter physics: an introduction. Springer, 2003.
- [105] T. Kozhukhov and T.N. Shendruk. Mesoscopic simulations of active nematics. Science Advances, 8(34):eabo5788, 2022.
- [106] K. Kruse, J. Joanny, F. Jülicher, J. Prost, and K. Sekimoto. Asters, vortices, and rotating spirals in active gels of polar filaments. *Physical Review Letters*, 92(7):078101, 2004.
- [107] K. Kruse, J. Joanny, F. Jülicher, J. Prost, and K. Sekimoto. Generic theory of active polar gels: a paradigm for cytoskeletal dynamics. *European Physical Journal E*, 16:5–16, 2005.
- [108] K. Kruse and F. Jülicher. Self-organization and mechanical properties of active filament bundles. *Physical Review E*, 67(5):051913, 2003.
- [109] N. Kumar, R. Zhang, S.A. Redford, J.J. de Pablo, and M.L. Gardel. Catapulting of topological defects through elasticity bands in active nematics. *Soft Matter*, 18(28):5271–5281, 2022.
- [110] N.M. Kuznetsov, V.V. Kovaleva, S.I. Belousov, and S.N. Chvalun. Electrorheological fluids: from historical retrospective to recent trends. *Materials Today Chemistry*, 26:101066, 2022.
- [111] E. Lauga and T.R. Powers. The hydrodynamics of swimming microorganisms.

 Reports on Progress in Physics, 72(9):096601, 2009.

- [112] O. Lehmann. Über fliessende krystalle. Zeitschrift für physikalische Chemie, 4(1):462–472, 1889.
- [113] F.M. Leslie. Some constitutive equations for anisotropic fluids. *The Quarterly Journal of Mechanics and Applied Mathematics*, 19(3):357–370, 1966.
- [114] F.M. Leslie. Continuum theory for nematic liquid crystals. *Continuum Mechanics* and *Thermodynamics*, 4(3):167–175, 1992.
- [115] F.M. Leslie. Liquid crystal devices. Technical Report, Instituut Wiskundige Dienstverlening, Technische Universiteit Eindhoven, 1992.
- [116] B. Li, H.P. Chan, K.T. Ahmmed, L. He, S. Zhu, and Q. Wu. High-sensitivity magnetic sensor based on the evanescent scattering by a magnetorheological film. *Optics Letters*, 45(24):6643–6646, 2020.
- [117] W. Li, K. Kostidis, X. Zhang, and Y. Zhou. Development of a force sensor working with mr elastomers. In 2009 IEEE/ASME International Conference on Advanced Intelligent Mechatronics, pages 233–238. IEEE, 2009.
- [118] Michael James Lighthill. On the squirming motion of nearly spherical deformable bodies through liquids at very small reynolds numbers. Communications on Pure and Applied Mathematics, 5(2):109–118, 1952.
- [119] Y.D. Liu and H.J. Choi. Electrorheological fluids: smart soft matter and characteristics. *Soft Matter*, 8(48):11961–11978, 2012.
- [120] T.B. Liverpool. Anomalous fluctuations of active polar filaments. *Physical Review* E, 67(3):031909, 2003.
- [121] T.B. Liverpool and M. C. Marchetti. Rheology of active filament solutions. *Physical Review Letters*, 97(26):268101, 2006.
- [122] T.B. Liverpool, M. C. Marchetti, J.F. Joanny, and J. Prost. Mechanical response of active gels. *Europhysics Letters*, 85(1):18007, 2009.

- [123] T.B. Liverpool and M.C. Marchetti. Instabilities of isotropic solutions of active polar filaments. *Physical Review Letters*, 90(13):138102, 2003.
- [124] W. Maier and A. Saupe. A simple molecular statistical theory of the nematic crystalline-liquid phase. *IZ Naturf. a*, 14:882–889, 1959.
- [125] D. Maoutsa, S. Reich, and M. Opper. Interacting particle solutions of fokker– planck equations through gradient–log–density estimation. *Entropy*, 22(8):802, 2020.
- [126] M.C. Marchetti, J. Joanny, S. Ramaswamy, T.B. Liverpool, J. Prost, M. Rao, and R.A. Simha. Hydrodynamics of soft active matter. *Reviews of Modern Physics*, 85(3):1143–1189, 2013.
- [127] D. Marenduzzo, E. Orlandini, M.E. Cates, and J.M. Yeomans. Steady-state hydrodynamic instabilities of active liquid crystals: Hybrid lattice boltzmann simulations. *Physical Review E*, 76(3):031921, 2007.
- [128] D. Marenduzzo, E. Orlandini, and J.M. Yeomans. Hydrodynamics and rheology of active liquid crystals: a numerical investigation. *Physical Review Letters*, 98(11):118102, 2007.
- [129] S. Mathews, G. Farrell, and Y. Semenova. Directional electric field sensitivity of a liquid crystal infiltrated photonic crystal fiber. *IEEE Photonics Technology Letters*, 23(7):408–410, 2011.
- [130] MATLAB. MATLAB version 9.12.0.1975300 (R2022a). The MathWorks Inc., Natick, Massachusetts, 2022.
- [131] C. Mauguin. Sur les cristaux liquides de m. lehmann. Bulletin de Minéralogie, 34(3):71–117, 1911.
- [132] C. Mettenheimer. Corr.-Blatt des Vereins für gemeinsame Arbeit zur Förderung der wissenschaftlichen Heilkunde. Springer, 1867.

- [133] M. Miesowicz. The three coefficients of viscosity of anisotropic liquids. *Nature*, 158(4001):27–27, 1946.
- [134] E. Miraldi, C. Oldano, and A. Strigazzi. Periodic fréedericksz transition for nematic-liquid-crystal cells with weak anchoring. *Physical Review A*, 34(5):4348, 1986.
- [135] P. Mishra. Pattern formation in active nematics. PhD thesis, Syracuse University, 2017.
- [136] S. Mishra and S. Ramaswamy. Active nematics are intrinsically phase separated. *Physical Review Letters*, 97(9):090602, 2006.
- [137] P.S. Mondal, P.K. Mishra, T. Vicsek, and A.S. Mishra. Dynamical swirl structures powered by microswimmers in active nematics. *Physica A: Statistical Mechanics* and its Applications, 659:130338, 2025.
- [138] M. Morozov and S. Michelin. Orientational instability and spontaneous rotation of active nematic droplets. *Soft Matter*, 15(39):7814–7822, 2019.
- [139] J.K. Moscicki. Measurements of viscosities in nematics. *EMIS Datareviews Series*, 25:387–404, 2001.
- [140] S. Muhuri, M. Rao, and S. Ramaswamy. Shear-flow-induced isotropic-to-nematic transition in a suspension of active filaments. *Europhysics Letters*, 78(4):48002, 2007.
- [141] I. Muševič. Nematic liquid-crystal colloids. *Materials*, 11(1):24, 2018.
- [142] K. Nayani, P. Rai, N. Bao, H. Yu, M. Mavrikakis, R.J. Twieg, and N.L. Abbott. Liquid crystals with interfacial ordering that enhances responsiveness to chemical targets. *Advanced Materials*, 30(27):1706707, 2018.
- [143] D.K. Nguyen and C.H. Jang. An acetylcholinesterase-based biosensor for the detection of pesticides using liquid crystals confined in microcapillaries. *Colloids* and Surfaces B: Biointerfaces, 200:111587, 2021.

- [144] J. Nijjer, C. Li, M. Kothari, T. Henzel, Q. Zhang, J.B. Tai, S. Zhou, T. Cohen, S. Zhang, and J. Yan. Biofilms as self-shaping growing nematics. *Nature Physics*, 19(12):1936–1944, 2023.
- [145] X. Niu, Y. Zhong, R. Chen, F. Wang, and D. Luo. Highly sensitive and selective liquid crystal optical sensor for detection of ammonia. Optics Express, 25(12):13549–13556, 2017.
- [146] J. Norman. Liquid crystal droplet lasers for chemical sensing. PhD thesis, The University of Edinburgh, 2024.
- [147] M.M. Norton, A. Baskaran, A. Opathalage, B. Langeslay, S. Fraden, and M.F. Hagan. Insensitivity of active nematic liquid crystal dynamics to topological constraints. *Physical Review E*, 97(1):012702, 2018.
- [148] C.W. Oseen. The theory of liquid crystals. *Transactions of the Faraday Society*, 29(140):883–899, 1933.
- [149] P. Oswald and P. Pieranski. Nematic and cholesteric liquid crystals: concepts and physical properties illustrated by experiments. CRC Press, 2005.
- [150] P. Oswald and P. Pieranski. Smectic and columnar liquid crystals: concepts and physical properties illustrated by experiments. CRC Press, 2005.
- [151] Y. Park and S. Choi. Sensors and sensing devices utilizing electrorheological fluids and magnetorheological materials—a review. *Sensors*, 24(9):2842, 2024.
- [152] Y. Park, B. Kim, E. Lee, and S. Choi. A novel tactile sensing system utilizing magnetorheological structures for dynamic contraction and relaxation motions. Sensors, 23(22):9035, 2023.
- [153] Y. Park, E. Lee, and S. Choi. A cylindrical grip type of tactile device using magneto-responsive materials integrated with surgical robot console: design and analysis. Sensors, 22(3):1085, 2022.

- [154] Y. Park, J. Yoon, B. Kang, G. Kim, and S. Choi. A tactile device generating repulsive forces of various human tissues fabricated from magnetic-responsive fluid in porous polyurethane. *Materials*, 13(5):1062, 2020.
- [155] D.S. Parmar and H.K. Holmes. Pressure sensor using liquid crystals, May 10 1994. US Patent 5,309,767.
- [156] O. Parodi. Stress tensor for a nematic liquid crystal. *Journal de Physique*, 31(7):581–584, 1970.
- [157] A.E. Patteson, A. Gopinath, and P.E. Arratia. Active colloids in complex fluids.

 *Current Opinion in Colloid & Interface Science, 21:86–96, 2016.
- [158] E. Pavlikova, T. Plachy, M. Urbanek, and M. Cvek. Engineering conductivity and performance in electrorheological fluids using a nanosilica grafting approach. ACS Applied Nano Materials, 6(11):9768–9776, 2023.
- [159] M. Peccianti and G. Assanto. Signal readdressing by steering of spatial solitons in bulk nematic liquid crystals. *Optics Letters*, 26(21):1690–1692, 2001.
- [160] T.J. Pedley and J.O. Kessler. The orientation of spheroidal microorganisms swimming in a flow field. Proceedings of the Royal Society of London. Series B. Biological Sciences, 231(1262):47–70, 1987.
- [161] T.J. Pedley and J.O. Kessler. Hydrodynamic phenomena in suspensions of swimming microorganisms. *Annual Review of Fluid Mechanics*, 24(1):313–358, 1992.
- [162] G. Pelzl, P. Schiller, and D. Demus. Fréedericksz transition of planar oriented smectic c phases. *Liquid Crystals*, 2(2):131–148, 1987.
- [163] G. Pepe, N. Roveri, and A. Carcaterra. Experimenting sensors network for innovative optimal control of car suspensions. *Sensors*, 19(14):3062, 2019.
- [164] F. Peruani, A. Deutsch, and M. Bär. Nonequilibrium clustering of self-propelled rods. *Physical Review E*, 74(3):030904, 2006.

- [165] A. Peshkov, I.S. Aranson, E. Bertin, H. Chaté, and F. Ginelli. Nonlinear field equations for aligning self-propelled rods. *Physical Review Letters*, 109(26):268701, 2012.
- [166] A.G. Petrov. The Lyotropic State of Matter: Molecular Physics and Living Matter Physics. CRC Press, 1999.
- [167] P. Pieranski, F. Brochard, and E. Guyon. Static and dynamic behavior of a nematic liquid crystal in a magnetic field. part ii: Dynamics. *Journal de Physique*, 34(1):35–48, 1973.
- [168] O.P. Pishnyak, S.V. Shiyanovskii, and O.D. Lavrentovich. Inelastic collisions and anisotropic aggregation of particles in a nematic collider driven by backflow. *Physical Review Letters*, 106(4):047801, 2011.
- [169] O.P. Pishnyak, S. Tang, J.R. Kelly, S.V. Shiyanovskii, and O.D. Lavrentovich. Levitation, lift, and bidirectional motion of colloidal particles in an electrically driven nematic liquid crystal. *Physical Review Letters*, 99(12):127802, 2007.
- [170] A.R. Plastino and R.S. Wedemann. Nonlinear fokker–planck equation approach to systems of interacting particles: thermostatistical features related to the range of the interactions. *Entropy*, 22(2):163, 2020.
- [171] P. Popov, E.K. Mann, and A. Jákli. Thermotropic liquid crystal films for biosensors and beyond. *Journal of Materials Chemistry B*, 5(26):5061–5078, 2017.
- [172] V.J. Pratley, E. Caf, M. Ravnik, and G.P. Alexander. Three-dimensional spontaneous flow transition in a homeotropic active nematic. *Communications Physics*, 7(1):127, 2024.
- [173] J. Prost, F. Jülicher, and J.F. Joanny. Active gel physics. *Nature Physics*, 11(2):111–117, 2015.
- [174] E.M. Purcell. Life at low reynolds number. *American Journal of Physics*, 45(1):3–11, 1977.

- [175] S. Ramaswamy. The mechanics and statistics of active matter. Annual Review of Condensed Matter Physics, 1(1):323–345, 2010.
- [176] S. Ramaswamy, R.A. Simha, and J. Toner. Active nematics on a substrate: Giant number fluctuations and long-time tails. *Europhysics Letters*, 62(2):196, 2003.
- [177] A. Rapini and M. Papoular. Distorsion d'une lamelle nématique sous champ magnétique conditions d'ancrage aux parois. Le Journal de Physique Colloques, 30(C4):C4-54, 1969.
- [178] M. Ravnik and J.M. Yeomans. Confined active nematic flow in cylindrical capillaries. *Physical Review Letters*, 110(2):026001, 2013.
- [179] J.A. Rego, J.A. Harvey, A.L. MacKinnon, and E. Gatdula. Asymmetric synthesis of a highly soluble 'trimeric' analogue of the chiral nematic liquid crystal twist agent merck s1011. *Liquid Crystals*, 37(1):37–43, 2009.
- [180] F. Reinitzer. Beiträge zur kenntniss des cholesterins. *Monatshefte für Chemie*, 9(1):421–441, 1888.
- [181] A. Repula, C. Gates, J.C. Cameron, and I.I. Smalyukh. Photosynthetically-powered phototactic active nematic liquid crystal fluids and gels. *Communications Materials*, 5(1):37, 2024.
- [182] D.P. Rivas, T.N. Shendruk, R.R. Henry, D.H. Reich, and R.L. Leheny. Driven topological transitions in active nematic films. Soft Matter, 16(40):9331–9338, 2020.
- [183] J. Rønning, C.M. Marchetti, M.J. Bowick, and L. Angheluta. Flow around topological defects in active nematic films. *Proceedings of the Royal Society A*, 478(2257):20210879, 2022.
- [184] C. Rorai, F. Toschi, and I. Pagonabarraga. Active nematic flows confined in a two-dimensional channel with hybrid alignment at the walls: A unified picture. *Physical Review Fluids*, 6(11):113302, 2021.

- [185] D. Saintillan and M. J. Shelley. Instabilities, pattern formation, and mixing in active suspensions. *Physics of Fluids*, 20(12), 2008.
- [186] D. Saintillan and M.J. Shelley. Active suspensions and their nonlinear models. Comptes Rendus Physique, 14(6):497–517, 2013.
- [187] A. Samui, J.M. Yeomans, and S.P. Thampi. Flow transitions and length scales of a channel-confined active nematic. *Soft Matter*, 17(47):10640–10648, 2021.
- [188] T. Sanchez, D.T.N. Chen, S.J. DeCamp, M. Heymann, and Z. Dogic. Spontaneous motion in hierarchically assembled active matter. *Nature*, 491(7424):431–434, 2012.
- [189] M. Schienbein and H. Gruler. Chemical amplifier, self-ignition mechanism, and amoeboid cell migration. *Physical Review E*, 52(4):4183, 1995.
- [190] C.D. Schimming, C.J.O. Reichhardt, and C. Reichhardt. Turbulence-to-order transitions in activity-patterned active nematics. *Physical Review E*, 111(3):035404, 2025.
- [191] F. Schmidt. Active Matter in a Critical State: From passive building blocks to active molecules, engines and active droplets. PhD thesis, University of Gothenburg, 2020.
- [192] C. Schütz, J.R. Bruckner, C. Honorato-Rios, Z. Tosheva, M. Anyfantakis, and J.P.F. Lagerwall. From equilibrium liquid crystal formation and kinetic arrest to photonic bandgap films using suspensions of cellulose nanocrystals. *Crystals*, 10(3):199, 2020.
- [193] J.V. Selinger. Interpretation of saddle-splay and the oseen–frank free energy in liquid crystals. *Liquid Crystals Reviews*, 6(2):129–142, 2018.
- [194] J.V. Selinger. Director deformations, geometric frustration, and modulated phases in liquid crystals. *Annual Review of Condensed Matter Physics*, 13(1):49–71, 2022.

- [195] A. Sengupta. Topological microfluidics: nematic liquid crystals and nematic colloids in microfluidic environment. Springer Science & Business Media, 2013.
- [196] M.R. Shaebani, A. Wysocki, R.G. Winkler, G. Gompper, and H. Rieger. Computational models for active matter. *Nature Reviews Physics*, 2(4):181–199, 2020.
- [197] T.N. Shendruk, A. Doostmohammadi, K. Thijssen, and J.M. Yeomans. Dancing disclinations in confined active nematics. *Soft Matter*, 13(21):3853–3862, 2017.
- [198] R.A. Simha and S. Ramaswamy. Statistical hydrodynamics of ordered suspensions of self-propelled particles: waves, giant number fluctuations and instabilities.

 Physica A: Statistical Mechanics and its Applications, 306:262–269, 2002.
- [199] A. Singh, Q. Vagne, F. Jülicher, and I.F. Sbalzarini. Spontaneous flow instabilities of active polar fluids in three dimensions. *Physical Review Research*, 5(2):L022061, 2023.
- [200] T. Spotowski, K. Osowski, I. Musiałek, A. Olszak, A. Kęsy, Z. Kęsy, and S. Choi. A feedback control sensing system of an electrorheological brake to exert a constant pressing force on an object. Sensors, 23(15):6996, 2023.
- [201] R.S.J.L. Stanway, J.L. Sproston, and A.K. El-Wahed. Applications of electrorheological fluids in vibration control: a survey. Smart Materials and Structures, 5(4):464, 1996.
- [202] I.W. Stewart. Static and Dynamic Continuum Theory of Liquid Crystals: A Mathematical Introduction. Taylor & Francis Group, 2004.
- [203] T. Strübing, A. Khosravanizadeh, A. Vilfan, E. Bodenschatz, R. Golestanian, and I. Guido. Wrinkling instability in 3d active nematics. Nano Letters, 20(9):6281–6288, 2020.
- [204] X. Su, J. Xu, J. Zhang, D. Yang, W. Huo, and C. He. Detection of cecropin b by liquid-crystal biosensor based on aunps signal amplification. *Liquid Crystals*, 47(12):1794–1802, 2020.

- [205] B. Sun, Y. Huang, D. Luo, C. Wang, J. He, C. Liao, G. Yin, J. Zhou, S. Liu, J. Zhao, Z. Jing, and W. Yiping. Broadband thermo-optic switching effect based on liquid crystal infiltrated photonic crystal fibers. *IEEE Photonics Journal*, 7(4):1–7, 2015.
- [206] H. Tan, X. Li, S. Liao, R. Yu, and Z. Wu. Highly-sensitive liquid crystal biosensor based on dna dendrimers-mediated optical reorientation. *Biosensors and Bioelectronics*, 62:84–89, 2014.
- [207] X. Tang and J.V. Selinger. Theory of defect motion in 2d passive and active nematic liquid crystals. *Soft Matter*, 15(4):587–601, 2019.
- [208] G.I. Taylor. Analysis of the swimming of microscopic organisms. *Proceedings of the Royal Society of London. Series A*, 209(1099):447–461, 1951.
- [209] M. Te Vrugt and R. Wittkowski. Metareview: a survey of active matter reviews. The European Physical Journal E, 48(3):12, 2025.
- [210] M.M. Tefelska, T.R. Woliński, S. Ertman, K. Mileńko, R. Łączkowski, A. Siarkowska, and A.W. Domański. Electric field sensing with photonic liquid crystal fibers based on micro-electrodes systems. *Journal of Lightwave Technol*ogy, 33(12):2405–2411, 2014.
- [211] S.P. Thampi. Channel confined active nematics. Current Opinion in Colloid & Interface Science, 61:101613, 2022.
- [212] S.P. Thampi, R. Golestanian, and J.M. Yeomans. Velocity correlations in an active nematic. *Physical Review Letters*, 111(11):118101, 2013.
- [213] S.P. Thampi, R. Golestanian, and J.M. Yeomans. Active nematic materials with substrate friction. *Physical Review E*, 90(6):062307, 2014.
- [214] S.P. Thampi, R. Golestanian, and J.M. Yeomans. Instabilities and topological defects in active nematics. *Europhysics Letters*, 105(1):18001, 2014.

- [215] S.P. Thampi, R. Golestanian, and J.M. Yeomans. Driven active and passive nematics. *Molecular Physics*, 113(17–18):2656–2665, 2015.
- [216] A. Tiribocchi, R. Wittkowski, D. Marenduzzo, and M.E. Cates. Active model h: scalar active matter in a momentum-conserving fluid. *Physical Review Letters*, 115(18):188302, 2015.
- [217] E. Tjhung, M.E. Cates, and D. Marenduzzo. Nonequilibrium steady states in polar active fluids. *Soft Matter*, 7(16):7453–7464, 2011.
- [218] E. Tjhung, D. Marenduzzo, and M.E. Cates. Spontaneous symmetry breaking in active droplets provides a generic route to motility. *Proceedings of the National Academy of Sciences*, 109(31):12381–12386, 2012.
- [219] J. Toner and Y. Tu. Long-range order in a two-dimensional dynamical xy model: how birds fly together. *Physical Review Letters*, 75(23):4326–4329, 1995.
- [220] J. Toner and Y. Tu. Flocks, herds, and schools: A quantitative theory of flocking.

 Physical Review E, 58(4):4828–4858, 1998.
- [221] J. Toner, Y. Tu, and S. Ramaswamy. Hydrodynamics and phases of flocks. *Annals of Physics*, 318(1):170–244, 2005.
- [222] G. Tóth, C. Denniston, and J.M. Yeomans. Hydrodynamics of topological defects in nematic liquid crystals. *Physical Review Letters*, 88(10):105504, 2002.
- [223] G. Tóth, C. Denniston, and J.M. Yeomans. Hydrodynamics of domain growth in nematic liquid crystals. *Physical Review E*, 67(5):051705, 2003.
- [224] D.Q. Truong and K.K. Ahn. Identification and application of black-box model for a self-sensing damping system using a magneto-rheological fluid damper. Sensors and Actuators A: Physical, 161(1-2):305–321, 2010.
- [225] J. Turk and D. Svenšek. Backflow-mediated domain switching in nematic liquid crystals. *Physical Review E*, 89(3):032508, 2014.

- [226] M. Urbanski, C.G. Reyes, J. Noh, A. Sharma, Y. Geng, V. Subba R. Jampani, and J.P.F. Lagerwall. Liquid crystals in micron-scale droplets, shells and fibers. Journal of Physics: Condensed Matter, 29(13):133003, 2017.
- [227] F. Vafa. Defect dynamics in active polar fluids vs. active nematics. *Soft Matter*, 18(42):8087–8097, 2022.
- [228] G. Valentin. Die Untersuchung der Pflanzen- und der Thiergewebe in polarisiertem Lichte. W. Engelmann, 1861.
- [229] M. Varghese, A. Baskaran, M.F. Hagan, and A. Baskaran. Confinement-induced self-pumping in 3d active fluids. *Physical Review Letters*, 125(26):268003, 2020.
- [230] I. Vélez-Ceron, R.C.V. Coelho, P. Guillamat, M. da Gama, F. Sagués, and J. Ignés-Mullol. Active nematic pumps. arXiv preprint arXiv:2407.09960, 2024.
- [231] L. Vicari. Optical applications of liquid crystals. CRC Press, 2016.
- [232] T. Vicsek, A. Czirók, E. Ben-Jacob, I. Cohen, and O. Shochet. Novel type of phase transition in a system of self-driven particles. *Physical Review Letters*, 75(6):1226, 1995.
- [233] R. Virchow. Ueber ein eigenthümliches verhalten albuminöser flüssigkeiten bei zusatz von salzen. Archiv für pathologische Anatomie und Physiologie und für klinische Medicin, 6(4):572–580, 1854.
- [234] E.G. Virga. Variational theories for liquid crystals. Chapman and Hall, 1994.
- [235] E.G. Virga. Variational theories for liquid crystals. Chapman and Hall/CRC, 2018.
- [236] R. Voituriez, J.F. Joanny, and J. Prost. Spontaneous flow transition in active polar gels. *Europhysics Letters*, 70(3):404, 2005.
- [237] R. Voituriez, J.F. Joanny, and J. Prost. Generic phase diagram of active polar films. *Physical Review Letters*, 96(2):028102, 2006.

- [238] J. Walton. Mathematical Modelling of Active Nematic Liquid Crystals in Confined Regions. PhD thesis, University of Strathclyde, 2020.
- [239] H. Wang, T. Xu, Y. Fu, Z. Wang, M.S. Leeson, J. Jiang, and T. Liu. Liquid crystal biosensors: principles, structure and applications. *Biosensors*, 12(8):639, 2022.
- [240] W. Wang and R. Zhang. Interplay of active stress and driven flow in self-assembled, tumbling active nematics. *Crystals*, 11(9):1071, 2021.
- [241] W. Wen, X. Huang, and P. Sheng. Electrorheological fluids: structures and mechanisms. *Soft Matter*, 4(2):200–210, 2008.
- [242] H.H. Wensink, J. Dunkel, S. Heidenreich, K. Drescher, R.E. Goldstein, H. Löwen, and J.M. Yeomans. Meso-scale turbulence in living fluids. *Proceedings of the National Academy of Sciences*, 109(36):14308–14313, 2012.
- [243] C.A. Whitfield and R.J. Hawkins. Instabilities, motion and deformation of active fluid droplets. *New Journal of Physics*, 18(12):123016, 2016.
- [244] H. Wioland, E. Lushi, and R.E. Goldstein. Directed collective motion of bacteria under channel confinement. *New Journal of Physics*, 18(7):075002, 2016.
- [245] H. Wioland, F.G. Woodhouse, J. Dunkel, J.O. Kessler, and R.E. Goldstein. Confinement stabilizes a bacterial suspension into a spiral vortex. *Physical Review Letters*, 110(26):268102, 2013.
- [246] R. Wittkowski, A. Tiribocchi, J. Stenhammar, R.J. Allen, D. Marenduzzo, and M.E. Cates. Scalar φ 4 field theory for active-particle phase separation. *Nature Communications*, 5(1):4351, 2014.
- [247] S.J. Woltman, G.D. Jay, and G.P. Crawford. Liquid-crystal materials find a new order in biomedical applications. *Nature Materials*, 6(12):929–938, 2007.
- [248] K. Wu, J.B. Hishamunda, D.T.N. Chen, S.J. DeCamp, Y. Chang, A. Fernández-Nieves, S. Fraden, and Z. Dogic. Transition from turbulent to coherent flows in

- confined three-dimensional active fluids. Science, 355(6331):eaal1979, 2017.
- [249] C.Y. Xue and K.L. Yang. Dark-to-bright optical responses of liquid crystals supported on solid surfaces decorated with proteins. *Langmuir*, 24(2):563–567, 2008.
- [250] T. Yakoh and T. Aoyama. Application of electro-rheological fluids to flexible mount and damper devices. In 2000 26th Annual Conference of the IEEE Industrial Electronics Society. IECON 2000. 2000 IEEE International Conference on Industrial Electronics, Control and Instrumentation. 21st Century Technologies, volume 3, pages 1815–1820. IEEE, 2000.
- [251] Y.I. Yaman, E. Demir, R. Vetter, and A. Kocabas. Emergence of active nematics in chaining bacterial biofilms. *Nature Communications*, 10(1):2285, 2019.
- [252] X. Yang, Q. Wang, and M.G. Forest. Near equilibrium dynamics and onedimensional spatial—temporal structures of polar active liquid crystals. *Chinese Physics B*, 23(11):118701, 2014.
- [253] Y. Yang, V. Marceau, and G. Gompper. Swarm behavior of self-propelled rods and swimming flagella. *Physical Review E*, 82(3):031904, 2010.
- [254] O. Yaroshchuk and Y. Reznikov. Photoalignment of liquid crystals: basics and current trends. *Journal of Materials Chemistry*, 22(2):286–300, 2012.
- [255] Z. You, D.J.G. Pearce, and L. Giomi. Confinement-induced self-organization in growing bacterial colonies. *Science Advances*, 7(4):eabc8685, 2021.
- [256] H. Zhang, A. Be'er, E.L. Florin, and H.L. Swinney. Collective motion and density fluctuations in bacterial colonies. *Proceedings of the National Academy of Sciences*, 107(31):13626–13630, 2010.
- [257] R. Zhang, Y. Zhou, M. Rahimi, and J.J. de Pablo. Dynamic structure of active nematic shells. *Nature Communications*, 7:13483, 2016.

- [258] X. Zhang, W. Li, W. Wen, Y. Wu, and G. Wallace. Development of electrorheological chip and conducting polymer-based sensor. Frontiers of Mechanical Engineering in China, 4(4):393–396, 2009.
- [259] K. Žiga and M. Ravnik. Field generated nematic microflows via backflow mechanism. *Scientific Reports*, 10(1):1446, 2020.
- [260] H. Zocher. The effect of magnetic field on nematic state. Transactions of the Faraday Society, 29:945–957, 1933.